

Introduction to Gravitational Lensing

With python examples

Massimo Meneghetti

Copyright © 2017 Massimo Meneghetti

PUBLISHED BY MASSIMO MENEGHETTI

[HTTP://PICO.BO.ASTRO.IT/MASSIMO/TEACHING.HTML](http://PICO.BO.ASTRO.IT/MASSIMO/TEACHING.HTML)

Licensed under the Creative Commons Attribution-NonCommercial 3.0 Unported License (the “License”). You may not use this file except in compliance with the License. You may obtain a copy of the License at <http://creativecommons.org/licenses/by-nc/3.0>. Unless required by applicable law or agreed to in writing, software distributed under the License is distributed on an “AS IS” BASIS, WITHOUT WARRANTIES OR CONDITIONS OF ANY KIND, either express or implied. See the License for the specific language governing permissions and limitations under the License.

First printing, March 2017

Contents

Part One: Generalities	
1	Light deflection
1.1	Deflection of a light corpuscle
1.2	Deflection of light according to General Relativity
1.2.1	Fermat principle and light deflection
1.2.2	Deflection of light in the strong field limit
1.3	Deflection by an ensemble of point masses
1.4	Deflection by an extended mass distribution
1.5	Python applications
1.5.1	Deflection by a black-hole
1.5.2	Deflection by an extended mass distribution
1.6	Problems
2	The general lens
2.1	Lens equation
2.2	Lensing potential
2.3	First order lens mapping
2.3.1	Lensing of circular source
2.4	Magnification
2.5	Lensing to the second order
2.5.1	Complex notation
2.6	Time delay surface
2.6.1	Gravitational and geometrical time delays

2.6.2	Multiple images and magnification	41
2.6.3	Examples	42
2.6.4	General considerations	47
2.7	Python applications	49
2.7.1	Implementing a ray-tracing algorithm	49
2.7.2	Derivation of the lensing potential	51
2.7.3	Lensing maps	53
2.7.4	Critical lines and caustics	56
2.7.5	Shear and flexion	60
2.7.6	Full ray-tracing simulation and time delay surface	62

II

Part Two: Applications

3	Microlensing	77
3.1	The point mass lens	77
3.2	Microlensing light-curve	81
3.2.1	Light-curve fitting	83
3.3	Microlensing parallax	85
3.4	Photometric microlensing: optical depth and event rates	88
3.4.1	Optical depth	88
3.4.2	Event rate	92
3.5	Results from MACHO searches	93
3.6	Astrometric microlensing	93
3.7	Multiple point masses	99
3.7.1	Generalities	99
3.7.2	Binary lenses	101
3.8	Planetary microlensing	105
3.9	Python applications	115
3.9.1	Standard microlensing light curve	115
3.9.2	Fitting the standard light curve	118
3.9.3	Distribution of microlensing event timescale	122
3.9.4	Astrometric microlensing effect	126
3.9.5	Critical lines and caustics of a binary lens	132
3.9.6	Solving the lens equation of the binary lens	135
3.9.7	Light curve in a binary microlensing event	136
4	Extended lenses	139
4.1	Axially symmetric lenses	139
4.2	Power-law lens	145
4.2.1	Lenses with $1 < n < 2$	145
4.2.2	Lenses with $n > 2$	151
4.2.3	Singular Isothermal Sphere	151

4.3	Softened (Isothermal) Lenses	153
4.4	Time delays	158
4.5	Elliptical lenses	159
4.5.1	Singular Isothermal Ellipsoid	160
4.5.2	Non-singular elliptical models	169
4.5.3	Pseudo-elliptical models	170
4.6	Other profiles	170
4.6.1	The Navarro-Frenk-White model	170
4.6.2	The Pseudo-Isothermal model	173
4.7	Environment	173
4.8	Substructures	174
4.9	Mass-sheet degeneracy	174
4.10	Python applications	174
4.10.1	Multiple images by SIE lenses	174
4.10.2	Images of extended sources	174

III

Part Three: Appendixes

A	Python tutorial	179
A.1	Installation	179
A.2	Documentation	179
A.3	Running python	179
A.4	Your first python code	180
A.5	Variables	180
A.6	Strings	180
A.7	Lists	182
A.8	Tuples	182
A.9	Dictionaries	183
A.10	Blocks and Indentation	183
A.11	IF / ELIF / ELSE	183
A.12	While loops	184
A.13	For loops	184
A.14	Functions	184
A.15	Classes	184
A.16	Modules	186
A.17	Importing packages	186
B	Cosmological background	189
B.1	The Robertson-Walker metric	189
B.2	Redshift	190
B.3	The Friedmann Equations	191
B.4	Cosmological parameters	192

B.5	Cosmological distances	193
B.6	The Friedmann models	194
B.6.1	Single component models	195
B.6.2	Multiple component models	196
B.7	Structure formation	197
B.7.1	Linear growth of density perturbations	197
B.7.2	Density power spectrum	200
B.7.3	Non-linear evolution	201
B.8	Mass function	203
B.9	Quintessence models	204
	Bibliography	207
	Index	211

Part One: Generalities

1	Light deflection	9
1.1	Deflection of a light corpuscle	
1.2	Deflection of light according to General Relativity	
1.3	Deflection by an ensemble of point masses	
1.4	Deflection by an extended mass distribution	
1.5	Python applications	
1.6	Problems	
2	The general lens	29
2.1	Lens equation	
2.2	Lensing potential	
2.3	First order lens mapping	
2.4	Magnification	
2.5	Lensing to the second order	
2.6	Time delay surface	
2.7	Python applications	

1. Light deflection

1.1 Deflection of a light corpuscle

The idea that light could be bent by gravity was mentioned by Isaac Newton in a note at the end of *Optiks*, published in 1704. Further calculations were made about a century later by the German astronomer Johann Georg Von Soldner (1776-1833), who ended up quantifying that the deflection of a photon grazing the surface of the sun would amount to about 0.9".

What were the assumptions under which this result was obtained? We should first of all introduce the framework within which the idea was proposed. This is the so called "Corpuscular Theory of Light", which assumes that photons are not mass-less.

In this framework, the derivation of the deflection angle of a photon by a body with mass M is rather straightforward. It can be done in many ways, but we re-propose here a simple calculation by Victor J. Stenger (2013), which is based on four ingredients:

- Newton's law of gravity;
- Newton's second law of motion;
- Einstein's principle of equivalence;
- Einstein's special relativity.

Newton's law of gravity says that the gravitational force between two bodies with masses m and M is

$$\vec{F} = \frac{GmM}{r^3} \vec{r}, \quad (1.1)$$

where r is the distance between the bodies, and G is the gravitational constant.

Newton's second law of motion states that

$$\vec{F} = \frac{d\vec{p}}{dt} = m\vec{a} \quad (1.2)$$

where \vec{p} and \vec{a} are the momentum and the acceleration of the body with inertial mass m , respectively.

Because of the principle of equivalence, the gravitational mass m in Eq. 1.1 equals the inertial mass m in Eq. 1.2.

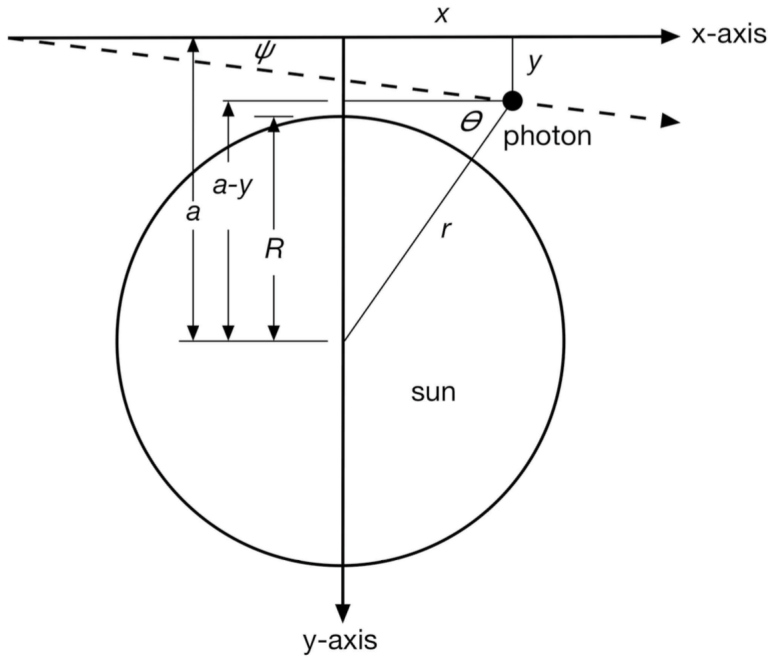


Figure 1.1.1: Schematic view of a photon grazing the surface of the Sun (from V. J. Stenger, 2013).

From Einstein's special relativity, we have that the inertial mass of a photon with energy E is E/c^2 , where c is the speed of light.

Let assume that a photon with initial momentum \vec{p} grazes the surface of the Sun, as shown in Fig. 1.1.1. The photon travels along the x -axis, while the y -axis was chosen to pass through the center of the sun, whose mass is M and whose radius is R . Let a be the impact parameter of the photon, i.e. the minimal distance of the un-deflected trajectory of the photon from the center of the Sun. When the photon is at the position (x, y) , the distance from the Sun is

$$r = \sqrt{x^2 + (a - y)^2}. \quad (1.3)$$

Let's assume that the momentum of the photon does not change significantly along its path. The components of the gravitational force acting on the photon are

$$\begin{aligned} F_x &= \frac{dp}{dt} \cos \theta &= \frac{G M p}{c[x^2 + (a - y)^2]} \cos \theta = \frac{G M p}{c} \frac{x}{[x^2 + (a - y)^2]^{3/2}}, \\ F_y &= \frac{dp}{dt} \sin \theta &= \frac{G M p}{c[x^2 + (a - y)^2]} \sin \theta = \frac{G M p}{c} \frac{a - y}{[x^2 + (a - y)^2]^{3/2}}. \end{aligned} \quad (1.4)$$

Now, let's assume that $dx = c dt$. We can then write:

$$\frac{dp_i}{dt} = \frac{dp_i}{dx} \frac{dx}{dt} = c \frac{dp_i}{dx}, \quad (1.5)$$

which allows to re-write Eqs. 1.4 as

$$\begin{aligned} \frac{dp_x}{dx} &= \frac{G M p}{c^2} \frac{x}{[x^2 + (a - y)^2]^{3/2}}, \\ \frac{dp_y}{dx} &= \frac{G M p}{c^2} \frac{a - y}{[x^2 + (a - y)^2]^{3/2}}. \end{aligned} \quad (1.6)$$

These equations allow us to calculate by how much does the momentum change along the x and the y axes as the x coordinate of the photon changes. Along the x -axis:

$$\Delta p_x = \frac{G M p}{c^2} \int_{-\infty}^{\infty} \frac{x}{[x^2 + (a-y)^2]^{3/2}} dx = 0. \quad (1.7)$$

Thus, the photon momentum is un-changed along the x -axis. On the contrary, along the y -axis, the photon momentum changes by

$$\begin{aligned} \Delta p_y &= \frac{G M p}{c^2} \int_{-\infty}^{\infty} \frac{a-y}{[x^2 + (a-y)^2]^{3/2}} dx \\ &= \frac{G M p}{c^2} \left[\frac{x}{(a-y) \sqrt{x^2 + (a-y)^2}} \right]_{-\infty}^{+\infty} \\ &= \frac{2 G M p}{c^2} \frac{1}{a-y}, \end{aligned} \quad (1.8)$$

which can be used to compute the deflection angle

$$\psi = \frac{\Delta p_y}{p} = \frac{2 G M}{c^2} \frac{1}{a-y}. \quad (1.9)$$

If the photon impact parameter is $a - y = R_\odot$, Eq. 1.9 reduces to

$$\psi = \frac{\Delta p_y}{p} = \frac{2 G M}{c^2 R_\odot} \approx 0.875'', \quad (1.10)$$

when inserting $M = M_\odot = 1.989 \times 10^{30}$ kg and $R_\odot = 6.96 \times 10^8$ m. Thus, using Newtonian gravity and assuming that photons are light corpuscles, we obtain that a photon grazing the surface of the Sun is deflected by $0.875''$. We will see shortly that this value is just half of what predicted by Einstein in the framework of his Theory of General Relativity.

1.2 Deflection of light according to General Relativity

1.2.1 Fermat principle and light deflection

Starting from the field equations of general relativity, light deflection can be calculated by studying geodesic curves. It turns out that light deflection can equivalently be described by Fermat's principle, as in geometrical optics. This will be our starting point.

Exercise 1.1 — Derive the Snell's law from Fermat principle. In its simplest form the Fermat's principle says that light waves of a given frequency traverse the path between two points which takes the least time. The speed of light in a medium with refractive index n is c/n , where c is its speed in a vacuum. Thus, the time required for light to go some distance in such a medium is n times the time light takes to go the same distance in a vacuum.

Referring to Fig. 1.2.1, the time required for light to go from A to B becomes

$$t = [\{h_1^2 + y^2\}^{1/2} + n\{h_2^2 + (w-y)^2\}^{1/2}]/c.$$

We find the minimum time by differentiating t with respect to y and setting the result to zero, with the result that

$$\frac{y}{\{h_1^2 + y^2\}^{1/2}} = n \frac{w-y}{\{h_2^2 + (w-y)^2\}^{1/2}}.$$

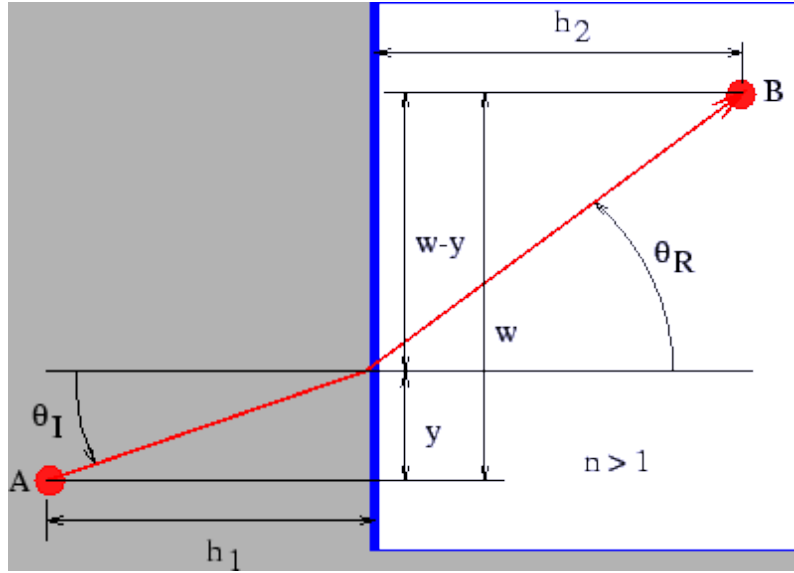


Figure 1.2.1: Definition sketch for deriving Snell's law of refraction from Fermat's principle. The shaded area has refractive index $n > 1$

However, we note that the left side of this equation is simply $\sin \theta_I$, while the right side is $n \sin \theta_R$, so that the minimum time condition reduces to

$$\sin \theta_I = n \sin \theta_R$$

We recognize this result as Snell's law. ▀

Taking inspiration from the Exercise above, we attempt to treat the deflection of light in a general relativity framework as a refraction problem. We need an refractive index n because Fermat's principle says that light will follow the path which makes extremal the travel time,

$$t_{\text{travel}} = \int \frac{n}{c} dl . \quad (1.11)$$

As in geometrical optics, we thus search for the path, $\vec{x}(l)$, for which

$$\delta \int_A^B n(\vec{x}(l)) dl = 0 , \quad (1.12)$$

where the starting point A and the end point B are kept fixed.



Deflection in the Minkowski's space-time

In order to find the refractive index, we make a first approximation: we assume that the lens is weak, and that it is small compared to the overall dimensions of the optical system composed of source, lens and observer. With "weak lens", we mean a lens whose Newtonian gravitational potential Φ is much smaller than c^2 , $\Phi/c^2 \ll 1$. Note that this approximation is valid in virtually all

cases of astrophysical interest. Consider for instance a galaxy cluster: its gravitational potential is $|\Phi| < 10^{-4}c^2 \ll c^2$. In addition, we also assume that the light deflection occurs in a region which is small enough that we can neglect the expansion of the universe.

In this case, the metric of (locally flat) unperturbed space-time is the Minkowski metric,

$$\eta_{\mu\nu} = \begin{pmatrix} 1 & 0 & 0 & 0 \\ 0 & -1 & 0 & 0 \\ 0 & 0 & -1 & 0 \\ 0 & 0 & 0 & -1 \end{pmatrix},$$

whose line element is

$$ds^2 = \eta_{\mu\nu} dx^\mu dx^\nu = (dx^0)^2 - (d\vec{x})^2 = c^2 dt^2 - (d\vec{x})^2. \quad (1.13)$$

Now, we consider a weak lens perturbing this metric, such that

$$\eta_{\mu\nu} \rightarrow g_{\mu\nu} = \begin{pmatrix} 1 + \frac{2\Phi}{c^2} & 0 & 0 & 0 \\ 0 & -(1 - \frac{2\Phi}{c^2}) & 0 & 0 \\ 0 & 0 & -(1 - \frac{2\Phi}{c^2}) & 0 \\ 0 & 0 & 0 & -(1 - \frac{2\Phi}{c^2}) \end{pmatrix}$$

for which the line element becomes

$$ds^2 = g_{\mu\nu} dx^\mu dx^\nu = \left(1 + \frac{2\Phi}{c^2}\right) c^2 dt^2 - \left(1 - \frac{2\Phi}{c^2}\right) (d\vec{x})^2. \quad (1.14)$$

■ Example 1.1 — Schwarzschild metric in the weak field limit. Assuming a spherically symmetric and static potential, the Einstein's field equations can be solved to obtain the *Schwarzschild metric*. The line element is written in spherical coordinates as

$$ds^2 = \left(1 - \frac{2GM}{Rc^2}\right) c^2 dt^2 - \left(1 - \frac{2GM}{Rc^2}\right)^{-1} dR^2 - R^2 (\sin^2 \theta d\phi^2 + d\theta^2).$$

To obtain a simpler expression, it is convenient to introduce the new radial coordinate r , defined through

$$R = r \left(1 + \frac{GM}{2rc^2}\right)^2$$

and the cartesian coordinates $x = r \sin \theta \cos \theta$, $y = r \sin \theta \sin \phi$, and $z = r \cos \theta$, so that $dl^2 = dx^2 + dy^2 + dz^2$. After some algebra, the metric can then be written in the form

$$ds^2 = \left(\frac{1 - GM/2rc^2}{1 + GM/2rc^2}\right)^2 c^2 dt^2 - \left(1 + \frac{GM}{2rc^2}\right)^4 (dx^2 + dy^2 + dz^2).$$

In the weak field limit, $\Phi/c^2 = -GM/rc^2 \ll 1$,

$$\begin{aligned} \left(\frac{1 - GM/2rc^2}{1 + GM/2rc^2}\right)^2 &\approx \left(1 - \frac{GM}{2rc^2}\right)^4 \\ &\approx \left(1 - \frac{2GM}{rc^2}\right) \\ &= \left(1 + \frac{2\Phi}{c^2}\right) \end{aligned}$$

and

$$\begin{aligned} \left(1 + \frac{GM}{2rc^2}\right)^4 &\approx \left(1 + 2\frac{GM}{rc^2}\right) \\ &= \left(1 - \frac{2\Phi}{c^2}\right). \end{aligned}$$

Therefore, the Schwarzschild metric in the weak field limit equals

$$ds^2 = \left(1 + \frac{2\Phi}{c^2}\right) c^2 dt^2 - \left(1 - \frac{2\Phi}{c^2}\right) dl^2,$$

thus recovering Eq. 1.14. ■

Effective refractive index

Light propagates at zero eigentime, $ds = 0$, from which we obtain

$$\left(1 + \frac{2\Phi}{c^2}\right) c^2 dt^2 = \left(1 - \frac{2\Phi}{c^2}\right) (d\vec{x})^2. \quad (1.15)$$

The light speed in the gravitational field is thus

$$c' = \frac{|d\vec{x}|}{dt} = c \sqrt{\frac{1 + \frac{2\Phi}{c^2}}{1 - \frac{2\Phi}{c^2}}} \approx c \left(1 + \frac{2\Phi}{c^2}\right), \quad (1.16)$$

where we have used that $\Phi/c^2 \ll 1$ by assumption. The refractive index is thus

$$n = c/c' = \frac{1}{1 + \frac{2\Phi}{c^2}} \approx 1 - \frac{2\Phi}{c^2}. \quad (1.17)$$

With $\Phi \leq 0$, $n \geq 1$, and the light speed c' is smaller than in absence of the gravitational potential.

Deflection angle

The refractive index n depends on the spatial coordinate \vec{x} and perhaps also on time t . Let $\vec{x}(l)$ be a light path. Then, the light travel time is

$$t_{travel} \propto \int_A^B n[\vec{x}(l)] dl, \quad (1.18)$$

and the light path follows from

$$\delta \int_A^B n[\vec{x}(l)] dl = 0. \quad (1.19)$$

This is a standard variational problem, which leads to the well known Euler equations. In our case we write

$$dl = \left| \frac{d\vec{x}}{d\lambda} \right| d\lambda, \quad (1.20)$$

with a curve parameter λ which is yet arbitrary, and find

$$\delta \int_{\lambda_A}^{\lambda_B} d\lambda n[\vec{x}(\lambda)] \left| \frac{d\vec{x}}{d\lambda} \right| = 0 \quad (1.21)$$

The expression

$$n[\vec{x}(\lambda)] \left| \frac{d\vec{x}}{d\lambda} \right| \equiv L(\dot{\vec{x}}, \vec{x}, \lambda) \quad (1.22)$$

takes the role of the Lagrangian, with

$$\dot{\vec{x}} \equiv \frac{d\vec{x}}{d\lambda}. \quad (1.23)$$

Finally, we have

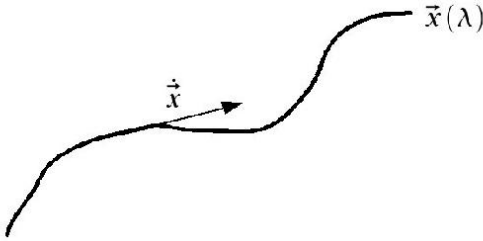
$$\left| \frac{d\vec{x}}{d\lambda} \right| = |\dot{\vec{x}}| = (\dot{\vec{x}}^2)^{1/2}. \quad (1.24)$$

The Euler equation writes:

$$\frac{d}{d\lambda} \frac{\partial L}{\partial \dot{\vec{x}}} - \frac{\partial L}{\partial \vec{x}} = 0. \quad (1.25)$$

Now,

$$\frac{\partial L}{\partial \vec{x}} = |\dot{\vec{x}}| \frac{\partial n}{\partial \vec{x}} = (\vec{\nabla} n) |\dot{\vec{x}}|, \frac{\partial L}{\partial \dot{\vec{x}}} = n \frac{\dot{\vec{x}}}{|\dot{\vec{x}}|}. \quad (1.26)$$



Evidently, $\dot{\vec{x}}$ is a tangent vector to the light path, which we can assume to be normalized by a suitable choice for the curve parameter λ . We thus assume $|\dot{\vec{x}}| = 1$ and write $\vec{e} \equiv \dot{\vec{x}}$ for the unit tangent vector to the light path. Then, we have

$$\frac{d}{d\lambda} (n\vec{e}) - \vec{\nabla} n = 0, \quad (1.27)$$

or

$$n\dot{\vec{e}} + \vec{e} \cdot [(\vec{\nabla} n)\dot{\vec{x}}] = \vec{\nabla} n,$$

$$\Rightarrow n\dot{\vec{e}} = \vec{\nabla} n - \vec{e}(\vec{\nabla} n \cdot \vec{e}). \quad (1.28)$$

The second term on the right hand side is the derivative along the light path, thus the whole right hand side is the gradient of n perpendicular to the light path. Thus

$$\dot{\vec{e}} = \frac{1}{n} \vec{\nabla}_{\perp} n = \vec{\nabla}_{\perp} \ln n. \quad (1.29)$$

As $n = 1 - 2\Phi/c^2$ and $\Phi/c^2 \ll 1$, $\ln n \approx -2\Phi/c^2$, and

$$\dot{\vec{e}} \approx -\frac{2}{c^2} \vec{\nabla}_{\perp} \Phi. \quad (1.30)$$

The total deflection angle of the light path is now the integral over $-\dot{\vec{e}}$ along the light path,

$$\hat{\alpha} = \vec{e}_{in} - \vec{e}_{out} = \frac{2}{c^2} \int_{\lambda_A}^{\lambda_B} \vec{\nabla}_{\perp} \Phi d\lambda, \quad (1.31)$$

or, in other words, the integral over the "pull" of the gravitational potential perpendicular to the light path. Note that $\vec{\nabla}\Phi$ points away from the lens center, so $\hat{\alpha}$ points in the same direction.

Born approximation

As it stands, the equation for $\hat{\alpha}$ is not useful, as we would have to integrate over the actual light path. However, since $\Phi/c^2 \ll 1$, we expect the deflection angle to be small. Then, we can adopt the *Born approximation*, familiar from scattering theory, and integrate over the unperturbed light path.

Suppose, therefore, that a light ray starts out into $+\vec{e}_z$ -direction and passes a lens at $z = 0$, with impact parameter b . The deflection angle is then given by

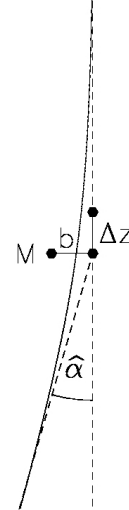
$$\hat{\alpha}(b) = \frac{2}{c^2} \int_{-\infty}^{+\infty} \vec{\nabla}_{\perp} \phi dz \quad (1.32)$$

■ **Example 1.2 — Deflection by a point mass.** If the lens is a point mass, then

$$\Phi = -\frac{GM}{r} \quad (1.33)$$

with $r = \sqrt{x^2 + y^2 + z^2} = \sqrt{b^2 + z^2}$, $b = \sqrt{x^2 + y^2}$ and

$$\vec{\nabla}_{\perp} \phi = \left(\begin{array}{c} \partial_x \Phi \\ \partial_y \Phi \end{array} \right) = \frac{GM}{r^3} \left(\begin{array}{c} x \\ y \end{array} \right). \quad (1.34)$$



The deflection angle is then

$$\begin{aligned} \hat{\alpha}(b) &= \frac{2GM}{c^2} \left(\begin{array}{c} x \\ y \end{array} \right) \int_{-\infty}^{+\infty} \frac{dz}{(b^2 + z^2)^{3/2}} \\ &= \frac{4GM}{c^2} \left(\begin{array}{c} x \\ y \end{array} \right) \left[\frac{z}{b^2(b^2 + z^2)^{1/2}} \right]_0^{\infty} \\ &= \frac{4GM}{c^2 b} \left(\begin{array}{c} \cos \phi \\ \sin \phi \end{array} \right), \end{aligned} \quad (1.35)$$

with

$$\left(\begin{array}{c} x \\ y \end{array} \right) = b \left(\begin{array}{c} \cos \phi \\ \sin \phi \end{array} \right) \quad (1.36)$$

Notice that $R_s = \frac{2GM}{c^2}$ is the Schwarzschild radius of a (point) mass M , thus

$$|\hat{\alpha}| = \frac{4GM}{c^2 b} = 2 \frac{R_s}{b}. \quad (1.37)$$

Also notice that $\hat{\alpha}$ is linear in M , thus the superposition principle can be applied to compute the deflection angle of an ensemble of lenses. ■

Deflection of light by the Sun's gravitational field

Note that the deflection angle found here in the framework of general relativity is very similar to the result found in the Newtonian limit for a photon grazing the surface of the Sun. However, we find here an extra factor two.

The reason for the factor of 2 difference is that both the space and time coordinates are bent in the vicinity of massive objects — it is four-dimensional space–time which is bent by the Sun.

The famous eclipse expedition of 1919 to Sobral, Brazil, and the island of Principe, in the Gulf of Guinea, led by Eddington, Dyson, and Davidson was a turning point in the history of relativity: it confirmed that masses bend light by the amount that is predicted by General Relativity.

For further reading on the Eddington expedition, we refer the reader to Smith (2015).

1.2.2 Deflection of light in the strong field limit

For the vast majority of gravitational lenses in the universe, the weak field limit holds. However, compact objects such as neutron stars and black holes can also act as lenses. In these cases, the approximations introduced above break down, as photons travel through very strong gravitational fields. In the following, we briefly discuss the deflection angle of a static (i.e. non-rotating) compact lens.

For a general static, spherically symmetric metric in the form

$$ds^2 = A(R)dt^2 - B(R)dR^2 - C(R)(d\theta^2 + \sin^2\theta d\phi^2) \quad (1.38)$$

the analysis of the geodesic equations leads to the following expression for the deflection angle:

$$\hat{\alpha} = -\pi + \frac{2G}{c^2} \int_{R_m}^{\infty} u \sqrt{\frac{B(R)}{C(R)[C(R)/A(R) - u^2]}} dR, \quad (1.39)$$

where u is the impact parameter of the unperturbed photon and R_m is the minimal distance of the deflected photon from the lens (Bozza, 2010). It can be shown that

$$u^2 = \frac{C(R_m)}{A(R_m)}. \quad (1.40)$$

Note that, in the case of the Schwarzschild metric, $A(R) = 1 - 2GM/Rc^2$, $B(R) = A(R)^{-1}$, and $C(R) = R^2$.

In the weak field limit ($R \geq R_m \gg 2GM/c^2$, i.e. for impact parameters much larger than the lens Schwarzschild radius), Eq. 1.39 reduces to the well known equation

$$\hat{\alpha} = \frac{4GM}{c^2 u}. \quad (1.41)$$

The exact solution of Eq. 1.39 was calculated by Darwin (1959) to be

$$\hat{\alpha} = -\pi + 4 \frac{G}{c^2} \sqrt{R_m/s} F(\varphi, m), \quad (1.42)$$

where $F(\varphi, m)$ is the elliptic integral of the first kind, and

$$s = \sqrt{(R_m - 2M)(R_m + 6M)} \quad (1.43)$$

$$m = (s - R_m + 6M)/2s \quad (1.44)$$

$$\varphi = \arcsin \sqrt{2s/(3R_m - 6M + s)} \quad (1.45)$$

Fig. 1.2.2 shows how the deflection angle varies as a function of the impact parameter of the photon. At large distances, Eq. 1.42 is well approximated by the solution in the weak field limit. For small impact parameters, the solutions in the strong and in the weak field limit differ significantly. In particular, the deflection angle in Eq. 1.42 diverges for $u = 3\sqrt{3}GM/c^2$ (or $R_m = 3GM/c^2$). Before reaching that point, the deflection angle exceeds 2π , meaning that the photon loops around the lens before leaving it.

1.3 Deflection by an ensemble of point masses

The deflection angle in Eq. 1.37 depends linearly on the mass M . This result was obtained by linearizing the equations of general relativity in the weak field limit. Under these circumstances, the superposition principle holds and the deflection angle of an array of lenses can be calculated as the sum of all contributions by each single lens.

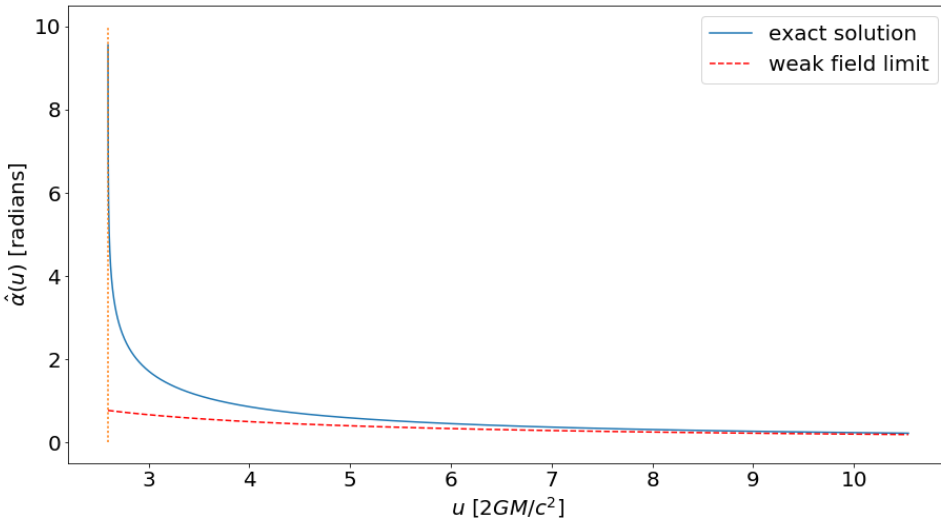


Figure 1.2.2: Deflection angle by a compact lens as a function of the photon impact parameter. Shown are the exact solution of the geodesic equations for a Schwarzschild metric (solid line) and the solution in the weak field approximation (dashed line). The dotted vertical line shows the impact parameter, $u = 3\sqrt{3}GM/c^2$, for which the exact solution diverges, indicating that the photon keeps looping around the lens.

Suppose we have a sparse distribution of N point masses on a plane, whose positions and masses are $\vec{\xi}_i$ and M_i , $1 \leq i \leq N$. The deflection angle of a light ray crossing the plane at $\vec{\xi}$ will be:

$$\hat{\alpha}(\vec{\xi}) = \sum_i \hat{\alpha}_i(\vec{\xi} - \vec{\xi}_i) = \frac{4G}{c^2} \sum_i M_i \frac{\vec{\xi} - \vec{\xi}_i}{|\vec{\xi} - \vec{\xi}_i|^2}. \quad (1.46)$$

Note that the formula above is similar to that we would use to compute the gravitational force between point masses on the plane. While the force depends on the inverse squared distance, the deflection angle scales as ξ^{-1} . In the case of many lenses, the computation of the deflection angle using Eq. 1.46 can become very computationally expensive, as it costs $O(N^2)$. However, as it is usually done to solve numerically N -body problems, algorithms employing meshes or hierarchies (such as the so-called tree algorithms (Barnes and Hut, 1986)) can significantly reduce the cost of calculations (e.g. to $O(N \log N)$). For some application of these algorithms in the computation of the deflection angles, we refer the reader to the works of Aubert, Amara, and Metcalf (2007) and Meneghetti et al. (2010).

1.4 Deflection by an extended mass distribution

We now consider more realistic lens models, i.e. three dimensional distributions of matter. Even in the case of lensing by galaxy clusters, the physical size of the lens is generally much smaller than the distances between observer, lens and source. The deflection therefore arises along a very short section of the light path. This justifies the usage of the *thin screen approximation*: the lens is approximated by a planar distribution of matter, the lens plane.

Within this approximation, the lensing matter distribution is fully described by its surface density,

$$\Sigma(\vec{\xi}) = \int \rho(\vec{\xi}, z) dz, \quad (1.47)$$

where $\vec{\xi}$ is a two-dimensional vector on the lens plane and ρ is the three-dimensional density.

As long as the thin screen approximation holds, the total deflection angle is obtained by summing the contribution of all the mass elements $\Sigma(\vec{\xi})d^2\xi$:

$$\vec{\alpha}(\vec{\xi}) = \frac{4G}{c^2} \int \frac{(\vec{\xi} - \vec{\xi}')\Sigma(\vec{\xi}')}{|\vec{\xi} - \vec{\xi}'|^2} d^2\xi'. \quad (1.48)$$

This equation shows that the calculation of the deflection angle is formally a convolution of the surface density $\Sigma(\vec{\xi})$ with the kernel function

$$\vec{K}(\vec{\xi}) \propto \frac{\vec{\xi}}{|\vec{\xi}|^2}. \quad (1.49)$$

This enables the calculation of the deflection angle field in the Fourier space as the product of the Fourier transforms of Σ and K :

$$\tilde{\vec{\alpha}}_i(\vec{k}) \propto \tilde{\Sigma}(\vec{k})\tilde{K}_i(\vec{k}), \quad (1.50)$$

where \vec{k} is the conjugate variable to $\vec{\xi}$ and the tilde denotes the Fourier Transforms. The subscript $i \in [1, 2]$ indicates the two components along the two axes on the lens plane (remember that $\hat{\alpha}$ is a vector!). This calculation can be implemented efficiently using the *Fast-Fourier-Transform (FFT)* algorithm (Cooley and Tukey, 1965). Note that this assumes that the integration extends to an infinite domain, while gravitational lenses have finite mass distributions. FFT algorithms implement this feature assuming periodic conditions on the boundaries of the integration domain.

1.5 Python applications

1.5.1 Deflection by a black-hole

In our first python application, we write a script to produce Fig. 1.2.2. A brief python tutorial can be found in Appendix A.

We want to implement the formula in Eq. 1.42. We also need to remind that

$$u^2 = \frac{C(R_m)}{A(R_m)}$$

We will compare the resulting deflection angle to

$$\hat{\alpha} = \frac{4GM}{c^2u} \quad (1.51)$$

which is the result we obtained in the weak-field limit.

We start by importing some useful packages:

```
from scipy import special as sy # need special functions for incomplete ||
# elliptic integrals of the first kind
import numpy as np # efficient vector and matrix operations
import matplotlib.pyplot as plt # a MATLAB-like plotting framework
%matplotlib inline # only needed in jupyter notebooks
```

Note that we import the module `special` from `scipy` in order to compute the elliptic integral of the first kind appearing in Eq. 1.42. See <https://docs.scipy.org/doc/scipy/reference/special.html>.

Our goal is to produce a graph. Let's setup the fonts and the character size

```

font = {'family' : 'normal',
        'weight' : 'normal',
        'size'   : 20}

import matplotlib
matplotlib.rcParams['font', **font]

```

The task can be completed in several ways. Here we chose to build a class for point black-holes:

```

class point_bh:

    def __init__(self,M):
        self.M=M

    # functions which define the metric.
    def A(self,r):
        return(1.0-2.0*self.M/r)

    def B(self,r):
        return (self.A(r)**(-1))

    def C(self,r):
        return(r**2)

    # compute u from rm
    def u(self,r):
        u=np.sqrt(self.C(r)/self.A(r))
        return(u)

    # functions concurring to the deflection angle calculation
    def ss(self,r):
        return(np.sqrt((r-2.0*self.M)*(r+6.0*self.M)))

    def mm(self,r,s):
        return((s-r+6.0*self.M)/2/s)

    def phif(self,r,s):
        return(np.arcsin(np.sqrt(2.0*s/(3.0*r-6.0*self.M+s)))))

    # the deflection angle
    def defAngle(self,r):
        s=self.ss(r)
        m=self.mm(r,s)
        phi=self.phif(r,s)
        F=sy.ellipkinc(phi, m) # using the ellipkinc function
                               # from scipy.special
        return(-np.pi+4.0*np.sqrt(r/s)*F)

```

The class contains several methods which will be used to compute the deflection angle. For example, we implement the functions $A(R)$, $B(R)$, and $C(R)$. These will be used to convert the

minimal distance R_m to u . We also implement the functions s, m, φ , which depend on the mass of the black-hole and on the minimal distance R_m . Finally, we implement the function `defAngle`, which enables to compute the deflection angle using Eq. 1.42. This function uses the method `elipkinc` from `scipy.special` to compute the incomplete elliptic integral of the first kind, $F(\varphi, m)$. Note that φ and m can be passed as numpy arrays, i.e. `elipkinc` can return values for a number of couples (φ, m) .

Following the same approach, we build another class which deals with point lenses in the weak field limit, i.e. it implements Eq. 1.51:

```
class point_mass:

    def __init__(self,M):
        self.M=M

        # the classical formula
    def defAngle(self,u):
        return(4.0*self.M/u)
```

We can now use the two classes above to build two objects, namely a black-hole lens (employing the exact solution for the deflection angle) and a point mass lens, for which we will adopt the weak-field limit. In both cases, the mass of the lens is fixed to $3M_\odot$. For a mass of this size, the Schwarzschild radius is $R_s \sim 9\text{km}$:

```
bh=point_bh(3.0)
pm=point_mass(3.0)
```

We now use the `linspace` method from `numpy` to initialize an vector of minimal distances R_m , which we will use to compute $\hat{\alpha}$. We use the method `u(r)` of `point_bh` to convert R_m into an array of impact parameters u :

```
r=np.linspace(3.0/2.0,10,1000)*2.0*bh.M
u=bh.u(r)/2.0/bh.M
```

The deflection angle as a function of u or R_m can be computed in the cases of the exact solution and in the weak field limit using the method `defAngle` applied to `bh` and `pm`:

```
a=bh.defAngle(r)
b=pm.defAngle(u*2.0*bh.M)
```

Note that u is in units of the Schwarzschild radius and that we have set $G/c^2 = 1$.

Finally, we can produce a nice figure displaying the results of the calculation. We use `matplotlib.pyplot` to do this:

```
# initialize figure and axes
# (single plot, 15" by 8" in size)
fig,ax=plt.subplots(1,1,figsize=(15,8))
# plot the exact solution in ax
ax.plot(u,a,'-',label='exact solution')
# plot the solution in the weak field limit
ax.plot(u,b,'--',label='weak field limit',color='red')
# set the labels for the x and the y axes
ax.set_xlabel(r'$u$ $[2GM/c^2]$')
```

```
ax.set_ylabel(r'$\hat{\alpha}(u)$ [radians]')
# add the legend
ax.legend()
```

We also want to show the vertical asymptote at $u_{lim} = 3\sqrt{3}/2$:

```
# plot a vertical dotted line at u=3\sqrt(3)/2
x=[np.min(u),np.min(u)]
y=[0,10]
ax.plot(x,y,':')
```

To conclude, we save the figure in a .png file:

```
# save figure in png format
fig.savefig('bhalpha.png')
```

1.5.2 Deflection by an extended mass distribution

In this application, we implement the calculation of the deflection angle field by an extended lens. A two-dimensional map of the lens surface-density is provided by the fits file `kappa_g1.fits` (see the data folder in the github repository). The map was obtained by projecting the mass distribution of a dark matter halo obtained from N-body simulations on a lens plane. To be precise, this is the surface density divided by a constant which depends on the lens and source redshifts (we will talk about this constant in the next lectures). Let's denote this quantity as κ . Accounting for this normalization, the calculation we want to implement is

$$\vec{\alpha}(\vec{x}) = \frac{1}{\pi} \int \kappa(\vec{x}') \frac{\vec{x} - \vec{x}'}{|\vec{x} - \vec{x}'|^2} d^2 x'.$$

This is a convolution, which can be written in the Fourier Space as

$$\vec{\alpha}(\vec{k}) = \frac{1}{\pi} \tilde{\kappa}(\vec{k}) \vec{K}(\vec{k})$$

where $\vec{K}(\vec{k})$ is the Fourier Transform of

$$\vec{K}(\vec{x}) = \frac{\vec{x}}{|\vec{x}|^2}$$

We use the `numpy.fft` module:

```
import numpy as np
import numpy.fft as fftengine
```

We define a class called `deflector`, where the `deflector` object is initialized by reading the fits file containing the surface density map of the lens. To deal with the fits files, we need to use the `astropy.io.fits` module.

The class contains some methods to

- build the kernel $K(\vec{x})$;
- compute the deflection angle map by convolving the convergence with the kernel;
- perform the so-called "zero-padding";
- crop the zero-padded maps.

```

import astropy.io.fits as pyfits

class deflector(object):

    # initialize the deflector using a surface density (convergence) map
    # the boolean variable pad indicates whether zero-padding is used
    # or not
    def __init__(self,filekappa,pad=False):
        kappa,header=pyfits.getdata(filekappa,header=True)
        self.kappa=kappa
        self.nx=kappa.shape[0]
        self.ny=kappa.shape[1]
        self.pad=pad
        if (pad):
            self.kpad()
        self.kx,self.ky=self.kernel()

    # implement the kernel function K
    def kernel(self):
        x=np.linspace(-0.5,0.5,self.kappa.shape[0])
        y=np.linspace(-0.5,0.5,self.kappa.shape[1])
        kx,ky=np.meshgrid(x,y)
        norm=(kx**2+ky**2+1e-12)
        kx=kx/norm
        ky=ky/norm
        return(kx,ky)

    # compute the deflection angle maps by convolving
    # the surface density with the kernel function
    def angles(self):
        # FFT of the surface density and of the two components of the kernel
        density_ft = fftengine.fftn(self.kappa,axes=(0,1))
        kernelx_ft = fftengine.fftn(self.kx,axes=(0,1),
                                    s=self.kappa.shape)
        kernely_ft = fftengine.fftn(self.ky,axes=(0,1),
                                    s=self.kappa.shape)
        # perform the convolution in Fourier space and transform the result
        # back in real space. Note that a shift needs to be applied using
        # fftshift
        alphax = 1.0/np.pi/(self.kappa.shape[0])*\
                 fftengine.fftshift(fftengine.ifftn(kappa_ft*kernelx_ft))
        alphay = 1.0/np.pi/(self.kappa.shape[0])*\
                 fftengine.fftshift(fftengine.ifftn(kappa_ft*kernely_ft))
        return(alphax.real,alphay.real)

    # returns the surface-density (convergence) of the deflector
    def kmap(self):
        return(self.kappa)

```

```

# performs zero-padding
def kpad(self):
    # add zeros around the original array
    def padwithzeros(vector, pad_width, iaxis, kwargs):
        vector[:pad_width[0]] = 0
        vector[-pad_width[1]:] = 0
        return vector
    # use the pad method from numpy.lib to add zeros (padwithzeros)
    # in a frame with thickness self.kappa.shape[0]
    self.kappa=np.lib.pad(self.kappa, self.kappa.shape[0],
                          padwithzeros)

    # crop the maps to remove zero-padded areas and get back to the
    # original region.
    def mapCrop(self,mappa):
        xmin=0.5*(self.kappa.shape[0]-self.nx)
        ymin=0.5*(self.kappa.shape[1]-self.ny)
        xmax=xmin+self.nx
        ymax=ymin+self.ny
        mappa=mappa[xmin:xmax,ymin:ymax]
        return(mappa)

```

We can now build a deflector and use it to compute the deflection angles employing the method `angles`:

```

df=deflector('data/kappa_gl.fits')
angx_nopad,angy_nopad=df.angles()
kappa=df.kmap()

import matplotlib.pyplot as plt
from matplotlib.colors import LogNorm, PowerNorm, SymLogNorm
%matplotlib inline

fig,ax = plt.subplots(1,3,figsize=(16,8))
ax[0].imshow(kappa,origin="lower")
ax[0].set_title('convergence')
ax[1].imshow(angx_nopad,origin="lower")
ax[1].set_title('angle 1')
ax[2].imshow(angy_nopad,origin="lower")
ax[2].set_title('angle 2')

```

Note that at this point we have not yet used the zero-padding trick. FFT assumes periodic boundary conditions, meaning that the lens mass distribution is replicated outside the boundaries. Given that the region around the lens considered in this example is relatively small, we expect that the deflection angles will be biased near the borders. The three panels in Fig. 1.5.1 show the maps of the convergence and of the two components of the deflection angles obtained with this setting.

Zero-padding consists of placing zeros all around the convergence map. By doing so, we double the size of the original map, but we expect to increase the accuracy of the calculations near the borders, because the periodic conditions are better reproduced in this setting. We activate zero-padding by just setting the variable `pad=True` when initializing the deflector. Fig. 1.5.2 shows

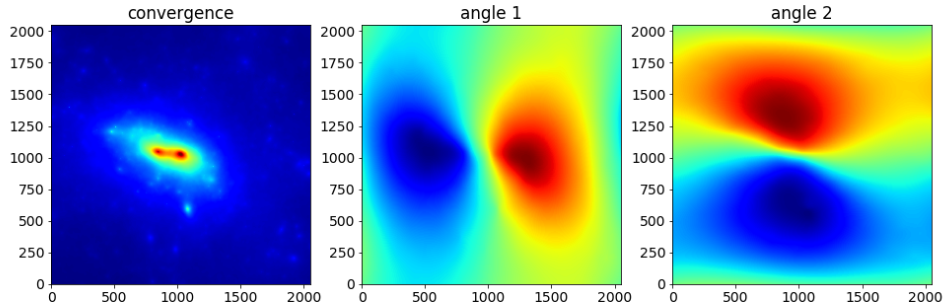


Figure 1.5.1: Left panel: the surface density (convergence) map of the lens. Middle and right panels: maps of the two components of the deflection angles.

the zero-padded convergence map and the two new maps of the deflection angle components.

```
df=deflector('data/kappa_gl.fits',True)
angx,angy=df.angles()
kappa=df.kmap()

fig,ax = plt.subplots(1,3,figsize=(16,8))
angx,angy=df.angles()
ax[0].imshow(kappa,origin="lower")
ax[0].set_title('convergence')
ax[1].imshow(angx,origin="lower")
ax[1].set_title('angle 1')
ax[2].imshow(angy,origin="lower")
ax[2].set_title('angle 2')
```

We are not interested in this large area, thus we can get rid of the values outside the lens convergence map by cropping the deflection angle maps. The results are shown in Fig. 1.5.3 and compared to the previous ones. In fact, significant differences are visible along the borders.

```
angx=df.mapCrop(angx)
angy=df.mapCrop(angy)

fig,ax = plt.subplots(2,2,figsize=(16,16))
ax[0,0].imshow(angx,origin="lower")
ax[0,0].set_title('angle 1')
ax[0,1].imshow(angy,origin="lower")
ax[0,1].set_title('angle 2')
ax[1,0].imshow(angx_nopad,origin="lower")
ax[1,0].set_title('angle 1 - no zero pad')
ax[1,1].imshow(angy_nopad,origin="lower")
```

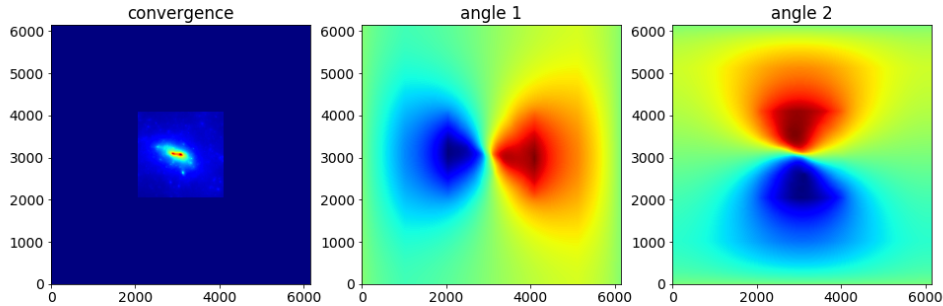


Figure 1.5.2: The figure shows the same maps as in Fig. 1.5.1, but with zero-padding. Indeed, as shown in the left panel, the lens is surrounded by a frame of zeros, and the deflection angle maps are computed on an area which has double the size of the maps in Fig. 1.5.1.

```
ax[1,1].set_title('angle 2 - no zero pad')
```

1.6 Problems

Problem 1.1 — Write a python script to produce a figure displaying $\hat{\alpha}(R_m)$ with R_m in the range 9-1000 km for two lenses with mass $M = 3M_\odot$ and $M = 10M_\odot$.

Problem 1.2 — Define a class for an ensemble of point masses. The class should be initialized with two numpy arrays containing the masses and the positions of the lenses. Use the thin screen approximation and write the method to compute the deflection angle at a certain location on the lens plane..

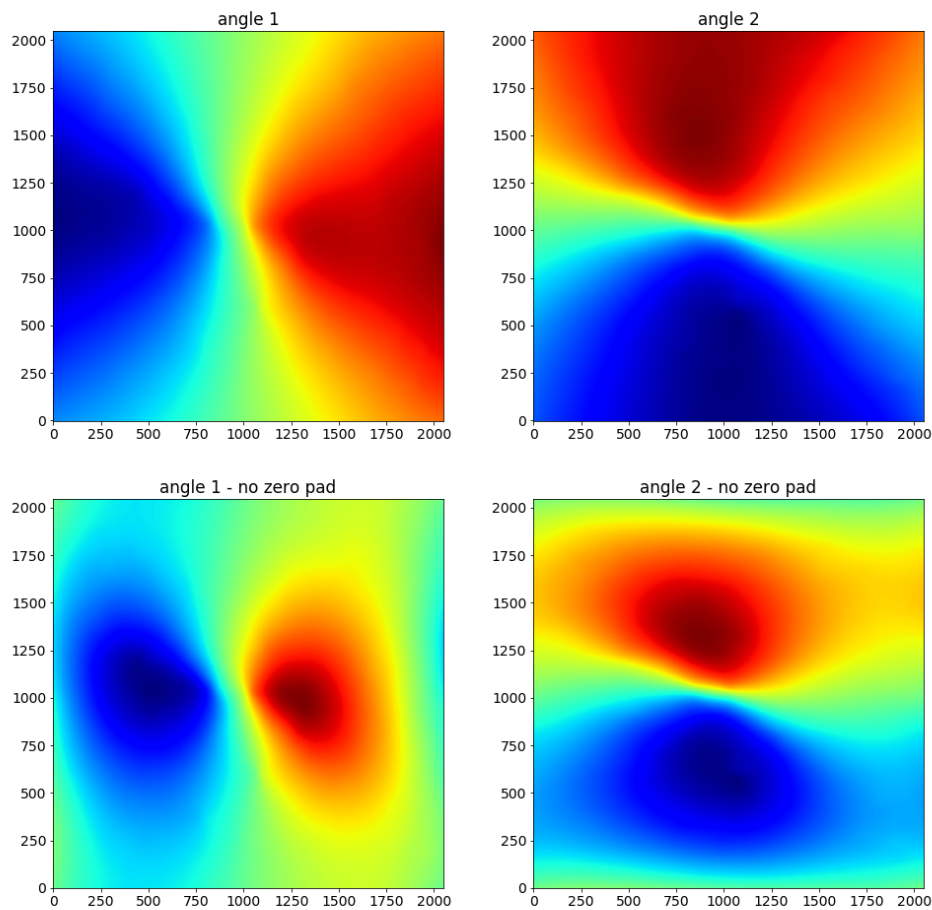


Figure 1.5.3: The upper panels show the same two maps displayed in the middle and right panels of Fig. 1.5.2, which have been cropped to match the original size of the input convergence map. The bottom panels show the maps obtained without padding, for comparison.



2. The general lens

2.1 Lens equation

Gravitational lensing is sensitive to the geometry of the universe. In particular, as in refractive phenomena, the amplitude of the lensing effects is heavily dependent on the distances between the observer, the lenses, and the sources. These are in turn related to the curvature and expansion rate of the universe, which suggests that gravitational lensing is indeed a powerful tool for cosmology.

Intrinsic and apparent source position

In this section, we seek a relationship between observed and intrinsic positions of a source in a gravitational lensing event. In absence of the lens, the light emitted by a distant source reaches an observer, who sees the source at a certain position on the sky, $\vec{\beta}$ (in angular units). This is the *intrinsic* position of the source. Instead, when photons are deflected by the gravitational lens, the observer collects them from a different direction, $\vec{\theta}$, which corresponds to the *apparent* (or *observed*) position of the source. We refer to the apparent position of the source as to the *image* position.

In Fig. (2.1.1), we sketch a typical gravitational lens system. A mass is placed at redshift z_L , corresponding to an angular diameter distance D_L . This lens deflects the light rays coming from a source at redshift z_S (or angular distance D_S). At the bottom of the diagram, an observer collects the photons from the distant source. The angular diameter distance between the lens and the source is D_{LS} .

R The angular diameter distance D_A is defined as the ratio of an object's physical transverse size to its angular size (in radians). Therefore, it is used to convert angular separations in the sky to physical separations on the plane of the sources.

This distance does not increase indefinitely with redshift, but it peaks at $z \sim 1$ and then it turns over. Due to the expansion of the universe the angular diameter distance between z_1 and z_2 (with $z_2 > z_1$) is not found by subtracting the two individual angular diameter distances:

$$D_A(z_1, z_2) \neq D_A(z_2) - D_A(z_1) \quad (2.1)$$

except for those situations where the expansion of the universe can be neglected (i.e. for

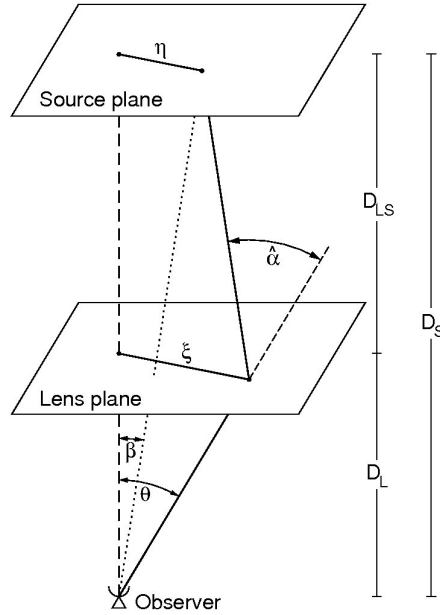


Figure 2.1.1: Sketch of a typical gravitational lensing system. Figure from Bartelmann and Schneider (2001).

(lenses and sources in our own galaxy). More in-depth discussions can be found in Appendix B and in several cosmology books (see e.g. Weinberg, 1972).

Thin screen approximation

If the physical size of the lens is small compared to the distances D_L , D_{LS} , and D_S , the extension of the lens along the line-of-sight can be neglected in the calculation of the light deflection. We can assume that this occurs on a plane, called the *lens plane*.

R Given that the apparent position of the source, or image position, originates on this plane, the lens plane is often referred as the *image plane*.

Similarly, we can assume that all photons emitted by the source originate from the same distance D_S , meaning that the source lies on a *source plane*. The approximation of the lens and of the source to planar distributions of mass and light, is called *thin screen approximation*.

Relating the intrinsic and apparent positions of the source

We first define an optical axis, indicated in Fig. (2.1.1) by the dashed line, perpendicular to the lens and source planes and passing through the observer. Then we measure the angular positions on the lens and on the source planes with respect to this reference direction.

Consider a source at the intrinsic angular position $\vec{\beta}$, which lies on the source plane at a distance $\vec{\eta} = \vec{\beta}D_S$ from the optical axis. The source emits photons (we may now use the term “light rays”) that impact the lens plane at $\vec{\xi} = \vec{\theta}D_L$, are deflected by the angle $\hat{\alpha}$, and finally reach the observer. The amplitude of the deflection is given by Eq. (1.32).

Due to the deflection, the observer receives the light coming from the source as if it was emitted at the apparent angular position $\vec{\theta}$. Note that we have used vectors to identify the source and image positions on the corresponding planes, either in the case of angular and physical positions.

If $\vec{\theta}$, $\vec{\beta}$, and $\hat{\alpha}$ are small, the true position of the source and its observed position on the sky are related by a very simple relation, which can be readily obtained from the diagram in Fig. 2.1.1.

This relation is called the *lens equation* and is written as

$$\vec{\theta} D_S = \vec{\beta} D_S + \hat{\alpha} D_{LS}, \quad (2.2)$$

where D_{LS} is the angular diameter distance between lens and source.

Defining the reduced deflection angle

$$\vec{\alpha}(\vec{\theta}) \equiv \frac{D_{LS}}{D_S} \hat{\alpha}(\vec{\theta}), \quad (2.3)$$

from Eq. (2.2), we obtain

$$\vec{\beta} = \vec{\theta} - \vec{\alpha}(\vec{\theta}). \quad (2.4)$$

This equation, called *lens equation*, is apparently very simple. However, $\vec{\alpha}(\vec{\theta})$ can be a complicated function of $\vec{\theta}$, which implies that the equation can only be solved numerically in many cases.

It is very common and useful to write Eq. (2.2) in dimensionless form. This can be done by defining a length scale ξ_0 on the lens plane and a corresponding length scale $\eta_0 = \xi_0 D_S / D_L$ on the source plane. Then, we define the dimensionless vectors

$$\vec{x} \equiv \frac{\vec{\xi}}{\xi_0} \quad ; \quad \vec{y} \equiv \frac{\vec{\eta}}{\eta_0}, \quad (2.5)$$

as well as the scaled deflection angle

$$\vec{\alpha}(\vec{x}) = \frac{D_L D_{LS}}{\xi_0 D_S} \hat{\alpha}(\xi_0 \vec{x}). \quad (2.6)$$

Carrying out some substitutions, Eq. (2.2) can finally be written as

$$\vec{y} = \vec{x} - \vec{\alpha}(\vec{x}). \quad (2.7)$$

Solving the lens equation

From Eqs. 2.4 and 2.7, it is obvious that knowing the intrinsic position of the source and the deflection angle field $\vec{\alpha}(\vec{\theta})$ of the lens, the positions of the image(s) can be found by solving the lens equation for $\vec{\theta}$. As it will be discussed later on, this can be achieved analytically only for very simple lens mass distributions. Indeed, the equation is typically highly non-linear. When multiple solutions exist, the source is lensed into *multiple images*.

When observing a lens system, the intrinsic position of the source is unknown, while the position of its images can be measured. Then the source intrinsic position can be recovered by assuming a model for the mass distribution of the lens, i.e. by solving the lens equation for $\vec{\beta}$. This is a much easier task, because the lens equation is linear in $\vec{\beta}$: for each image there is a unique solution. Thus, if multiple images of the same source are identified, and the lens mass model is correct, the same solution of the lens equation should be found for all images.

2.2 Lensing potential

An extended distribution of matter is characterized by its *effective lensing potential*, obtained by projecting the three-dimensional Newtonian potential on the lens plane and by properly rescaling it:

$$\hat{\Psi}(\vec{\theta}) = \frac{D_{LS}}{D_L D_S} \frac{2}{c^2} \int \Phi(D_L \vec{\theta}, z) dz. \quad (2.8)$$

The lensing potential satisfies two important properties:

1. the gradient of $\hat{\Psi}$ is the reduced deflection angle:

$$\vec{\nabla}_\theta \hat{\Psi}(\vec{\theta}) = \vec{\alpha}(\vec{\theta}) . \quad (2.9)$$

Indeed, by taking the gradient of the lensing potential we obtain:

$$\begin{aligned} \vec{\nabla}_\theta \hat{\Psi}(\vec{\theta}) &= D_L \vec{\nabla}_\perp \hat{\Psi} = \vec{\nabla}_\perp \left(\frac{D_{LS}}{D_S} \frac{2}{c^2} \int \hat{\Phi}(\vec{\theta}, z) dz \right) \\ &= \frac{D_{LS}}{D_S} \frac{2}{c^2} \int \vec{\nabla}_\perp \Phi(\vec{\theta}, z) dz \\ &= \vec{\alpha}(\vec{\theta}) \end{aligned} \quad (2.10)$$

Note that, using the dimensionless notation,

$$\vec{\nabla}_x = \frac{\xi_0}{D_L} \vec{\nabla}_\theta . \quad (2.11)$$

We can see that

$$\vec{\nabla}_x \hat{\Psi}(\vec{\theta}) = \frac{\xi_0}{D_L} \vec{\nabla}_\theta \hat{\Psi}(\vec{\theta}) = \frac{\xi_0}{D_L} \vec{\alpha}(\vec{\theta}) . \quad (2.12)$$

By multiplying both sides of this equation by D_L^2/ξ_0^2 , we obtain

$$\frac{D_L^2}{\xi_0^2} \vec{\nabla}_x \hat{\Psi} = \frac{D_L}{\xi_0} \vec{\alpha} . \quad (2.13)$$

This allows us to introduce the dimensionless counterpart of $\hat{\Psi}$:

$$\Psi = \frac{D_L^2}{\xi_0^2} \hat{\Psi} . \quad (2.14)$$

Substituting Eq. 2.14 into Eq 2.13, we see that

$$\vec{\nabla}_x \Psi(\vec{x}) = \vec{\alpha}(\vec{x}) . \quad (2.15)$$

2. the Laplacian of $\hat{\Psi}$ is twice the *convergence* κ :

$$\Delta_\theta \hat{\Psi}(\vec{\theta}) = 2\kappa(\vec{\theta}) . \quad (2.16)$$

The *convergence* is defined as a dimensionless surface density

$$\kappa(\vec{\theta}) \equiv \frac{\Sigma(\vec{\theta})}{\Sigma_{cr}} \quad \text{with} \quad \Sigma_{cr} = \frac{c^2}{4\pi G} \frac{D_S}{D_L D_{LS}} , \quad (2.17)$$

where Σ_{cr} is called the *critical surface density*, a quantity which characterizes the lens system and which is a function of the angular diameter distances of lens and source.

Eq. 2.16 is derived from the Poisson equation,

$$\Delta \Phi = 4\pi G \rho . \quad (2.18)$$

The surface mass density is

$$\Sigma(\vec{\theta}) = \frac{1}{4\pi G} \int_{-\infty}^{+\infty} \Delta \Phi dz \quad (2.19)$$

and

$$\kappa(\vec{\theta}) = \frac{1}{c^2} \frac{D_L D_{LS}}{D_S} \int_{-\infty}^{+\infty} \Delta \Phi dz . \quad (2.20)$$

Let us now introduce a two-dimensional Laplacian

$$\triangle_\theta = \frac{\partial^2}{\partial \theta_1^2} + \frac{\partial^2}{\partial \theta_2^2} = D_L^2 \left(\frac{\partial^2}{\partial \xi_1^2} + \frac{\partial^2}{\partial \xi_2^2} \right) = D_L^2 \left(\Delta - \frac{\partial^2}{\partial z^2} \right), \quad (2.21)$$

which gives

$$\Delta \Phi = \frac{1}{D_L^2} \triangle_\theta \Phi + \frac{\partial^2 \Phi}{\partial z^2}. \quad (2.22)$$

Inserting Eq. 2.22 into Eq. 2.20, we obtain

$$\kappa(\vec{\theta}) = \frac{1}{c^2} \frac{D_{LS}}{D_S D_L} \left[\triangle_\theta \int_{-\infty}^{+\infty} \Phi dz + D_L^2 \int_{-\infty}^{+\infty} \frac{\partial^2 \Phi}{\partial z^2} dz \right]. \quad (2.23)$$

If the lens is gravitationally bound, $\partial \Phi / \partial z = 0$ at its boundaries and the second term on the right hand side vanishes. From Eqs. 2.8 and 2.14, we find

$$\kappa(\theta) = \frac{1}{2} \triangle_\theta \hat{\Psi} = \frac{1}{2} \frac{\xi_0^2}{D_L^2} \triangle_\theta \Psi. \quad (2.24)$$

Since

$$\triangle_\theta = D_L^2 \triangle_\xi = \frac{D_L^2}{\xi_0^2} \triangle_x, \quad (2.25)$$

using dimensionless quantities, Eq. 2.24 reads

$$\kappa(\vec{x}) = \frac{1}{2} \triangle_x \Psi(\vec{x}) \quad (2.26)$$

Integrating Eq. (2.16), the effective lensing potential can be written in terms of the convergence as

$$\Psi(\vec{x}) = \frac{1}{\pi} \int_{\mathbf{R}^2} \kappa(\vec{x}') \ln |\vec{x} - \vec{x}'| d^2 x', \quad (2.27)$$

from which we obtain that the scaled deflection angle is

$$\vec{\alpha}(\vec{x}) = \frac{1}{\pi} \int_{\mathbf{R}^2} d^2 x' \kappa(\vec{x}') \frac{\vec{x} - \vec{x}'}{|\vec{x} - \vec{x}'|}. \quad (2.28)$$

2.3 First order lens mapping

One of the main consequences of gravitational lensing is image distortion. This is particularly evident when the source has an extended size. For example, background galaxies can appear as very long arcs when lensed by galaxy clusters or other galaxies.

The distortion arises because light bundles are deflected differentially. Ideally, the shape of the images can be determined by solving the lens equation for all the points within the extended source. In particular, if the source is much smaller than the angular scale on which the lens deflection angle field changes, the relation between source and image positions can locally be linearized.

This situation is sketched in Fig. 2.3.1. Let us consider a point on the lens (or image) plane at position $\vec{\theta}$, where the deflection angle is $\vec{\alpha}$. If the deflection angle satisfies the above conditions, at the nearby location $\vec{\theta}' = \vec{\theta} + d\vec{\theta}$, the deflection will be

$$\vec{\alpha}' \simeq \vec{\alpha} + \frac{d\vec{\alpha}}{d\vec{\theta}} d\vec{\theta}. \quad (2.29)$$

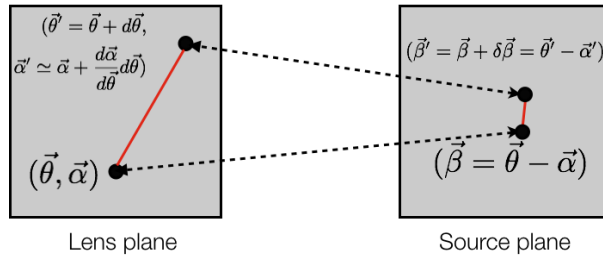


Figure 2.3.1: Linear mapping between the lens and the source plane, assuming a slowly varying deflection angle.

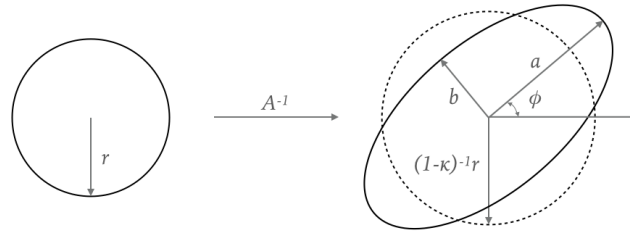


Figure 2.3.2: Distortion effects due to convergence and shear on a circular source.

Using the lens equation, the points $\vec{\theta}$ and $\vec{\theta}'$ can be mapped on the points $\vec{\beta}$ and $\vec{\beta}' = \vec{\beta} + d\vec{\beta}$ onto the source plane. Through this mapping, the vector $(\vec{\beta}' - \vec{\beta})$ is given by

$$(\vec{\beta}' - \vec{\beta}) = \left(I - \frac{d\vec{\alpha}}{d\vec{\theta}} \right) (\vec{\theta}' - \vec{\theta}). \quad (2.30)$$

In other words, the distortion of images can be described by the Jacobian matrix

$$A \equiv \frac{\partial \vec{\beta}}{\partial \vec{\theta}} = \left(\delta_{ij} - \frac{\partial \alpha_i(\vec{\theta})}{\partial \theta_j} \right) = \left(\delta_{ij} - \frac{\partial^2 \hat{\Psi}(\vec{\theta})}{\partial \theta_i \partial \theta_j} \right), \quad (2.31)$$

where θ_i indicates the i -component of $\vec{\theta}$ on the lens plane.

Eq. (2.31) shows that the elements of the Jacobian matrix can be written as combinations of the second derivatives of the lensing potential. For brevity, we will use the shorthand notation

$$\frac{\partial^2 \hat{\Psi}(\vec{\theta})}{\partial \theta_i \partial \theta_j} \equiv \hat{\Psi}_{ij}. \quad (2.32)$$

We can now split off the isotropic part from the Jacobian, to obtain its traceless part:

$$\left(A - \frac{1}{2} \text{tr} A \cdot I \right)_{ij} = \delta_{ij} - \hat{\Psi}_{ij} - \frac{1}{2}(1 - \hat{\Psi}_{11} + 1 - \hat{\Psi}_{22})\delta_{ij} \quad (2.33)$$

$$= -\hat{\Psi}_{ij} + \frac{1}{2}(\hat{\Psi}_{11} + \hat{\Psi}_{22})\delta_{ij} \quad (2.34)$$

$$= \begin{pmatrix} -\frac{1}{2}(\hat{\Psi}_{11} - \hat{\Psi}_{22}) & -\hat{\Psi}_{12} \\ -\hat{\Psi}_{12} & \frac{1}{2}(\hat{\Psi}_{11} - \hat{\Psi}_{22}) \end{pmatrix}. \quad (2.35)$$

This allows us to define the *shear* tensor

$$\Gamma = \begin{pmatrix} \gamma_1 & \gamma_2 \\ \gamma_2 & -\gamma_1 \end{pmatrix}, \quad (2.36)$$

often written in the form of a pseudo-vector $\vec{\gamma} = (\gamma_1, \gamma_2)$, whose components are

$$\gamma_1 = \frac{1}{2}(\hat{\Psi}_{11} - \hat{\Psi}_{22}) \quad (2.37)$$

$$\gamma_2 = \hat{\Psi}_{12} = \hat{\Psi}_{21}. \quad (2.38)$$

The shear is manifestly an symmetric, traceless tensor. It quantifies the projection of the gravitational tidal field (the gradient of the gravitational force), which describes distortions of background sources.

The eigenvalues of the shear tensor are

$$\pm\sqrt{\gamma_1^2 + \gamma_2^2} = \pm\gamma. \quad (2.39)$$

Thus, there exist a rotation $R(\varphi)$ such that the shear tensor (and therefore the Jacobian) can be written in a diagonal form. Generally, the Jacobian transforms as

$$A \rightarrow A' = R(\varphi)^T A R(\varphi) \quad (2.40)$$

where T indicates the transposed matrix. This shows that the shear components transform under rotations as

$$\begin{aligned} \gamma_1 &\rightarrow \gamma'_1 = \gamma_1 \cos(2\varphi) + \gamma_2 \sin(2\varphi) \\ \gamma_2 &\rightarrow \gamma'_2 = -\gamma_1 \sin(2\varphi) + \gamma_2 \cos(2\varphi), \end{aligned} \quad (2.41)$$

unlike a vector. Since the shear components are invariant under rotations of $\varphi = \pi$ rather than $\varphi = 2\pi$, they form a spin-2 tensor.

We can write the shear tensor as

$$\begin{pmatrix} \gamma_1 & \gamma_2 \\ \gamma_2 & -\gamma_1 \end{pmatrix} = \gamma \begin{pmatrix} \cos 2\phi & \sin 2\phi \\ \sin 2\phi & -\cos 2\phi \end{pmatrix}, \quad (2.42)$$

where we have introduced the angle ϕ , which identifies the direction of the eigenvector of the shear tensor corresponding to the eigenvalue $+\gamma$.



Note the factor 2 on the angle ϕ , which reminds that the shear component are elements of a 2×2 tensor and not a vector.

The remainder of the Jacobian is

$$\frac{1}{2}\text{tr}A \cdot I = \left[1 - \frac{1}{2}(\hat{\Psi}_{11} + \hat{\Psi}_{22})\right] \delta_{ij} \quad (2.43)$$

$$= \left(1 - \frac{1}{2}\Delta\hat{\Psi}\right) \delta_{ij} = (1 - \kappa) \delta_{ij}. \quad (2.44)$$

Thus, the Jacobian matrix becomes

$$\begin{aligned} A &= \begin{pmatrix} 1 - \kappa - \gamma_1 & -\gamma_2 \\ -\gamma_2 & 1 - \kappa + \gamma_1 \end{pmatrix} \\ &= (1 - \kappa) \begin{pmatrix} 1 & 0 \\ 0 & 1 \end{pmatrix} - \gamma \begin{pmatrix} \cos 2\phi & \sin 2\phi \\ \sin 2\phi & -\cos 2\phi \end{pmatrix}. \end{aligned} \quad (2.45)$$

The last equation explains the meaning of both convergence and shear. The convergence determines an isotropic transformation, i.e. the images are only rescaled by a constant factor $1/(1 - \kappa)$ in all directions. On the other hand, the shear stretches the intrinsic shape of the source along privileged directions. Specifically, the stretch corresponds to an extra term $+\gamma$ in the direction set by angle ϕ and $-\gamma$ in the perpendicular direction. Indeed, the eigenvalues of the Jacobian matrix are

$$\lambda_t = 1 - \kappa - \gamma \quad (2.46)$$

$$\lambda_r = 1 - \kappa + \gamma. \quad (2.47)$$

2.3.1 Lensing of circular source

Let consider the reference frame where the Jacobian is diagonal. Then,

$$A = \begin{pmatrix} 1 - \kappa - \gamma & 0 \\ 0 & 1 - \kappa + \gamma \end{pmatrix}. \quad (2.48)$$

Consider a circular source, whose isophotes have equation $\beta_1^2 + \beta_2^2 = r^2$. The lens equation implies that the points on the source plane satisfying this equation are mapped onto the points (θ_1, θ_2) , such that

$$\begin{pmatrix} \beta_1 \\ \beta_2 \end{pmatrix} = \begin{pmatrix} 1 - \kappa - \gamma & 0 \\ 0 & 1 - \kappa + \gamma \end{pmatrix} \begin{pmatrix} \theta_1 \\ \theta_2 \end{pmatrix}. \quad (2.49)$$

Thus

$$\beta_1 = (1 - \kappa - \gamma)\theta_1 \quad (2.50)$$

$$\beta_2 = (1 - \kappa + \gamma)\theta_2. \quad (2.51)$$

Summing in quadrature, we obtain

$$r^2 = \beta_1^2 + \beta_2^2 = (1 - \kappa - \gamma)^2\theta_1^2 + (1 - \kappa + \gamma)^2\theta_2^2, \quad (2.52)$$

which is the equation of an ellipse on the lens plane. Thus, a circular source, which is small enough compared to the typical length-scale over which the lens deflection field varies, like is mapped onto an ellipse when κ and γ are both non-zero, as shown in Fig. (2.3.2).

The semi-major and -minor axes of the ellipse are

$$a = \frac{r}{1 - \kappa - \gamma}, \quad b = \frac{r}{1 - \kappa + \gamma}. \quad (2.53)$$

Obviously, the ellipse reduces to a circle if $\gamma = 0$.

As said in the previous section, in an arbitrary reference frame, the ellipse will have its axes aligned with the eigenvectors of the shear tensor. Note that:

- if $\gamma_1 > 0$ and $\gamma_2=0$, then the major axis of the ellipse will be along the θ_1 axis;
- if $\gamma_1 = 0$ and $\gamma_2>0$, then the major axis of the ellipse will form an angle $\pi/4$ with the θ_1 axis;
- if $\gamma_1 < 0$ and $\gamma_2=0$, then the major axis of the ellipse will be perpendicular to the θ_1 axis;
- if $\gamma_1 = 0$ and $\gamma_2<0$, then the major axis of the ellipse will form an angle $3\pi/4$ with the θ_1 axis.

In Fig. 2.3.3, the ellipse orientation is shown for different values of the two components of the shear.

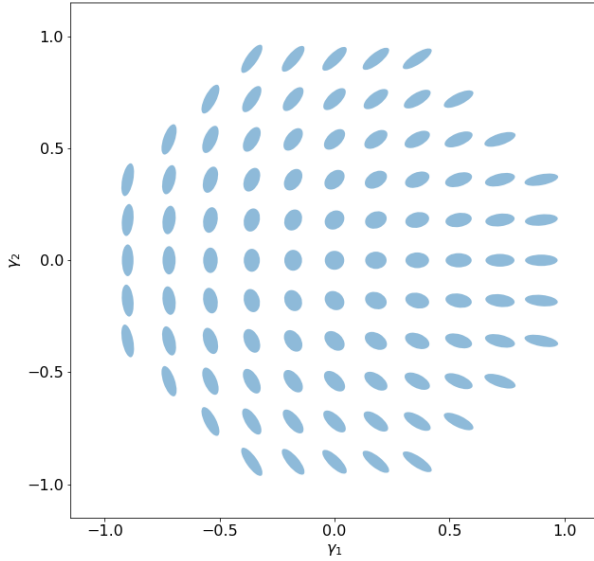


Figure 2.3.3: Orientation of the images of a circular source for different values of γ_1 and γ_2 .

2.4 Magnification

An important consequence of the lensing distortion is the magnification. Through the lens equation, the solid angle element $\delta\beta^2$ (or equivalently the surface element $\delta\eta^2$ or δy^2) is mapped onto the solid angle $\delta\theta^2$ (or on the surface element $\delta\xi^2$ or δx^2). Because of the Liouville theorem, in absence of emission and absorbtion of photons, the source surface brightness is conserved despite light deflection. Thus, the change of the solid angle under which the source is observed implies that the flux received is magnified (or demagnified).

Given Eq. (2.31), the *magnification* is given by the inverse of the determinant of the Jacobian matrix. For this reason, the matrix $M = A^{-1}$ is called the *magnification tensor*. We therefore define

$$\mu \equiv \det M = \frac{1}{\det A} = \frac{1}{(1-\kappa)^2 - \gamma^2}. \quad (2.54)$$

The eigenvalues of the magnification tensor (or the inverse of the eigenvalues of the Jacobian matrix) measure the amplification in the direction of the eigenvectors of the shear tensor. For an axially symmetric lens, these are tangentially and radially oriented with respect to the lens iso-surface density contours. Thus, the quantities

$$\mu_t = \frac{1}{\lambda_t} = \frac{1}{1-\kappa-\gamma} \quad (2.55)$$

$$\mu_r = \frac{1}{\lambda_r} = \frac{1}{1-\kappa+\gamma} \quad (2.56)$$

are often called the *tangential* and *radial* magnification factors.

The magnification is ideally infinite where $\lambda_t = 0$ and where $\lambda_r = 0$. These two conditions define two curves in the lens plane, called the *tangential* and the *radial critical lines*.

2.5 Lensing to the second order

We extend now the lens equation including the second order terms in the expansion of the deflection angle. The lens equation then becomes

$$\beta_i \simeq \frac{\partial \beta_i}{\partial \theta_j} \theta_j + \frac{1}{2} \frac{\partial^2 \beta_i}{\partial \theta_j \partial \theta_k} \theta_j \theta_k . \quad (2.57)$$

We introduce the tensor

$$D_{ijk} = \frac{\partial^2 \beta_i}{\partial \theta_j \partial \theta_k} = \frac{\partial A_{ij}}{\partial \theta_k} . \quad (2.58)$$

Then, Eq. 2.57 reads

$$\beta_i \simeq A_{ij} \theta_j + \frac{1}{2} D_{ijk} \theta_j \theta_k \quad (2.59)$$

By simple algebra, it can be shown that

$$D_{ij1} = \begin{pmatrix} -2\gamma_{1,1} - \gamma_{2,2} & -\gamma_{2,1} \\ -\gamma_{2,1} & -\gamma_{2,2} \end{pmatrix} , \quad (2.60)$$

and

$$D_{ij2} = \begin{pmatrix} -\gamma_{2,1} & -\gamma_{2,2} \\ -\gamma_{2,2} & 2\gamma_{1,2} - \gamma_{2,1} \end{pmatrix} . \quad (2.61)$$

Thus, the second order lensing effect can be expressed in terms of the derivatives of the shear (or in terms of the third derivatives of the potential).

2.5.1 Complex notation

It is quite useful to use complex notation to map vectors or pseudo-vectors on the complex plane. Indeed, in this case we can also use complex differential operators to write down some relations between the lensing quantities in a very concise way.

In complex notation, any vector or pseudo-vector $v = (v_1, v_2)$ is written as

$$v = v_1 + i v_2 . \quad (2.62)$$

Similarly we can define the complex deflection angle $\alpha = \alpha_1 + i \alpha_2$ and the complex shear $\gamma = \gamma_1 + i \gamma_2$.

It is also possible to define some complex differential operators, namely

$$\partial = \partial_1 + i \partial_2 \quad (2.63)$$

and

$$\partial^\dagger = \partial_1 - i \partial_2 . \quad (2.64)$$

Using this formalism, we can easily see that

$$\partial \hat{\Psi} = \partial_1 \hat{\Psi} + i \partial_2 \hat{\Psi} = \alpha_1 + i \alpha_2 = \alpha . \quad (2.65)$$

Moreover

$$\partial^\dagger \partial = \partial_1^2 + \partial_2^2 = \Delta . \quad (2.66)$$

Thus,

$$\partial^\dagger \partial \hat{\Psi} = \Delta \hat{\Psi} = 2\kappa . \quad (2.67)$$

Note that while $\hat{\Psi}$ is a spin-0 scalar field, the application of the ∂ operator gives the deflection angle, i.e. a spin-1 vector field. On the contrary, the ∂^\dagger operator applied to the deflection field gives another spin-0 scalar field (the convergence). Therefore, the ∂ and ∂^\dagger operators can be considered as spin raising and lowering operators.

By applying twice the raising operator, we obtain

$$\frac{1}{2} \partial \partial \hat{\Psi} = \frac{1}{2} \partial \alpha = \gamma : \quad (2.68)$$

the shear field is indeed a spin-2 tensor field, which is invariant for rotations by multiples of π .

Note also that

$$\partial^{-1} \partial^\dagger \gamma = \frac{1}{2} \partial^{-1} \partial^\dagger \partial \partial \hat{\Psi} = \partial^\dagger \partial \hat{\Psi} = \kappa \quad (2.69)$$

We can use the raising and lowering operators to define

$$F = \frac{1}{2} \partial \partial^\dagger \partial \hat{\Psi} = \partial \kappa \quad (2.70)$$

$$G = \frac{1}{2} \partial \partial \partial \hat{\Psi} = \partial \gamma \quad (2.71)$$

After some math, it can be shown that

$$F = F_1 + iF_2 = (\gamma_{1,1} + \gamma_{2,2}) + i(\gamma_{2,1} - \gamma_{1,2}) \quad (2.72)$$

and

$$G = G_1 + iG_2 = (\gamma_{1,1} - \gamma_{2,2}) + i(\gamma_{2,1} + \gamma_{1,2}) . \quad (2.73)$$

The quantities F and G are called *first and second flexion*, respectively. It is easy to show that D_{ijk} can be written in terms of F and G . Thus, they describe second order distortions of the images of lensed sources. Note that F is a spin-1 vector field. Indeed, it is

$$\vec{F} = \vec{\nabla} \kappa . \quad (2.74)$$

Thus, it describes transformations that are invariant under rotations by 2π . For this reason, F stretches the images along one particular direction, introducing asymmetries in their shape. On the contrary, G is a spin-3 tensor field. The transformations described by G are invariant under rotations by $2\pi/3$. This is manifested in the "triangular" pattern in the image shapes, as shown in Fig. 2.5.1.

2.6 Time delay surface

2.6.1 Gravitational and geometrical time delays

The deflection of light rays causes a delay in the travel-time of light between the source and the observer. This time delay has two components:

$$t = t_{\text{grav}} + t_{\text{geom}} \quad (2.75)$$

The first one is the *gravitational time delay*, also known as the Shapiro delay. It can be derived by comparing the time required for light to travel through a space-time with an effective refractive index and through empty space, by assuming *same trajectories*.

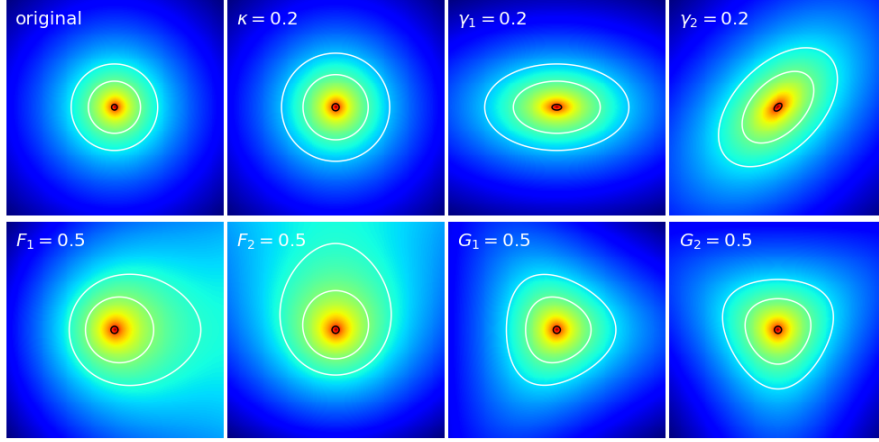


Figure 2.5.1: First and second order distortions on the image of a circular source. The unlensed source is shown in the top left panel. The convergence simply changes the size (second-left upper panel). While the shear deforms the image such that it becomes elliptical (third and fourth panels on the upper row), the first and the second flexion introduce curvature and other distortions (panels on the bottom).

Let $n = 1 - 2\Phi/c^2$ be the effective refractive index. We have that

$$t_{\text{grav}} = \int \frac{dz}{c'} - \int \frac{dz}{c} = \frac{1}{c} \int (n-1) dz = -\frac{2}{c^3} \int \Phi dz \quad (2.76)$$

Using the definition of the lensing potential, this can be written as

$$t_{\text{grav}} = -\frac{D_L D_S}{D_{LS}} \frac{1}{c} \hat{\Psi}. \quad (2.77)$$

The second term in the time delay is called *geometrical* and is due to the different path length of the deflected light rays compared to the unperturbed ones. This time delay is proportional to the squared angular separation between the intrinsic position of the source and the location of its image. This result can be derived from the metric, but it can be estimated also through a simple geometrical construction, shown in Fig. 2.6.1. The extra-path of the light in presence of the lens can be written as

$$\Delta l = \xi \frac{\hat{\vec{\alpha}}}{2} = (\vec{\theta} - \vec{\beta}) \frac{D_L D_S}{D_{LS}} \frac{\vec{\alpha}}{2} = \frac{1}{2} (\vec{\theta} - \vec{\beta})^2 \frac{D_L D_S}{D_{LS}}, \quad (2.78)$$

and the corresponding time-delay is

$$t_{\text{geom}} = \frac{\Delta l}{c} \quad (2.79)$$

Both the time delays occur at the lens position, thus they need to be multiplied by a factor $(1 + z_L)$ for accounting for the expansion of the universe. Then, the total time delay introduced by

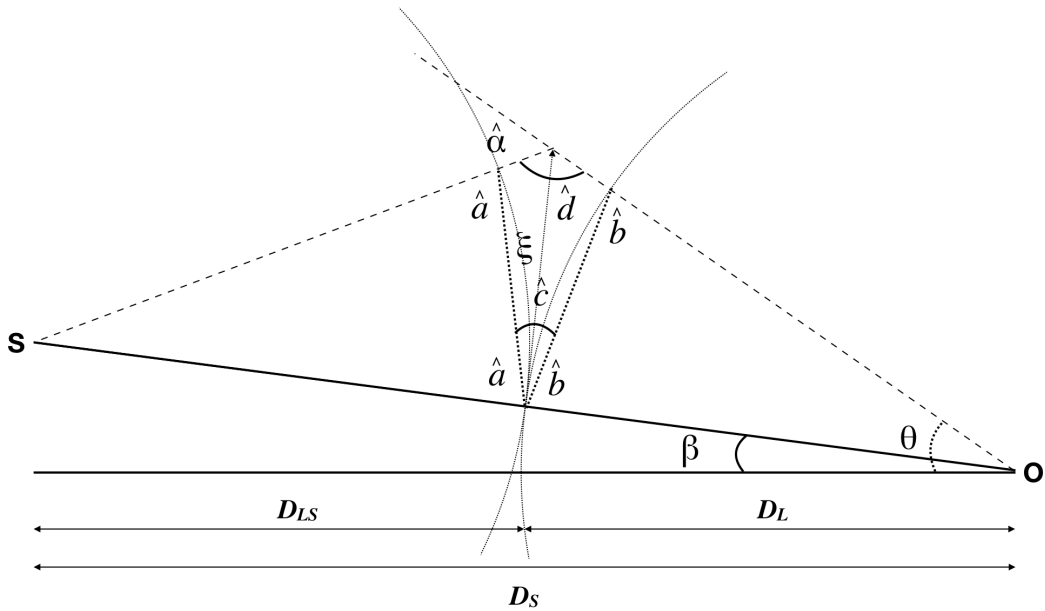


Figure 2.6.1: Illustration of the geometrical time delay.

gravitational lensing at the position $\vec{\theta}$ on the lens plane is¹

$$\begin{aligned} t(\vec{\theta}) &= \frac{(1+z_L)}{c} \frac{D_L D_S}{D_{LS}} \left[\frac{1}{2} (\vec{\theta} - \vec{\beta})^2 - \hat{\Psi}(\vec{\theta}) \right] \\ &= \frac{D_{\Delta t}}{c} \tau(\vec{\theta}) . \end{aligned} \quad (2.80)$$

The quantities

$$D_{\Delta t} = (1+z_L) \frac{D_S D_L}{D_{LS}} \quad (2.81)$$

and

$$\tau(\vec{\theta}) = \frac{1}{2} (\vec{\theta} - \vec{\beta})^2 - \hat{\Psi}(\vec{\theta}) , \quad (2.82)$$

are often called *time delay distance* and *Fermat potential*, respectively.

2.6.2 Multiple images and magnification

Through the effective lensing potential, the lens equation can be written as

$$(\vec{\theta} - \vec{\beta}) - \nabla \hat{\Psi}(\vec{\theta}) = \nabla \left[\frac{1}{2} (\vec{\theta} - \vec{\beta})^2 - \hat{\Psi}(\vec{\theta}) \right] = 0 . \quad (2.83)$$

Eqs. (2.80) and (2.83) imply that images satisfy the Fermat Principle, $\nabla t(\vec{\theta}) = 0$. Images therefore are located at the stationary points of the time delay surface given by Eq. (2.80). The Hessian matrix of this surface is

$$T = \frac{\partial^2 t(\vec{\theta})}{\partial \theta_i \partial \theta_j} \propto (\delta_{ij} - \hat{\Psi}_{ij}) = A \quad (2.84)$$

¹The dimensionless form of the time delay can be obtained by multiplying and dividing by the factor $(\xi_0/D_L)^2$.

Given that the Hessian matrix of the time delay surface coincides with the lensing Jacobian, and that the magnification $\mu = \det A^{-1}$, it is clear that the curvature of the time delay surface at the image position is inversely proportional to the image magnification. In particular, a flat time delay surface implies an infinite magnification, while a large curvature means that the magnification is small.

One can also measure the curvature along a specific direction on the time delay surface. This will provide a way to quantify the image distortions. Therefore, the shape of the time delay surface near the stationary points will also provide hints on the shape of the images.

We can distinguish between three types of images:

1. type I images arise at the minima of the time delay surface, where the eigenvalues of the Hessian matrix are both positive, hence $\det A > 0$ and $\text{tr} A > 0$. Therefore, they have positive magnifications;
2. type II images arise at the saddle points of the time delay surface, where eigenvalues have opposite signs. Since $\det A < 0$, they have negative magnifications;
3. finally, type III images arise at the maxima of the time delay surface. Here, the eigenvalues are both negative, hence $\det A > 0$ and $\text{tr} A < 0$. These images therefore have positive magnification.



Note that a negative magnification does not mean that the image is de-magnified! The absolute value of the magnification accounts for how much larger is the solid angle of the image with respect to that of the unlensed source. Thus, the image is de-magnified only if $|\mu| < 1$. Instead, the sign of the magnification is related to the *parity* of the image. The parity determines the orientation of the image with respect to the unlensed source.

2.6.3 Examples

Eq. 2.80 shows that the time delay surface is obtained by summing the paraboloid $\propto (\vec{\theta} - \vec{\beta})^2$, which has a minimum at the position of the source, and the surface $-\hat{\Psi}(\vec{\theta})$. The lensing potential of a centrally concentrated lens has a minimum at the lens center. Thus, because of the negative sign, the function $-\hat{\Psi}$ peaks at the center of the lens, regardless of the position of the source. For simplicity, we choose the reference frame, (θ_1, θ_2) such that the lens center is at $(0, 0)$, and we study how the shape of the time delay surface changes as a function of the position of the source, $\vec{\beta}$.

Axially symmetric lenses: one dimensional case

We begin with an axially symmetric lens. Let us forget for the moment that the $t(\vec{\theta}|\beta)$ is a surface and consider the azimuthal cut of the surface along an arbitrary direction passing through the center of the lens and the source position. As an example, we consider the potential

$$\hat{\Psi}(\theta) \propto \frac{1}{\sqrt{\theta^2 + \theta_c^2}}. \quad (2.85)$$

As we will see in Chapter 4, this potential corresponds to a cored isothermal lens. The core radius θ_c prevents the potential from diverging for $\theta \rightarrow 0$.

In Fig. 2.6.2, we show the geometrical and the gravitational components of the time delay and their combination for a few positions of the source relative to the lens, given by the vertical dashed lines. Given that β is a parameter defining the shape of the time delay surface, we use the notation $t(\theta) \equiv t(\theta, \beta)$. For $\beta = 0$ (upper left panel), the time delay function $t(\theta, 0)$ has a local maximum at $\theta_0 = 0$, and two minima on both sides of the origin, θ_- and θ_+ (of course, in this one-dimensional example there are no saddle points). Thus, the source at $\beta = 0$ has three images, forming at θ_0 , θ_- and θ_+ , with $\theta_- = -\theta_+$.

We shift the source with respect to the lens along the positive θ axis, and we notice that the symmetry of the time delay function breaks. In the upper-right panel, the maximum is now

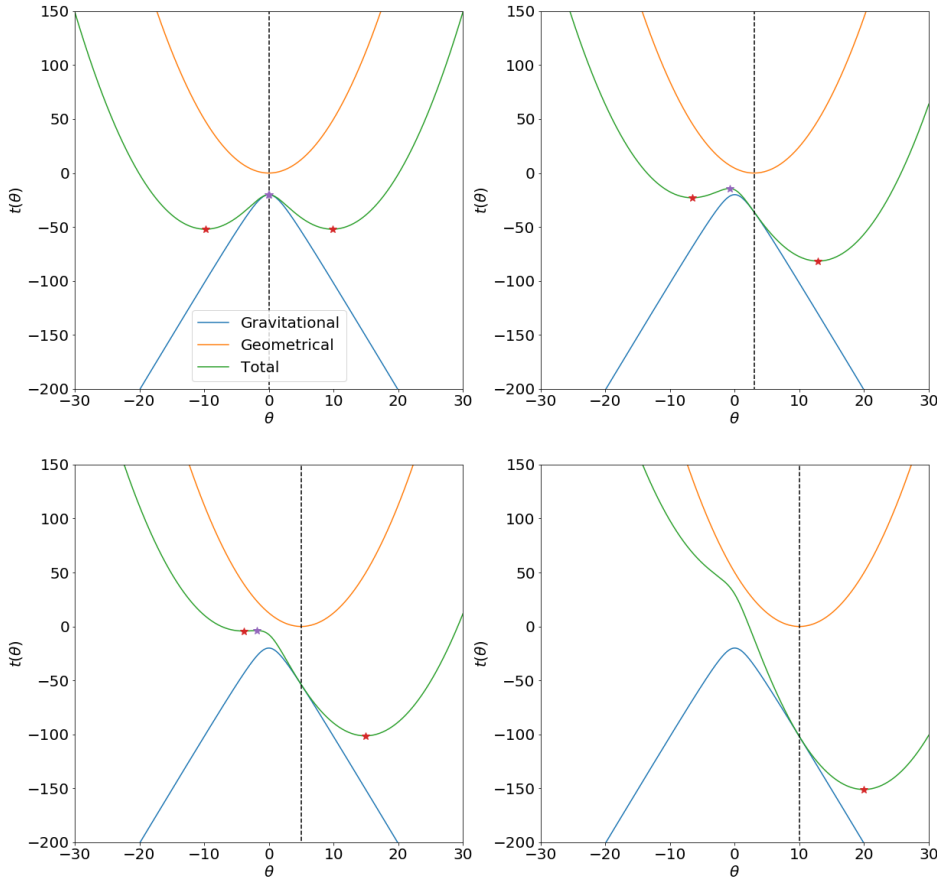


Figure 2.6.2: One-dimensional time-delay functions for a non-singular isothermal potential. Each panel corresponds to a different position of the source relative to the lens (dashed line). The two components of the time delay are shown separately and then combined. The positions of the images are indicated by stars.

shifted along the negative θ axis, $\theta_0 < 0$. One of the two minima, θ_+ moves away from the origin, following the source (i.e. along the positive θ axis), while the other moves towards the maximum. Note also that the difference between the time delays of the images θ_0 and θ_- , $t(\theta_0, \beta) - t(\theta_-, \beta)$, is smaller than in the previous case ($\beta = 0$). On the other hand, $t(\theta_+, \beta) < t(\theta_-, 0)$.

Let us focus on the curvature of $t(\theta, \beta)$. Clearly, moving the source along the positive θ axis, $t(\theta, \beta)$ flattens off in between θ_- and θ_0 . This implies an increasing magnification along the direction connecting the two images. Therefore, these will be stretched towards each other.

Moving the source further away from the lens, we will reach the situation where the two images θ_0 and θ_- will merge. At that point, the function $t(\theta, \beta)$ will only have one minimum, corresponding to the image θ_+ . The source will no longer have multiple images (bottom left panel). As $\beta \rightarrow \infty$, the image θ_+ will tend to coincide with β (bottom right panel).

It is interesting to see how the results are affected by the choice of the lensing potential. The

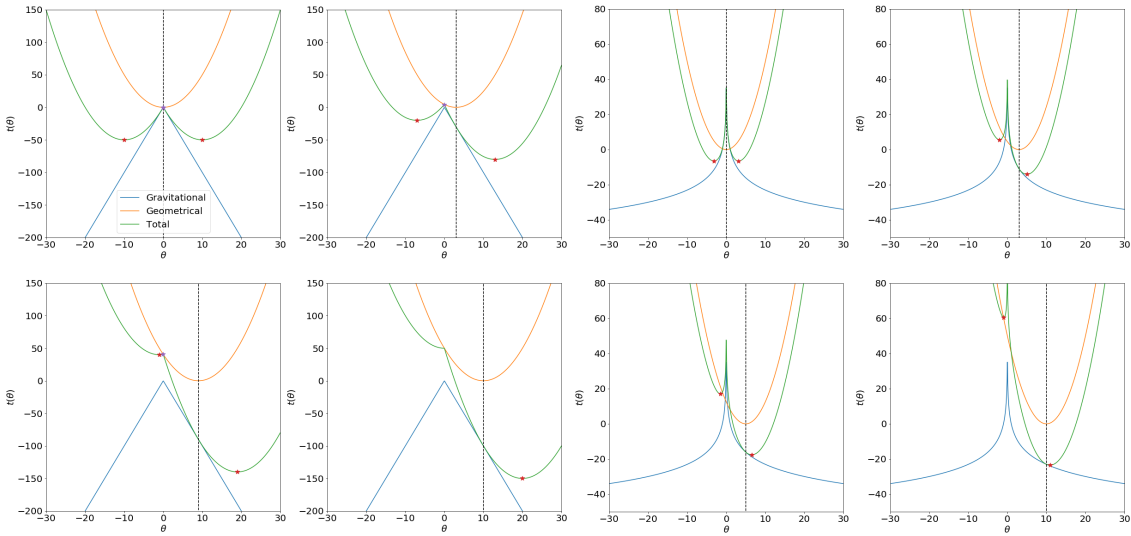


Figure 2.6.3: One-dimensional time-delay functions for singular-isothermal (left panels) and point-mass (right panels) potentials. Each panel corresponds to a different position of the source relative to the lens (dashed line). The two components of the time delay are shown separately and then combined. The positions of the images are indicated by stars.

examples in Fig. 2.6.3 show the results obtained by setting the core radius to $\theta_c = 0$ (left four panels) and by using a potential in the form

$$\hat{\Psi} \propto \ln |\theta|. \quad (2.86)$$

The second of these cases (right four panels) corresponds to the point-mass lens.

In both cases, the presence of the central singularity makes the function $t(\theta, \beta)$ non continuously deformable. This implies that, for every choice of β , the central image θ_0 , if any, will correspond to infinite curvature of the time-delay surface. Consequently, for these images the magnification will be $\mu = 0$. Note that, in the case of the point-mass lens, there are always two minima on the opposite sides of the lens. However, as $\beta \rightarrow \infty$, the curvature at $t(\theta_-, \beta)$ becomes increasingly higher, meaning that the image is increasingly de-magnified.

Axially symmetric lenses: two dimensional case

The correct representation of the time delay is through a surface, not a one-dimensional function. In Fig. 2.6.4, we show the two-dimensional analog of Fig 2.6.2, where the time-delay surfaces correspond to several positions of the source along the θ_1 axis (i.e. $\beta_2 = 0$). We also show the projection of the surfaces on the (θ_1, θ_2) planes and the sections of the surfaces along the θ_1 axis ($\theta_2 = 0$).

The upper left panel shows the time-delay surface $t(\vec{\theta}, 0)$. In this two-dimensional representation, we see that the minima $\vec{\theta}_-$ and $\vec{\theta}_+$ are part of a ring, due to the symmetry properties of the lens. We will see later that this ring is called *Einstein ring*. The central image, $\vec{\theta}_0$, still coincides with the center of the lens. Thus a point-source perfectly aligned with this axially symmetric (circular) lens is imaged into a point at the lens center and into a ring surrounding the lens.

Along the ring, the curvature of the time-delay surface is zero, meaning that the magnification diverges. This condition is met along the lens critical lines. More precisely, the Einstein ring corresponds to the tangential critical line of the lens. Given that the ring is originated by a source at $\vec{\beta} = (0, 0)$, this point on the source plane coincides with the lens tangential caustic.

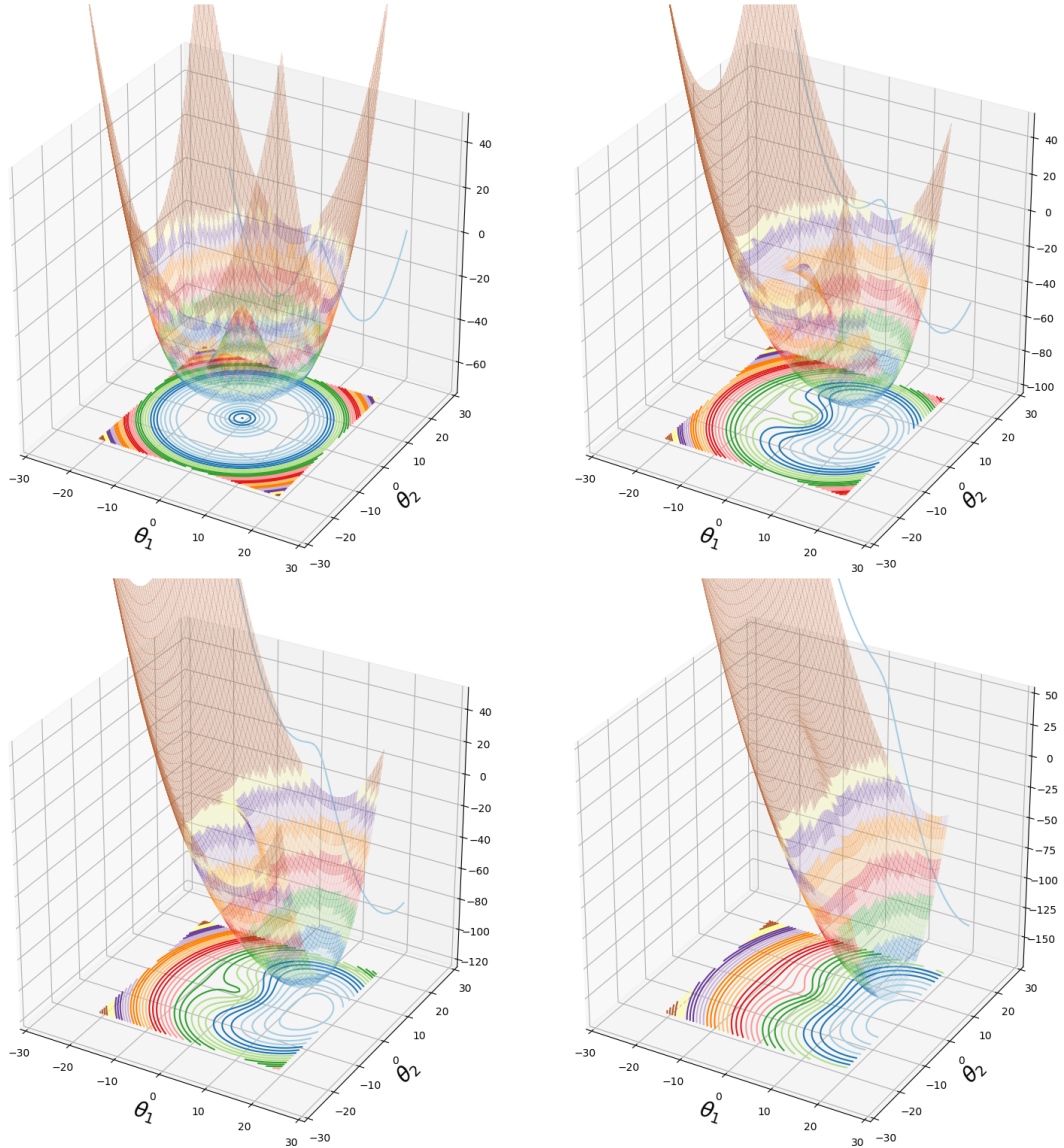


Figure 2.6.4: Time delay surfaces for the same lens used in Fig. 2.6.2. Different panels correspond to different positions of the source relative to the lens. The surfaces are projected onto the plane (θ_1, θ_2) on the bottom of each panel. The blue curves on the vertical plane behind the surfaces show the sections of the surfaces along the θ_1 axis at $\theta_2 = 0$.

Shifting the source with respect to the lens breaks the symmetry of the time-delay surface. In the upper-right panel of Fig. 2.6.4, we notice that the image at $\vec{\theta}_-$ is not a minimum, but a saddle point. As the source moves away from the lens, the saddle and the maximum points approach each other and the curvature of $t(\vec{\theta}, \vec{\beta})$ in between these two stationary points becomes increasingly smaller in the radial direction. When the two images coincide, the time-delay surface is radially flat (bottom left panel): the images $\vec{\theta}_-$ and $\vec{\theta}_0$ merge on another critical line: the radial critical line. The corresponding source position $\vec{\beta} = \vec{\beta}_{rad}$ marks the position of the radial caustic on the source plane. Due to the symmetry of the lens, the radial caustic of an axially symmetric lens is a circle with radius β_{rad} .

For large distances between the lens and the source, only the image $\vec{\theta}_+$ exists, which corresponds to the minimum of the time-delay surface.

As discussed earlier, adopting singular potentials, the time-delay surface becomes non continuously deformable. As a consequence, there are no configurations where the time-delay surface can become radially flat. This implies that these lenses do not have a radial critical line. In the case of the singular-isothermal lens ($\theta_c = 0$), there is a particular distance of the source from the lens center, β_{cut} , for which $\vec{\theta}_- = 0$. This condition defines a circle on the source plane called *cut*. The lens produces two images only if the source lays within the cut. Otherwise there is only one image.

Elliptical potentials

While axially symmetric lenses can produce up to three multiple images, depending on the relative position of the source relative to the lens, elliptical lenses behave differently. We can introduce ellipticity in the potentials considered in any of the previous examples by making the substitution

$$|\theta| \rightarrow \sqrt{\frac{\theta_1^2}{1-\varepsilon} + \theta_2^2(1-\varepsilon)} . \quad (2.87)$$

The resulting lens have elliptical iso-potential contours with major axes oriented along the θ_2 axis.



Lenses with elliptical potentials are not elliptical lenses. Indeed, their convergence maps do not have elliptical iso-contours. Instead, these contours typically have dumbbell shapes. Introducing large ellipticity in the potential can even lead to unphysical negative convergence. Lenses with elliptical potentials are dubbed *pseudo-elliptical* lenses.

When combined with the paraboloid describing the usual geometrical time delay, the resulting surface can have up to five stationary points, depending on the potential radial profile and of the relative positions of lens and source.

The examples displayed in Figs. 2.6.5 and 2.6.6 illustrate the case of a lens with cored isothermal potential and ellipticity $\varepsilon = 0.4$. The upper panels of Fig. 2.6.5 show the maps of the lensing potential before and after introducing the ellipticity. The left and the right bottom panels show the critical lines and the caustics of the lens, respectively. Fig. 2.6.6 displays the time delay surfaces corresponding to the source positions marked by the blue dots in the bottom left panel of Fig. 2.6.5. In the upper left panel (1), the source is at $\vec{\beta} = 0$. Such source have five multiple images: one maximum at the lens center, two minima symmetric with respect to the center of the lens along the θ_1 axis, and two saddle points, also symmetric with respect to the center of the lens, but forming along the θ_2 axis. This image configuration is called *Einstein cross*.

In the upper right panel (2), the source is shifted along the positive θ_1 axis. One of the two minima moves in the same direction, while the central maximum moves in the direction opposite to the source. The saddle points also move opposite to the source approaching the maximum and the minimum. Eventually, for even larger separations between the lens and the source, the saddle points, the maximum and the minimum merge, producing and image which is both radially and tangentially magnified. When this happens, the source is close to both the radial and the tangential caustics.

The middle panels show the case of a source moving along the positive θ_2 axis instead. Two minima and one saddle point move in the same direction. The maximum and the other saddle point approach each other along the negative θ_2 axis. As shown by the flatness of the time delay surface in between these two images, they are are radially magnified until the merge and disappear. This indicates that the source has crossed the radial caustic (3). Shifting the source further, also the two minima and the remaining saddle point merge, forming a very elongated, tangentially magnified image. Such configurations occur when the source is the proximity of the cusp of the caustic, while laying within the caustic itself (4). The largest gravitational arcs form in this way.

Finally, in the panels on the bottom the source is shifted along the diagonal in the (θ_1, θ_2) plane. As the source departs from the lens center, one of the minima follows the source. The other

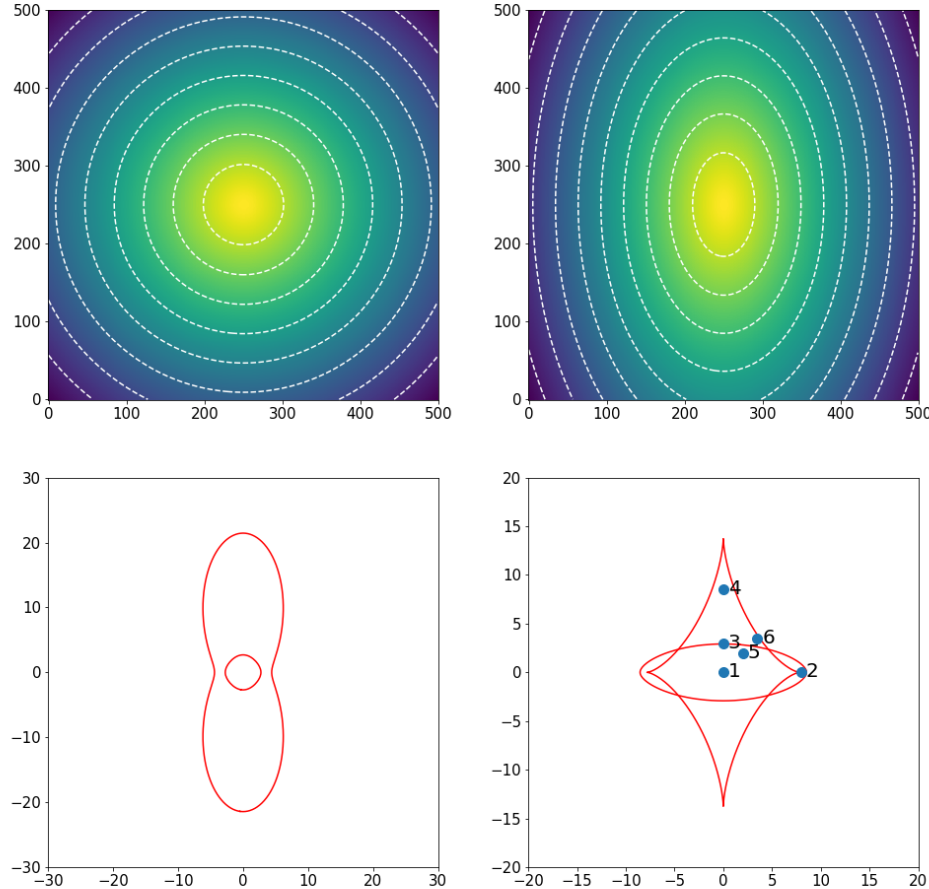


Figure 2.6.5: Pseudo-elliptical lens. Upper panels: the lensing potential before and after adding an ellipticity $\epsilon = 0.4$. Bottom panels: critical lines (left) and caustics (right). The blue dots mark the positions of the sources used to generate the time delay surfaces shown in Fig. 2.6.6.

minimum and one of the saddle points approach each other. The maximum and the other saddle point merge forming a radially elongate image opposite to the source with respect to the lens (5). Again, this happens when the source is located at the radial caustic. Shifting it further, we see that also one of the minima and the remaining saddle point merge, forming a tangentially elongated image. At this point, the source is on the tangential caustic (6).

2.6.4 General considerations

Here follows a number of other important properties of the continuously deformable time-delay surface:

- the height difference at different images of the surface $t(\vec{\theta})$ gives the difference in arrival time between these images. This time delay can be measured if the source is variable, and provides one way of potentially measuring the Hubble constant, as we will discuss in Chapter ??;

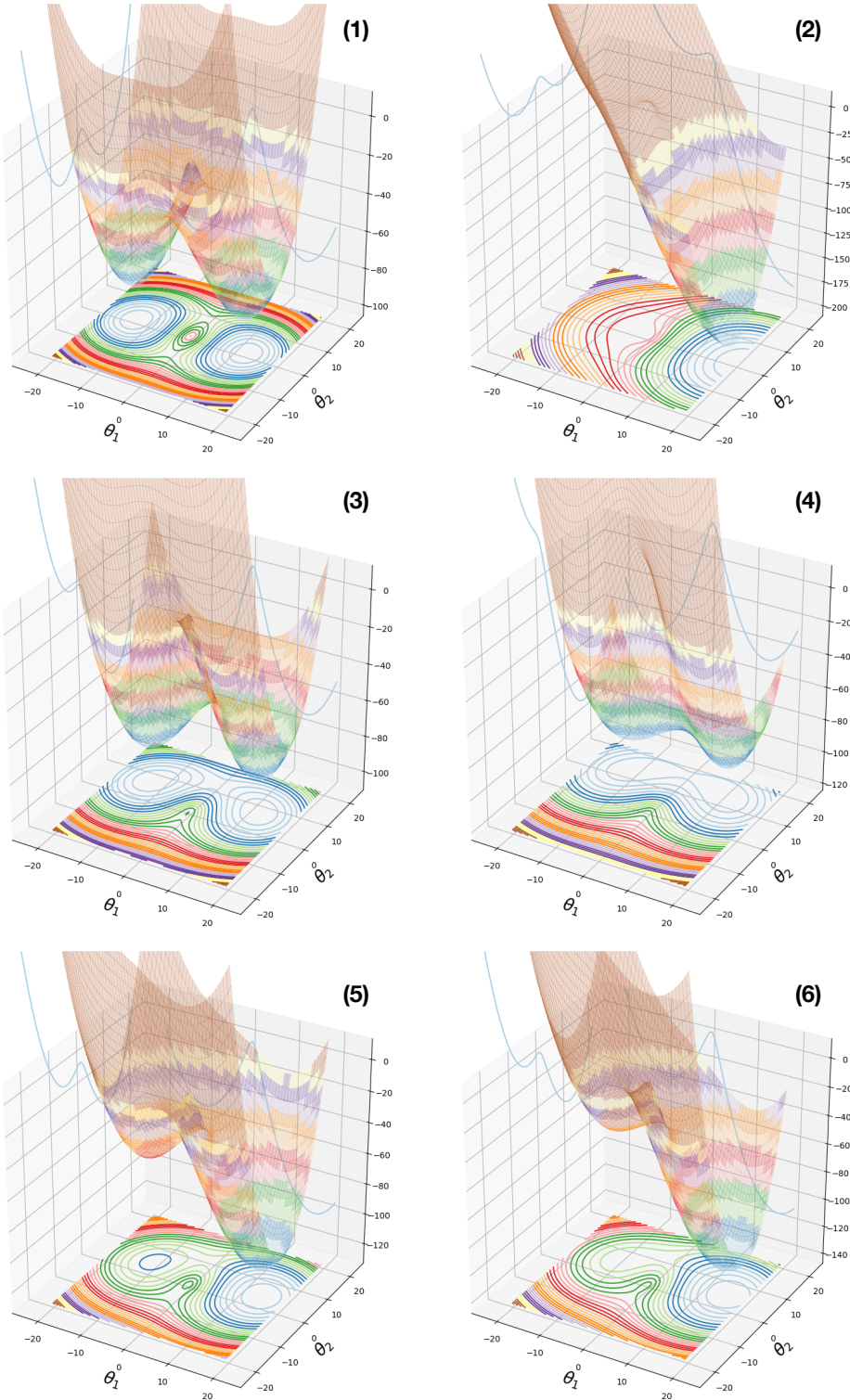


Figure 2.6.6: Time delay surfaces for a pseudo-elliptical lens with cored isothermal profile. Different panels correspond to different positions of the source relative to the lens. The surfaces are projected onto the plane (θ_1, θ_2) on the bottom of each panel. The blue curves on the vertical plane behind the surfaces show the sections of the surfaces along the θ_1 axis at $\theta_2 = 0$.

- in absence of the lens, the time-delay surface is a parabola which has a single extremum (a minimum); additional extrema have to come in pairs, thus the total number of images must be odd (as we showed earlier by continuously deforming the time-delay surface);
- when two additional images are formed, they must be a maximum and a saddle point; in between them, the curvature changes from negative to positive, thus it is zero between them; remember that $\det A = 0$ is the condition for having a critical point, where the magnification is (formally) infinite. The critical lines thus separate multiple-image pairs; these pairs merge and disappear (as discussed above) at the critical lines. In other words, the critical lines separate regions of different image multiplicities.

2.7 Python applications

2.7.1 Implementing a ray-tracing algorithm

In this exercise, we will implement a simple ray-tracing algorithm. In ray-tracing, we make use of the lens equation to propagate a bundle of light-rays from the observer position, through a regular grid covering the lens plane, to the source plane. For each ray passing through the position \vec{x}^{ij} , we will evaluate the deflection angle $\vec{\alpha}(\vec{x}^{ij})$ and compute the arrival position on the source plane as

$$\vec{y}^{ij} = \vec{x}^{ij} - \vec{\alpha}(\vec{x}^{ij}).$$

In the formula above, (i, j) identify the ray passing through the grid point with indexes i and j along the x_1 and x_2 axes, respectively.

The deflector used in this example is the same of the previous exercise. In particular, we will use the deflection angle maps shown in the upper panels of the figure above to propagate the light rays towards the sources.

We start by creating a mesh, where each grid-point has two coordinates. Suppose coordinates along the x_1 and x_2 axes are represented by the n_{pix} -dimensional vectors $|x_1^i|$ and $|x_2^j|$, with $i, j \in [1, n_{pix}]$ (so that n_{pix} is the number of grid points along one axis on the mesh). The mesh can be created using the `numpy.meshgrid` method, as e.g.

```
npix=angx.shape[0]
x1=np.linspace(0.0,1.0,npix)*(npix-1) # define x1 coordinates
x2=np.linspace(0.0,1.0,npix)*(npix-1) # define x2 coordinates
x1_,x2_=np.meshgrid(x1,x2) # lens plane mesh
```

This will generate two numpy arrays, $x1_$ and $x2_$, with size $n_{pix} \times n_{pix}$. In the first, the values on the i -th column will be equal to x_1^i ; in the second, the values on the j -th row will be equal to x_2^j .

We may now implement the lens equation for the two components along x_1 and x_2 :

```
y1=x1_-angx
y2=x2_-angy
```

In fact, we could arrive to the same result by using a feature in numpy called *broadcasting*. The term broadcasting describes how numpy treats arrays with different shapes during arithmetic operations. Subject to certain constraints, the smaller array is “broadcast” across the larger array so that they have compatible shapes.

Using this feature, we can write the first component of the lens equation as

$$\begin{bmatrix} y_1^{1,1} & \dots & y_1^{1,n_{pix}} \\ \vdots & \ddots & \vdots \\ y_1^{n_{pix},1} & \dots & y_1^{n_{pix},n_{pix}} \end{bmatrix} = B(n_{pix}, n_{pix}) \begin{bmatrix} x_1^1 \\ \vdots \\ x_1^{n_{pix}} \end{bmatrix} - \begin{bmatrix} \alpha_1^{1,1} & \dots & \alpha_1^{1,n_{pix}} \\ \vdots & \ddots & \vdots \\ \alpha_1^{n_{pix},1} & \dots & \alpha_1^{n_{pix},n_{pix}} \end{bmatrix}$$

The vector x_1 is then broadcast to match the size of α_1 (the broadcasting function is here indicated as $B(n_{pix}, n_{pix})$). The result will be to add $|x_1^i|$ to each column of the matrix $-|\alpha_1^{ij}|$.

Computing the coordinates $|y_2^{ij}|$ involves few more steps. Again, using the lens equation, we obtain:

$$\begin{bmatrix} y_1^{1,1} & \cdots & y_1^{n_{pix},1} \\ \vdots & \ddots & \vdots \\ y_1^{1,n_{pix}} & \cdots & y_1^{n_{pix},n_{pix}} \end{bmatrix} = B(n_{pix}, n_{pix}) \begin{bmatrix} x_2^1 \\ \vdots \\ x_2^{n_{pix}} \end{bmatrix} - \begin{bmatrix} \alpha_1^{1,1} & \cdots & \alpha_1^{n_{pix},1} \\ \vdots & \ddots & \vdots \\ \alpha_1^{1,n_{pix}} & \cdots & \alpha_1^{n_{pix},n_{pix}} \end{bmatrix}$$

This equation implements the column-wise addition of $|x_2^i|$ to $-|\alpha_2^{ji}| = |\alpha_2^{ij}|^T$, where T indicates the transposed matrix. The result is $|y_2^{ji}| = |y_2^{ij}|^T$.

The python implementation is quite easy:

```
y1=(x1-angx) # y1 coordinates on the source plane
y2=np.transpose(x2-np.transpose(angy)) # y2 coordinates on the source plane
```

There is not much difference between this approach and the previous one in terms of execution time and memory usage.

This example builds on the deflection angles derived in Sect. 1.5.2, for a numerically simulated dark matter halo. In this case the lens is at redshift $z_L = 0.3$ and the source plane is at $z_S = 2$. The deflection angles are stored in the arrays `angx` and `angy` and the maps contain 512×512 pixels. In order to improve the visualization of the results, we downsample the maps by tracing a lower number of rays through the lens plane. We reduce the number of points on the lens plane mesh by a factor `ndown=16` along the two axes, x_1 and x_2 .

```
ndown=16
x1=np.linspace(0.0,1.0,npix/ndown)*(npix-1) # downsampled x1,x2 coordinates
x2=np.linspace(0.0,1.0,npix/ndown)*(npix-1) #
x1_,x2_=np.meshgrid(x1,x2) # downsampled grid
# now we need to interpolate the defl. angle maps at (x1_,x2_)
# we can use the method map_coordinates from scipy.ndimage
from scipy.ndimage import map_coordinates
# first, we need to reshape x1_ and y1_:
x=np.reshape(x1_,x1_.size)
y=np.reshape(x2_,x2_.size)
# then we interpolate:
angx_=map_coordinates(angx,[[y],[x]],order=1)
angy_=map_coordinates(angy,[[y],[x]],order=1)
# now we reshape the angles back to a mesh
angx_=angx_.reshape((npix/ndown,npix/ndown))
angy_=angy_.reshape((npix/ndown,npix/ndown))
y1=x1_-angx_
y2=x2_-angy_
# or
#y1=(x1-angx_)
#y2=np.transpose(x2-np.transpose(angy_))
```

The result of this calculation is shown in Fig. 2.7.1. In the left panel, we show the regular grid on the lens plane, through which light-rays are traced starting from the observer position. In the right panel, we show the arrival positions of the light-rays on the source plane. We can see that 1) the

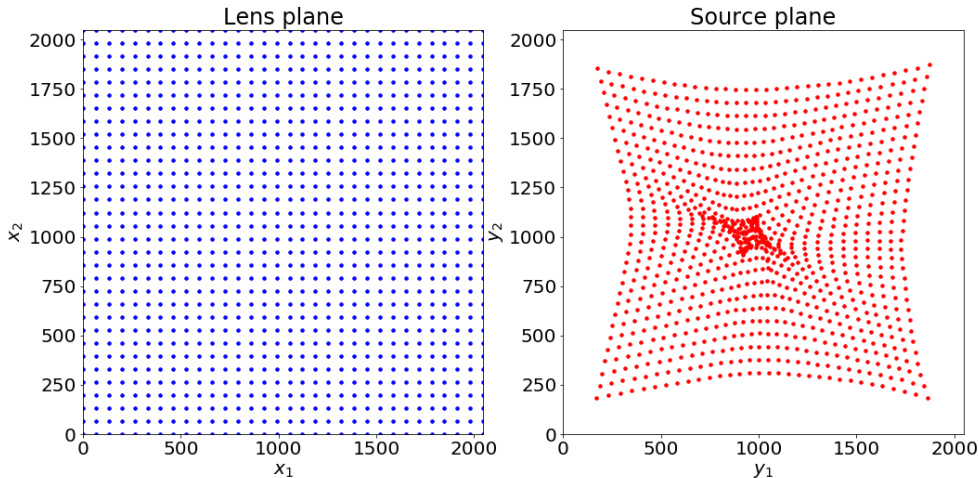


Figure 2.7.1: Ray-tracing through a regular grid on the lens plane (left panel). The arrival positions of the light-rays on the source plane are shown in the right panel. The lens is the same used in Sect. 1.5.2.

grid on the source plane is no longer regular, as the consequence of the variations of the deflection angles across the field of view; 2) the source plane is crunched, specially near the center of the lens, where many points are brought very close to each other. This is a manifestation of the lensing magnification: a small area on the source plane is mapped onto a larger area on the lens plane.

2.7.2 Derivation of the lensing potential

Deriving the lensing potential from the lens convergence map requires to solve the Poisson equation in two dimensions (Eqs. 2.26 and 2.27). This can be done numerically by means of Fast-Fourier-Transform.

The Fourier transform of the Laplace operator is

$$\tilde{\Delta}(\vec{k}) = -4\pi^2 k^2$$

where $k^2 = k_1^2 + k_2^2$. Therefore, in Fourier space, the Poisson equation reads

$$-4\pi^2 k^2 \tilde{\Psi}(\vec{k}) = 2\tilde{\kappa}(\vec{k}) .$$

The Fourier transform of the lensing potential is then

$$\tilde{\Psi}(\vec{k}) = -\frac{\tilde{\kappa}(\vec{k})}{2\pi^2 k^2} .$$

As shown in Sect. 1.5.2, the numerical calculation of the Fourier transforms can be implemented using e.g. the `numpy.fft` module. The following function could be added to the class `deflector` in Sect. 1.5.2:

```
def potential(self):
    # define an array of wavenumbers (two components k1,k2)
    k = np.array(np.meshgrid(fftengine.fftfreq(self.kappa.shape[0])\
                           ,fftengine.fftfreq(self.kappa.shape[1])))
```

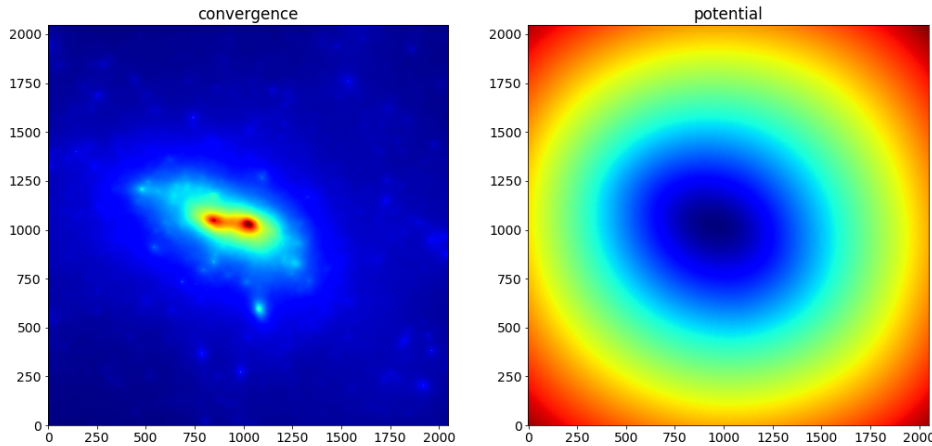


Figure 2.7.2: Maps of the convergence and of the lensing potential maps for the same lens used in Sect. 1.5.2

```

pix=1 # pixel scale (now using pixel units)
#Compute Laplace operator in Fourier space
kk = k[0]**2 + k[1]**2
kk[0,0] = 1.0
#FFT of the convergence
kappa_ft = fftengine.fftn(kappa)
#compute the FT of the potential
kappa_ft *= - pix**2 / (kk * (2.0*np.pi**2))
kappa_ft[0,0] = 0.0
potential=fftengine.ifftn(kappa_ft) #units should be rad**2
return potential.real

```

We can compute the lensing potential and display the resulting map as follows:

```

pot=df.potential() # compute the potential
kappa=df.mapCrop(kappa) # remove zero-padded region from
                        # convergence and potential maps
pot=df.mapCrop(pot)

# display the results
fig,ax = plt.subplots(1,2,figsize=(17,8))
ax[0].imshow(kappa,origin="lower")
ax[0].set_title('convergence')
ax[1].imshow(pot,origin="lower")
ax[1].set_title('potential')

```

The maps of the convergence and of the lensing potential for the lens considered are shown in Fig. 2.7.2. Clearly, the potential is much smoother than the convergence. This reflects the fact that the convergence is obtained by means of second derivatives of the potential.

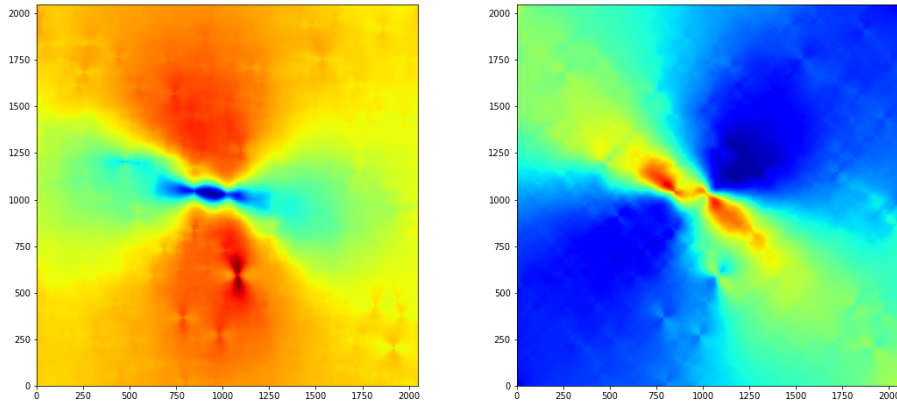


Figure 2.7.3: Maps of the shear components for the same lens used in Sect. 1.5.2

2.7.3 Lensing maps

Once the potential is known, it is easy to compute maps of many other properties of the lens. For example, the gradient of $\hat{\Psi}$ is the deflection angle. Thus, we can implement a method to compute $\vec{\alpha}$ which is alternative to that discussed in Sect. 1.5.2.

The python implementation shown here makes usage of the `numpy.gradient` method. Precisely,

```
a2,a1=np.gradient(pot)
```

returns two maps of the deflection angle components α_1 and α_2 . Note that, because of the axis convention in python, the derivatives of $\hat{\Psi}$ along the second dimension is given first. We do not display the maps, as they are analogous to those shown e.g. in Fig. 1.5.3.

By computing further gradients of the maps of the two components of the deflection angle, we obtain maps of the second derivatives of the potential. By combining them, we can compute the convergence (which is already known, as it was the input to derive the potential) and the shear components. The python implementation of Eq. 2.38 is as follows:

```
# First we compute the second derivatives of pot
psi12,psi11=np.gradient(a1)
psi22,psi21=np.gradient(a2)
# Then we combine them to form the first and the second component of
# the shear tensor
gamma1=0.5*(psi11-psi22)
gamma2=psi12
```

In Fig. 2.7.3, we show the maps both γ_1 and γ_2 .

As discussed in Sect. 2.3.1, the shear introduces an anisotropic distortion of the images of sources. For example, a circular source is mapped onto an elliptical image (in the case of a slowly varying deflection angle). The direction of the axes of the ellipse is given by the angle ϕ in Eq. 2.42, which can be computed using the `arctan2` function:

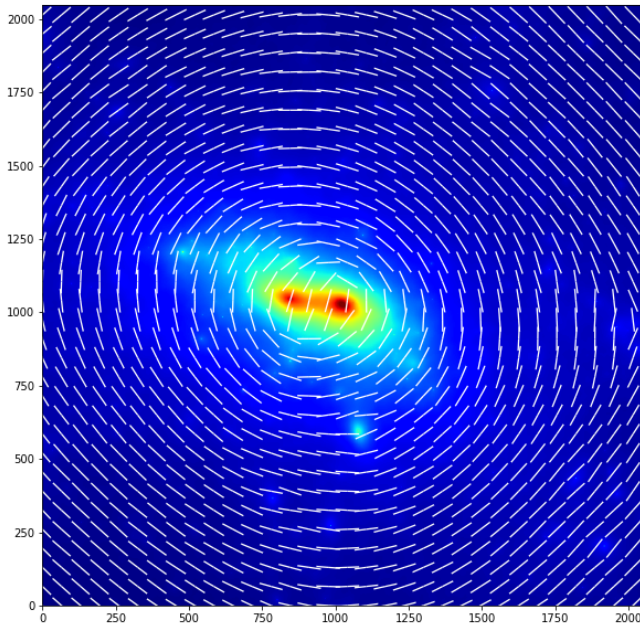


Figure 2.7.4: Shear orientation overlaid to the convergence map of the same lens used in Sect. 1.5.2

```
phi=np.arctan2(gamma2,gamma1)/2.0
```

Note that we have to divide by 2 in order to account for the fact that γ is a spin-2 tensor. It is interesting to display the direction into which the shear distorts images and compare it to lens mass distribution. Fig. 2.7.4 shows the direction of the first eigenvector of the shear overlaid to the lens convergence. The code to produce the figure is

```
pixel_step=gamma_1.shape[1]/32+1
x,y = np.meshgrid(np.arange(0,gamma_1.shape[1],pixel_step),
                  np.arange(0,gamma_1.shape[0],pixel_step))
fig,ax=plt.subplots(1,1,figsize=(10,10))
ax.imshow(ka,origin='lower',vmax=3)
ax[1].imshow(kappa,origin='lower',vmax=3)

# showing only the orientation of the shear. This will create two sticks
# departing from the point where the shear is evaluated (x,y) and directed
# in opposite directions
ax[1].quiver(y,x,np.cos(phi[x,y]),np.sin(phi[x,y]),
              headwidth=0,units="height",scale=x.shape[0],color="white")
ax[1].quiver(y,x,-np.cos(phi[x,y]),-np.sin(phi[x,y]),
              headwidth=0,units="height",scale=x.shape[0],color="white")
```

From the maps of the shear, we can derive the maps of the flexions F and G. Each of these quantities have two components, corresponding to the real and to imaginary parts of the complex

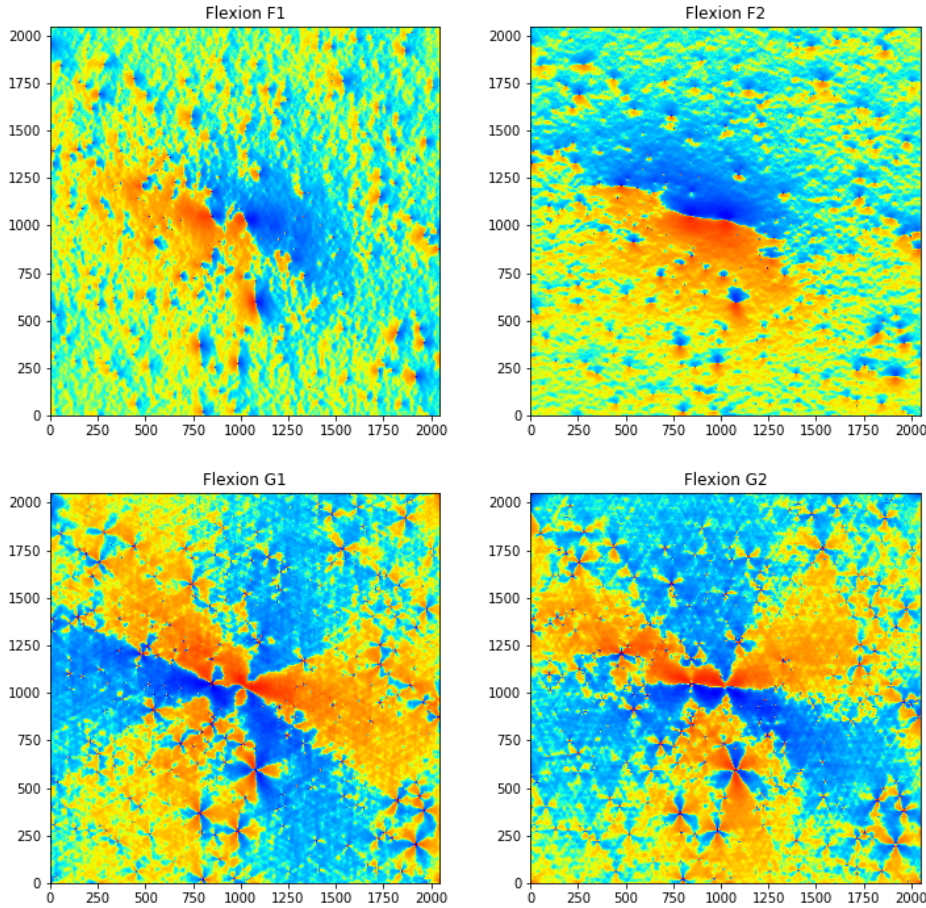


Figure 2.7.5: Maps of the components of the flexions F and G for the same lens used in Sect. 1.5.2

quantities in Eqs. 2.72 and 2.73:

```
gamma12,gamma11=np.gradient(gamma_1)
gamma22,gamma21=np.gradient(gamma_2)
F1,F2=gamma11+gamma22,gamma21-gamma12
G1,G2=gamma11-gamma22,gamma21+gamma12
```

Their maps are shown in Fig. 2.7.5. These maps show some interesting features:

- the features in the flexion F maps have dipole symmetry, as expected for a spin-1 field;
- the features in the flexion G maps have triangular symmetry, denoting the spin-3 nature of this field, which is invariant under rotations by $2\pi/3$ radians;
- in both the cases of the flexion F and G , the signal of the small scale structures in the convergence map is amplified (flexion is obtained via third-order derivatives of the lensing potential).

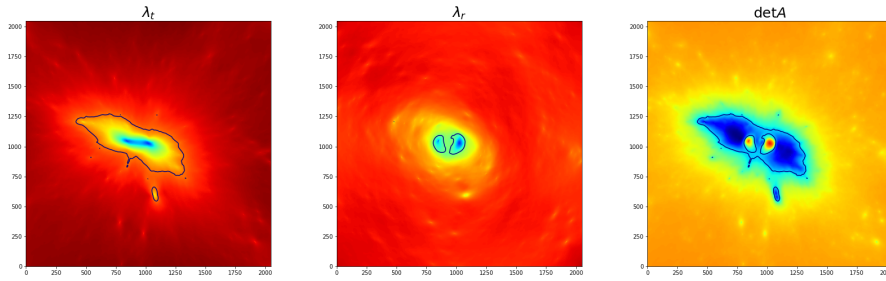


Figure 2.7.6: The left and the central panel show the maps of the eigenvalues of the lensing Jacobian with overlaid their zero-level contours, i.e. the critical lines. Instead, the right panel shows the map of $\det A$, i.e. the product of the two previous maps.

2.7.4 Critical lines and caustics

Critical lines are defined by the equations

$$\lambda_t = 1 - \kappa - \gamma = 0 \quad (2.88)$$

$$\lambda_r = 1 - \kappa + \gamma = 0 \quad (2.89)$$

where $\gamma = (\gamma_1^2 + \gamma_2^2)^{1/2}$. There are several methods to identify the points belonging to the critical lines. A simple way to visualize them is draw the zero-level contours in the maps of λ_t and λ_r . Since the λ_t and λ_r are the eigenvalues of the lensing Jacobian, the critical lines correspond also to the zero-level contours in the map of $\det A$. The following code implements the search for the critical lines using this method.

```
from matplotlib.colors import LogNorm, PowerNorm, SymLogNorm

gamma=np.sqrt(gamma_1**2+gamma_2**2)
lambdat=1.0-kappa-gamma
lambdar=1.0-kappa+gamma
detA=lambdat*lambdar

fig,ax=plt.subplots(1,3,figsize=(28,8))
ax[0].imshow(lambdat,origin='lower')
ax[0].contour(lambdat,levels=[0.0])
ax[0].set_title('$\lambda_t$',fontsize=25)
ax[1].imshow(lambdar,origin='lower')
ax[1].contour(lambdar,levels=[0.0])
ax[1].set_title('$\lambda_r$',fontsize=25)
ax[2].imshow(detA,origin='lower',norm=SymLogNorm(0.3))
ax[2].contour(detA,levels=[0.0])
ax[2].set_title('$\det A$',fontsize=25)
```

The results are displayed in Fig. 2.7.6. The left and the central panels show the maps of λ_t and λ_r , respectively. In the right panel, we show the map of $\det A$. In all panels, we overlay the zero-level contours, i.e. the critical lines. In the left and in the central panels the tangential and the radial critical lines are shown separately, while in the right panel they are displayed simultaneously. Note that these are the critical lines for a specific source redshift. In fact, the convergence map

used to compute the lensing potential is normalized to $z_{s,norm} = 9^2$. To obtain the critical lines for different source redshifts z_s , we need to rescale both κ and γ by the distance ratio

$$\Xi = \frac{D_{S,norm}}{D_{LS,norm}} \frac{D_{LS}(z_s)}{D_S(z_s)}, \quad (2.90)$$

where the distances $D_{S,norm}$ and $D_{LS,norm}$ are computed for $z_s = z_{s,norm}$. The code below repeats this operation for 20 equally spaced redshifts between z_l and $z_s = 10$. The corresponding critical lines are shown in Fig. 2.7.7. In order to compute the distances, we have to assume a cosmological model. This can be done by using the `astropy.cosmology` module. Here, we import a pre-defined flat Λ CDM cosmological model with density parameter $\Omega_M = 0.3$ and $\Omega_\Lambda = 0.7$. We assume the Hubble parameter to be $H_0 = 70$ km/s/Mpc. The angular diameter distances are computed using the `angular_diameter_distance` and the `angular_diameter_distance_z1z2` methods.

```
from astropy.cosmology import FlatLambdaCDM
cosmo = FlatLambdaCDM(H0=70, Om0=0.3)

zl=0.5
zs_norm=9.0

zs=np.linspace(zl,10.0,20)
dl=cosmo.angular_diameter_distance(zl)
ds=cosmo.angular_diameter_distance(zs)
dls=[]

for i in range(ds.size):
    dls.append(cosmo.angular_diameter_distance_z1z2(zl,zs[i]).value)

ds_norm=cosmo.angular_diameter_distance(zs_norm)
dls_norm=cosmo.angular_diameter_distance_z1z2(zl,zs_norm)

fig,ax=plt.subplots(1,2,figsize=(16,8))
ax[0].imshow(lambdat,origin='lower')
ax[1].imshow(lambdar,origin='lower')
for i in range(ds.size):
    kappa_new=kappa*ds_norm.value/dls_norm.value*dls[i]/ds[i].value
    gamma_new=gamma*ds_norm.value/dls_norm.value*dls[i]/ds[i].value
    lambdat_new=(1.0-kappa_new-gamma_new)
    lambdar_new=(1.0-kappa_new+gamma_new)
    ax[0].contour(lambdat_new,levels=[0.0])
    ax[1].contour(lambdar_new,levels=[0.0])

ax[0].contour(lambdat,levels=[0.0],colors="yellow",linewidths=2)
ax[1].contour(lambdar,levels=[0.0],colors="magenta",linewidths=2)
```

The caustics are the "sources" of the critical lines. In other words, if $\vec{\theta}_c$ defines a set of points belonging to the critical lines, then

$$\vec{\beta}_c = \vec{\theta}_c - \vec{\alpha}(\vec{\theta}_c) \quad (2.91)$$

²The lens redshift is $z_l = 0.5$.

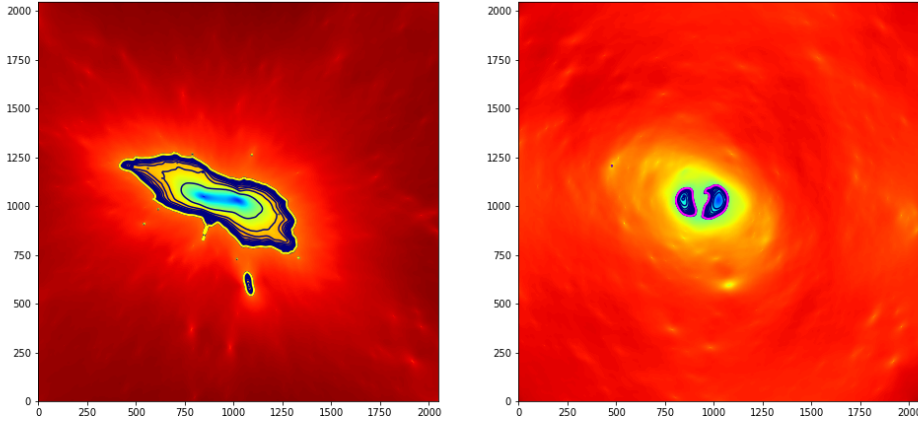


Figure 2.7.7: Tangential (left) and radial (right) critical lines of the lens for different source redshifts.

defines a set of points belonging to the caustics.

To proceed to the calculation of the caustics, we need first to gather the deflection angles at the position of the critical points. These can be read from the maps of the deflection angles computed earlier by means of an interpolation. We will use the `map_coordinates` method from the `scipy.ndimage` module. In the following, we will work in pixel units:

```
fig,ax=plt.subplots(1,2,figsize=(18,8))
# first we extract the level-0 contours of the map of detA
cs=ax[0].contour(detA,levels=[0.0])

# then, we take the path of each closed contour
contour=cs.collections[0]
p=contour.get_paths() # p contains the paths of each individual
                      # critical line

sizevs=np.empty(len(p),dtype=int)

from scipy.ndimage import map_coordinates

# if we found any contour, then we proceed
if (sizevs.size > 0):
    for j in range(len(p)):
        # for each path, we create two vectors containing the x1
        # and x2 coordinates of the vertices
        vs = contour.get_paths()[j].vertices
        sizevs[j]=len(vs)
        x1=[]
        x2=[]
        for i in range(len(vs)):
            xx1,xx2=vs[i]
```

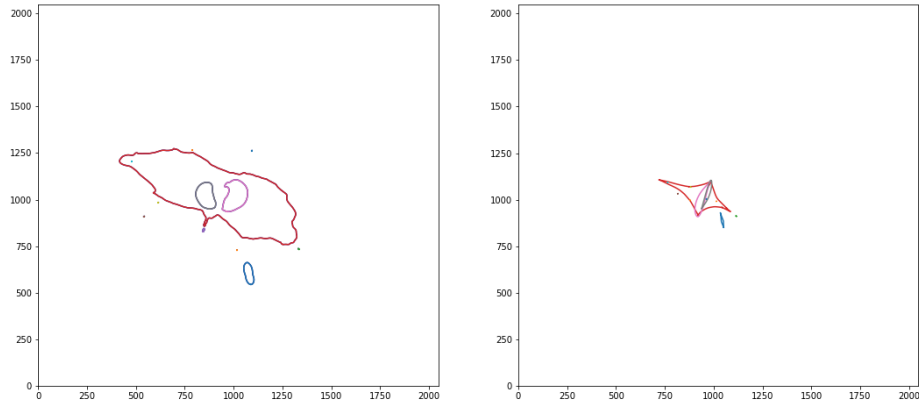


Figure 2.7.8: Critical lines (left panel) and caustics (right panel) for $z_s = 9$. Different closed critical lines in the left panel have different colors. These can be used to identify the corresponding caustics in the right panel.

```

x1.append(float(xx1))
x2.append(float(xx2))

# these are the points we want to map back on the source plane.
# To do that we need to evaluate the deflection angle at their
# positions using scipy.ndimage.interpolate.map_coordinates
# we perform a bi-linear interpolation

a_1=map_coordinates(a1, [[x2],[x1]],order=1)
a_2=map_coordinates(a2, [[x2],[x1]],order=1)

# now we can make the mapping using the lens equation:
y1=x1-a_1[0]
y2=x2-a_2[0]

# plot the results!
ax[0].plot(x1,x2,'-')
ax[1].plot(y1,y2,'-')

ax[1].set_xlim([0,2048])
ax[1].set_ylim([0,2048])

```

The left and right panels in Fig. 2.7.8 show the critical lines and the caustics on the lens and the source planes, respectively. They display exactly the same region of the sky. The shape of the caustics should be compared to the pattern visible in the right panel of Fig. 2.7.1. Performing ray-tracing, we found that starting from a regular grid of ray positions on the lens plane, we end up with an irregular grid on the source plane, which also covers a smaller area of the sky due to magnification. Now, we can easily see that the arrival positions of light rays on the source plane are clustered around the caustics of the lens.

2.7.5 Shear and flexion

In this example we use Eq. 2.57 to build an application to visualize the lensing distortions due to shear and flexion.

As we have seen, the elements of D , D_{ijk} , are expressed as third derivatives of the lensing potential. These in turn can be written in terms of the flexions F and G . After some math, we find that

$$\begin{aligned} D_{111} &= -2\gamma_{11} - \gamma_{22} = -\frac{1}{2}(3F_1 + G_1) \\ D_{211} &= D_{121} = D_{112} = -\gamma_{21} = -\frac{1}{2}(F_2 + G_2) \\ D_{122} &= D_{212} = D_{221} = -\gamma_{22} = -\frac{1}{2}(F_1 - G_1) \\ D_{222} &= 2\gamma_{12} - \gamma_{21} = -\frac{1}{2}(3F_2 - G_2) \end{aligned} \quad (2.92)$$

Then, the two components of $\vec{\beta}$ are

$$\begin{aligned} \beta_1 &= A_{11}\theta_1 + A_{12}\theta_2 + \frac{1}{2}D_{111}\theta_1^2 + D_{121}\theta_1\theta_2 + \frac{1}{2}D_{122}\theta_2^2 \\ \beta_2 &= A_{21}\theta_1 + A_{22}\theta_2 + \frac{1}{2}D_{211}\theta_1^2 + D_{212}\theta_1\theta_2 + \frac{1}{2}D_{222}\theta_2^2 \end{aligned} \quad (2.93)$$

We consider a circular source centered at $\vec{\beta}_0 = (0,0)$. We assign to this source a surface brightness profile. For this exercise we can choose a generic Sérsic profile (Sérsic, 1963) in the form

$$I_s(\beta) \propto \exp[-b_n((\beta/r_e)^{1/n} - 1)]. \quad (2.94)$$

The shape parameter b_n is given by the approximated formula (Capaccioli et al., 1989)

$$b_n = 1.992n - 0.3271, \quad (2.95)$$

which is valid for for $0.5 < n < 10$. The parameter r_e is the effective radius of the source and n is the Sersic index.

Since the surface brightness is conserved, we can relate the surface brightness $i(\vec{\theta})$ on the lens and $I_s(\vec{\beta})$ on the source plane using the lens equation:

$$I(\vec{\theta}) = I_s(\vec{\beta}). \quad (2.96)$$

This allows us to straightforwardly reconstruct the image of the source on the lens plane. In fact, the lens equation above allows to map the coordinates $\vec{\theta}$ into the coordinates $\vec{\beta}$ on the plane of the source. This is a ray-tracing procedure. We can indeed cover the lens plane with a grid of coordinates $\vec{\theta}$ and, once we know the corresponding coordinates $\vec{\beta}$, we can read-off the surface brightness at $\vec{\theta}$ from the map of $I_s(\vec{\beta})$.

Note that the lens equation above does not include any shift of the image of the image position (i.e. the source and the image will be at the same position on the plane of the sky, i.e. within our field-of-view).

We start by implementing a class for Sérsic sources. To initialize each instance of this class, we provide the parameters of the brightness profile, namely n and r_e . For this example, no other parameters are necessary to define the appearance of the source. Indeed, we will generate circular sources. However, we also need to specify the size, `size`, and the number of pixels, N , of the image of the source that we want to produce.

```
# import the usual packages: numpy and matplotlib
import numpy as np
import matplotlib.pyplot as plt

class sersic(object):
    def __init__(self, side, N, **kwargs):

        if ('n' in kwargs):
            self.n=kwargs['n']
        else:
            self.n=4

        if ('re' in kwargs):
            self.re=kwargs['re']
        else:
            self.re=50.0

        self.N=N
        self.side=float(side)

        # define the pixel coordinates
        pc=np.linspace(-side/2.,side/2.,self.N)
        self.x1,self.x2 = np.meshgrid(pc,pc)
        y1,y2=self.x1,self.x2
        self.unlensed = self.brightness(y1,y2)

    def brightness(self,y1,y2):
        r = np.sqrt(y1**2+y2**2)
        bn = 1.992*self.n - 0.3271
        return (np.exp(-bn*((r/self.re)**(1.0/self.n)-1.0)))
```

The method `brightness` implements the calculation of the surface brightness on the source plane using the Sérsic profile. As it is now, the brightness is calculated on the regular grid of light rays (x_1, x_2), which covers the lens plane and is propagated to the source plane without deflections. The resulting brightness distribution is recorded in the array `unlensed`.

Now we implement Eq. 2.93. This is done in the function `lens` below

```
def lens(self,**kwargs):
    if ('kappa' in kwargs):
        self.kappa = kwargs['kappa']
    else:
        self.kappa=0.0

    if ('gamma1' in kwargs):
        self.gamma1 = kwargs['gamma1']
    else:
        self.gamma1=0.0

    if ('gamma2' in kwargs):
```

```

        self.gamma2 = kwargs['gamma2']
    else:
        self.gamma2=0.0

    if ('g1' in kwargs):
        self.g1 = kwargs['g1']
    else:
        self.g1=0.0
    if ('g2' in kwargs):
        self.g2 = kwargs['g2']
    else:
        self.g2=0.0

    if ('f1' in kwargs):
        self.f1 = kwargs['f1']
    else:
        self.f1=0.0
    if ('f2' in kwargs):
        self.f2 = kwargs['f2']
    else:
        self.f2=0.0

    a11=1.0-self.kappa-self.gamma1
    a22=1.0-self.kappa+self.gamma1
    a12=-self.gamma2
    a111=-0.5*(self.g1+3.0*self.f1)
    a222=-0.5*(3.0*self.f2-self.g2)
    a112=-0.5*(self.f2+self.g2)
    a221=-0.5*(self.f1-self.g1)

    y1 = a11*self.x1 + a12*self.x2 + 0.5*a111*self.x1**2 + \
          a112*self.x1*self.x2 + 0.5*a221*self.x2**2
    y2 = a22*self.x2 + a12*self.x1 + 0.5*a222*self.x2**2 + \
          a221*self.x1*self.x2 + 0.5*a112*self.x1**2

    self.lensed=self.brightness(y1,y2)

```

At this point, we can create an instance of the Sérsic source and lens it by choosing the values of the convergence, shear, and F and G flexions. Some results are shown in Fig. 2.5.1.

2.7.6 Full ray-tracing simulation and time delay surface

The procedure outlined above for lensing a Sérsic source can be extended to include also distortions described by higher order terms in the expansion of the deflection angle. By design, all these terms are included in a full ray-tracing simulation employing the algorithm discussed in Sect. 2.7.1.

In this example, we will build an application to visualize the distortions of an elliptical source with Sérsic profile by virtually any lens. The application will also compare the shape and location of the distorted images with the contours of equal time-delay. Compared to the example shown in Sect. 2.7.5, we will extend the class Sérsic to allow elliptical shapes with random orientation. We will also use inheritance to build a parent class for generic lenses and child classes for specific

lensing potentials.

We start by importing some useful packages:

```
# import numpy and matplotlib
import numpy as np
import matplotlib.pyplot as plt

# import map_coordinates from scipy
from scipy.ndimage import map_coordinates

# import fits from astropy
import astropy.io.fits as pyfits

# import fft from numpy
import numpy.fft as fftengine
```

The parent class `gen_lens` will contain methods that can be applied to any lens. The initialization function is empty. It contains only one instruction to set the logic variable `pot_exist=False`, meaning that the parent class itself has no potential specified a priori. This will be given in the child class.

```
# the parent class
class gen_lens(object):

    # in the beginning, the class does not have a potential
    def __init__(self):
        self.pot_exists=False
```

The functions to derive convergence, shear, Jacobian determinant (inverse magnification) are part of the generic lens class, because they can work with any potential.

```
# convergence
def convergence(self):
    if (self.pot_exists):
        kappa=0.5*(self.a11+self.a22)
    else:
        print ("The lens potential is not initialized yet")

    return(kappa)

#shear
def shear(self):
    if (self.pot_exists):
        g1=0.5*(self.a11-self.a22)
        g2=self.a12
    else:
        print ("The lens potential is not initialized yet")
    return(g1,g2)

# determinant of the Jacobian matrix
def detA(self):
```

```

    if (self.pot_exists):
        deta=(1.0-self.a11)*(1.0-self.a22)-self.a12*self.a21
    else:
        print ("The lens potential is not initialized yet")
    return(deta)

# critical lines overlaid to the map of deta, returns a set of
# contour objects
def crit_lines(self,ax=None,show=True):
    if (ax==None):
        print ("specify the axes to display the critical lines")
    else:
        deta=self.deta()
        #ax.imshow(deta,origin='lower')
        cs=ax.contour(deta,levels=[0.0],colors='white',alpha=0.0)
        if show==False:
            ax.clear()
    return(cs)

# plot of the critical lines in the axes ax
def clines(self,ax=None,color='red',alpha=1.0,lt='-' ):
    cs=self.crit_lines(ax=ax,show=False)
    contour=cs.collections[0]
    p=contour.get_paths()
    sizevs=np.empty(len(p),dtype=int)

    no=self.pixel
    # if we found any contour, then we proceed
    if (sizevs.size > 0):
        for j in range(len(p)):
            # for each path, we create two vectors containing
            #the x1 and x2 coordinates of the vertices
            vs = contour.get_paths()[j].vertices
            sizevs[j]=len(vs)
            x1=[]
            x2=[]
            for i in range(len(vs)):
                xx1,xx2=vs[i]
                x1.append(float(xx1))
                x2.append(float(xx2))

            # plot the results!
            ax.plot((np.array(x1)-self.npix/2.)*no,
                    (np.array(x2)-self.npix/2.)*no,lt,color=color,
                    alpha=alpha)

# plot of the caustics in the axes ax
def caustics(self,ax=None,alpha=1.0,color='red',lt='-' ):
    cs=self.crit_lines(ax=ax,show=True)

```

```

contour=cs.collections[0]
p=contour.get_paths() # p contains the paths of each individual
# critical line
sizevs=np.empty(len(p),dtype=int)

# if we found any contour, then we proceed
if (sizevs.size > 0):
    for j in range(len(p)):
        # for each path, we create two vectors containing
        # the x1 and x2 coordinates of the vertices
        vs = contour.get_paths()[j].vertices
        sizevs[j]=len(vs)
        x1=[]
        x2=[]
        for i in range(len(vs)):
            xx1,xx2=vs[i]
            x1.append(float(xx1))
            x2.append(float(xx2))

        a_1=map_coordinates(self.a1, [[x2],[x1]],order=1)
        a_2=map_coordinates(self.a2, [[x2],[x1]],order=1)

        # now we can make the mapping using the lens equation:
        no=self.pixel
        y1=(x1-a_1[0]-self.npix/2.)*no
        y2=(x2-a_2[0]-self.npix/2.)*no

        # plot the results!
        ax.plot(y1,y2,lt,color=color,alpha=alpha)

```

Note that all the functions included in the generic lens were discussed in the details in the previous examples.

We can now add the functions to compute the time-delay surface and to plot its contour levels:

```

# geometrical time delay
def t_geom_surf(self, beta=None):
    x = np.arange(0, self.npix, 1, float)*self.pixel
    y = x[:,np.newaxis]
    if beta is None:
        x0 = y0 = self.npix / 2*self.pixel
    else:
        x0 = beta[0]+self.npix/2*self.pixel
        y0 = beta[1]+self.npix/2*self.pixel

    return 0.5*((x-x0)*(x-x0)+(y-y0)*(y-y0))

# gravitational time delay (this will need a potential to be specified):
def t_grav_surf(self):

```

```

    return -self.pot

    # total time delay
def t_delay_surf(self,beta=None):
    t_grav=self.t_grav_surf()
    t_geom=self.t_geom_surf(beta)
    td=(t_grav+t_geom)
    return(t_grav+t_geom)

    # display the time delay contours
def show_contours(self,surf0,ax=None,minx=-25,miny=-25,
                  cmap=plt.get_cmap('Paired'),
                  linewidth=1,fontsize=20,nlevels=40,levmax=100,
                  offz=0.0):
    if ax==None:
        print ("specify the axes to display the contours")
    else:
        minx=minx
        maxx=-minx
        miny=miny
        maxy=-miny
        surf=surf0-np.min(surf0)
        levels=np.linspace(np.min(surf),levmax,nlevels)
        ax.contour(surf, cmap=cmap,levels=levels,
                   linewidth=linewidth,
                   extent=[-self.size/2,self.size/2,
                           -self.size/2,self.size/2])
        ax.set_xlim(minx, maxx)
        ax.set_ylim(miny, maxy)
        ax.set_xlabel(r'$\theta_1$', fontsize=fontsize)
        ax.set_ylabel(r'$\theta_2$', fontsize=fontsize)
        ax.set_aspect('equal')

```

It remains to be specified the child class. This will contain the definition of the lensing potential. We define two of such classes. The first is the elliptical pseudo-isothermal model with core (PSIEc).

The PSIEc potential has the form:

$$\hat{\Psi}(\vec{\theta}) = \frac{\hat{\Psi}_0}{\sqrt{\theta^2 + \theta_c^2}}, \quad (2.97)$$

where $\hat{\Psi}_0$ is a normalization factor, $\theta^2 = \theta_1^2/(1-e) + \theta_2^2(1-e)$, and θ_c is the core radius. The lens has iso-potential contours with ellipticity e .

As said, PSIEc is a child class of `gen_lens`, and inherits all its methods. For using them, we just need to define a lensing potential. We define it on the map pot. The map has a certain dimension, `size`, and number of pixels, `npix`. The function `potential` also computes the first and the second derivatives of the lensing potential. These quantities are used in the `gen_lens` class to derive the lens properties.

```

# psiec: pseudo elliptical isothermal lens with core
class PSIEc(gen_lens):
    def __init__(self, size=100.0, npix=200, **kwargs):

        if ('theta_c' in kwargs):
            self.theta_c=theta_c
        else:
            self.theta_c=0.0

        if ('ell' in kwargs):
            self.ell=ell
        else:
            ell=0.0

        if ('norm' in kwargs):
            norm=norm
        else:
            norm=1.0

        self.size=size
        self.npix=npix
        self.pixel=float(self.size)/float((self.npix-1))
        self.potential()

# lensing potential and its derivatives
    def potential(self):
        x = np.arange(0, self.npix, 1, float)
        y = x[:,np.newaxis]
        x0 = y0 = self.npix / 2
        no=self.pixel**2
        self.pot_exists=True
        pot=np.sqrt(((x-x0)*self.pixel)**2/(1-self.ell)
                    +((y-y0)*self.pixel)**2*(1-self.ell)
                    +self.theta_c**2)*self.norm
        self.pot=pot#/no
        self.a2,self.a1=np.gradient(self.pot/self.pixel**2)
        self.a12,self.a11=np.gradient(self.a1)
        self.a22,self.a21=np.gradient(self.a2)

```

The last step is to modify the class Sérsic to include the full ray-tracing. We will also allow for elliptical sources. The initialization function is written as follows

```

class sersic(object):

    def __init__(self, size, N, gl=None, **kwargs):

        if ('n' in kwargs):
            self.n=kwargs['n']
        else:

```

```

    self.n=4

    if ('re' in kwargs):
        self.re=kwargs['re']
    else:
        self.re=5.0

    if ('q' in kwargs):
        self.q=kwargs['q']
    else:
        self.q=1.0

    if ('pa' in kwargs):
        self.pa=kwargs['pa']
    else:
        self.pa=0.0

    if ('ys1' in kwargs):
        self.ys1=kwargs['ys1']
    else:
        self.ys1=0.0

    if ('ys2' in kwargs):
        self.ys2=kwargs['ys2']
    else:
        self.ys2=0.0

    self.N=N
    self.size=float(size)
    self.df=g1

    # define the pixel coordinates
    pc=np.linspace(-self.size/2.0,self.size/2.0,self.N)
    self.x1, self.x2 = np.meshgrid(pc,pc)
    if self.df != None:
        y1,y2 = self.ray_trace()
    else:
        y1,y2 = self.x1,self.x2

    self.image=self.brightness(y1,y2)

```

In addition to the parameters `N` and `size`, we need to assign to the source a generic lens `g1`. We will use its deflection angles to perform the ray-tracing. Among the arguments that define the intrinsic properties of the source, we include

- the Sérsic index, `n`, and the effective radius, `re`;
- the axis ratio, `q`, and the position angle, `pa`;
- the coordinates of the center of the lens, `ys1`, `ys2`.

The parameters `N` and `size` define the grid of light rays to be propagated towards the source. The coordinates of the rays are `x1` and `x2`. If `g1` is provided, the deflections are calculated and the

lens equation is applied. The arrival positions of the rays on the source plane have coordinates y_1 and y_2 .

```
def ray_trace(self):
    px=self.df.pixel#size/(self.df.npix-1)
    x1pix=(self.x1+self.df.size/2.0)/px
    x2pix=(self.x2+self.df.size/2.0)/px

    # compute the deflection angles at the light positions
    # on the lens plane. Use the deflection angles of self.df
    a1 = map_coordinates(self.df.a1,
                          [x2pix,x1pix],order=2)*px
    a2 = map_coordinates(self.df.a2,
                          [x2pix,x1pix],order=2)*px
    # apply the lens equation
    y1=(self.x1-a1) # y1 coordinates on the source plane
    y2=(self.x2-a2) # y2 coordinates on the source plane
    return(y1,y2)
```

Note that the deflection angles are reduced, i.e. they already contain the factor D_{LS}/D_S which accounts for the distances of the lens and of the source.

Finally, the brightness is computed at the coordinates (y_1, y_2) using the function `brightness`:

```
def brightness(self,y1,y2):
    x = np.cos(self.pa)*(y1-self.ys1)+np.sin(self.pa)*(y2-self.ys2)
    y = -np.sin(self.pa)*(y1-self.ys1)+np.cos(self.pa)*(y2-self.ys2)
    r = np.sqrt(((x)/self.q)**2+(y)**2)
    # profile
    bn = 1.992*self.n - 0.3271
    brightness = np.exp(-bn*((r/self.re)**(1.0/self.n)-1.0))
    return(brightness)
```

We implement here the ellipticity and the rotation of the source by the angle `pa`.

The following code shows how to use the classes above to produce Fig. 2.7.9.

```
# lens params
kwargs={'theta_c': 2.0, 'norm': 10.0, 'ell': 0.4}
el=psie(size=80,npix=1000,**kwargs)

# size of the source image
size_stamp=150.0
npix_stamp=1000

xmin,xmax=-el.size/2,el.size/2
ymin,ymax=-el.size/2,el.size/2

fig,ax=plt.subplots(1,2,figsize=(14,8))

# sersic source with no lensing
```

```

kwargs={'q': 0.5, 're': 1.0, 'pa': np.pi/4.0, 'n': 1,
        'ys1': beta[0], 'ys2': beta[1]}
se_unlensed=sersic(size_stamp,npix_stamp,**kwargs)

# same source with lensing by the lens el
se=sersic(size_stamp,npix_stamp,gl=el,**kwargs)

# compute the time delay surface for a source at beta
beta=[0,0]
td=el.t_delay_surf(beta=beta)

# draw caustics (on the left) and critical lines (on the right)
el.caustics(ax=ax[0],lt='--',alpha=1.0)
el.clines(ax=ax[1],lt='--',alpha=1.0)

# show unlensed (on the left) and lensed (on the right) images
ax[0].imshow(se_unlensed.image,origin='lower',
              extent=[-se.size/2,se.size/2,
                      -se.size/2,se.size/2],
              cmap='gray_r')
ax[1].imshow(se.image,origin='lower',
              extent=[-se.size/2,se.size/2,
                      -se.size/2,se.size/2],
              cmap='gray_r')

# show contours of the time delay surface
el.show_contours(td,ax=ax[1],minx=xmin,miny=ymin,
                  nlevels=35,levmax=500,fontsize=20)

x0,x1=-20,20
y0,y1=-20,20
ax[0].set_xlim([x0,x1])
ax[0].set_ylim([y0,y1])

fig.tight_layout()

```

We clearly see that the images of the source shown in the left hand panel are located at the stationary points of the time-delay surface.

Our smart implementation of the general lens class, allows us to easily switch between lens models. Aiming at distorting the source using the usual numerically simulated lens, it is sufficient to initialize the lensed sersic model using a deflector built from the lens convergence map. For example, this could be obtained from the deflector class shown below:

```

# child class deflector
class deflector(gen_lens):

```

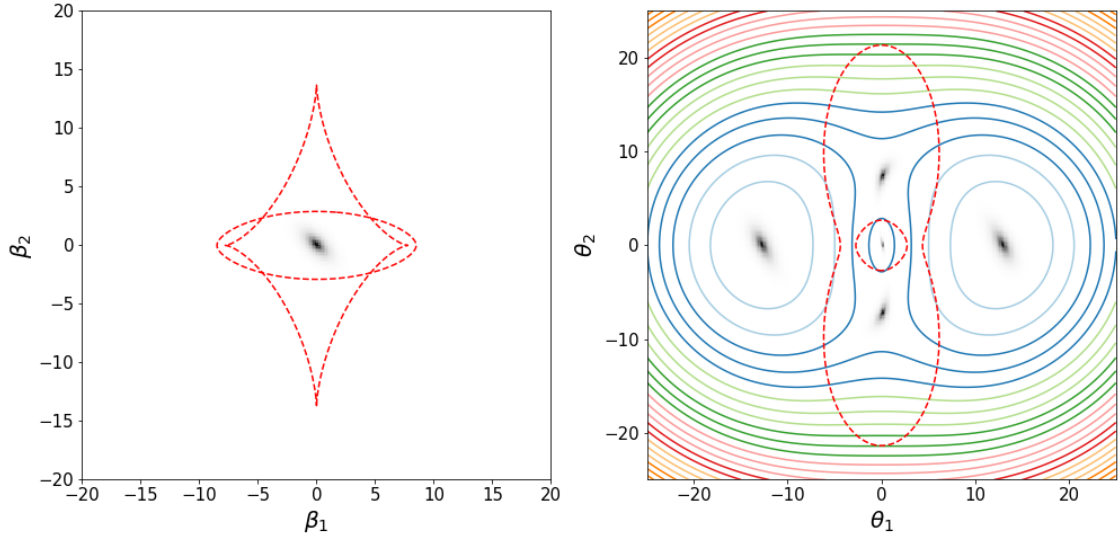


Figure 2.7.9: Left panel: Caustics of a PSIEc lens. A Sérsic source is placed at the center of the caustics. Right panel: critical lines (dashed) and lensed images of the source shown in the left panel. The colored solid contours show the levels of equal time delay for the same source.

```
# initialize the deflector using a surface density (convergence) map
# the boolean variable pad indicates whether zero-padding is used or not

def __init__(self,filekappa,pad=False,npix=200,size=100):
    kappa,header=pyfits.getdata(filekappa,header=True)
    self.pixel_scale=header['CDELT2']*3600.0
    self.kappa=kappa
    self.nx=kappa.shape[0]
    self.ny=kappa.shape[1]
    self.pad=pad
    self.npix=npix
    self.size=size
    self.pixel=float(self.size)/float(self.npix-1)
    if (pad):
        self.kpad()
    self.potential()

# performs zero-padding
def kpad(self):
    # add zeros around the original array
    def padwithzeros(vector, pad_width, iaxis, kwargs):
        vector[:pad_width[0]] = 0
        vector[-pad_width[1]:] = 0
        return vector
    # use the pad method from numpy.lib to add zeros (padwithzeros)
```

```

# in a frame with thickness self.kappa.shape[0]
self.kappa=np.lib.pad(self.kappa, self.kappa.shape[0],
                      padwithzeros)

# calculate the potential by solving the poisson equation
def potential_from_kappa(self):
    # define an array of wavenumbers (two components k1,k2)
    k = np.array(np.meshgrid(fftengine.fftfreq(self.kappa.shape[0])\
                           ,fftengine.fftfreq(self.kappa.shape[1])))

    pix=1 # pixel scale (now using pixel units)
    #Compute Laplace operator in Fourier space = -4*pi*k^2
    kk = k[0]**2 + k[1]**2
    kk[0,0] = 1.0
    #FFT of the convergence
    kappa_ft = fftengine.fftn(self.kappa)
    #compute the FT of the potential
    kappa_ft *= - pix**2 / (kk * (2.0*np.pi**2))
    kappa_ft[0,0] = 0.0
    potential=fftengine.ifftn(kappa_ft) #units should be rad**2
    if self.pad:
        pot=self.mapCrop(potential.real)
    return pot

# returns the map of the gravitational time delay
def potential(self):
    no=self.pixel
    x_ = np.linspace(0,self.npix-1,self.npix)
    y_ = np.linspace(0,self.npix-1,self.npix)
    x,y=np.meshgrid(x_,y_)
    potential=self.potential_from_kappa()
    x0 = y0 = potential.shape[0] / 2*self.pixel_scale-self.size/2.0
    x=(x0+x*no)/self.pixel_scale
    y=(y0+y*no)/self.pixel_scale
    self.pot_exists=True
    pot=map_coordinates(potential,[y,x],order=1)
    self.pot=pot*self.pixel_scale**2/no/no
    self.a2,self.a1=np.gradient(self.pot)
    self.a12,self.a11=np.gradient(self.a1)
    self.a22,self.a21=np.gradient(self.a2)
    self.pot=pot*self.pixel_scale**2

# crop the maps to remove zero-padded areas and get back to the original
# region.
def mapCrop(self,mappa):
    xmin=int(self.kappa.shape[0]/2-self.nx/2)
    ymin=int(self.kappa.shape[1]/2-self.ny/2)
    xmax=int(xmin+self.nx)
    ymax=int(ymin+self.ny)

```

```
mappa=mappa[xmin:xmax,ymin:ymax]
return(mappa)
```

Here is an example:

```
size=200.0
npix=500
df=deflector('data/kappa_2.fits',True,npix=npix,size=size)

beta=[-30,8]
td=df.t_delay_surf(beta=beta)

xmin,xmax=-df.size/2,df.size/2
ymin,ymax=-df.size/2,df.size/2

fig,ax=plt.subplots(1,2,figsize=(14,8))
kwargs={'q': 0.5, 're': 1.0, 'pa': np.pi/4.0, 'n': 1,
        'ys1': beta[0], 'ys2': beta[1]}

se_unlensed=sersic(size_stamp,npix_stamp,**kwargs)
se=sersic(size_stamp,npix_stamp,gl=df,**kwargs)
df.caustics(ax=ax[0],lt='--',alpha=1.0)
df.clines(ax=ax[1],lt='--',alpha=1.0)
ax[0].imshow(se_unlensed.image,origin='lower',
              extent=[-se_unlensed.size/2,se_unlensed.size/2,
                      -se_unlensed.size/2,se_unlensed.size/2],
              cmap='gray_r')
ax[1].imshow(se.image,origin='lower',
              extent=[-se.size/2,se.size/2,-se.size/2,se.size/2],
              cmap='gray_r')
df.show_contours(td,ax=ax[1],minx=xmin,miny=ymin,nlevels=25,
                  levmax=1600,fontsize=20)

x0,x1=-40,10
y0,y1=-25,25
ax[0].set_xlim([x0,x1])
ax[0].set_ylim([y0,y1])
x0,x1=-80,50
y0,y1=-65,65
ax[1].set_xlim([x0,x1])
ax[1].set_ylim([y0,y1])
fig.tight_layout()
```

The code above produces the figure shown in Fig. 2.7.10. The source is placed near the cusp of the tangential caustic. Being inside the caustic, it produces three images, which are distorted and merge into a tangential arc. Note that the shape of the arc reflects the shape of the levels of equal time delay near the image.

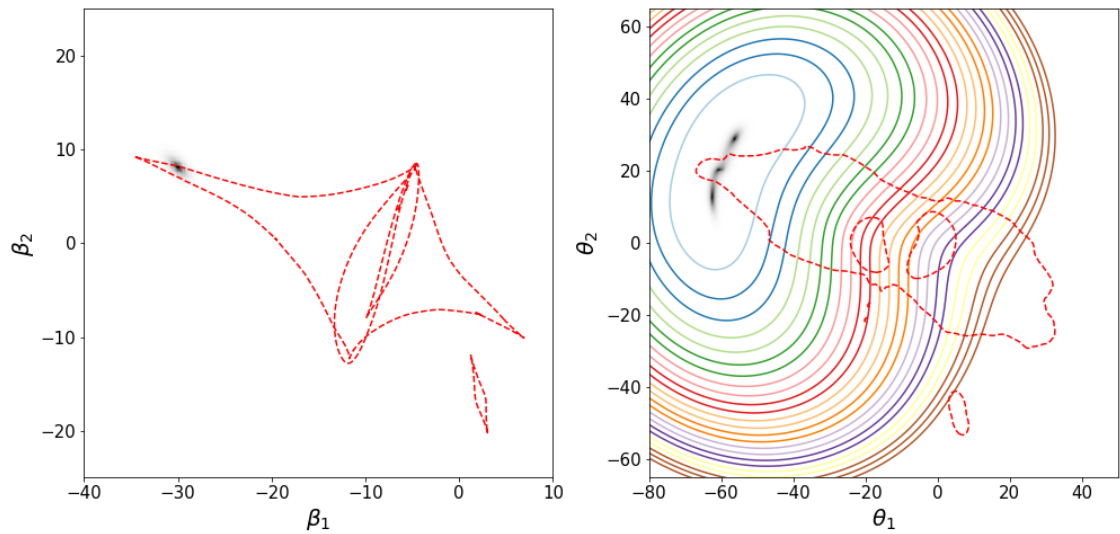


Figure 2.7.10: Left panel: Caustics of a numerically simulated lens. A Sérsic source is placed near the cusp of the caustics. Right panel: critical lines (dashed) and lensed images of the source shown in the left panel. The colored solid contours show the levels of equal time delay for the same source.

Part Two: Applications

3	Microlensing	77
3.1	The point mass lens	
3.2	Microlensing light-curve	
3.3	Microlensing parallax	
3.4	Photometric microlensing: optical depth and event rates	
3.5	Results from MACHO searches	
3.6	Astrometric microlensing	
3.7	Multiple point masses	
3.8	Planetary microlensing	
3.9	Python applications	
4	Extended lenses	139
4.1	Axially symmetric lenses	
4.2	Power-law lens	
4.3	Softened (Isothermal) Lenses	
4.4	Time delays	
4.5	Elliptical lenses	
4.6	Other profiles	
4.7	Environment	
4.8	Substructures	
4.9	Mass-sheet degeneracy	
4.10	Python applications	

3. Microlensing

This chapter is dedicated to microlensing, i.e. the lensing effects caused by lenses of very small size in the universe. In fact, a broad range of masses enter this class of lenses: from planets to stars. Given the small size of the lenses, microlenses are (to first order) assimilated to point masses or ensembles of point masses. Microlensing effects are mostly detectable and searched within our own galaxy, in particular by monitoring huge amounts of stars in the bulge of the Milky Way or towards the Magellanic clouds. Nevertheless, microlensing effects are relevant also in extragalactic gravitational lensing. Indeed, small mass lenses contained in galaxies other than ours produce small scale perturbations to the lensing signal of their hosts, which can be revealed in some situations.

3.1 The point mass lens

Deflection angle and lensing potential

In Example 1.2, we derived the deflection angle of a point mass. By choosing the lens position as the center of the reference frame (i.e. by counting the angles β and θ starting from the lens position), the deflection angle turns out to be

$$\hat{\alpha}(\vec{\xi}) = \frac{4GM}{c^2} \frac{\vec{\xi}}{|\vec{\xi}|^2} = \frac{4GM}{c^2 D_L} \frac{\vec{\theta}}{|\vec{\theta}|^2} = \hat{\alpha}(\vec{\theta}), \quad (3.1)$$

where, as usual, we have used the relation between the physical length ξ , the angle θ , and the angular diameter distance D_L , $\xi = D_L \theta$. Given that

$$\vec{\alpha}(\vec{\theta}) = \frac{D_{LS}}{D_S} \hat{\alpha}(\vec{\theta}) = \vec{\nabla} \hat{\Psi}(\vec{\theta}) \quad (3.2)$$

and that

$$\nabla \ln |\vec{x}| = \frac{\vec{x}}{|\vec{x}|^2}, \quad (3.3)$$

we can see that the lensing potential of the point mass lens is given by

$$\hat{\Psi}(\vec{\theta}) = \frac{4GM}{c^2} \frac{D_{LS}}{D_L D_S} \ln |\vec{\theta}|, \quad (3.4)$$

as we anticipated in Sect. 2.6.3.

Lens equation

The vector $\hat{\alpha}$ points away from the lens. Therefore, we may omit the vector sign in many of the following equations. Then

$$\hat{\alpha}(\theta) = \frac{4GM}{c^2 D_L \theta} . \quad (3.5)$$

The lens equation reads

$$\beta = \theta - \frac{4GM}{c^2 D_L \theta} \frac{D_{LS}}{D_S} . \quad (3.6)$$

This is a quadratic equation in θ , i.e. for a given position of the source β there always exist two images, whose positions can be determined by solving the lens equation.

Multiple images

Eq. 3.6 can be written in a more concise way by introducing the *Einstein radius*,

$$\theta_E \equiv \sqrt{\frac{4GM}{c^2} \frac{D_{LS}}{D_L D_S}} . \quad (3.7)$$

The importance of this quantity will be clear shortly.

By inserting Eq. 3.7 into Eq. 3.6, we obtain

$$\beta = \theta - \frac{\theta_E^2}{\theta} . \quad (3.8)$$

Dividing by θ_E and setting $y = \beta/\theta_E$ and $x = \theta/\theta_E$, i.e. by expressing all angles in units of the Einstein radius, we obtain the lens equation

$$y = x - \frac{1}{x} . \quad (3.9)$$

Multiplication with x leads to

$$x^2 - xy - 1 = 0 , \quad (3.10)$$

which has two solutions:

$$x_{\pm} = \frac{1}{2} \left[y \pm \sqrt{y^2 + 4} \right] . \quad (3.11)$$

The right panel of Fig. 3.1.1 shows a sequence of sources at different angular distances from the lens (indicated by a red star). Each source is shown using a different color, so that its images can be easily recognized in the left panel. For convenience the sources have been placed on the axis $y_2 = 0$.

Each source have two images, both on the axis $x_2 = 0$, but one with $x_+ > 0$ and one with $-1 < x_- < 0$. Thus, they are on opposite sides with respect to the lens, and the image at x_- is always within a circle of radius $x = 1$. Such circle coincides with the image of the source at $y = 0$, $x_{\pm} = \pm 1$; that is, a source exactly behind the point lens has a ring-shaped image with radius θ_E , also called *Einstein ring*. The size of the Einstein radius is

$$\begin{aligned} \theta_E &\approx (10^{-3})'' \left(\frac{M}{M_{\odot}} \right)^{1/2} \left(\frac{D}{10 \text{kpc}} \right)^{-1/2} , \\ &\approx 1'' \left(\frac{M}{10^{12} M_{\odot}} \right)^{1/2} \left(\frac{D}{\text{Gpc}} \right)^{-1/2} , \end{aligned} \quad (3.12)$$

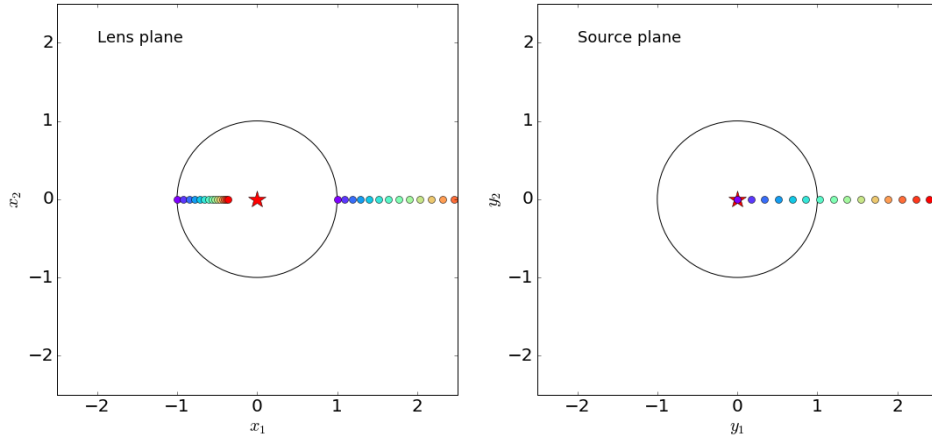


Figure 3.1.1: Solutions of the lens equation for a point mass lens. In both panels, the lens is given by the star at the center of the figure. The Einstein ring is shown in black. In the right panel, the positions of several source are indicated by colored circles. The corresponding images, as obtained by Eq. 3.11, are shown in the left panel.

where

$$D \equiv \frac{D_L D_S}{D_{LS}} \quad (3.13)$$

is the *effective lensing distance*.

As $\beta \rightarrow \infty$, we see that $\theta_- = x_- \theta_E \rightarrow 0$, while obviously $\theta_+ = x_+ \theta_E \rightarrow \beta$: when the angular separation between the lens and the source becomes large, the source is unlensed. Formally, there is still an image at $\theta_- = 0$, but as we have seen when discussing the properties of the time-delay surface, this central image has zero magnification.

Critical lines, caustics, and magnification

Given that the lens is axially-symmetric, the Jacobian determinant is:

$$\det A(x) = -\frac{y \, dy}{x \, dx}. \quad (3.14)$$

From Eq. 3.14 and from Eq. 3.6, that the eigenvalues of the Jacobian matrix are

$$\begin{aligned} \lambda_t(x) &= \frac{y}{x} = \left(1 - \frac{1}{x^2}\right) \\ \lambda_r(x) &= \frac{dy}{dx} = \left(1 + \frac{1}{x^2}\right). \end{aligned} \quad (3.15)$$

Obviously, the second eigenvalue is never zero. Therefore, the point mass lens only have one critical line, namely a circle with equation $x^2 = 1$. This is the equation of the Einstein ring, which thus coincides with the tangential critical line.

Using the lens equation, as seen above, this line is mapped onto the tangential caustic, which is a point at $\beta = 0$ ($y = 0$).

The magnification is the inverse of the Jacobian determinant, thus

$$\mu(x) = 1 - \frac{1}{x^4}. \quad (3.16)$$

Source magnification

From Eq. 3.11, we can see that, at the image positions,

$$\begin{aligned}\frac{x}{y} &= \frac{1}{2} \left(1 \pm \frac{\sqrt{y^2+4}}{y} \right) \\ \frac{dx}{dy} &= \frac{1}{2} \left(1 \pm \frac{y}{\sqrt{y^2+4}} \right).\end{aligned}\quad (3.17)$$

Thus, the image magnification can be written as a function of the source position as

$$\begin{aligned}\mu_{\pm}(y) &= \frac{1}{4} \left(1 \pm \frac{\sqrt{y^2+4}}{y} \right) \left(1 \pm \frac{y}{\sqrt{y^2+4}} \right) \\ &= \frac{1}{4} \left(1 \pm \frac{\sqrt{y^2+4}}{y} \pm \frac{y}{\sqrt{y^2+4}} + 1 \right) \\ &= \frac{1}{4} \left(2 \pm \frac{2y^2+4}{y\sqrt{y^2+4}} \right) = \frac{1}{2} \left(1 \pm \frac{y^2+2}{y\sqrt{y^2+4}} \right).\end{aligned}\quad (3.18)$$

Note that, for $y > 0$, $\mu_-(y) < 0$ and $\mu_+(y) > 0$, showing that the parity of the two images is different¹.

The total source magnification is

$$\mu(y) = \mu_+(y) + |\mu_-(y)| = \frac{y^2+2}{y\sqrt{y^2+4}}, \quad (3.19)$$

while the sum of the *signed* magnifications is $\mu = 1$. By means of a power series expansion of the function above, we see that $\mu \propto 1 + 2/y^4$ for $y \rightarrow \infty$, i.e. the magnification drops quickly as the source moves away from the lens.

The magnification ratio of the two images is

$$\begin{aligned}\left| \frac{\mu_+}{\mu_-} \right| &= \frac{1 + \frac{y^2+2}{y\sqrt{y^2+4}}}{\frac{y^2+2}{y\sqrt{y^2+4}} - 1} \\ &= \frac{y^2+2+y\sqrt{y^2+4}}{y^2+2-y\sqrt{y^2+4}}.\end{aligned}\quad (3.20)$$

Given that

$$\frac{1}{2} \left(y + \sqrt{y^2+4} \right)^2 = y^2 + 2 + y\sqrt{y^2+4} \quad (3.21)$$

and

$$\frac{1}{2} \left(y - \sqrt{y^2+4} \right)^2 = y^2 + 2 - y\sqrt{y^2+4}, \quad (3.22)$$

we find that

$$\begin{aligned}\left| \frac{\mu_+}{\mu_-} \right| &= \left(\frac{y + \sqrt{y^2+4}}{y - \sqrt{y^2+4}} \right)^2 \\ &= \left(\frac{x_+}{x_-} \right)^2.\end{aligned}\quad (3.23)$$

¹For $y > 0$, $x_+ > 0$ and $x_- < 0$. Thus, $\mu_t = x/y$ is positive at x_+ and negative at x_- . Given that $\mu_r = dx/dy > 0$, the magnifications of the two images, $\mu_{\pm} = \mu_t(x_{\pm})\mu_r(x_{\pm})$ have the same signs of x_{\pm} .

We can see that $\lim_{y \rightarrow \infty} \mu_- = 0$ and that $\lim_{y \rightarrow \infty} \mu_+ = 1$. Moreover, a power series expansion shows that for large y ,

$$\left| \frac{\mu_+}{\mu_-} \right| \propto y^4, \quad (3.24)$$

i.e. the image at x_+ dominates the magnification budget pretty quickly as the source is moved away from the lens.

Microlensing cross section

A source at $y = 1$ has two images at

$$x_{\pm} = \frac{1 \pm \sqrt{5}}{2}, \quad (3.25)$$

and their magnifications are

$$\mu_{\pm} = \left[1 - \left(\frac{2}{1 \pm \sqrt{5}} \right)^4 \right]^{-1}. \quad (3.26)$$

Thus, the total source magnification is $\mu = |\mu_+| + |\mu_-| = 1.17 + 0.17 = 1.34$. In terms of magnitudes, this correspond to $\Delta m = -2.5 \log \mu \sim 0.3$ only. The image at x_+ contributes for $\sim 87\%$ of the total magnification. As seen above, for $y > 1$ the magnification drops quickly meaning that the only chance to detect microlensing events via magnification effects is by finding sources well aligned with the lenses, i.e. within their Einstein rings. For this reason, the area of the Einstein ring is generally assumed to be the cross-section for microlensing,

$$\sigma_{micro} = \pi \theta_E^2. \quad (3.27)$$

This is the solid angle within which a source has to be placed in order to produce a detectable microlensing signal.

3.2 Microlensing light-curve

The order-of-magnitude of the image separation in microlensing events is given by the Einstein radius of the typical lens. As seen above, for a one solar-mass star within our galaxy, this is of the order of $\sim 10^{-3}$ arcseconds, thus undetectable with the current instrumentation.

Microlenses in the Milky Way or its surrounding can however be detected by exploiting the relative motion of the lenses and of the sources, due to the (differential) rotation of our own galaxy. If the source and the lens are in relative motion, i.e. if the relative distance between the lens and the source, y , is a function of time, then Eq. 3.19 shows that the magnification is a function of time as well, $\mu \equiv \mu(t)$. Therefore, a source with intrinsic flux f_s will appear to have a flux $f(t) = \mu(t)f_s$, while being lensed. The curve describing the variation of the source flux as a function of time during the microlensing event is called the *microlensing light-curve*.

We assume that the relative path of the source with respect to the lens can be approximated by a straight line, as shown by the blue-dashed line in the diagram in Fig. 3.2.1. The source (indicated by the blue dot) reaches the minimum dimensionless distance y_0 from the lens at time t_0 . y_0 is the dimensionless *impact parameter* of the source. Assuming that the source moves with transverse velocity v relative to the lens, we can write the dimensionless distance of the source from the point of minimum distance from the lens as

$$y_1(t) = \frac{v(t - t_0)}{D_L \theta_E}, \quad (3.28)$$

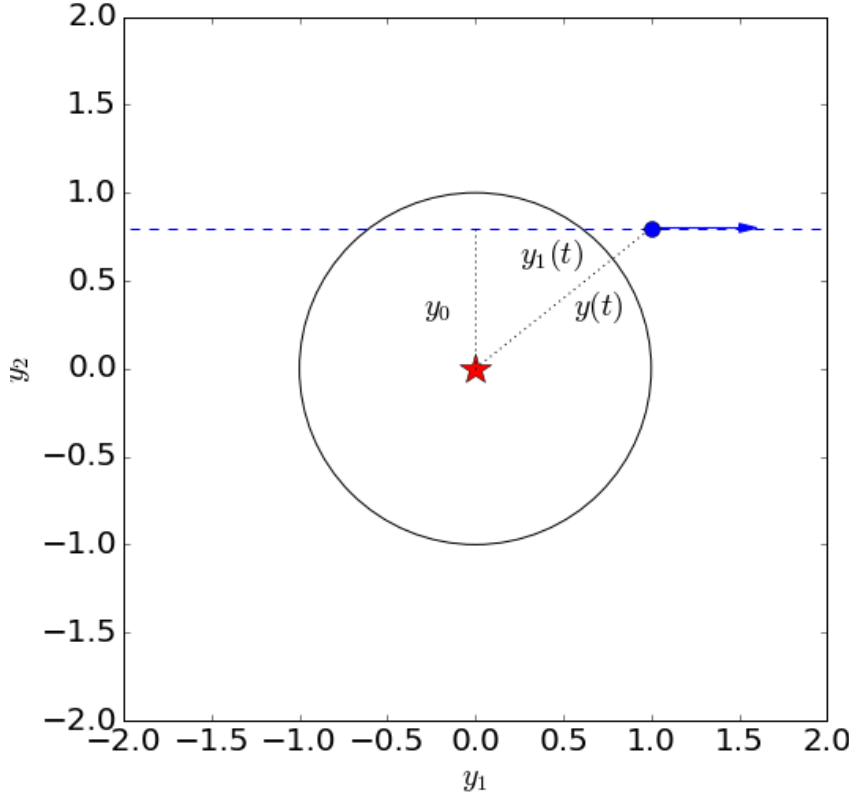


Figure 3.2.1: Illustration for the lens position and source trajectory. The dimensionless impact parameter is y_0 . $y_1(t)$ is the dimensionless distance of the source from the point of minimum distance from the lens. Finally, $y(t)$ is the dimensionless distance of the source from the lens.

where D_L indicates, as usual, the angular diameter distance between the observer and the lens.

If the source moves at velocity v , it will take a time

$$t_E = \frac{D_L \theta_E}{v} = \frac{\theta_E}{\mu_{rel}} \quad (3.29)$$

to cross the Einstein radius of the lens. In the equation above, we have introduced the relative proper motion of the source with respect to the lens, $\mu_{rel} = v/D_L$. Since, as we discussed in the previous section, the magnification significantly deviates from unity only for sources with $|y| \lesssim 1$, we can assume that the *Einstein radius crossing time*, t_E , is the timescale of the microlensing event. If we use the definition of Einstein radius given in Eq. 3.7, we see that

$$t_E \approx 19 \text{ days} \sqrt{4 \frac{D_L}{D_S} \left(1 - \frac{D_L}{D_S}\right)} \left(\frac{D_S}{8 \text{kpc}}\right)^{1/2} \left(\frac{M}{0.3 M_\odot}\right)^{1/2} \left(\frac{v}{200 \text{km/s}}\right)^{-1} \quad (3.30)$$

To write this equation, we have used the approximation $D_{LS} = D_S - D_L$, which is valid only for non-cosmological distances, and thus applies in our galaxy.

Inserting Eq. 3.29 into Eq. 3.28, we obtain:

$$y_1(t) = \frac{(t - t_0)}{t_E}. \quad (3.31)$$

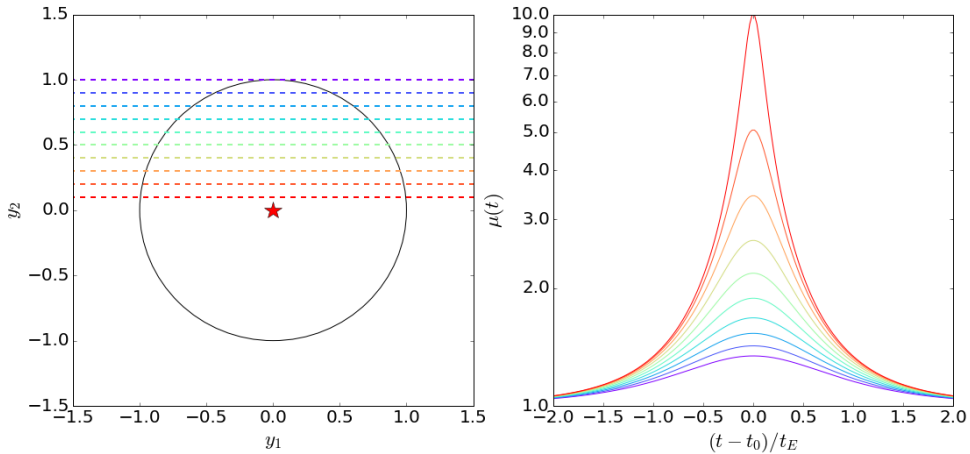


Figure 3.2.2: Left panel: source trajectories corresponding to different values of the impact parameter y_0 , varying from 0.1 (red) to 1 (purple). Right panel: color-coded light-curves corresponding to the source trajectories displayed in the left panel.

Thus,

$$y(t) = \sqrt{y_0^2 + y_1^2(t)} = \sqrt{y_0^2 + \frac{(t - t_0)^2}{t_E^2}}. \quad (3.32)$$

Combining Eqs. 3.32 and 3.19, we obtain the microlensing light-curve:

$$\mu(t) = \frac{y(t)^2 + 2}{y(t)\sqrt{y(t)^2 + 4}}. \quad (3.33)$$

Some examples of light-curves corresponding to different values of the impact parameter y_0 are shown in Fig. 3.2.2.

3.2.1 Light-curve fitting

The shape of the *standard* microlensing light-curve is characterized by a peak which occurs at t_0 . The peak height is determined by the value of y_0 : the closer the source trajectory passes to the lens, the highest is the peak. The peak width is instead determined by t_E , which in turn depends on the lens mass, the relative transverse velocity, the lens and the source distances. Therefore from an observed light curve well fitted by the standard model, one cannot infer the distances, the velocity, and the lens mass uniquely. This is the so-called *microlensing degeneracy*. However, given a lens mass function and some kinematic model of the Milky Way, we can infer the lens masses statistically.

In addition, to fit an observed light-curve we need the baseline flux f . Generally, a *blending parameter*, b_s , which describes the fraction of light contributed by the lensed source is also included. In presence of crowded fields, the measured flux is indeed the sum of the flux from the source, from the lens, and from other unrelated stars within the seeing disk. Since these may be wavelength dependent, the blending parameter is generally different in different filters. Note that blending biases the magnification estimate low.

While the standard light-curve model works well in about 90% of the cases, there are situations where one or more of the assumptions at the basis of the standard model break down. In these *exotic* cases, it may be possible to derive extra constraints which help to partially lift the microlensing

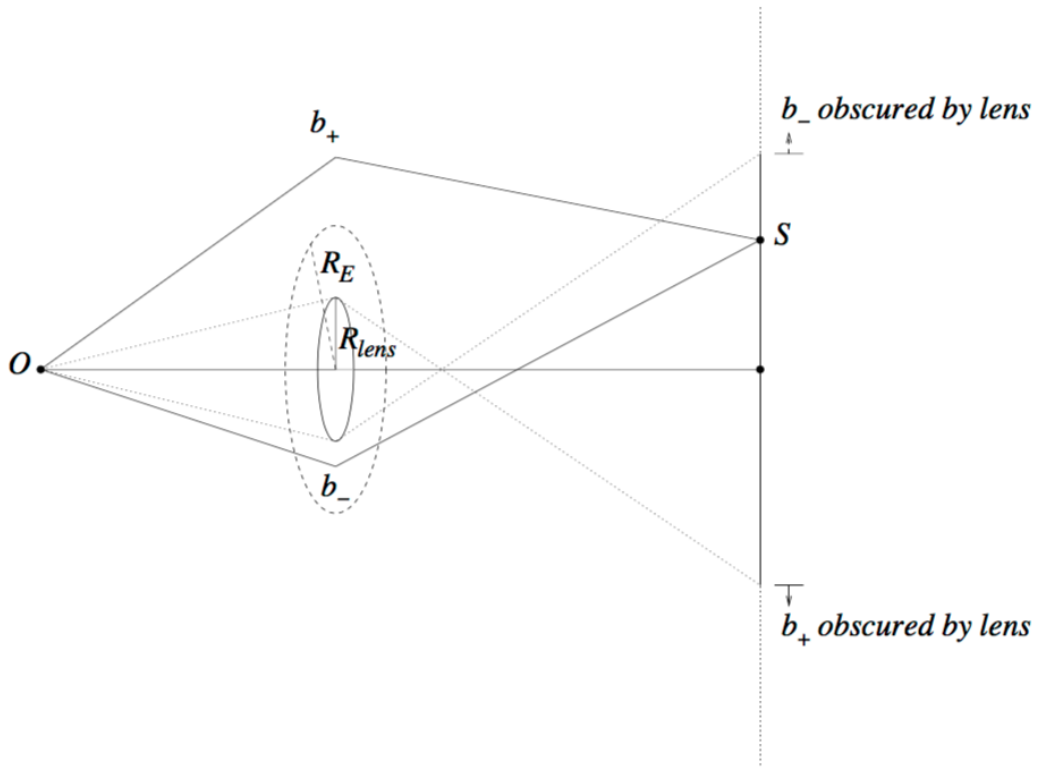


Figure 3.2.3: Illustration of the finite lens size effect. Depending on the distance of the source from the center of the finite lens, the images in x_+ or in x_- (here indicated with b_{\pm}) are obscured. Figure from (Lee et al., 2009).

degeneracy. Non-standard light-curves occur, for example, when the source or the lens are not point-like (finite source size and finite lens size effects) or when the motion of the source relative to the lens is not linear. This is the case when the lens and/or the source are in binary systems, for example.

If the lens has finite size, one can always find a time interval when the lens obscures the inner (and the outer, depending on the lens size) lensed image in the early rising stage and in the final declining stage of the light curve. This is shown in Fig. 3.2.3, taken from (Lee et al., 2009). Thus, the impact of these effects is to dim the wings of the light curve.

The finite source size effect occurs when the size of the source is not negligible and it is particularly important in the high-magnification limits (Gould, 1994; Lee et al., 2009; Witt and Mao, 1994). In this case, the light-curve is broadened near the peak, as the result of the fact that different parts of the source experience different magnifications. Assuming that the surface brightness of the source is uniform, the magnification near the peak of the light curve can be approximated by the following formula (Gould, 1994):

$$\mu'(y) \simeq \mu(y) \frac{4y}{\pi\rho} E(\vartheta_{\max}, y/\rho), \quad (3.34)$$

where $E(\vartheta, \varphi)$ is the Elliptical integral of the second kind and ϑ is defined as

$$\vartheta_{\max} = \begin{cases} \frac{\pi}{2} & y \leq \rho \\ \arcsin(\rho/y) & y > \rho \end{cases}. \quad (3.35)$$

Fitting the light curve allows to measure $\rho = \theta_{\star}/\theta_E$, i.e. the source size, θ_{\star} , in units of the Einstein radius. thus, if θ_{\star} can be measured in an independent way, the finite source effect allows

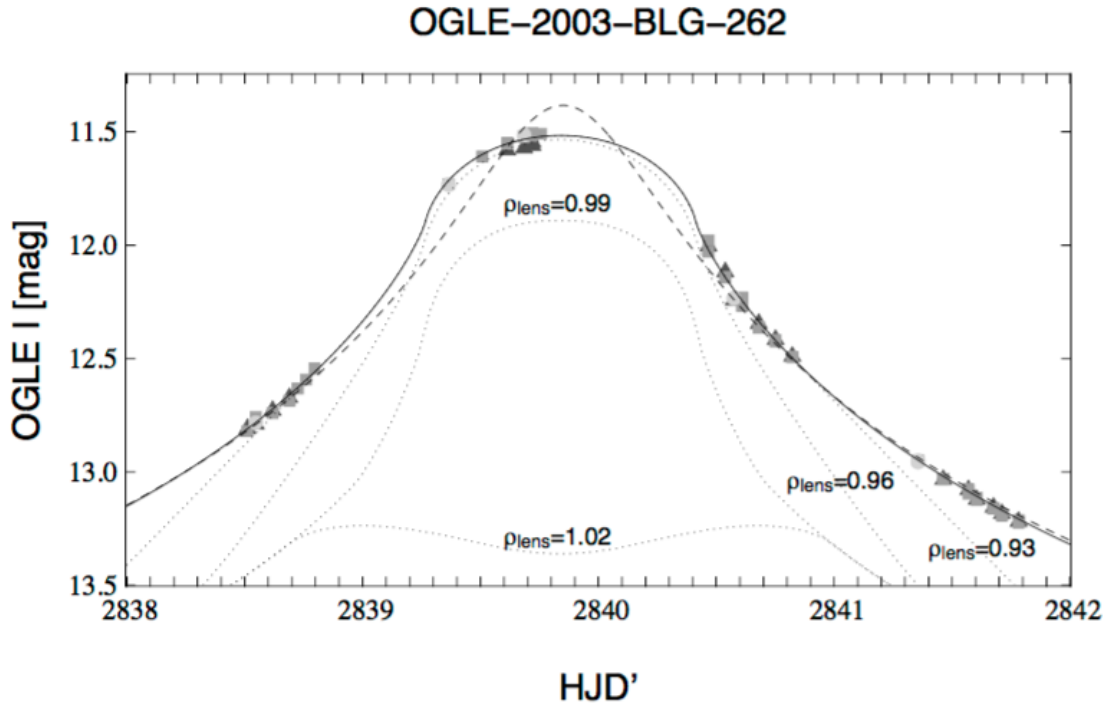


Figure 3.2.4: Light curve of the microlensing event OGLE-2003-BLG-262. The shape of the light curve is fitted with a model which accounts for finite source size effects (solid line). The dotted lines illustrate the effects of finite lens sizes on top of finite-source size for lens sizes of $\rho_{\text{lens}} = 0.93, 0.96, 0.99$, and 1.02 . Figure from (Lee et al., 2009).

to measure the size of the Einstein radius. For example, the source size can be derived from empirical relations between the surface brightness and the colors. Kervella et al. (2004) proposed the following relation between the angular diameter for A0-M2 dwarf stars or A0-K0 sub-giants, the $V - K$ color and K -band magnitude:

$$\log 2\theta_* = 0.0755(V - K) + 0.5170?0.2K . \quad (3.36)$$

Measuring θ_E and t_E then allows to measure $\mu_{\text{rel}} = \theta_E/t_E$.

Note that, given the large difference between the sizes of θ_E ($\sim 1\text{mas}$) and θ_* ($\sim 0.5\mu\text{as}$), the finite source size effect can be measured only in very high magnification events (when the source overlaps with the point-like caustic). An example of light-curve being fitted including both finite source and lens size effects is shown in Fig. 3.2.4.

3.3 Microlensing parallax

For a point mass lens in the Milky Way, using the fact that $D_{\text{LS}} = D_{\text{S}} - D_{\text{L}}$, the Einstein radius can be written as

$$\theta_E = \sqrt{\frac{4GM}{c^2} \frac{D_{\text{LS}}}{D_{\text{L}} D_{\text{S}}}} = \sqrt{\frac{4GM}{c^2} \left(\frac{1}{D_{\text{L}}} - \frac{1}{D_{\text{S}}} \right)} = \sqrt{\frac{4GM}{c^2} \pi_{\text{rel}}} . \quad (3.37)$$

In the above equation, $\pi_{\text{rel}} = 1/D_{\text{L}} - 1/D_{\text{S}}$ is the *relative parallax* of the lens and the source. From Eq. 3.37, we can also see that

$$\theta_E = \frac{4GM}{c^2} \frac{\pi_{\text{rel}}}{\theta_E} = \frac{4GM}{c^2} \pi_E , \quad (3.38)$$

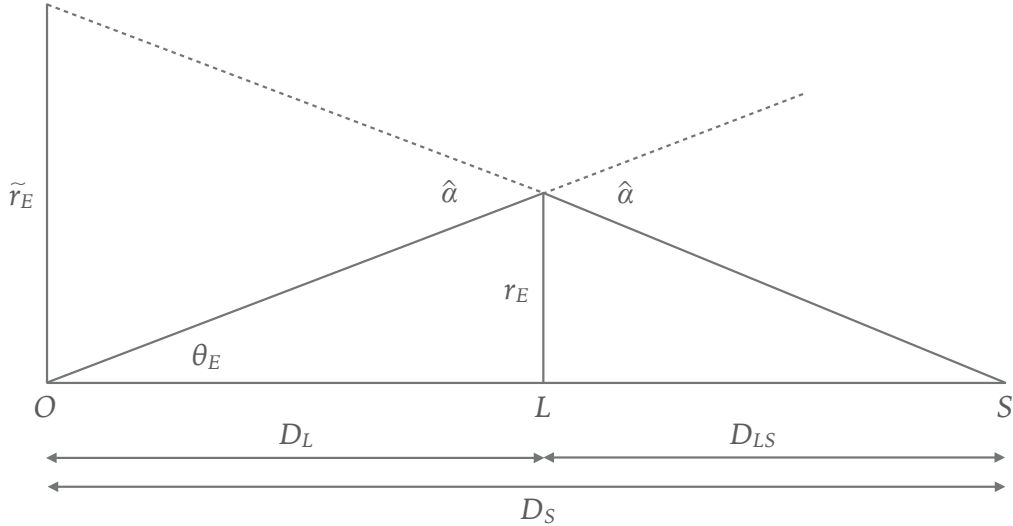


Figure 3.3.1: Relationship between projected Einstein radius, \tilde{r}_E and angular Einstein radius θ_E .

where we have introduced the *microlensing parallax*, $\pi_E = \pi_{\text{rel}}/\theta_E$. By setting

$$k = \frac{4G}{c^2} = 8.14 \text{ mas } M_\odot^{-1}, \quad (3.39)$$

we find that

$$M = \frac{\theta_E}{k\pi_E}, \quad (3.40)$$

which shows that measuring the microlensing parallax, π_E , and the Einstein radius, θ_E , allows to break the microlensing degeneracies and measure the lens mass.

The diagram in Fig. 3.3.1 also shows that the microlensing parallax is the inverse of the projection of the physical Einstein radius, $r_E = \theta_E D_L$, onto the observer plane, \tilde{r}_E . Indeed,

$$\tilde{r}_E = D_L \hat{\alpha}(\theta_E) = \frac{r_E}{\theta_E} \hat{\alpha}(\theta_E) = \frac{kM}{\theta_E} = \frac{1}{\pi_E}. \quad (3.41)$$

It has now to be explained how the microlensing parallax can be measured. This requires the observer to look at the microlensing event from different points of view. This can happen in two ways. First, the observer moves from one location to another. Second, the observer uses two telescopes to simultaneously observe the event from different locations. In fact, there are three types of microlensing parallax:

1. orbital or annual parallax: the observer on the earth participates to orbital motion of the earth around the sun;

2. satellite parallax: the observer uses a ground based facility and a space telescope to observe the same event;
3. terrestrial parallax: the observer uses a network of ground based facilities to observe the same event.

In all these circumstances, because of the different line-of-sight to the source, the observer will see a variation of the relative positions of the lens and of the sources. Since the magnification in Eq. 3.33 depends on the absolute separation of lens and source in units of the Einstein radius, the source light-curve will be affected.

Orbital parallax

The orbital motion of the earth around the sun implies that the line-of-sight to the source changes in the course of the microlensing event for a ground based observer. In the frame where the observer and the source are fixed, the lens moves both because of its intrinsic motion relative to the source (which may be assumed to be on a rectilinear trajectory) and because of the earth orbital motion. While the first motion produces the standard light curve, the second distorts it. The first detection of orbital microlensing parallax was reported by Alcock et al. (1995). The light curves in the B and R -bands of the microlensing event are shown in Fig. 3.3.2. The data do not follow standard microlensing light-curve (dotted line). Instead, they are fitted well by a model that accounts for the orbital parallax effect (solid curve).



The microlensing parallax is a vector. An important aspect of the microlensing parallax is that it is a vector, rather than a scalar quantity. Indeed, the microlensing effects will be different depending on the direction into which the lens position is shifted relative to the source. For example, we may consider the shift due to parallax as made of two components, one along the intrinsic lens trajectory and one perpendicular to it. The first component implies an acceleration of the lens relative to the source. The effect on the source light curve will be that of introducing an asymmetric distortion of the shape of the light curve (with respect to t_0). Instead, the second component changes the impact parameter y_0 , bringing the lens trajectory closer or farther from the source. Consequently, the distortion of the light curve will be symmetric.

Since the timescale of the variation of the observer baseline is ~ 1 year, the orbital parallax effect can be measured in events that are not too short (~ 100 days). In addition, the effect is more easy observable in spring and in fall, because in these seasons the motion of the earth around the sun is mostly perpendicular to the direction to the galactic bulge.

Satellite parallax

The satellite parallax effect is measurable combining observations from the ground and from a space observatory. At the moment, the instrument which offers the best opportunity to measure this effect is the *Spitzer* space telescope. This is one of the large Space Observatories of NASA, observing at infrared wavelengths from an earth trailing orbit. *Spitzer* happens to be at a distance of ~ 1 AU from the earth. When projected on the observer plane, the Einstein radii, \tilde{r}_E of lenses in the galaxy are \sim few–10 AU. Thus, *Spitzer* offers the right baseline to detect parallax effects in most of the microlensing events involving from M -dwarfs to solar-mass lenses.

Two different light-curves are measured from the ground and from space. An example is shown in Fig. 3.3.3, which refers to the first detection of satellite parallax for an isolated star (Yee et al., 2015). The event, dubbed OGLE-2014-BLG-0939, was observed by the OGLE collaboration from the ground and then followed up by *Spitzer*. Both light-curves are well-represented by standard microlensing curves (blue), but they have substantially different maximum magnifications and times of maximum, whose differences yield a measurement of the “microlens parallax” vector, $\vec{\pi}_E$.

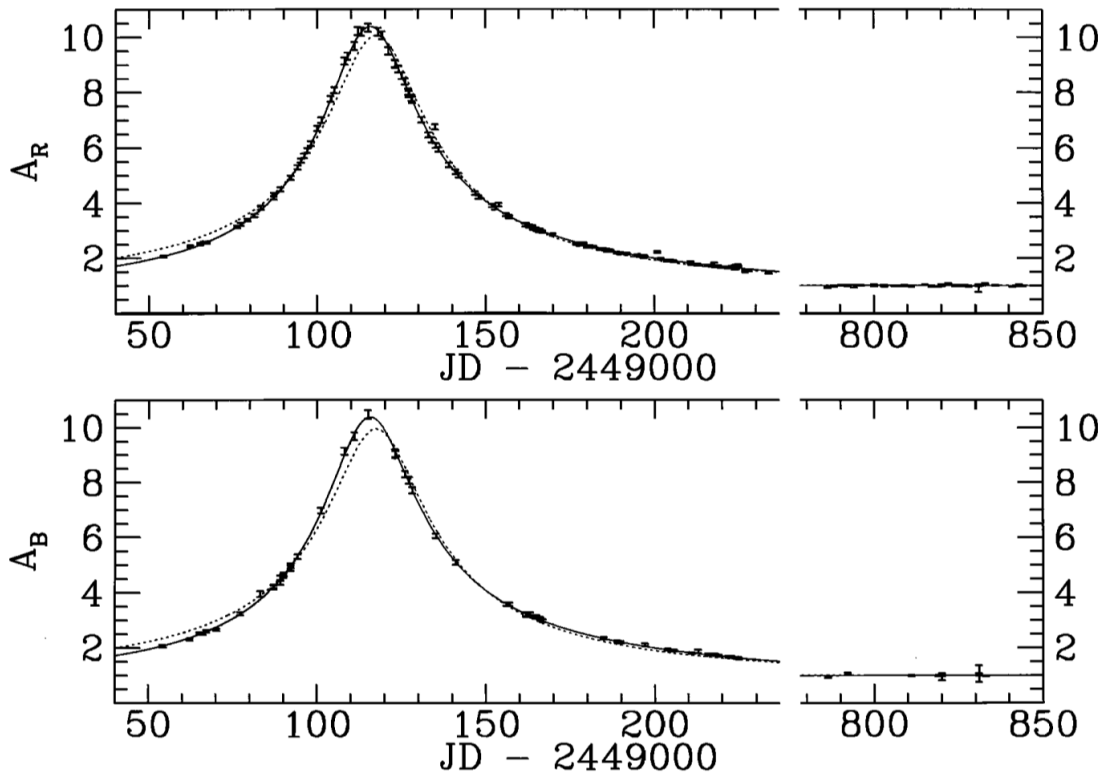


Figure 3.3.2: First detection of orbital parallax effect. The two panels show the light-curves of the event in the B band and in the R-bands. The data are shown with their $\pm 1\sigma$ error bars. The dotted curve is the best-fit standard light-curve model (i.e. assuming a constant relative velocity). The solid line shows the best-fit model accounting for the earth orbital motion. Figure from Alcock et al. (1995).

Terrestrial parallax

Terrestrial parallax effects are detectable in extreme (fast) microlensing events observed from two or more observatories on the earth. Similarly to the case of satellite parallax, using multiple telescopes on the ground to observe the same microlensing event allows to measure the parallax by means of comparing the light-curves measured from each location.

Fig. 3.3.4 refers to the event OGLE-2007-BLG-224 (Gould, Udalski, et al., 2009). Three light-curves were measured from three locations in Chile (red), Canary Island (blue), and South Africa (green). The differences between the light-curves are due to terrestrial parallax and allow to measure it.

Note that shape of the light-curves near the peak is rounded due to finite source effects. Thus fitting the light-curve and accounting for the finite size of the source, allows to measure the Einstein radius. Combining this measurement with that of the microlensing parallax, both the mass and the distance of the lens can be measured.

3.4 Photometric microlensing: optical depth and event rates

3.4.1 Optical depth

The optical depth to some distance D_S is the probability that a source at that distance gives rise to a detectable microlensing event. As discussed earlier, we can assume that the lens cross section (in steradians) coincides with the solid angle enclosed by the Einstein ring, $\pi\theta_E^2$. Therefore, the optical

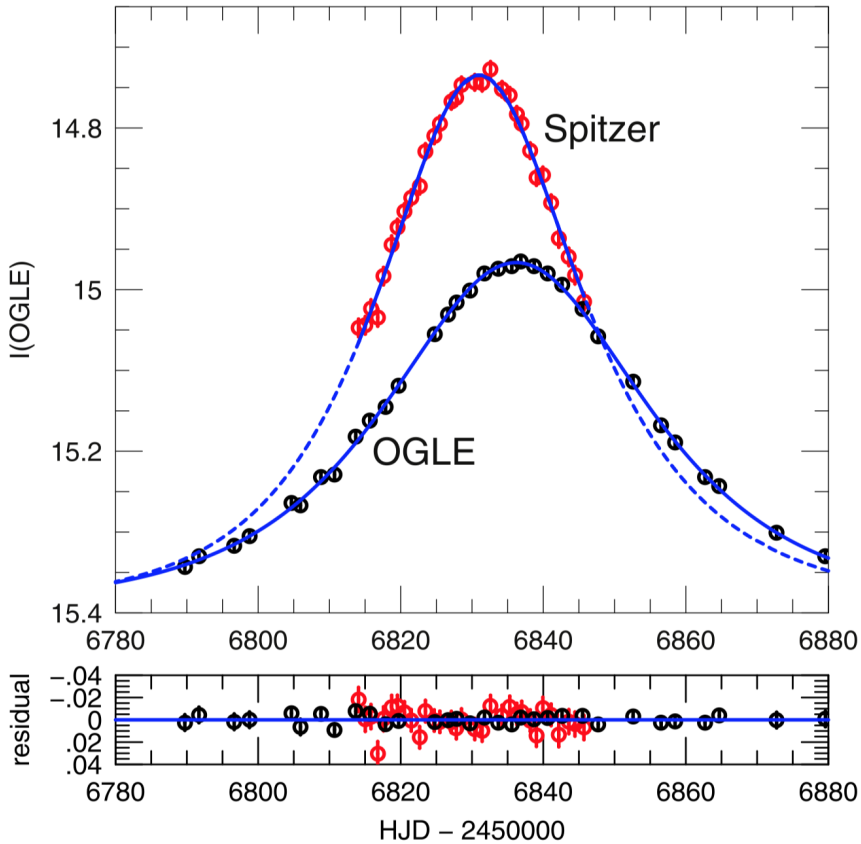


Figure 3.3.3: Satellite parallax effect in the event OGLE-2014-BLG-0939. The figure shows the two light-curves measured in the I -band by the OGLE collaboration (black) and from Spitzer (red). Both light-curves are well described by standard light-curve models (blue). The residuals are shown in the bottom panel. Figure from Yee et al. (2015).

depth can be computed as the sum of the cross sections of all lenses up to distance D_S , divided by the area of the sky. Let assume that the number density of lenses varies as a function of the lens distance as $n(D_L)$. Then, the number of lenses within the solid angle Ω at distances between D_L to $D_L + dD_L$ is

$$dN_L = \Omega D_L^2 n(D_L) dD_L. \quad (3.42)$$

Thus, the optical depth is

$$\tau(D_S) = \frac{1}{\Omega} \int_0^{D_S} [\Omega D_L^2 n(D_L)] (\pi \theta_E^2) dD_L. \quad (3.43)$$

If all lenses have the same mass M , then $n(D_L) = \rho(D_L)/M$, where $\rho(D_L)$ is the mass density. Note that, since $\theta_E \propto M^{1/2}$, the optical depth depends on the total mass density but not on the lens mass. This result can be generalized also to the case where the lens have a mass distribution (a.k.a. the *lens mass function*), if the spatial distribution of the lenses is independent on the mass. Indeed, we can write

$$n(D_L) = \int n(D_L, M) dM = \int \rho_M(D_L) M^{-1} dM. \quad (3.44)$$

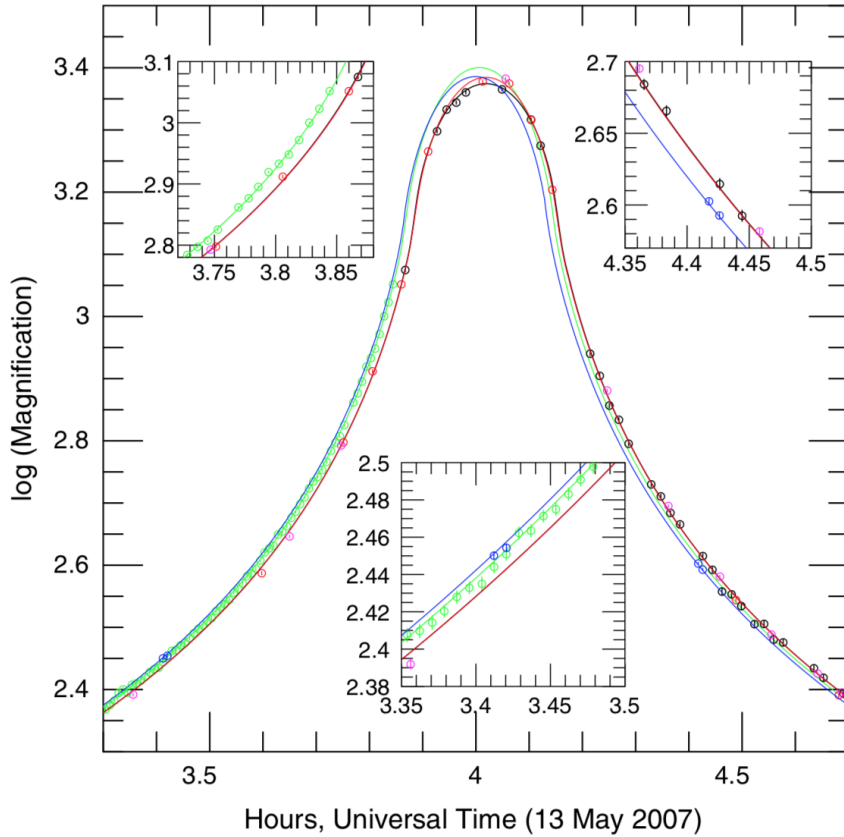


Figure 3.3.4: Terrestrial parallax effect in the event OGLE-2007-BLG-224. The blue, red, and green light-curves refer to the measurements conducted from Chile, Canary Island, and South Africa, respectively. Figure from Gould, Udalski, et al. (2009).

Under this assumption, and using Eq. 3.7, we obtain

$$\begin{aligned}\tau(D_S) &= \frac{4\pi G}{c^2} \int_0^{D_S} \rho(D_L) D_L^2 \frac{D_{LS}}{D_L D_S} dD_L \\ &= \frac{4\pi G}{c^2} \int_0^{D_S} \rho(D_L) D_L \frac{D_S - D_L}{D_S} dD_L \\ &= \frac{4\pi G}{c^2} \int_0^{D_S} \rho(D_L) \frac{D_L}{D_S} \left(1 - \frac{D_L}{D_S}\right) D_S dD_L.\end{aligned}\quad (3.45)$$

Setting $x = D_L/D_S$, $dx = dD_L/D_S$, the optical depth is thus

$$\tau(D_S) = \frac{4\pi G}{c^2} D_S^2 \int_0^1 \rho(x) x (1-x) dx. \quad (3.46)$$

By taking the derivative with respect to x , we see that

$$\frac{d\tau}{dx} \propto \rho(x) x (1-x). \quad (3.47)$$

The function $f(x) = x(1-x)$, which weights the contribution of lenses to the optical depth, has a maximum at $x = 0.5$, i.e. the lenses which are located about half way between the observer and the sources contribute the most to the optical depth. However, one has to consider $\rho(x)$ to establish where most of the microlensing signal comes from.

Note that, since sources are not all at distance D_S , the total optical depth should be calculated by integrating $\tau(D_S)$ over the distribution of D_S .

We consider a very crude model of the galaxy, assuming that it is a spherical, self-gravitating system of lenses of mass M . Then, with $\rho(x) = \rho_0 = \text{const}$, we obtain

$$\tau(D_S) = \frac{4\pi G}{c^2} \rho_0 D_S^2 \int_0^1 x(1-x)dx = \frac{2}{3} \frac{\pi G}{c^2} D_S^2 \rho_0. \quad (3.48)$$

Let's consider the case of microlensing in the Milky Way. The sphere centered on the center of the galaxy and with radius D_S contains a mass $M_{gal} = \frac{4}{3}\pi D_S^3 \rho_0$, thus

$$\tau(D_S) = \frac{GM_{gal}}{2c^2 D_S} = \frac{V_{circ}^2}{2c^2}. \quad (3.49)$$

where $V_{circ} \approx 220$ km/s is the circular velocity. Assuming that the sources are all at galactocentric distance, the optical depth for microlensing is

$$\tau \approx 2.6 \times 10^{-7}. \quad (3.50)$$

Thus we need to monitor many millions of stars in order to have a realistic yield of microlenses, meaning that observational campaigns have to target regions where the numerical density of stars is very high. In fact, several microlensing experiments have been carried out since the 90's, which have targeted the galactic bulge and the Magellanic Clouds.



The calculations reported above assume that the mass density of lenses is constant. However, this is an over-simplification: in the case of microlensing towards the galactic bulge, we should account for the far more complex structure of our galaxy, which includes several components (bulge, bar, disk, halo), each of which have its own mass density. In fact, the true optical depth towards the galactic center is $\sim 3 - 10$ times larger due to flattened nature of the galactic disk and to the presence of a bar.

Exercise 3.1 — Optical depth of an exponential disk. We report here the calculations for computing the optical depth to the galactic center for a distribution of lenses resembling the galactic disk (i.e. having an exponential density profile). This exercise was proposed in the nice review paper by Mao (2008).

The mass density in the exponential disk is described, with respect to an observer near the sun, by the function

$$\rho(R) = \rho_0 \exp(-(R - R_0)/R_D), \quad (3.51)$$

where ρ_0 is the mass density in the solar neighborhood, R is the distance of the lens from the galactic center, R_0 is the distance of the sun from the galactic center and R_D is the disk scale (i.e. a parameter which defines how quickly the density falls as a function of radius). Using the standard notation, we have that $R = D_{LS}$ and $R_0 = D_S$, thus

$$\rho(D_L) = \rho_0 \exp(D_L/R_D). \quad (3.52)$$

Scaling the distances by D_S , the density can be written as

$$\rho(x) = \rho_0 \exp x/x', \quad (3.53)$$

where $x' = R_D/D_S$. This can be inserted into Eq. 3.46 to obtain

$$\tau(D_S) = \frac{4\pi G}{c^2} \rho_0 D_S^2 \int_0^1 \exp(x/x') x(1-x) dx . \quad (3.54)$$

Solving the last integral, we find that

$$\tau(D_S) = \frac{4\pi G}{c^2} \rho_0 D_S^2 x'^2 [2x' - 1 + \exp(1/x')(2x' - 1)] ; . \quad (3.55)$$

Assuming $D_S = 8$ kpc, $R_D = 3$ kpc, $\rho_0 = 0.1 M_\odot \text{pc}^{-3}$, we obtain

$$\tau \approx 2.9 \times 10^{-6} . \quad (3.56)$$

■

3.4.2 Event rate

While the optical depth gives the probability that a source is undergoing a microlensing event at any given instant, we are interested in knowing what is the rate of microlensing events we may see while monitoring a certain number of sources for a certain time.

To calculate the event rate it is more natural to imagine that sources form a static background in front of which lenses move at some transverse velocity v . For simplicity, we can assume that this velocity is the same for all the lenses (although, in a realistic case, both the lenses and the sources have some velocity distributions). The lens cross section has diameter $2r_E$, where r_E is the physical size of the Einstein radius on the lens plane, $r_E = D_L \theta_E$. In order to compute the probability to observe a microlensing event in a given time dt , we have to consider that the lens, while moving in front of the sources at velocity v , swipes a certain area. The area swept in the time dt is

$$dA = 2r_E v dt = 2r_E^2 \frac{dt}{t_E} . \quad (3.57)$$

Multiplying by the number of lenses in the solid angle Ω between D_L and $D_L + dD_L$, and then dividing by Ω , we obtain the probability that a source undergoes a new microlensing event in the time dt

$$d\tau = \frac{1}{\Omega} \int_0^{D_S} n(D_L) \Omega dA dD_L = 2 \int_0^{D_S} n(D_L) r_E^2 \frac{dt}{t_E} dD_L . \quad (3.58)$$

If we monitor N_\star sources during the time dt , we obtain the expected number of microlensing events observed by multiplying the probability that one source undergoes a microlensing event by the number of stars monitored. Finally, by dividing by the time dt , we obtain the *event rate*:

$$\Gamma = \frac{d(N_\star \tau)}{dt} = \frac{2N_\star}{\pi} \int_0^{D_S} n(D_L) \frac{\pi r_E^2}{t_E} dD_L . \quad (3.59)$$

Assuming that all the Einstein crossing times are identical, we obtain

$$\Gamma = \frac{2N_\star}{\pi t_E} \tau . \quad (3.60)$$

Therefore, if $t_E \approx 19$ days,

$$\Gamma \approx 1200 \text{yr}^{-1} \frac{N_\star}{10^8} \frac{\tau}{10^{-6}} \left(\frac{t_E}{19 \text{days}} \right)^{-1} , \quad (3.61)$$

meaning that by monitoring $\sim 10^8$ stars, we would expect to observe ~ 1200 microlensing events per year. For comparison, the OGLE-IV collaboration, by monitoring 2×10^8 stars in the galactic bulge, detected $\sim 1500 - 2000$ event candidates/year between 2011 and 2017.

Note that while the optical depth does not depend on the mass, the event rate is mass-dependent, because $\Gamma \propto t_E^{-1} \propto M^{-1/2}$. This is very important, because it means that we can use the distribution of event timescales to probe the kinematics of the Milky Way and the stellar population in the galaxy.

3.5 Results from MACHO searches

Since 1991, several collaborations between groups of astronomers around the globe were born with the goal of monitoring the densest regions of stars inside and nearby our galaxy: the bulge and the Small and the Large Magellanic Clouds (SMC and LMC). The main motivation for these observational campaigns was to search for *Massive Astrophysical Compact Halo Objects* (MACHOs), i.e. very faint or invisible compact objects such as black holes, neutron stars, white and brown dwarfs. These compact objects were among the *baryonic* candidates for dark matter, in alternative to weakly interacting particles or WIMPs. As suggested by Paczynski (1986), compact objects in the halo of the galaxy would produce a microlensing signal in addition to that produced by known stellar populations in the galaxy. As discussed earlier, the optical depth for microlensing is very small and the event timescales can vary between fraction of days and hundreds of days. Thus, to have the chance to detect some events, hundreds of millions of stars have to be monitored with a sufficiently short cadence. This requires to build networks of telescopes dedicated to these observations.

The LMC and SMC are the obvious sites that host sources that might be microlensed by MACHOs. The galactic bulge is less interesting for searching MACHOs, but searching for microlensing events in this direction can serve to probe the structure of the galaxy. Lately, MACHOs searches have been extended also towards the galaxy M31 (Andromeda).

A list of some groups working on microlensing is given in Table ???. One of them (OGLE) is still in operation (OGLE IV). Some of the most interesting results found by these groups can be summarized as follows:

- the relatively high rate of detections favored a barred model of the galaxy;
- towards the Magellanic Clouds, no ?short? events (timescales from a few hours up to 20 days) have been seen by any group. This places strong limits on ?Jupiters? in the dark halo: specifically, compact objects in the mass range $10^{-6} - 0.05$ solar masses contribute less than 10% of the dark matter around our Galaxy. This is a very important result, as these objects were previously thought to be the most plausible form of baryonic dark matter, and (for masses below 0.01 solar masses) they would have been virtually impossible to detect directly;
- the detections of microlensing events towards the bulge are most likely caused by known stellar populations. BHs can contribute to 2% of the total mass of the halo. Sumi, Kamiya, et al. (2011) reported however an excess of short events which indicates the presence of free-floating planets in the disk of the Milky Way.

3.6 Astrometric microlensing

While the totality of microlensing events has been observed so far only photometrically, there is another potential way to detect microlensing and to measure the Einstein radius which is becoming possible thanks to the dramatic improvements in the precision of astrometric measurements. The GAIA satellite, for example, is performing micro-arcsecond (μas) global astrometry for nearly 10^9 stars down to magnitude G 20.

Table 3.1: List of some of the collaborations which have undertaken searches for microlensing events from dark-matter candidates.

Group	Target	Operation time	Reference
DUO (Disk Unseen Objects)	Bulge	1994-1997	Alard et al. (1995)
EROS (Experience pour la Recherche d'Objets sombres)	SMC, LMC	1990-2003	http://eros.in2p3.fr
MACHO	Bulge, LMC	1992-2003	http://wwwmacho.anu.edu.au
MOA (Microlensing Observations in Astrophysics)	1995-2013	Bulge, LMC, SMC	http://www.phys.canterbury.ac.nz/moa/
OGLE (Optical Gravitational Lensing Experiment)	1992- <i>now</i>	Bulge, LMC, SMC	http://ogle.astrow.u.edu.pl
POINT-AGAPE (Andromeda Galaxy and Amplified Pixels Experiment)	1999-2006	M31	Paulin-Henriksson et al. (2003)

The idea behind the so-called *astrometric microlensing* is the following (Dominik and Sahu, 1998; Hog, Novikov, and Polnarev, 1995; Miyamoto and Yoshii, 1995; Proft, Demleitner, and Wambsganss, 2011). During the microlensing event, the positions as well as the relative magnifications of the images vary as a function of time. Consequently, the light-centroid of the images will reflect this time variation and will move along a trajectory which can be calculated easily.

First of all, we consider the motion of the images forming outside and inside the Einstein ring in response to the motion of the source. Thus, as done earlier for photometric microlensing, we consider the frame where the lens is fixed and the source is moving. The vector giving the source position as a function of time, $\vec{y}(t)$, has two components, namely $y_{\parallel} = (t - t_0)/t_E$ and $y_{\perp} = y_0$, along and perpendicular to the direction of motion of the source, respectively. The two images always lay on the line passing through the lens and the source. Their distances from the lens in units of the Einstein radius are given in Eq. 3.11. For the images external and internal to the Einstein ring, we have that

$$\begin{aligned} x_{\pm,\parallel} &= \frac{1}{2}(1 \pm Q)y_{\parallel} \\ x_{\pm,\perp} &= \frac{1}{2}(1 \pm Q)y_{\perp}, \end{aligned} \quad (3.62)$$

where

$$Q = \frac{\sqrt{y^2 + 4}}{y}. \quad (3.63)$$

The path of the two images is shown for a source moving on a trajectory with $y_0 = 0.2$ in Fig. 3.6.1.

The corresponding magnifications are given in Eq. 3.18. The light centroid of the images can be computed as

$$\vec{x}_c = \frac{\vec{x}_+ \mu_+ + \vec{x}_- |\mu_-|}{\mu_+ + |\mu_-|}. \quad (3.64)$$

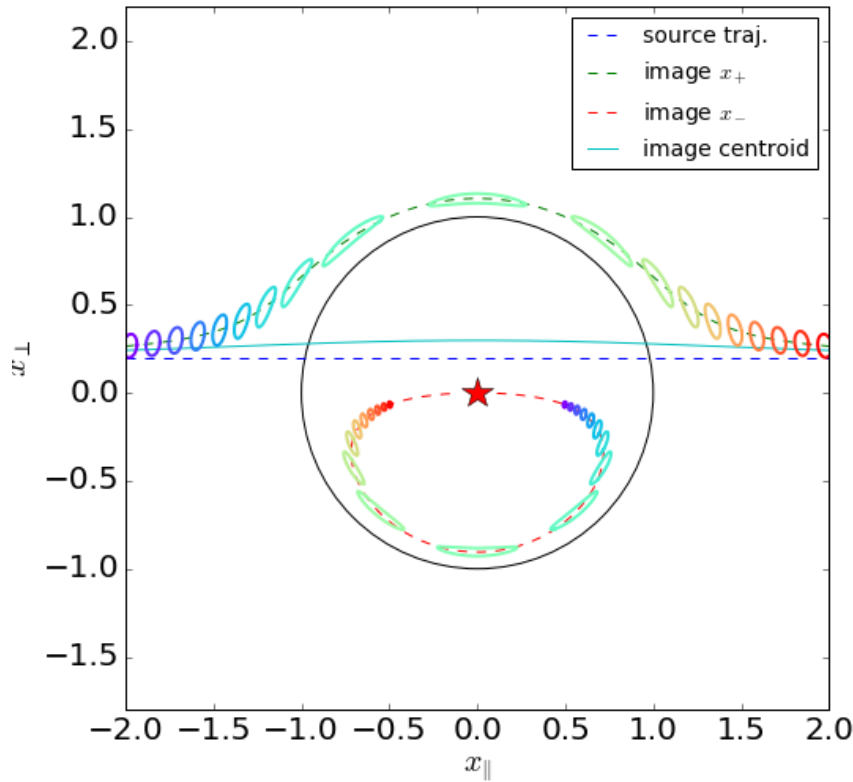


Figure 3.6.1: Illustration of a microlensing event. The source trajectory (corresponding to an impact parameter $y_0 = 0.2$) is given by the dashed line. The red star indicates the lens position in $(0,0)$. The green and the red dashed lines show the trajectories of the images external and internal to the Einstein ring (black circle), respectively. For better visualizing the magnification of the images, we assign to the source a circular shape. As the source moves from left to right, the color of the two images changes from blue to red. Obviously, the size of the external image is always bigger than the size on the internal image, showing that the former will generally provide a larger fraction of the flux. As a consequence, the light centroid will follow a path (cyan solid line) which will differ from the path of the source, being pulled towards the external image.

As discussed in Sect. 3.1, the magnified flux received from the two images is strongly unbalanced in favor of the image external to the Einstein radius for most of the time. Therefore, the light centroid is pulled towards the external image.

In practice, however, we observe microlensing events by monitoring the source, rather than the lens. In other words, the source position is fixed (in the bulge, for example). Therefore, we will not measure the centroid shift with respect to lens, as calculated above. Rather, during the microlensing event, we may observe a centroid moving with respect to the un-lensed source position. This shift is given by

$$\delta \vec{x}_c = \vec{x}_c - \vec{y}. \quad (3.65)$$

As shown in Fig. 3.6.2, this has the characteristic shape of an ellipse. The axis ratio of the ellipse and its extension depend on the impact parameter of the source, y_0 , as it will be discussed below.

Since the lens, the source and the images are aligned on the plane of the sky, \vec{x}_c and \vec{y} in Eq. 3.65

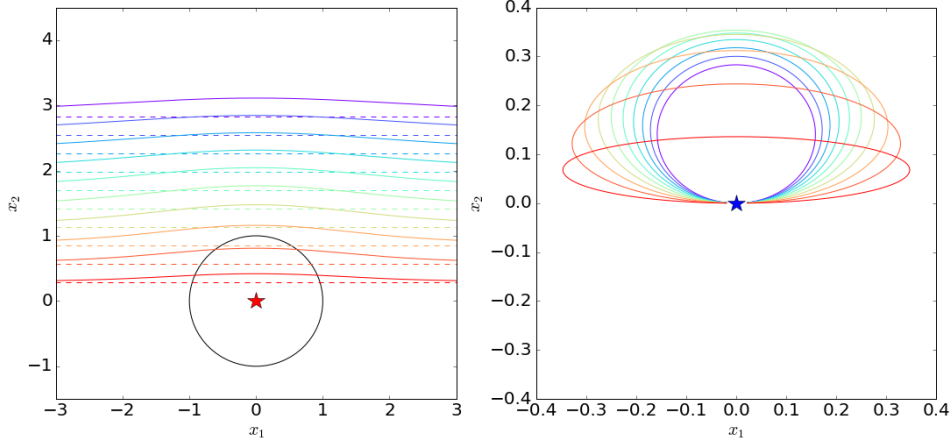


Figure 3.6.2: Left panel: Light centroid trajectories (solid lines) for sources with decreasing impact parameter (from blue to red). The un-lensed source trajectories are given by the dashed lines. Right panel: the corresponding light centroid paths compared to the paths of the un-lensed sources.

are aligned too. Thus, using Eqs. 3.11 and 3.18, we can compute the amplitude of the shift as

$$\begin{aligned} \delta x_c &= \frac{\frac{1}{4} \left[(y + \sqrt{y^2 + 4}) \left(1 + \frac{y^2 + 2}{y\sqrt{y^2 + 4}} \right) - (y - \sqrt{y^2 + 4}) \left(1 - \frac{y^2 + 2}{y\sqrt{y^2 + 4}} \right) \right]}{\frac{y^2 + 2}{y\sqrt{y^2 + 4}}} - y \\ &= \frac{\frac{1}{4} \left(y + \sqrt{y^2 + 4} + \frac{y^2 + 2}{\sqrt{y^2 + 4}} + \frac{y^2 + 2}{y} - y + \sqrt{y^2 + 4} + \frac{y^2 + 2}{\sqrt{y^2 + 4}} - \frac{y^2 + 2}{y} \right)}{\frac{y^2 + 2}{y\sqrt{y^2 + 4}}} - y \\ &= \frac{y}{y^2 + 2}. \end{aligned} \quad (3.66)$$

Given the sign of the result, $\delta \vec{x}_c$ points in the same direction of \vec{y} . An interesting property is that, for $y \gg \sqrt{2}$,

$$\delta x_c \approx \frac{1}{y}, \quad (3.67)$$

meaning that the amplitude of the astrometric microlensing effect decreases with the distance of the source from the lens much slower than the photometric microlensing effect. In addition,

$$\frac{d(\delta x_c)}{dy} = \frac{2 - y^2}{(y^2 + 2)^2}, \quad (3.68)$$

which shows that the shift has a maximum amplitude for $y = \sqrt{2}$, where $\delta x_c = \delta x_{c,max} = (2\sqrt{2})^{-1} \approx 0.354$. Assuming $\theta_E \approx 1$ mas, then $\delta \theta_c = \delta x_c \theta_E \approx 1/3$ mas, which is well above the accuracy of GAIA at least for bright stars in the bulge of the galaxy.

We can now decompose the shift into the components parallel and perpendicular to the source trajectory:

$$\delta x_{c,\parallel} = \frac{y_{\parallel}}{y^2 + 2} = \frac{(t - t_0)/t_E}{[(t - t_0)/t_E]^2 + y_0^2 + 2} \quad (3.69)$$

$$\delta x_{c,\perp} = \frac{y_{\perp}}{y^2 + 2} = \frac{y_0}{[(t - t_0)/t_E]^2 + y_0^2 + 2}. \quad (3.70)$$

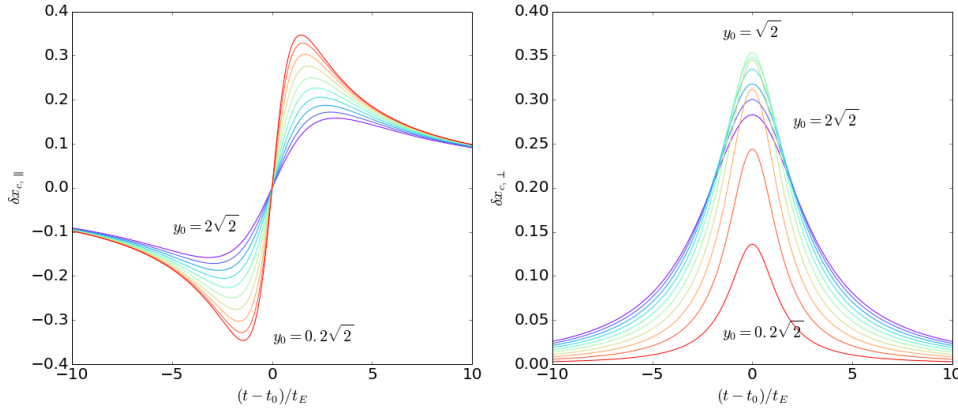


Figure 3.6.3: Components of the light centroid shift as a function of time. The left and the right panels show the shift components parallel and perpendicular to the trajectory of the source, respectively. Different colors are used to illustrate the results for different impact parameters y_0 .

The functions $\delta x_{c,||}(t)$ and $\delta x_{c,⊥}(t)$ are shown in Fig. 3.6.3.

We can see that $\delta x_{c,||}$ is negative for $t < t_0$ and positive otherwise. We define $p \equiv (t - t_0)/t_E$. By taking the derivative with respect to p , we see that

$$\frac{d(\delta x_{c,||})}{dp} = \frac{y_0^2 + 2 - p^2}{(p^2 + y_0^2 + 2)^2}. \quad (3.71)$$

Thus, the function is extremal at the times t_m such that $(t_m - t_0)/t_E = \pm\sqrt{y_0^2 + 2}$, where

$$\delta x_{c,||,min}, \delta x_{c,||,max} = \pm \frac{1}{2\sqrt{y_0^2 + 2}}. \quad (3.72)$$

For $y_0 \ll 1$, the minimum and the maximum occur at $(t_m - t_0)/t_E \approx \pm\sqrt{2}$ and $\delta x_{c,||,min/max} \approx \pm\delta x_{c,max}$.

On the other hand, $\delta x_{c,⊥}$ has a maximum at $(t - t_0)/t_E = 0$, i.e. at $t = t_0$, where it reaches the value

$$\delta x_{c,⊥,max} = \frac{y_0}{y_0^2 + 2}. \quad (3.73)$$

Since $\delta x_{c,||}(t = t_0) = 0$, the shift is only perpendicular to the motion of the source at this time. For $y_0 = \sqrt{2}$, $\delta x_{c,⊥,max}$ reaches its maximum amplitude $\delta x_{c,max}$.

If Fig. 3.6.4, we show how the total amplitude of the centroid shift varies as a function of time for a variety of values of y_0 . We can see that

$$\frac{d(\delta x_c)}{dp} = p \frac{2 - y_0^2 - p^2}{\sqrt{y_0^2 + p^2(y_0^2 + p^2 + 2)^2}}. \quad (3.74)$$

For $y_0 < \sqrt{2}$, $\delta x_c(t)$ has two maxima at t_{max} such that $(t_{max} - t_0)/t_E = \pm\sqrt{2 - y_0^2}$ and one minimum at $t_{min} = t_0$. On the contrary, for $y_0 > \sqrt{2}$, only one maximum exists at $t_{max} = t_0$. These results can be interpreted as follows. For a small impact parameter y_0 , the centroid shift is mainly parallel to the motion of the lens relative to the source, thus two maxima exist, which correspond to the minimum

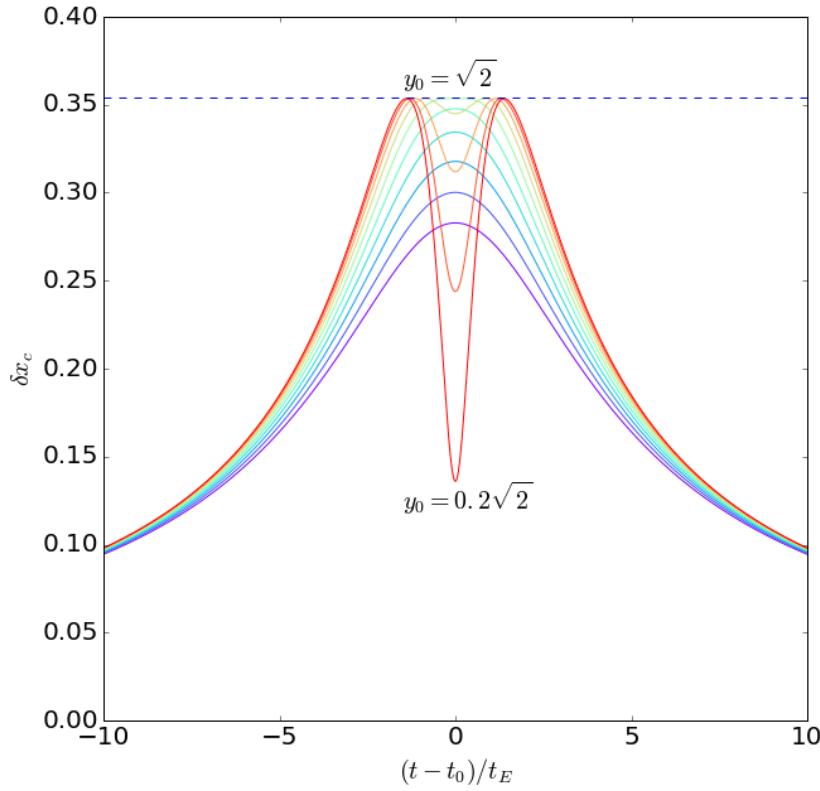


Figure 3.6.4: Total amplitude of the light centroid shift as a function of time. Different colors are used to illustrate the results for different impact parameters y_0 .

and to the maximum of $\delta x_{c,\parallel}$ shown in Fig. 3.6.3. On the contrary, for large impact parameters, the dominant component of the shift is the one perpendicular to the direction of motion of the lens relative to the source, which peaks at $t = t_0$.

When combined, these motions generate the elliptical paths shown in the right panel of Fig. 3.6.2. The ellipses are centered in $(0, y_0)$. Their major-axes and the semi-minor axes are oriented along the δ_{\parallel} and δ_{\perp} directions, respectively. As it results from Eqs. 3.72 and 3.73, their sizes are

$$a = \frac{1}{2} \frac{1}{\sqrt{y_0^2 + 2}} \quad (3.75)$$

$$b = \frac{1}{2} \frac{y_0}{y_0^2 + 2}. \quad (3.76)$$

For $y_0 \rightarrow \infty$, the ellipse degenerates to a circle with radius $r \approx 1/2y_0$ (thus, with size tending to zero). For $y_0 \rightarrow 0$, the ellipse degenerates to straight line, as $b \rightarrow 0$ and $a \rightarrow 1/2$.

Obviously, measuring the size of the ellipse defining the centroid path allows an independent measurement of the Einstein radius. Therefore, the combination of astrometric and photometric microlensing effects allows to break the microlensing degeneracy.

3.7 Multiple point masses

3.7.1 Generalities

Deflection angle

The deflection angle of an ensemble of N point masses was given in Eq. 1.46. Even for such lens, the proper choice of an angular scale allows to write the deflection angle in a convenient form. Generalizing the case of a single point mass, we can define an equivalent Einstein radius for a mass equal to the sum of the point masses, $M_{tot} = \sum_{i=1}^N M_i$. The reduced deflection angle can be written as

$$\vec{\alpha}(\vec{\theta}) = \sum_{i=1}^N \frac{D_{LS}}{D_L D_S} \frac{4GM_i}{c^2} \frac{(\vec{\theta} - \vec{\theta}_i)}{|\vec{\theta} - \vec{\theta}_i|^2} \frac{M_{tot}}{M_{tot}} = \sum_{i=1}^N m_i \frac{\theta_E^2}{|\vec{\theta} - \vec{\theta}_i|^2} (\vec{\theta} - \vec{\theta}_i), \quad (3.77)$$

where we have set $m_i = M_i/M_{tot}$. By further dividing by θ_E , we obtain:

$$\vec{\alpha}(\vec{x}) = \sum_{i=1}^N \frac{m_i}{|\vec{x} - \vec{x}_i|^2} (\vec{x} - \vec{x}_i), \quad (3.78)$$

where $x = \theta/\theta_E$.

Lens equation

The lens equation in the adimensional form then reads

$$\vec{y} = \vec{x} - \sum_{i=1}^N \frac{m_i}{|\vec{x} - \vec{x}_i|^2} (\vec{x} - \vec{x}_i). \quad (3.79)$$

Witt (1990) showed that it is convenient to use the complex notation instead of the vectorial form to write this lens equation. Using this notation, $z = x_1 + ix_2$ and $z_s = y_1 + iy_2$ are the positions on the lens and on the source planes. The complex deflection angle is $\alpha(z) = \alpha_1(z) + i\alpha_2(z)$ which can then be written as

$$\alpha(z) = \sum_{i=1}^N m_i \frac{(z - z_i)}{(z - z_i)(z^* - z_i^*)} = \sum_{i=1}^N \frac{m_i}{z^* - z_i^*}, \quad (3.80)$$

where the * symbol denotes the complex conjugate. The lens equation is

$$z_s = z - \sum_{i=1}^N \frac{m_i}{z^* - z_i^*}. \quad (3.81)$$

By taking the complex conjugate of both sides, we can then solve for z^* :

$$z^* = z_s^* + \sum_{i=1}^N \frac{m_i}{z - z_i}. \quad (3.82)$$

This can be inserted into Eq. 3.81 to obtain a complex polynomial equation of degree $N^2 + 1$. Thus, the lens equation formally have up to $N^2 + 1$ solutions, some of which may, however, be spurious. Rhie (2001); Rhie (2003) probed that, in fact, a lens composed of $N > 3$ point masses produces a maximum of $5(N - 1)$ images.

Critical lines

To find the critical lines, we first need to compute the determinant of the lensing Jacobian. In Sect. 2.3, this was found to be

$$\det A = \frac{\partial y_1}{\partial x_1} \frac{\partial y_2}{\partial x_2} - \left(\frac{\partial y_1}{\partial x_2} \right)^2. \quad (3.83)$$

Using the complex differential operators, we see that

$$\frac{\partial z_s}{\partial z} = \frac{1}{2} \left(\frac{\partial}{\partial x_1} - i \frac{\partial}{\partial x_2} \right) (y_1 + iy_2) = \frac{1}{2} \left(\frac{\partial y_1}{\partial x_1} + \frac{\partial y_2}{\partial x_2} \right) + \frac{i}{2} \left(\frac{\partial y_2}{\partial x_1} - \frac{\partial y_1}{\partial x_2} \right) \quad (3.84)$$

$$\frac{\partial z_s}{\partial z^*} = \frac{1}{2} \left(\frac{\partial}{\partial x_1} + i \frac{\partial}{\partial x_2} \right) (y_1 + iy_2) = \frac{1}{2} \left(\frac{\partial y_1}{\partial x_1} - \frac{\partial y_2}{\partial x_2} \right) + \frac{i}{2} \left(\frac{\partial y_2}{\partial x_1} + \frac{\partial y_1}{\partial x_2} \right). \quad (3.85)$$

The imaginary part of Eq. 3.84 is zero, because $\partial y_1 / \partial x_2 = \partial y_2 / \partial x_1$. Thus,

$$\left(\frac{\partial z_s}{\partial z} \right)^2 = \frac{1}{4} \left[\left(\frac{\partial y_1}{\partial x_1} \right)^2 + \left(\frac{\partial y_1}{\partial x_2} \right)^2 + 2 \frac{\partial y_1}{\partial x_1} \frac{\partial y_2}{\partial x_2} \right] \quad (3.86)$$

and

$$\left(\frac{\partial z_s}{\partial z^*} \right) \left(\frac{\partial z_s}{\partial z^*} \right)^* = \frac{1}{4} \left[\left(\frac{\partial y_1}{\partial x_1} \right)^2 + \left(\frac{\partial y_1}{\partial x_2} \right)^2 - 2 \frac{\partial y_1}{\partial x_1} \frac{\partial y_2}{\partial x_2} \right] + \left(\frac{\partial y_1}{\partial x_2} \right)^2. \quad (3.87)$$

By taking the difference of Eqs. 3.86 and 3.87, we obtain that

$$\left(\frac{\partial z_s}{\partial z} \right)^2 - \left(\frac{\partial z_s}{\partial z^*} \right) \left(\frac{\partial z_s}{\partial z^*} \right)^* = \frac{\partial y_1}{\partial x_1} \frac{\partial y_2}{\partial x_2} - \left(\frac{\partial y_1}{\partial x_2} \right)^2 = \det A \quad (3.88)$$

Using the lens equation in the form given in Eq. 3.81, we finally see that

$$\frac{\partial z_s}{\partial z} = 1 \quad (3.89)$$

and

$$\frac{\partial z_s}{\partial z^*} = \sum_{i=1}^N \frac{m_i}{(z^* - z_i^*)^2}. \quad (3.90)$$

Thus,

$$\det A = 1 - \left| \sum_{i=1}^N \frac{m_i}{(z^* - z_i^*)^2} \right|^2. \quad (3.91)$$

It follows that the critical lines are defined by

$$\left| \sum_{i=1}^N \frac{m_i}{(z^* - z_i^*)^2} \right|^2 = 1. \quad (3.92)$$

The sum in the above equation must be satisfied on the unit circle. The complex solutions of this equation can be found by solving

$$\sum_{i=1}^N \frac{m_i}{(z^* - z_i^*)^2} = e^{i\phi} \quad (3.93)$$

for each $\phi \in [0, 2\pi)$. The above equation is a complex polynomial of order $2N$ with respect to z . Thus, for each value of ϕ , there are $2N$ or less critical points. By varying ϕ continuously, the solutions will trace out $2N$ (or less) critical lines. Critical lines corresponding to different solutions may join smoothly (see e.g. Witt, 1990). Note that for $N = 1$, $m_1 = 1$ and, by taking $z_1 = 0$, we obtain that the critical line is the Einstein ring ($|z| = 1$). In the case of multiple point masses, however, the critical lines are much more complicated, as we will see in the next Section.

As usual the critical lines can be mapped onto the source plane through the lens equation. This will give the caustics.

3.7.2 Binary lenses

Lens equation

The binary lens is a particular case of multiple point mass lenses, where $N = 2$. In this case, the lens equation is

$$z_s = z - \frac{m_1}{z^* - z_1^*} - \frac{m_2}{z^* - z_2^*}. \quad (3.94)$$

Since the choice of the reference frame is arbitrary, we may opt for selecting the real axis to pass through the two lenses. We may further set $z_2 = -z_1$.

As discussed in the previous Section, the lens equation for the binary lens can be reduced to a complex polynomial equation of degree 5:

$$c_0 + c_1 z + c_2 z^2 + c_3 z^3 + c_4 z^4 + c_5 z^5 = 0, \quad (3.95)$$

where

$$\begin{aligned} c_0 &= z_1^2 [4(\Delta m)^2 z_s + 4m\Delta m z_1 + 4\Delta m z_s z_s^* z_1 + 2m z_s^* z_1^2 + z_s z_s^* z_1^2 - 2\Delta m z_1^3 - z_s z_1^4] \\ c_1 &= -8m\Delta m z_s z_1 - 4(\Delta m)^2 z_1^2 - 4m^2 z_1^2 - 4m z_s z_s^* z_1^2 - 4\Delta m z_s^* z_1^3 - z_s^* z_1^4 + z_1^6 \\ c_2 &= 4m^2 z_s + 4m\Delta m z_1 - 4\Delta m z_s z_s^* z_1 - 2z_s z_s^* z_1^2 + 4\Delta m z_1^3 + 2z_s z_1^4 \\ c_3 &= 4m z_s z_s^* + 4\Delta m z_s^* z_1 + 2z_s^* z_1^2 - 2z_1^4 \\ c_4 &= -2m z_s^* + z_s z_s^* - 2\Delta m z_1 - z_s z_1^2 \\ c_5 &= z_1^2 - z_s^* z_1^2. \end{aligned} \quad (3.96)$$

In the above equations we have introduced $\Delta m = (m_1 - m_2)/2$ and $m = (m_1 + m_2)/2$ (Witt and Mao, 1995).

Critical lines and caustics

It can be shown that Eq. 3.95 has 3 or 5 images depending on the distance between the two point masses and on their mass ratio. This can be better understood by looking at the structure of the critical lines and caustics. The critical lines can be found as explained above by solving the Eq. 3.93. In the case of the binary lens, this assumes the form

$$\frac{m_1}{(z^* - z_1^*)^2} + \frac{m_2}{(z^* - z_2^*)^2} = \frac{m_1}{(z^* - z_1^*)^2} + \frac{m_2}{(z^* + z_1^*)^2} = e^{i\phi} \quad (3.97)$$

for $\phi \in [0, 2\pi)$. By getting rid of the fractions, the equation can be turned into

$$z^4 - z^2(2z_1^{*2} + e^{i\phi}) - z z_1^{*2}(m_1 - m_2)e^{i\phi} + z_1^{*2}(z_1^{*2} - e^{i\phi}) = 0. \quad (3.98)$$

The left side is a fourth degree polynomial. Thus, for each ϕ there are up to four solutions of this equation.

In the python application in Sect. 3.9.5 we show how to find the solutions of the above equation and to derive the critical lines of the binary lens. The critical points are mapped onto the caustics

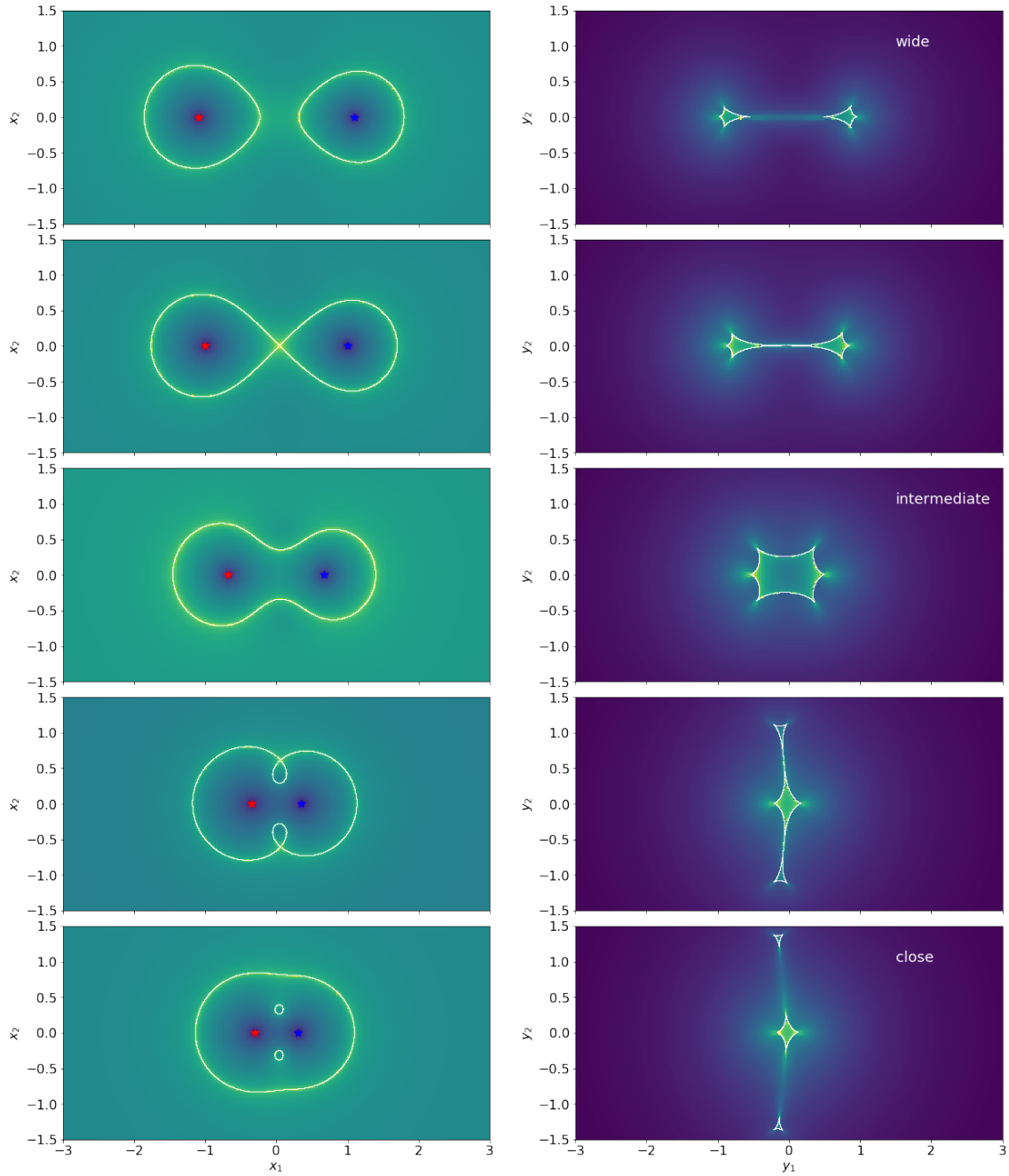


Figure 3.7.1: Critical lines (left panels) and caustics (right panels) of a binary lens system for different values of the separation between the point masses, d . From the top to the bottom, we show examples of wide, intermediate, and close topologies. The results refer to the case of a lens with $M_1 = 1M_{\odot}$ and $q = 0.8$. The critical lines and the caustics are overlaid to the maps of the magnification on the lens and on the source planes, respectively.

via the lens equation. Depending on the ratio of the two masses, $q = m_1/m_2$, and on the separation between the two lenses in units of the equivalent Einstein radius, $d = |z_1 - z_2|$, the resulting caustics can be one, two, or three.

We distinguish between wide, intermediate, and close systems on the basis of the topology of the caustics, as shown in Fig. 3.7.1. More precisely:

- in wide systems, there exist two separate extended caustics, which correspond to the point-

like caustics associated with the individual lenses. The shape of the caustics resemble that of an astroid with four cusps. This is the result of the reciprocal perturbation of each lens. Indeed, the presence of two masses breaks the symmetry of the point-mass lens. The wide topologies are typical of binary systems with large separations between the two lenses;

- in intermediate systems, there exist a single caustic, characterized by six cusps. This caustic is the result of the merging of the two individual astroid-like caustics in wide systems, which happens when the lenses are brought closer to each other (or when the masses of the individual lenses are increased, thus making the equivalent Einstein radius bigger, and reducing d);
- finally, in close systems, there are three caustics. Two have triangular-like shapes and one is an astroid-like caustic with four cusps. The triangular shape caustics are at equal distance from the axis connecting the two lenses. In binary lenses with $q \sim 1$, they are located nearly on an axis passing also through the central caustic.

The transitions between these topologies occur when two critical lines merge at one point (Mollerach and Roulet, 2002). This happens where, not only $\det A = 0$, but also $\partial \det A / \partial z^* = 0$ (the gradient of the Jacobian determinant is zero). These are saddle points of the *surface* $\det A(\vec{\theta})$. In particular, it can be shown that the transition between wide and intermediate regimes occurs for a separation between the lenses (in units of the equivalent Einstein radius) of

$$d_{WI} = (m_1^{1/3} + m_2^{1/3})^{3/2}. \quad (3.99)$$

On the other hand, the transition between intermediate and close regimes occurs when

$$d_{IC} = (m_1^{1/3} + m_2^{1/3})^{-3/4}. \quad (3.100)$$

A detailed discussion about caustic topologies in binary lenses is presented in Erdl and Schneider (1993).

If q significantly differs from unity, i.e. one mass component is dominant over the other, the shape of the caustics changes as shown in Fig. 3.8.1. In particular:

- in wide lenses, the caustic of the primary (i.e. most massive) component is smaller than the caustic of the secondary. In addition, it is highly asymmetric and elongated towards the secondary. The two caustics are shifted towards the the primary lens.
- in intermediate lenses, the caustic is thinner on the side of the primary and fatter on the side of the of the secondary;
- in close lenses, the triangular caustics are located behind the primary lens, opposite to the secondary lens. They are still equidistant from the axis passing through the two point masses.

Multiple images

Solving Eq. 3.95 leads to finding the multiple images of a source at z_s . This must be done numerically, as illustrated in Sect. 3.9.6. Here, we give some brief and qualitative statements about the occurrence of multiple images.

- a source outside the caustics has only three images, meaning that two solution of the lens equation are spurious. Two of these images form inside the critical lines and, for large distances of the source from the binary lens, their positions are very close to the two point masses. This is very similar to the behavior of the image with negative parity in the case of the point-mass lens (see Eq. 3.11). The image outside the critical lines correspond to a local minimum of the time-delay surface, and have positive parity;
- when the source is on the caustic, two additional images appear on the critical line (thus they are formally indistinguishable and have infinite magnification);
- when the source is inside the caustics, five images exist.

- R** Note that, due to the singularity of lensing potential of the two point-masses, there are always at least three images of a single source.

The above statements can be verified by looking at Fig. 3.7.2. In the left panel, we show the critical lines of a binary lens. The case chosen corresponds to values of $q = 1$ and $d = 1$, respectively. The corresponding caustics are shown in the right panel, where we also display the trajectory of a source in motion relative to the binary lens. A color sequence is used to indicate the source position as a function of time. The images, which are also color-coded, are shown in the left panel.

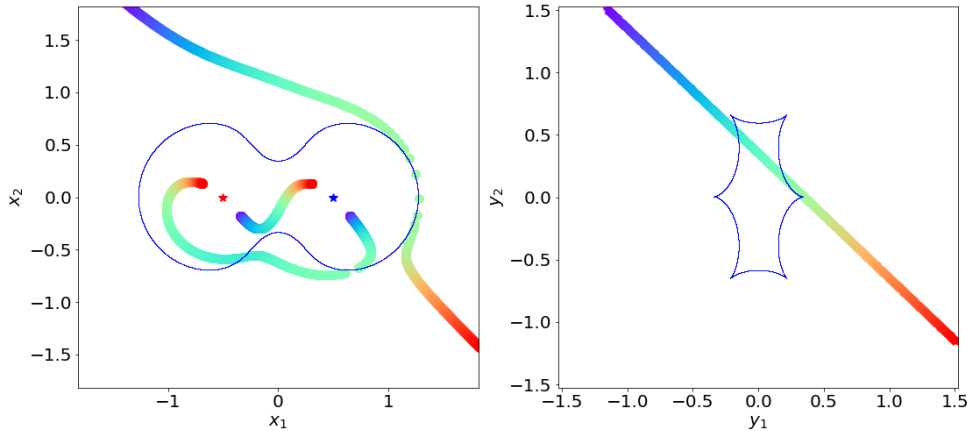


Figure 3.7.2: Images of a source in relative motion with respect to a foreground binary lens. In the right panel, the caustics of the lens and the trajectory of the source are shown. We color-code the source position as a function of time. The corresponding images are shown in the left panel, together with the lens critical line. The binary lens is made of two stars of equal mass at a distance $d = 1$, thus the caustic is resonant.

The source trajectory crosses the lens caustics at two points. Let us call the corresponding crossing times t_1 (light blue) and t_2 (green). Before t_1 and after t_2 , there are three images of the background source. Between t_1 and t_2 , the images are five. In particular, two images appear at the time t_1 on the lens critical line. While the source moves across the caustic, one of the images moves outside the critical line, while the other follows a trajectory which brings it near the star of mass m_1 . The outer image approaches the critical line again at t_2 , when it merges with one of the inner images. The two images disappear once the source has crossed the caustic again.

Image magnifications and light-curves

As in the case of microlensing by single lenses, the multiple images are not spatially resolved. Thus, the microlensing events involving binary lenses are also revealed through variations of the source luminosity. The shape of the source light curves, however, have much more complex shapes compared to the case of the single point-mass lens².

The shape of the light curve reflects how the sum of the magnifications of the images changes as a function of time:

$$\mu(t) = \sum_{j=1}^{N_{ima}} |\mu_j(t)| . \quad (3.101)$$

²Even in the case of binary lenses, microlensing events produce astrometric signatures.

The magnification of image j is obtained by inserting the image position $z_j(t)$ in Eq. 3.91:

$$\mu_j(t) = \left[1 - \left| \sum_{i=1}^N \frac{m_i}{z_j^*(t) - z_i^*} \right|^2 \right]^{-1}. \quad (3.102)$$

In Sect. 3.9.7 we discuss how to compute the light-curve of a source in the background of a binary lens. The shape of the light curve reflects the pattern of the magnification along the trajectory of the source. In the left panel of Fig. 3.7.1, the caustics are overlaid to the maps of the magnification on the source plane (the maps in the left panels show the magnification on the image plane instead). This is the total source magnification, computed at each position using Eq. ???. Some features of the magnification maps are important to remind:

- lobes of high magnification surround the cusps of the caustics. Thus, when they pass near the cusps, sources will experience high magnifications, which are expected to produce bumps in their light curves;
- the folds of the caustics mark sharp transitions in magnification from outside to inside the caustics. The magnification rises suddenly when a source crosses the caustics fold, declines more gently while the source is inside the caustic, before rising again when the source approaches another fold. Then, after crossing the fold, the magnification drops. Because of the magnification pattern, caustic crossings appear in the light curves as sharp transitions characterized by asymmetric profiles. Witt and Mao (1995) showed analytically that, while the source is inside the caustic, the total magnification cannot be smaller than 3;
- extended regions of high magnification are present along the direction connecting the caustics of wide and close lenses. Therefore, the passage of the source in between caustics also produces a bump in the light curve.

We show in Fig. 3.7.3 the light-curve corresponding to the example in Fig. 3.7.2. This shows a source moving past a six-cusp caustic in an intermediate lens. As discussed, the signatures of the passage of a source across the caustic are two very sharp spikes in the light-curve. In between them the light curve has a characteristic “U”-shape. The passage of the source near the cusp of the lens produces another single bump in the light curve.

Finite source-size effects affect the sharpness of these transitions in the light-curves. Indeed, if the size of the source is not negligible the light-curve appears smoothed, while the event lasts longer (as the result of the fact that the source takes more time to cross the fold of the caustic). Because of the more extended size of the caustics, finite source size effects are more easily detected in binary lenses than in single lenses (where they can only be detected if the impact parameter y_0 is very small). As discussed earlier, such effects are important to constrain the size of the caustics and derive θ_E , helping to break the model degeneracies.

3.8 Planetary microlensing

A system made of a planet orbiting a star is a particular kind of binary lens, where the mass budget is dominated by the star. For Jupiter-like planet orbiting a solar mass star $q \sim 10^{-3}$. Conversely, for an Earth-like planet $q \sim 3 \times 10^{-6}$. Given the small mass ratio, for most of the time, the light-curve is very similar to the standard microlensing light-curve by a single star. The presence of a secondary lens (the planet) produces localized perturbations to the magnification pattern, which can be revealed through short-time variations of the standard light-curve. The features produced by the planet have shapes which strongly depend on the trajectory of the source with respect to the lens.

Perturbations of the central caustic

As discussed earlier, the shape of the caustic matters. Also in the case of planetary microlensing, three types of caustic (and critical line) topologies are possible: wide, intermediate (or resonant),

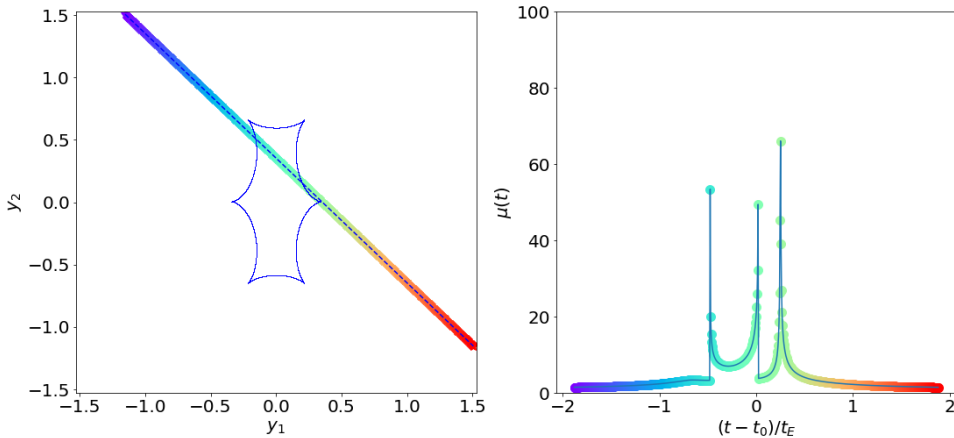


Figure 3.7.3: Light-curve of the source whose multiple images are shown in Fig. 3.7.2.

and close. In Fig. 3.8.1 we show how the caustics and an the critical lines of a binary lens change when we keep d fixed and we vary the mass ratio q . The three examples shown refer to the three topologies. In the case of a wide system (left column), the caustic of the primary (i.e. most massive) component becomes smaller and smaller as q decreases. In addition, the angular distance between the lens and this caustic becomes smaller. This is not surprising: as long as the two masses are well separated, putting most of the mass into one of the two lenses makes the overall system very similar to a single point-mass lens. Similarly, bringing the star and the planet close to each other, the central caustic shrinks (close topology).

Because of the small value of q , the central caustics are very elongated in the direction of the planet. Indeed, they are characterized by a pronounced cusp. Three additional cusps are located on the back of the caustic with respect to the planet. The insets in Fig. 3.8.1 show that, for $q \ll 1$, there is a degeneracy between close and wide topologies in terms of the shape of the central caustic. In fact, close and wide systems where $d_c = d_w^{-1}$ (as in the examples shown in the left and in the right panels) have identical central caustics. Thus, the planet signatures in the light-curve in central caustic events do not allow to distinguish between wide and close topologies (wide-close degeneracy).

Fig. 3.8.2 is analogous to Fig. 3.7.1 but refers to the case of a star-planet system where the primary lens has mass $M_1 = 1M_\odot$ and $q = 10^{-3}$. The magnification maps in the right panels show some interesting features that are important to interpret the shape of the light curves. In particular, they show that in close and wide systems the back of the central caustic is a region of de-magnification. Dips in the light curves are therefore strong indications of the presence of a planet.

In Fig. 3.8.3, we show some examples of the effects of the central caustic perturbations by planets on the source light-curve. The source trajectory is given by the dotted line in each of the left panels. The central panels zoom over the central caustic. The source trajectory is indicated here by a color-sequence, which allows to read-off where the source is located at the time when a perturbation of the light-curve is detected in the right panels. From the upper to the lower panels, the source trajectory is such to pass behind, across, or in front of the central caustic (with the respect to the position of the planet, which is given by the blue dot in the left panels). The standard light curve, i.e. the light curve which could be measured in absence of the planet is given by the dashed black lines in the right panels.

When the source passes behind the central caustic (upper panels), we first see a negative

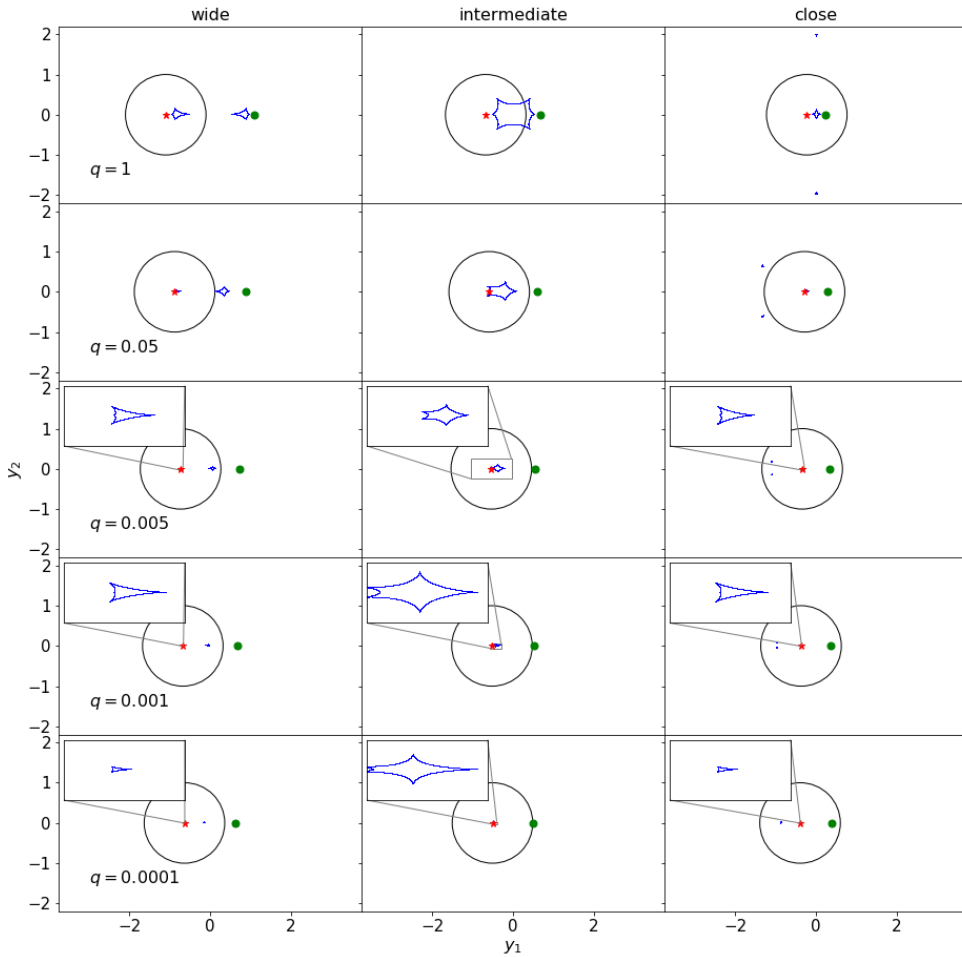


Figure 3.8.1: Caustics of a binary lens for different values of the mass ratio q . The left, central, and right panels refer to wide, intermediate, and close topologies, respectively. In each panel the two mass components are indicated with a red star and with a circle. In the cases with $q \ll 1$, the green circle represents a planet-like mass. The equivalent Einstein radius is given by the black circle in each panel. The insets show zooms over the central caustics.

perturbation (with respect to the standard light-curve), followed by positive perturbation of the light-curve. In the case where the source crosses the caustic (middle panels), we see two peaks in the light curve, which occur at the times when the source enters and exits the central caustic. Finally, in the case when the source passes in front of the pronounced cusp, which is a location where the magnification is particularly strong, we see a single, sharp peak in the light curve (bottom panels).

It is worth noticing that all these perturbations are near the peak of the light-curve, i.e. they occur in an high-magnification regime. This is particularly relevant in terms of event detectability. In some sense, events like these are predictable, because the primary microlensing event can be revealed earlier than the planet perturbation appears. If the search strategy consists of detecting the primary event and triggering a follow-up (as in the first generation of microlensing surveys),

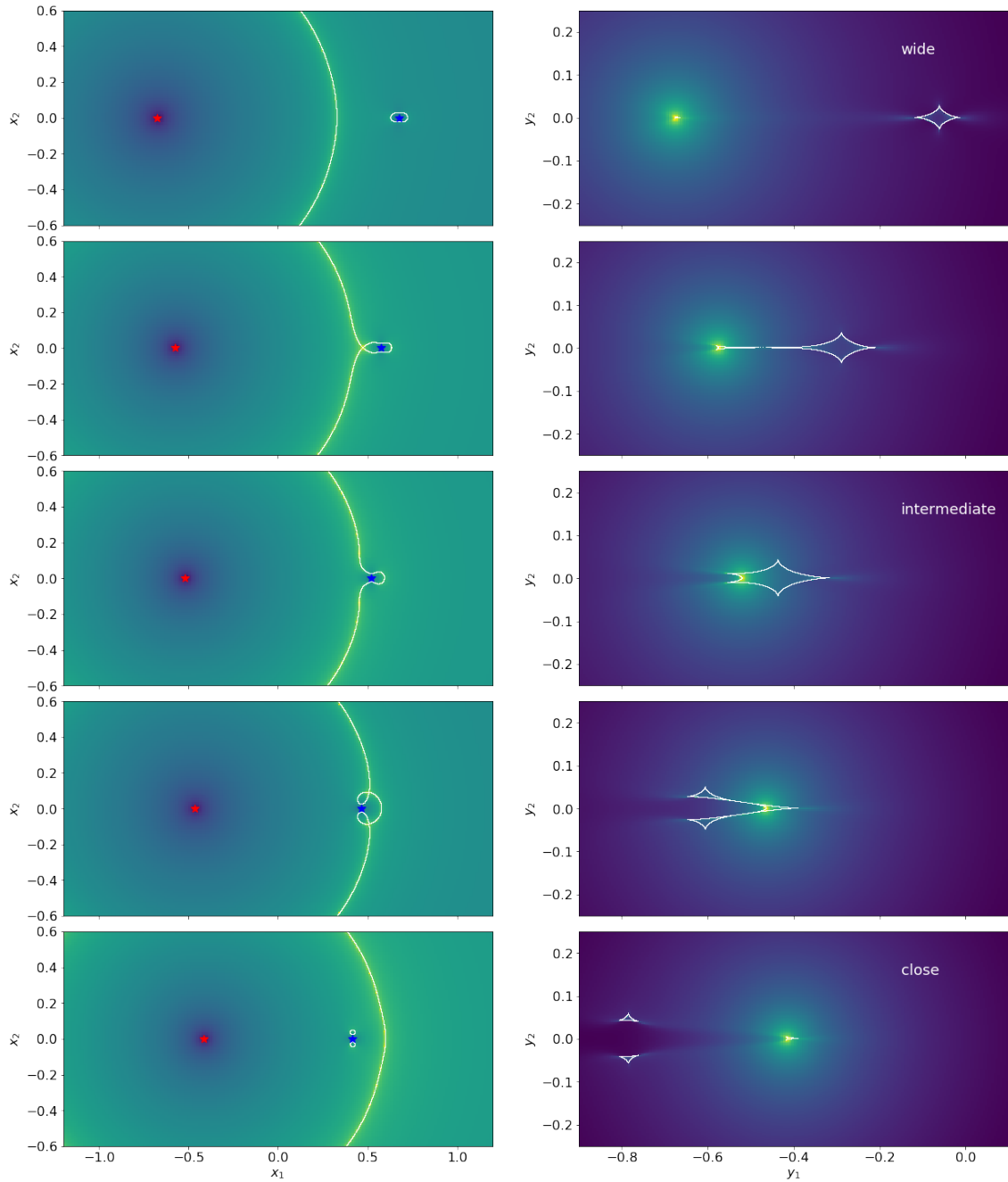


Figure 3.8.2: As in Fig. 3.7.1, but for the case of a lens with $M_1 = 1M_\odot$ and $q = 10^{-3}$.

the cadence at which the light-curve is monitored can be adjusted such to make the detection of such planet perturbations possible. In addition, since they occur in high-magnification regimes, photometric measurements in such events can be more accurate (Gaudi, 2012).

Perturbations of the planetary caustic

Another way to detect the presence of a planet around a star is by means of signatures of the planetary caustics. These are located at a distance from the central caustic (which in turn is roughly coincident with the projected position of the host star) which can be estimated from the lens equation: if the planet is at distance d from the host star, then the distance between the planetary and the central caustic is $\sim |d - d^{-1}|$.

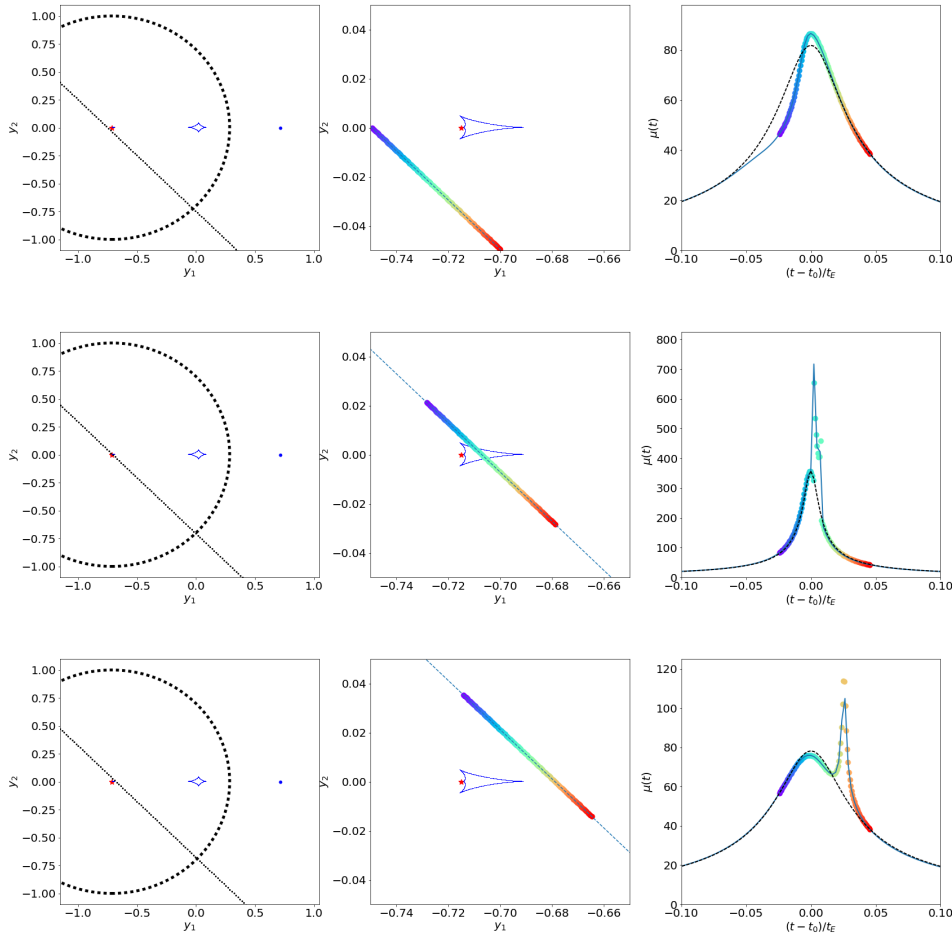


Figure 3.8.3: Central caustic perturbations by planets.

In wide topologies, the planetary caustic is an astroid-like caustic with four cusps. Han (2006) showed that the size of this caustic scales as $\sim q^{1/2}d^{-2}$. Signatures of this caustic in the light-curve are single- or double-peaks occurring when the source passes close to a cusp or across the caustic. Some example of these perturbations are shown in the upper panels of Fig. 3.8.4. The perturbations can be detected near the peak of the primary light curve, if the source trajectory is nearly perpendicular to the axis of the binary lens, in the wings otherwise. The impact parameter y_0 is larger than in the case of central caustic events. For this reason, planetary caustic events occur in low- to medium-magnification regimes.

In close topologies, there are two triangular planetary caustics, which are located on the opposite side of the star with respect to the planet (see the bottom panels in Fig. 3.8.4). The positions of the two caustics is symmetric with respect to the axis passing through the star and the planet. Han (2006) showed that the size of the triangular caustics scales as $\sim q^{1/2}d^3$. The separation between the two caustics is $\sim 2q^{1/2}(d^{-2}-1)^{1/2}$, and their distance from the star is $\sim d^{-1}-d$. The signatures of these caustics in the source-light curve can be single or double peaks corresponding to the cases where the source passes near the cusps or across the caustics. In addition, the region in between the two triangular caustics is characterized by a relatively low magnification, as shown in Fig. 3.8.2. Thus, a dip in the light-curve, with respect to the primary microlensing event, can be seen if the source trajectory passes near these planetary caustics and crosses the axis of the binary lens.

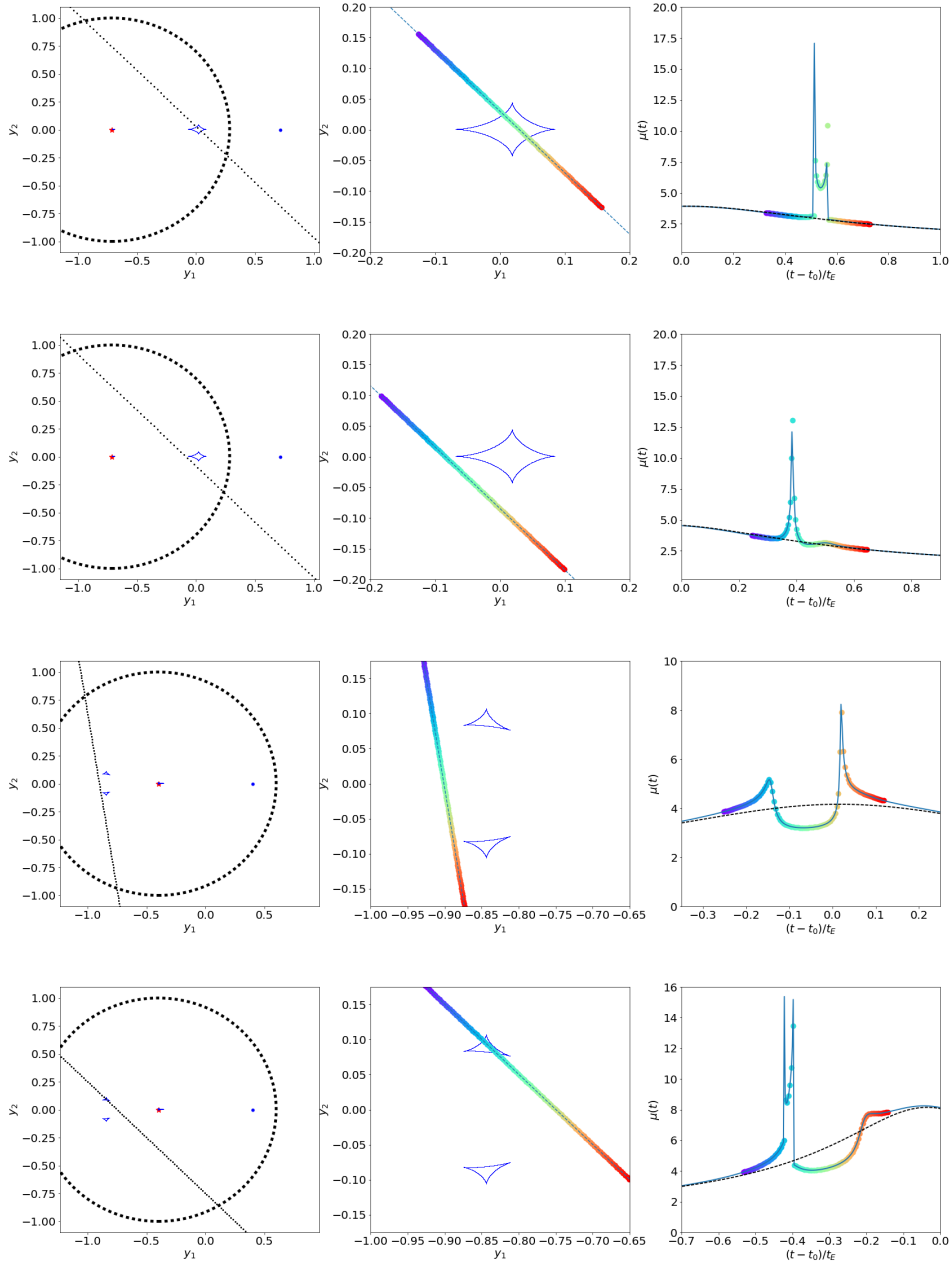


Figure 3.8.4: Planetary caustic perturbations of the light-curves.

R De-magnifications are signatures of planets.

Perturbations of the resonant caustic

For $q \ll 1$, intermediate (or resonant) caustics are possible only for a narrow range of separations. This can be shown as follows. Let us consider the transition between wide and intermediate topologies, which occurs for $d_{WI} = (m_1^{1/3} + m_2^{1/3})^{3/2}$. Some simple algebra shows that

$$d_{WI} = (1 + q^{1/3})^{3/2} m_1^{1/2}. \quad (3.103)$$

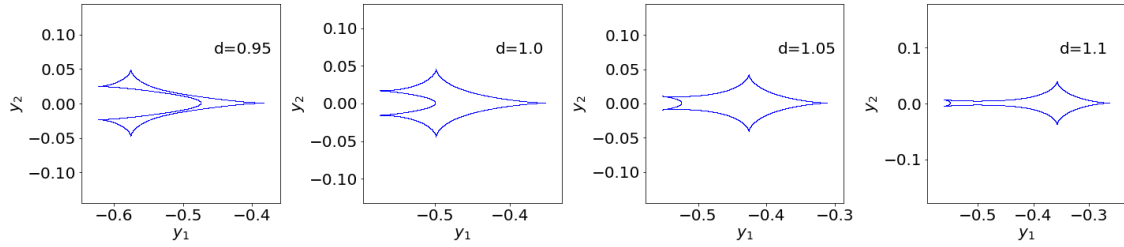


Figure 3.8.5: Shape of the resonant caustic of a star-planet lens with $q = 10^{-3}$ for several values of d .

We recall that d is the angular separation between the two masses in units of the equivalent Einstein radius, θ_E , which is in turn related to the Einstein radius of the primary by

$$\theta'_E = m_1^{1/2} \theta_E. \quad (3.104)$$

Thus, the separation between the star and the planet at the transition between wide and intermediate topologies, in units of the Einstein radius of the star, is

$$d'_{WI} = d_{WI}/m_1^{1/2} = (1 + q^{1/3})^{3/2} \sim 1 + 3/2q^{1/3}. \quad (3.105)$$

Similarly, since $d_{IC} = (m_1^{1/3} + m_2^{1/3})^{-3/4}$, we obtain that

$$d'_{IC} = d_{IC}/m_1^{-1/4} = (1 + q^{1/3})^{-3/4} \sim 1 - 3/4q^{1/3}. \quad (3.106)$$

Therefore, the range of distances between the star and the planet for which the caustic is resonant is

$$d'_{WI} - d'_{IC} \sim \frac{9}{4}q^{1/3}, \quad (3.107)$$

Obviously, this range is very narrow for small values of q .

R For a given q , even small changes of d have dramatic effects on the shape of the resonant caustic. This is shown in Fig. 3.8.5 for a star-planet lens with $q = 10^{-3}$. Consider a source that enters the resonant caustic at the time t . Due to the relatively large extension of the caustic, the time $\Delta t = t' - t$ needed to the source to exit the caustic can be long enough that in the meanwhile d has changed because of the orbital motion of the planet. Consequently the overall shape of the resonant caustic has changed too. Thus, in such cases, it is possible to detect signatures of the orbital motion of the planet (see e.g. Gaudi et al., 2008)

Some examples of light-curve perturbations by a resonant caustic are shown in Fig. ???. The passage of the source in front, across, or behind the caustic correspond to either positive or negative deviations from the standard light curve. These perturbations are located near the peak of the standard light curve, and, because the caustic is close to the star, these events occur in intermediate-to high-magnification regimes.

One important property of the resonant caustic is that it is generally weak, as shown in Fig. ???. As the source approaches the caustic folds, the magnification rises sharply (see the middle panels of Fig. ??). However, such short magnification boosts can be washed-out by finite source size effects, resulting to be difficult to be detected.

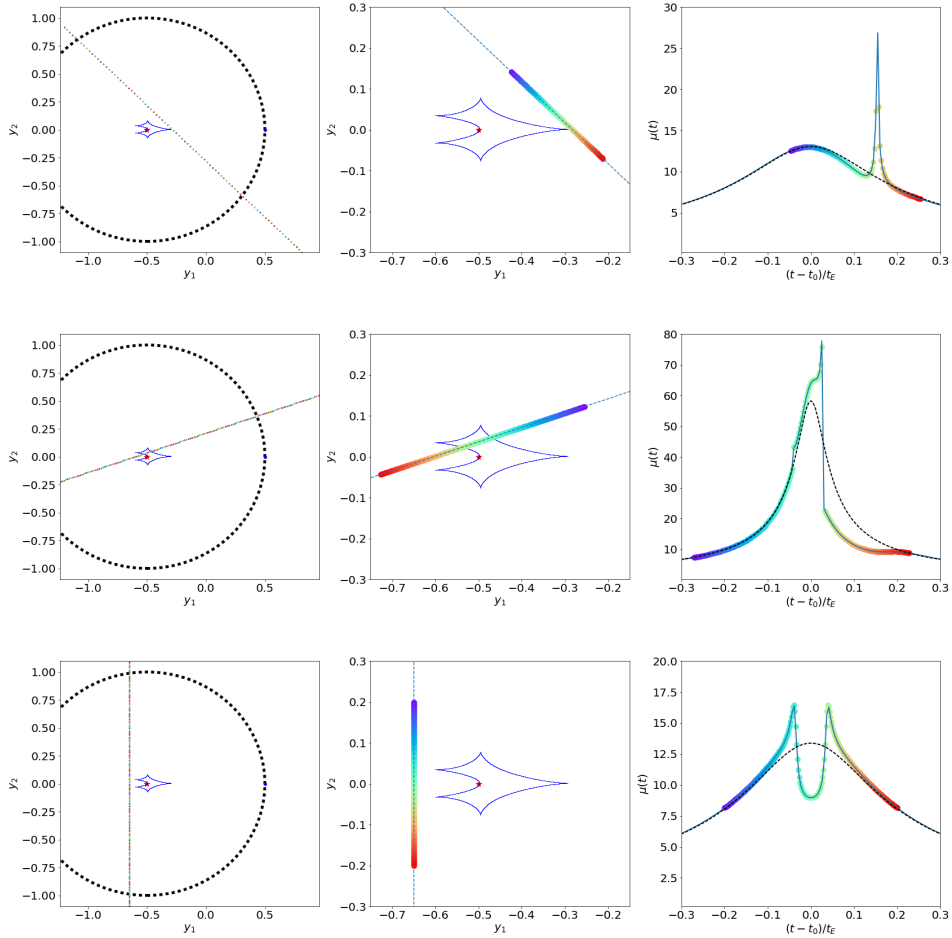


Figure 3.8.6: Resonant caustic perturbations of the light-curves.

Perturbations of the inner and outer images

As discussed above, during a planetary microlensing event, we detect anomalies in the standard light-curve of the primary microlensing event produced by the star. While we have learned that the anomalies are produced by the source passing near or across the central or the planetary caustics, we show now that the anomalies are the result of the perturbation of either the inner or the outer images in the primary microlensing events.

Some examples are shown in Fig. ???. The upper panels refer a wide caustic topology, as shown in the left panel. We consider the positions of the source at different times along its trajectory, indicated with different colors. The trajectory is such that the source crosses the planetary caustic (see green color). The source images and the critical lines are shown in the second panel. When the source is far from the planet, it has two images, one inside and one outside the Einstein ring of the host star. In the third panel, we zoom over the planetary critical line. For illustration purposes, we have assumed that the source has circular shape and that its radius is $r = 0.01\theta_E$. Thus, also the images are extended and we can appreciate their distortion and magnification. When the source is inside the planetary caustic, the outer image is clearly affected by the planet. Specifically, it is split into additional multiple images. Therefore, the anomaly in the source light curve, which is shown in the right panel, is the consequence of the perturbation by the planet of the outer image in the primary microlensing event.

Similarly, the middle panels show the planetary perturbation of the inner image in the case of

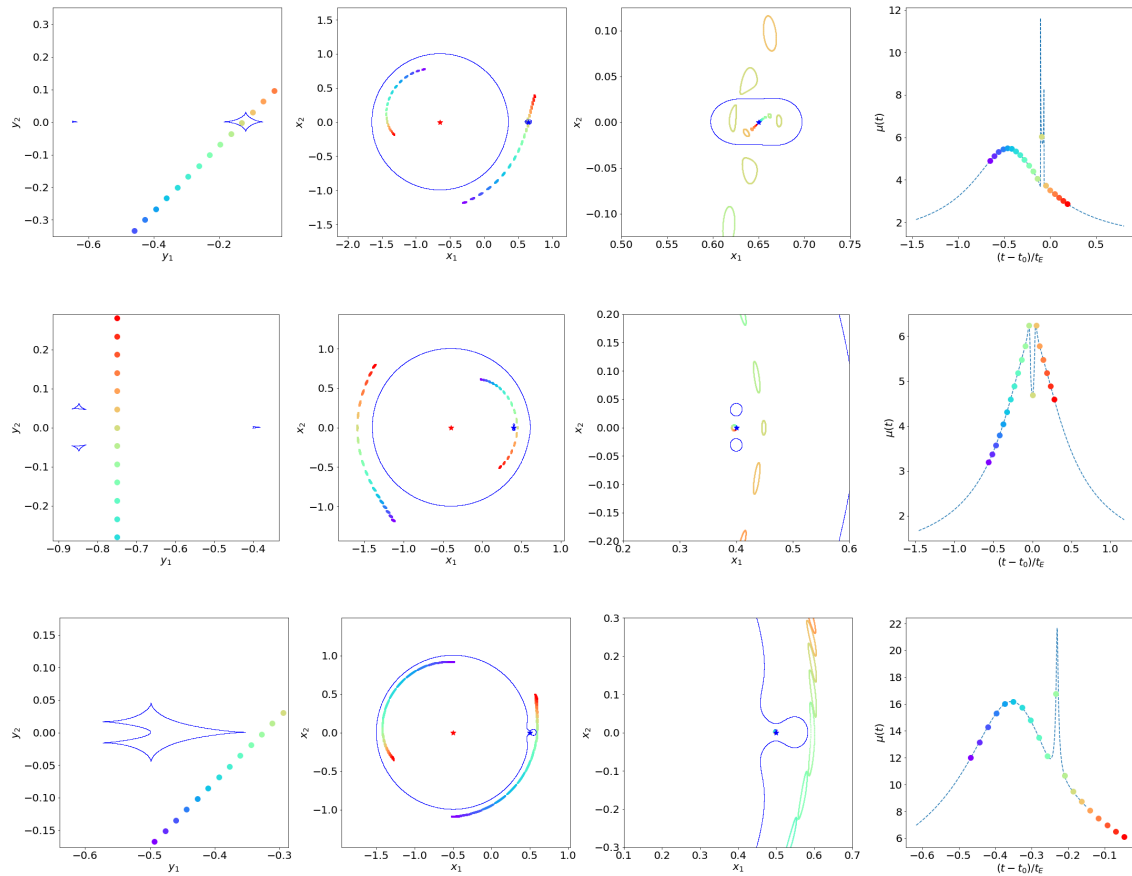


Figure 3.8.7: Perturbation of the inner and of the outer images in the primary microlensing event by planets. We assume that the host star has mass $M = 1M_\odot$ and that $q = 10^{-3}$. Each row of panels refers to a different caustic topology (wide, close, and resonant, from the upper to the lower panels). In each row, we show the caustics and the source positions at different times in the first panel on the left. The time is color-coded from blue to red. The second panel shows the critical lines and the positions of source images. The positions of the host star and of the planet are given by the red and the blue stars. Even in this case, the colors help to associate the images to the corresponding source positions in the left panel. In the third panel, we zoom over the planetary critical lines to show how the images are affected by the planet. The sources are assumed to have circular shapes, with radius $r = 0.01\theta_E$. The fourth panel shows the source light-curve during the microlensing event.

a close topology. In this case, the inner image is de-magnified when it is close to the planetary critical lines. Consequently, we observe a dip in the source light-curve.

The bottom panels illustrate the case of source passing near the cusp of a resonant caustic. In this case, the planet magnifies the outer image in the primary event.

- The examples shown above illustrate that microlensing is sensitive to planets near Einstein radius of the host star.

Analysis of the light curve in a planetary caustic crossing event

The connection between anomalies in the light curve and image locations allows to read important information about the star and the planet off the light curves in planetary microlensing events. For example, let consider the case illustrated in the upper panels of Fig. 3.8.7. We can use the standard

light curve model given in Eq. 3.33 for describing the primary event, which allows us to obtain t_E , t_0 , and y_0 .

The time of the planetary anomaly, t_p , can be used to find the distance of the planet from the host star. Indeed, the anomaly in the light curve denotes the passage of the source on the top of the planetary caustic. The distance of the planetary caustic from the central caustic (and from the host star) is thus

$$y_p(t_p) = \sqrt{y_0^2 + \left(\frac{t_p - t_0}{t_E}\right)^2}. \quad (3.108)$$

Using the lens equation, the distance of the planet from the host star is thus

$$d = \frac{y_p \pm \sqrt{y_p^2 + 4}}{2}, \quad (3.109)$$

The sign to choose in the above equation depends on caustic topology. In the case considered here, we choose the plus sign because the planet perturbs the outer image.

From the light curve, we can also measure the length of the planetary perturbation, which is approximately equal to the Einstein crossing time of the planet, $t_{E,p}$. As shown in Eq. 3.30, t_E and $t_{E,p}$ are proportional to square root of the masses of host star and of the planet, respectively. Therefore, the mass ratio q can be estimated as

$$q \approx \left(\frac{t_{E,p}}{t_E}\right)^2 \quad (3.110)$$

Of course, a more detailed model of the system is necessary to measure the lens parameters accurately. In addition, the microlensing degeneracy discussed in the case of single point masses persists. To break the degeneracy, sometimes measurements of finite source size and microlensing parallax effects can be used (Udalski et al., 2005). In rare cases, imaging with HST or with adaptive optics on large telescopes allows to detect and resolve the host star (Batista, Beaulieu, et al., 2015; Bennett, Anderson, et al., 2006; Bennett, Bhattacharya, et al., 2015). As discussed earlier, astrometric microlensing will be measured for some lenses in the near future.

Modeling planetary events remains however an hard job. As discussed earlier, a fundamental degeneracy exist between close and wide systems. In addition similar features in the light curves can be produced by planetary microlensing and by close/wide binary lenses (Han and Gaudi, 2008). Although rare, binary sources lensed by single lenses can produce features similar to those produced by a planetary caustic perturbation (Jung, Udalski, Bond, et al., 2017; Jung, Udalski, Yee, et al., 2017).

Planetary microlensing detections

The search for planets using microlensing is a relatively young field of research. To date, 58 planets have been discovered using microlensing³.

The first detection is dated back in 2004, when the OGLE and MOA collaborations observed the event dubbed OGLE-2003-BLG-235/MOA-2003-BLG-53 towards the bulge of the Milky Way (Bond et al., 2004). The light curve is a single lens profile with a short (~ 7 days) deviation exhibiting the U-profile typical of a caustic crossing. The data are consistent with resonant caustic crossing event produced by a star-planet lens with $t_E = 61.5 \pm 1.8$ days, $q = 3.9_{-0.7}^{+1.1} \times 10^{-3}$, and $d = 1.120 \pm 0.007$. The identification of the host star with HST allowed to derive further physical properties of this system Bennett, Anderson, et al. (2006). The planet turned out to be a super

³<https://exoplanetarchive.ipac.caltech.edu>

jupiter with mass $M_p = 2.6_{-0.6}^{+0.8} M_J$ orbiting around a M -dwarf star with mass $M = 0.63_{-0.09}^{+0.07} M_\odot$. The semi-major axis of the planet orbit is $a = 4.3_{-0.8}^{+2.5}$ AU.

Also the second planet discovered via microlensing (MOA-2007-BLG-400) is a super Jupiter planet orbiting around an M-dwarf star Dong et al. (2009); Udalski et al. (2005). This immediately raised the suspect that such planetary systems are far from being rare. In fact, about $\sim 20\%$ of the microlensing detected planets are of this kind (Batista, Gould, et al., 2011; Calchi Novati et al., 2018; Han, Jung, et al., 2013; Jung, Udalski, Sumi, et al., 2015; Koshimoto, Shvartzvald, et al., 2017; Koshimoto, Udalski, et al., 2014; Poleski et al., 2014; Shin et al., 2016; Shvartzvald et al., 2014; Street et al., 2013; Udalski et al., 2005).

The third and the fourth planet detections with microlensing are instead mini-Neptune-like planets (Beaulieu et al., 2006) 2006ApJ...644L..37G. Given their low mass (\sim few Earth masses), these planets are more difficult to detect compared to Jupiter-like planets. Thus, simple statistical arguments suggest that they are even more common than Jupiters. As new detections were made, it was possible to measure the mass ratio function of cold exoplanets (Sumi, Bennett, et al., 2010), which was found to scale as

$$\frac{dN}{d \log q} \propto q^{-0.7 \pm 0.2} \quad (3.111)$$

with a 95% confidence level upper limit of $n < -0.35$ (where $dN/d \log q \propto q^n$). This implies that Neptune-mass planets are at least three times more common than Jupiters at the 95% confidence level.

As seen in the previous sections, microlensing is particularly sensitive to planets near the Einstein radius of the host star, $\sim r_E = D_L \theta_E$. For a solar mass star at $D_L \sim 4$ kpc and a source at $D_S \sim 8$ kpc, the Einstein ring radius is ~ 4 AU. This is close to the Jupiter's semi-major axis (5.2 AU). Gould and Loeb (1992) pointed out that the Einstein radius falls just beyond the region of the protoplanetary disk, where the midplane disk temperature is below the sublimation temperature of water, the so-called snow line. This is a particularly important boundary for planet formation, as several core-accretion models predict that gas giants can only form beyond this line (e.g. Lissauer, 1987). Other techniques to find exoplanets (based on radial velocity shifts, transits, direct imaging, etc) are not efficient at these distances from their host stars, except for very massive planets. On the other hand, microlensing has allowed detections of planets of relatively small mass. Microlensing is thus complementary to the techniques to explore an otherwise difficult to reach region in the planet mass vs semi-major axis plane (Gaudi, 2012).

3.9 Python applications

3.9.1 Standard microlensing light curve

In the following example, we derive the standard light curve in a microlensing event involving a point lens and a point source. The source moves with a constant transverse velocity v or relative motion

$$\mu_{rel} = \frac{v}{D_L} .$$

Assuming that the trajectory of the source relative to the lens is linear, during the microlensing event, the magnification of the source changes as

$$\mu(t) = \frac{y^2(t) + 2}{y(t) \sqrt{y^2(t) + 4}}$$

with

$$y(t) = \sqrt{y_0^2 + \left(\frac{t - t_0}{t_E} \right)^2} .$$

For more explanations about these formulas, we refer the reader to Sects. 3.1 and 3.2.

First, we import some useful packages. In particular, we will make use here of some constants defined in the module `constants` of `astropy` and we will need to make proper unit conversions using the module `units` of `astropy`.

```
# import useful packages

import numpy as np
import matplotlib.pyplot as plt
from astropy import constants as const
from astropy import units as u
import matplotlib.ticker as ticker
```

We begin implementing the relevant functions, namely:

- the Einstein radius θ_E ;
- the Einstein crossing time t_E ;
- the relative distance between the source and the lens as a function of time, $y(t)$;
- the magnification as a function of time, $\mu(t)$.

```
# the Einstein radius
def theta_e_func(M,DL,DS):
    mass=M*const.M_sun#.value
    G=const.G#.value
    c=c=const.c#.value
    aconv=180.0*3600.0/np.pi*u.arcsecond
    return((np.sqrt(4.0*(G*mass/c*c)).to('kpc'))*(DS-DL)/DL/DS/u.kpc))*aconv

# the Einstein radius crossing time
def EinsteinCrossTime(M,DL,DS,v):
    theta_e=theta_e_func(M,DL,DS)
    return(((theta_e.to('radian')).value*DL*u.kpc).to('km')/v/u.km*u.s).to('day')).value

# the distance of the source from the lens as a function of time
def yt(tE,y0,t0,t):
    return (np.sqrt(y0**2+((t-t0)/tE)**2))

# the lens magnification as a function of time
def mut_func(tE,y0,t0,t):
    y=yt(tE,y0,t0,t)
    return ((y**2+2)/y/np.sqrt(y**2+4))
```

The lens system consists of a lens with mass $M = 0.3M_\odot$ at $D_L = 4$ kpc and a source at $D_S = 8$ kpc. We assume that the relative velocity of the source with respect to the lens is $v = 200$ km/s. The following code sets these initial values up:

```
M_lens=0.3 # solar masses
DL=4.0 # kpc
DS=8.0 # kpc
vel=200 # km/s
```

We will display the light curves for a variety of impact parameters y_0 . The choice of the time of the passage of the source at the minimum distance from the lens happens is not important, as we will display the light-curves as a function of $(t - t_0)/t_E$:

```
# initialize the impact parameters
y0=np.linspace(1.0,0.1,10)
# passage at the minimum distance from the lens
t_0=365 # days
# compute the Einstein radius crossing time
t_einst=EinsteinCrossTime(M_lens,DL,DS,vel) # days
t=t_0+np.linspace(-2,2,200)*t_einst
```

Finally, we can create the plot. We will loop on the values of the impact parameters and for each of them we will compute the light-curve $\mu(t)$. We will use a sequence of colors from the rainbow color-map to color-code the impact parameters:

```
xx=[-2,2]

fig,ax=plt.subplots(1,2,figsize=(18,8))
ax[1].set_ylim([1.0,10.0])
ax[1].set_xlim([-2,2])
ax[1].set_yscale('log')
ax[1].set_xlabel(r'$\frac{t-t_0}{t_E}$',fontsize=23)
ax[1].set_ylabel(r'$\mu(t)$',fontsize=23)
ax[1].set_yticks(np.arange(1, 11, 1.0))
ax[1].yaxis.set_major_formatter(ticker.FormatStrFormatter('%0.1f'))
ax[1].xaxis.set_tick_params(labelsize=20)
ax[1].yaxis.set_tick_params(labelsize=20)

# create a circle with radius 1 (the Einstein ring)
circle=plt.Circle((0,0),1,color='black',fill=False)
ax[0].set_xlim([-1.5,1.5])
ax[0].set_ylim([-1.5,1.5])
ax[0].add_artist(circle) # display the Einstein ring
ax[0].plot([0.0],[0.0],'*',markersize=20,color='red')
ax[0].xaxis.set_tick_params(labelsize=20)
ax[0].yaxis.set_tick_params(labelsize=20)

from matplotlib.pyplot import cm
# create a color sequence using the rainbow color-map
color=iter(cm.rainbow(np.linspace(0,1,y0.size)))

# loop over the impact parameters and plot the light curves
for i in range(y0.size):
    c=next(color)
    mut=mut_func(t_einst,y0[i],t0,t)
    ax[1].plot((t-t0)/t_einst,mut,'-',color=c)
    yy=[y0[i],y0[i]]
    ax[0].plot(xx,yy,'--',color=c,lw=2)
```

```
ax[0].set_xlabel(r'$y_1$', fontsize=23)
ax[0].set_ylabel(r'$y_2$', fontsize=23)
```

The resulting plot is shown in Fig. 3.2.2.

3.9.2 Fitting the standard light curve

The microlensing light-curve is a function of t_0 , y_0 , and t_E . This last parameter is in turn a function of M , v , D_L , and D_S . The normalization of the light-curve is given by the base-line flux f_0 , which can be regarded as an additional parameter. Once a microlensing event has been detected and the light-curve has been measured, we wonder how well the parameters listed above can be derived.

Here, we set up the following experiment:

- we simulate the observation of a microlensing event and generate synthetic data, including measurement errors;
- we use the package `lmfit` to find the maximum-likelihood model fitting the data;
- we perform a bayesian analysis based on the package `emcee` to estimate the posterior probability distributions of the parameters and estimate the uncertainties.

The lens system is composed by a lens of mass $M = 0.3M_\odot$ at $D_L = 4$ kpc and by a source at $D_S = 8$ kpc. The source baseline flux is chosen to be $f_0 = 10$ (the units are arbitrary). The relative velocity of the source is $v = 210$ km/s and we assume that impact parameter y_0 is 0.3. We assume to monitor the source star for a long period (2 years) and to collect data continuously. This is clearly unrealistic, but we want to test a very ideal situation. In addition, we assume that the accuracy of the measurement is 5%. The passage of the source at the minimum distance from the lens occurs at $t_0 = 365$ days after we begin monitoring the source star.

The code used to generate the synthetic data is here below. To compute the light curve, we use the functions defined in the previous example discussed in Sect. 3.9.1.

```
# input parameters for the light-curve
t=np.linspace(0,730,730)
M_lens=0.3 # solar masses
DL=4.0 # kpc
DS=8.0 # kpc
vel=210 # km/s
y0=0.3
t0=365.0 # days
flux0=10.0 # some arbitrary flux unit

t_einst=EinsteinCrossTime(M_lens,DL,DS,vel)
# lightcurve plus random noise
mut=flux0*(mut_func(t_einst,y0,t0,t)+(np.random.randn(len(t))*0.02))

# we assign to the data some errors, which we assume to be a
# constant fraction of the measurement
emut=mut*0.05
```

The light-curve is displayed in Fig. 3.9.1 (blue points with error bars).

As said, in order to fit the data, we use the python package `lmfit`. This package allows to build complex fitting models for non-linear least-squares problems. The implementation shown here was obtained by closely following the examples in the package documentation, which can be found at this link: http://cars9.uchicago.edu/software/python/lmfit_MinimizerResult/intro.html

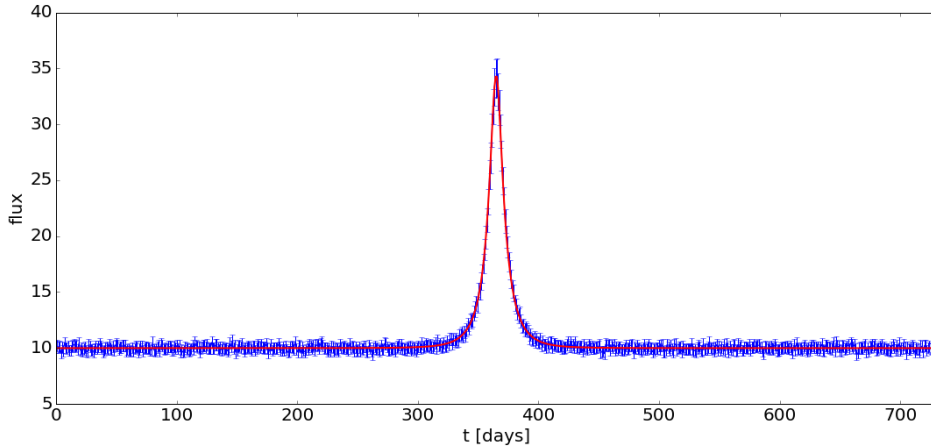


Figure 3.9.1: Simulated light curve of a microlensing event (blue points with error bars. The best fit to the data is shown in red.

We begin by setting up some initial guesses for the model parameter, storing them in a `lmfit.Parameters` object, including also some plausible ranges where the parameters are free to vary. Then, we write the function to be minimized, a.k.a. the *objective* function:

```
import lmfit

# initial guesses
p = lmfit.Parameters()
p.add_many(('t0', 360., True, 0, 720), ('M_lens', 0.5, True, 0.001, 100.0),
           ('DL', 5., True, 0.1, 10.), ('DS', 10., True, 5., 15.),
           ('vel', 200, True, 100., 300.), ('y0', 0.2, True, 0.01, 1.0),
           ('flux0', 12, True, 8, 12.0))

# objective function
def residual(p):

    v = p.valuesdict()
    t_einst=EinsteinCrossTime(v['M_lens'],v['DL'],v['DS'],v['vel'])
    res=(mut_func(t_einst,v['y0'],v['t0'],t)*v['flux0']-mut)/emut

    return (res)
```

This function simply compares the model to the data, returning the residuals, weighted by the measurement errors.

The next step is use a minimizer to minimize the objective function (i.e. the residuals). Several algorithms are available in `lmfit`. Here, we perform the minimization using the Nelder-Mead method.

```
# minimize the objective function using the Nelder-Mead method
mi = lmfit.minimize(residual, p, method='Nelder')
# print report on the fit
lmfit.printfuncs.report_fit(mi.params, min_correl=0.5)
```

```
# plot the maximum likelihood solution on the top of the data
fig,ax=plt.subplots(1,1,figsize=(18,8))
ax.errorbar(t, mut, emut)
ax.set_xlabel('t [days]', fontsize=20)
ax.set_ylabel('flux', fontsize=20)
ax.xaxis.set_tick_params(labelsize=20)
ax.yaxis.set_tick_params(labelsize=20)
ax.set_xlim([0,730])

t_einst=EinsteinCrossTime(mi.params['M_lens'],mi.params['DL'],
                           mi.params['DS'],mi.params['vel'])
ax.plot(t,mi.params['flux0']*mut_func(t_einst,mi.params['y0'],
                                         mi.params['t0'],t), 'r',lw=2)
```

The figure generated by this piece of code is that shown in Fig. 3.9.1. The report of the maximum likelihood parameters reads:

```
[[Variables]]
t0:      365.002446 (init= 360)
M_lens:  0.22162718 (init= 0.5)
DL:       5.17859669 (init= 5)
DS:       9.89082660 (init= 10)
vel:      200.691012 (init= 200)
y0:       0.29997367 (init= 0.2)
flux0:   9.98550295 (init= 12)
```

To derive the probability distribution for the parameters, we use a Bayesian approach. More precisely, we perform a Bayesian sampling of the posterior distribution for the parameters using the emcee Markov Chain Monte Carlo package. You need to have `emcee` installed to use this method.

The method requires to define a log-likelihood function, which is used to compute the log-posterior probability of the model parameters as

$$\ln P(p|d) \propto \ln P(d|p) + \ln P(p), \quad (3.112)$$

where p are the parameters and d are the data. The method (implemented in `lmfit`) assumes that the prior is uniform, i.e. $\ln P(p) = 0$.

The log-likelihood function is given by

$$\ln P(d|p) = -\frac{1}{2} \sum_n \left[\frac{(model_n - data_n)^2}{s_n^2} + \ln 2\pi s_n^2 \right]. \quad (3.113)$$

```
# log-likelihood function
def lnprob(p):
    from numpy import inf
    resid = residual(p)
    s = emut
    resid *= resid
    resid += np.log(2 * np.pi * s**2)
    lnp=-0.5 * np.sum(resid)
```

```

if (np.isnan(lnp)):
    lnp=-1e10

return lnp

```

We can not perform the sampling of the posterior distribution:

```

# build a general minimizer for curve fitting and optimization.
mini = lmfit.Minimizer(lnprob, mi.params, nan_policy='propagate')
# sampling of the posterion distribution
res = mini.emcee(burn=300, steps=2000, thin=10, params=mi.params)

```

This will generate 2000 samples. The posterior distributions for the parameters can be displayed in a corner plot, shown in Fig. 3.9.2. This requires installation of the corner package:

```

# show corner plot (confidence limits, parameter distributions,
# correlations)
import corner
figure=corner.corner(res.flatchain, labels=res.var_names,
                      truths=list(res.params.valuesdict().values()),
                      show_titles=True, title_kwargs={"fontsize": 12})

```

The values reported in the MinimizerResult are the medians of the probability distributions and a 1σ quantile, estimated as half the difference between the 15.8 and 84.2 percentiles:

```

median of posterior probability distribution
-----
[[Variables]]
t0:      365.005389 +/- 0.150172 (0.04%) (init= 365.0024)
M_lens:   0.29572066 +/- 0.129853 (43.91%) (init= 0.2216272)
DL:       4.77833889 +/- 2.478843 (51.88%) (init= 5.178597)
DS:       10.8725461 +/- 2.892918 (26.61%) (init= 9.890827)
vel:      224.631948 +/- 56.98840 (25.37%) (init= 200.691)
y0:       0.29996274 +/- 0.005893 (1.96%) (init= 0.2999737)
flux0:    9.98410492 +/- 0.019299 (0.19%) (init= 9.985503)
[[Correlations]] (unreported correlations are < 0.100)
C(M_lens, vel)          = 0.751
C(DL, DS)               = 0.428
C(DS, vel)               = 0.378
C(DL, vel)               = 0.212
C(M_lens, DS)            = -0.173
C(M_lens, DL)             = -0.123

```

There are correlations between the parameters `vel`, `M_lens`, `DL`, and `DS`, which highlight the microlensing degeneracy: with a single microlensing event, it is only possible to constrain the parameter t_E , which is a combination of all these parameters.

Fig. 3.9.3 shows the results of the fit to the measured light-curve with a model which depends only on `tE`, `t0`, and `y0`.

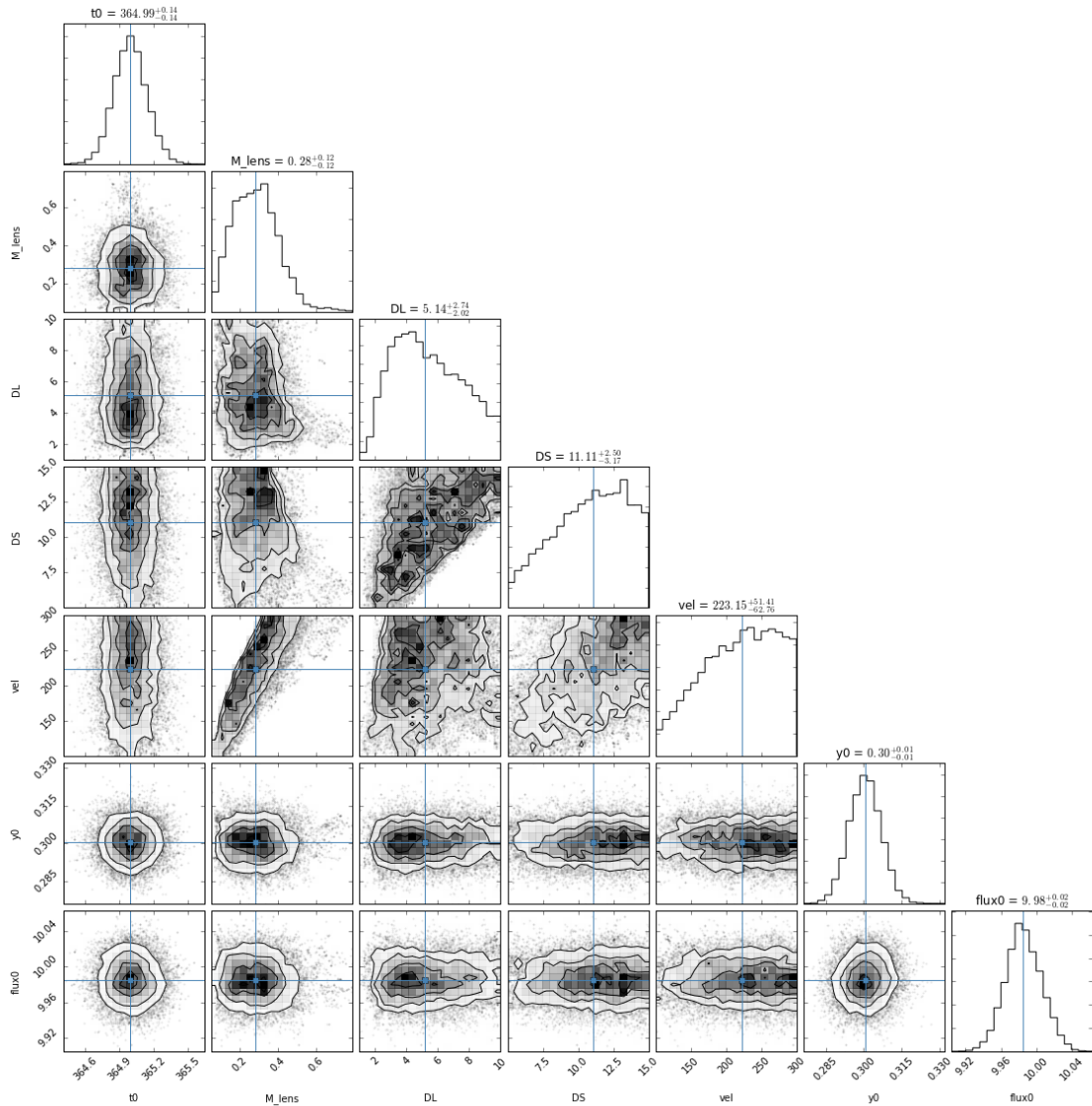


Figure 3.9.2: Corner plot showing the posterior distributions for the parameters.

3.9.3 Distribution of microlensing event timescale

In this example, we will construct a model to predict the distribution of microlensing event timescales. The problem to be addressed is that of drawing samples from several Probability Distribution Functions (PDF). For arbitrary distributions this can be done by employing a method called *inverse transform sampling* which involves the following steps:

1. we compute the cumulative distribution function of the PDF we want to sample;
2. we invert the cumulative function;
3. we generate random numbers uniformly distributed between 0 and 1;
4. we read-off the corresponding values returned by the inverted cumulative function.

For example, for an exponential PDF,

$$p(x) = \lambda \exp(-\lambda x), \quad (3.114)$$

the cumulative distribution function is

$$P(x) = \int_0^x p(x)dx = 1 - \exp(-\lambda x). \quad (3.115)$$

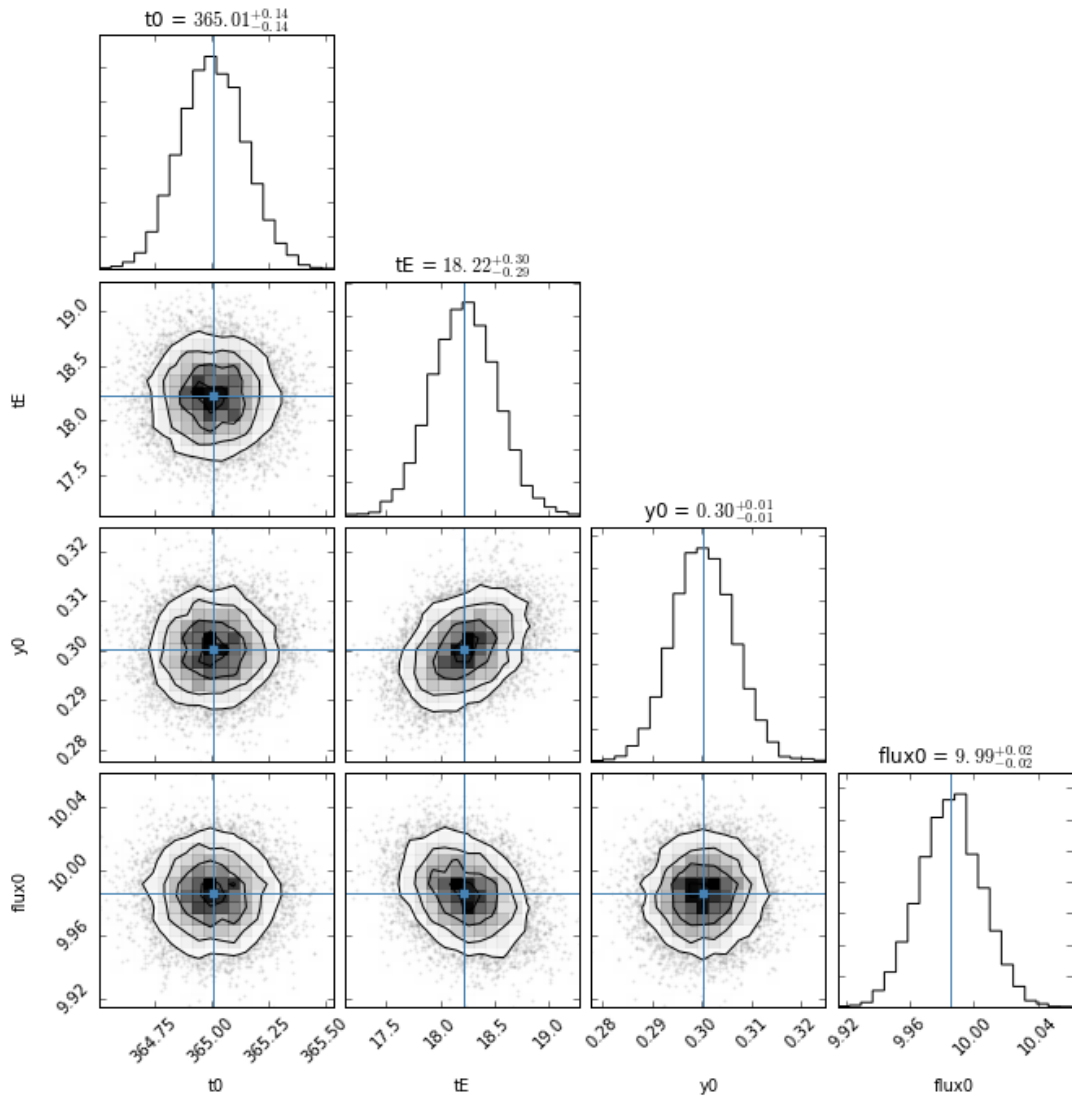


Figure 3.9.3: Corner plot showing the posterior distributions for the parameters.

This can be readily inverted to find:

$$x = -\ln(1 - P)/\lambda . \quad (3.116)$$

In python, to generate 1000 samples of this distribution, we may write

```
def exp_icdf(p, lambd=1):
    return(-np.log(1-p)/lambd)

samples=1000
lambd=1
p=np.random.random(samples)
x=exp_icdf(p, lambd=lambd)
```

The rate parameter λ is chosen to be 1 here.

Actually, the sampling of several common PDFs, including the exponential PDF, is already implemented in `numpy.random`. For example:

```
# draw samples from an exponential PDF with rate parameter lambd:
x_exp=np.random.exponential(size=samples,scale=1.0/lambd)
# draw samples from a gaussian PDF with mean mu and
# standard deviation sigma:
mu=1.0
sigma=0.2
x_norm=np.random.normal(loc=mu,scale=sigma,size=samples)
# draw samples from a uniform distribution
a=0
b=1
x_unif=np.random.uniform(low=a,high=b,size=samples)
```

Suppose that we have observed a thousand microlensing events towards the bulge of the Milky Way, measuring their Einstein crossing times. We may try to reproduce the observed distribution of event timescales with a simple model to test it. The aim of this exercise is to show how these calculations are made, rather than building a realistic model.

Our assumptions will be:

- the distribution of lens masses is modeled either using a power-law or an exponential distribution, so that we can compare the results;
- the distribution of source distances is gaussian and peaked at $D_S = 8$ kpc;
- the distribution of lens distances is uniform between $D_L = 0$ and $\min(D_S)$;
- the distribution of the lens-source relative velocities is gaussian and it peaks at $v = 200$ km/s.

We begin by drawing the lens masses from a power distribution. The power function of `numpy.random` draws samples in $[0, 1]$, but we want to generate a larger range of masses. Thus, we rescale the sampled values to cover the desired values (e.g. $[0, 10] M_\odot$):

```
a = 0.5 # shape
samples = 1000
# use the 'power' PDF in numpy.random
mass_pow = np.random.power(a, samples)
mass_pow = mass_pow*10.0
```

We draw a second sample of masses from an exponential mass distribution:

```
a = 0.5
samples = 1000
# use the 'exponential' PDF in numpy.random
mass_exp = np.random.exponential(size=samples,scale=1.0/lambd)
```

Then we generate the distances of the sources and of the lenses. The first are drawn from a gaussian distribution with mean $\mu = 8$ kpc and standard deviation $\sigma = 0.3$ kpc. The second are drawn from a uniform distribution in the range $[0, \min(D_S)]$:

```
# generate D_S
mu, sigma = 8.0, 0.3
ds=np.random.normal(loc=mu,scale=sigma,size=samples)
# generate D_L
dmin, dmax = 0.0, np.min(x_norm)
dl = np.random.uniform(low=dmin,high=dmax,size=samples)
```

Finally, we generate the velocities, drawing them from a gaussian distribution with mean 220 km/s and standard deviation 10 km/s:

```
# generate vel
mu, sigma = 220, 10
vel=np.random.normal(loc=mu,scale=sigma,size=samples)
```

The distributions of the four variables M , D_L , D_S , and v_{rel} are shown in Fig. 3.9.4. Assuming that these are not correlated, we can combine them to derive the expected distribution of event timescales. However, we need first to code a few functions for computing t_E :

```
from astropy import constants as const
from astropy import units as u
# the Einstein radius
def theta_e_func(M,DL,DS):
    mass=M*const.M_sun
    G=const.G
    c=c=const.c
    aconv=180.0*3600.0/np.pi*u.arcsecond
    theta_E=np.sqrt(4.0*(G*mass/c*c).to('kpc')*(DS-DL)/DL/DS/u.kpc)*aconv
    return(theta_E)

# the Einstein radius crossing time
def EinsteinCrossTime(M,DL,DS,v):
    theta_e=theta_e_func(M,DL,DS)
    return(((theta_e.to('radian').value*DL*u.kpc).to('km')
           /v/u.km*u.s).to('day'))

fig,ax=plt.subplots(1,1,figsize=(10,7))
tE_pow=EinsteinCrossTime(mass_pow,dl,ds,vel)

tE_exp=EinsteinCrossTime(mass_exp,dl,ds,vel)
```

Note that we used the module units from `astropy` to deal with the units of the different quantities. The results are shown in Fig. 3.9.5, which is produced using the following instructions:

```
count, bins, ignored = ax.hist(tE2_pow,alpha=0.2,
                               bins=np.logspace(-1,2.5,60),
                               color='blue',label='P.L.')
count, bins, ignored = ax.hist(tE_exp,alpha=0.5,
                               bins=np.logspace(-1,2.5,60),
                               color='orange',label='exponential')
ax.legend(fontsize=20)
ax.set_xscale('log')
ax.set_yscale('log')

ax.set_xlabel(r'$t_E$',fontsize=20)
ax.set_ylabel(r'$N(t_E)$',fontsize=20)
ax.xaxis.set_tick_params(labelsize=20)
ax.yaxis.set_tick_params(labelsize=20)
```

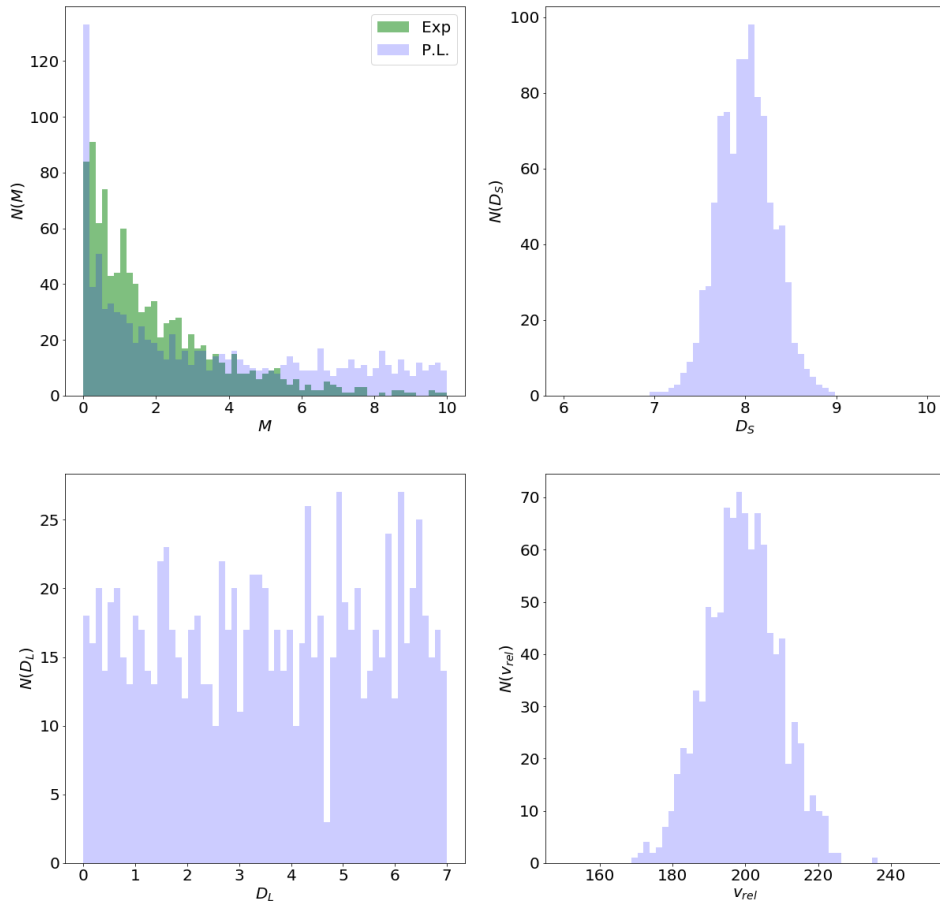


Figure 3.9.4: From the upper left to the bottom right panels, distributions of the lens masses, of the source and of the lens distances, and of the relative velocities between the lenses and the sources. The distributions of the lens masses are modeled with a power-law (blue) and with an exponential (green) function.

One can use this approach to predict the event timescales from several populations of lenses as done in Sumi, Kamiya, et al. (2011) (see also Gaudi, 2012; Gould, 1994).

3.9.4 Astrometric microlensing effect

We have shown that during the microlensing event, the center of light, once removed the intrinsic motion of the source, shifts as:

$$\delta(y) = \frac{\vec{y}}{y^2 + 2}$$

Since $\vec{y} = ((t - t_0)/t_E, y_0)$, if one chooses the reference frame such as the x -axis is parallel to the direction of motion of the source, this shift has two components, one parallel and one perpendicular to the motion of the source:

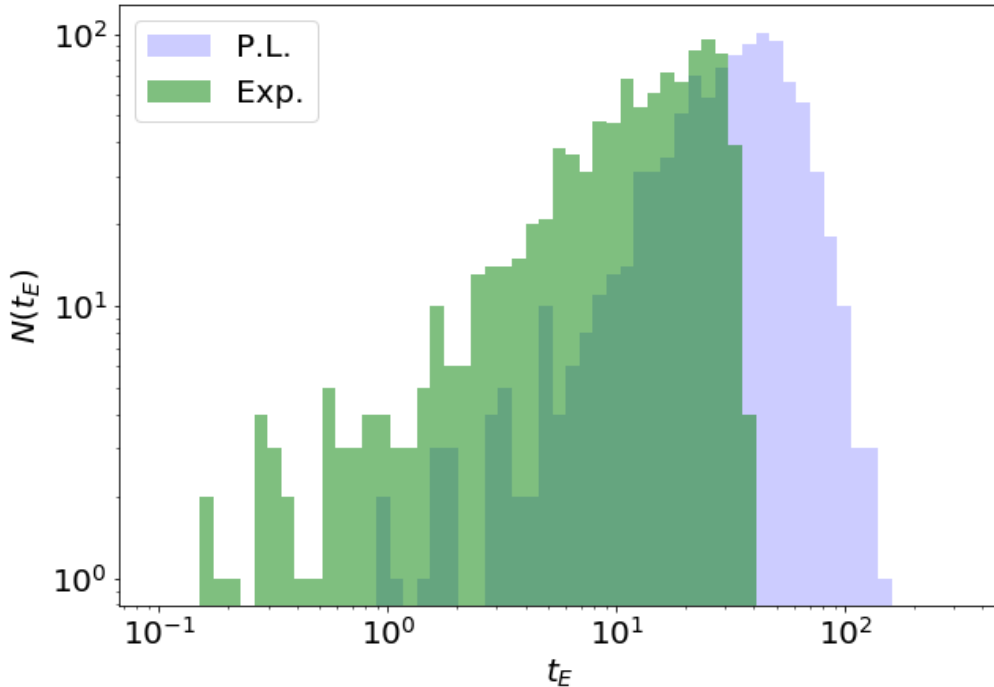


Figure 3.9.5: Expected distribution of microlensing event timescales from the model outlined in Sect. ??.
Results are shown for two mass distributions of lenses (power-law and exponential).

$$\delta(y)_\parallel = \frac{(t - t_0)/t_E}{y^2 + 2}$$

and

$$\delta(y)_\perp = \frac{y_0}{y^2 + 2}.$$

Considering that $y(t) = \sqrt{y_0^2 + (t - t_0)^2/t_E^2}$, we have all the ingredients to investigate what kind of geometrical figure is traced by the center of light (corrected for the intrinsic motion of the source!).

In the following, we build some classes to deal with the point mass lens and its source.

The point source class is very simple:

```
class point_source(object):

    def __init__(self, flux=1.0, ds=10.0, vel=200.):
        self.ds=ds
        self.flux=flux
        self.vel=vel
```

It does not contain any method. The source is defined by means of its distance, intrinsic flux, and velocity relative to the lens.

The point lens class incorporates some of the functions introduced in the previous examples. We initialize the lens object by specifying a source object ps and then the mass, the distance, the

impact parameter y_0 , and the time t_0 .

```
class point_lens(object):

    # the constructor of the microlens
    def __init__(self,ps,mass=1.0,dL=5.0,dS=8.0,t0=0.0,y0=0.1):
        self.M=mass
        self.dL=dL
        self.ps=ps
        self.y0=y0
        self.t0=t0
        self_tE=self.EinsteinCrossTime()

    # a function returning the Einstein radius
    def EinsteinRadius(self):
        mass=self.M*const.M_sun
        G=const.G
        c=c=const.c
        aconv=180.0*3600.0/np.pi*u.arcsecond
        return((np.sqrt(4.0*(G*mass/c*c)).to('kpc'))*(self.ps.ds-self.dL)
               /self.dL/self.ps.ds/u.kpc))*aconv

    # a function returning the Einstein radius crossing time
    def EinsteinCrossTime(self):
        theta_e=self.EinsteinRadius()
        return(((theta_e.to('radian').value*self.dL*u.kpc).to('km')
               /self.ps.vel/u.km*u.s).to('day')))
```

Here we define a new function to compute the source position at the time t . The function returns the two components of the vector $\vec{y}(t)$:

```
# a function returning the coordinates of the unlensed source
# at time t
def y(self,t):
    y1=(t-self.t0)/self_tE.value
    y2=np.ones(len(t))*self.y0
    return(y1,y2)
```

In addition, we define two function returning the coordinates of the outer (x_p) and of the inner (x_m) image of the source. These functions implement Eqs. 3.62.

```
# a function returning the coordinates of the x_+ image at time t
def xp(self,t):
    y1, y2 = self.y(t)
    Q = np.sqrt(y1**2 + y2**2 + 4)/(np.sqrt(y1**2 + y2**2))
    xp1= 0.5 *(1 + Q)* y1
    xp2= 0.5 *(1 + Q)* y2
    return(xp1, xp2)

# a function retruning the coordinates of the x_- image at time t
def xm(self,t):
```

```

y1, y2 = self.y(t)
Q = np.sqrt(y1**2 + y2**2 + 4) / (np.sqrt(y1**2 + y2**2))
xm1= 0.5 *(1 - Q)* y1
xm2= 0.5 *(1 - Q)* y2
return(xm1, xm2)

```

The following step is to compute the magnifications of the two images, using Eq. 3.18:

```

# the magnification of the x_+ image
def mup(self,t):
    y1, y2 = self.y(t)
    yy=np.sqrt(y1**2+y2**2)
    mup=0.5*(1+(yy**2+2)/yy/np.sqrt(yy**2+4))
    return (mup)

# the magnification of the x_- image
def mum(self,t):
    y1, y2 = self.y(t)
    yy=np.sqrt(y1**2+y2**2)
    mum=0.5*(1-(yy**2+2)/yy/np.sqrt(yy**2+4))
    return (mum)

```

Finally, the image centroid is computed using Eq. 3.64:

```

# a function returning the coordinate of the light centroid
def xc(self,t):
    xp=self.xp(t)
    xm=self.xm(t)
    xc=(xp*np.abs(self.mup(t))+xm*np.abs(self.mum(t)))/
        (np.abs(self.mup(t))+np.abs(self.mum(t)))
    return (xc)

```

Now, we can add some extra feature. For example, to draw Fig. 3.6.1, the source is assumed to have an extended size. The images of an extended source are distorted into extended images.

To implement the extended images, we add another couple of functions to the class above:

```

def xp_ext_source(self,t,r):
    phi=np.linspace(0.0,2*np.pi,360)
    dy1=r*np.cos(phi)
    dy2=r*np.sin(phi)
    y1,y2=self.y(t)
    yy1=y1+dy1
    yy2=y2+dy2
    Q=np.sqrt(yy1**2+yy2**2+4.0)/np.sqrt(yy1**2+yy2**2)
    xp1=0.5*(1+Q)*yy1
    xp2=0.5*(1+Q)*yy2
    return(xp1,xp2)

def xm_ext_source(self,t,r):
    phi=np.linspace(0.0,2*np.pi,360)
    dy1=r*np.cos(phi)

```

```

dy2=r*np.sin(phi)
y1,y2=self.y(t)
yy1=y1+dy1
yy2=y2+dy2
Q=np.sqrt(yy1**2+yy2**2+4.0)/np.sqrt(yy1**2+yy2**2)
xm1=0.5*(1-Q)*yy1
xm2=0.5*(1-Q)*yy2
return(xm1,xm2)

```

These two functions perform the following operation. Let assume that the source is a circle with radius r at position \vec{y} . Then, the source can be seen as a collection of point sources at positions

$$\vec{y} + d\vec{y}_i$$

where

$$d\vec{y}_i = r(\cos \phi, \sin \phi)$$

with $\phi \in [0, 2\pi]$. Each of these point sources produce two images $\vec{x}_{i,+}$ and $\vec{x}_{i,-}$, which can be found using the functions defined earlier. By doing this for all points on the perimeter of the source, we obtain the lensed contours of the two images.

The following code was used to produce Fig. 3.6.1.

```

# define a source and a lens
ps = point_source()
pl = point_lens(ps=ps, mass=1.0, dl=5.0, y0 = 0.2)

# define an array of times
t = np.linspace(-300,300,2000)

# compute the source, the image, and the centroid
# positions as function of time
y1, y2 = pl.y(t)
xp1, xp2= pl.xp(t)
xm1,xm2=pl.xm(t)
xc1,xc2=pl.xc(t)

# plot results
fig,ax=plt.subplots(1,1,figsize=(8,8))
ax.plot(y1,y2,'--',label='source traj.')
ax.plot(xp1,xp2,'--',label='image $x_+'$')
ax.plot(xm1,xm2,'--',label='image $x_-'$')
ax.plot(xc1,xc2,label='image centroid')

# define a coarser array of times
t_sparse=np.linspace(-60,60,19)
from matplotlib.pyplot import cm
color=iter(cm.rainbow(np.linspace(0,1,t_sparse.size)))
# at each time, compute the images of an extended
# circular source of radius r=0.05
for tt in t_sparse:
    c=next(color)

```

```

xp1_e,xp2_e=pl.xp_ext_source(np.array([tt]),0.05)
ax.plot(xp1_e,xp2_e,color=c,lw=2)
xm1_e,xm2_e=pl.xm_ext_source(np.array([tt]),0.05)
ax.plot(xm1_e,xm2_e,color=c,lw=2)

ax.set_xlim([-2,2])
ax.set_ylim([-1.8,2.2])
ax.plot([0.0],[0.0],'*',markersize=20,color='red')
circle=plt.Circle((0,0),1,color='black',fill=False)
ax.add_artist(circle)
ax.legend(fontsize=14)
ax.xaxis.set_tick_params(labelsize=20)
ax.yaxis.set_tick_params(labelsize=20)
ax.set_xlabel(r'$x_{\parallel}$',fontsize=20)
ax.set_ylabel(r'$x_{\perp}$',fontsize=20)

```

Now, imagine that you are monitoring a source over time. The source is fixed on the sky and at some time a microlensing event occurs. What we would measure is a shift of the source compared to its intrinsic position. In other words, we would measure the quantity

$$\delta x_c = \vec{x}_c - \vec{y}.$$

What kind of trajectory would the lensed source follow on the sky?

First, we add this function to the class:

```

def deltaxc(self,t):
    y1,y2=self.y(t)
    yy=(y1**2+y2**2)
    return(y1/(yy+2),y2/(yy+2))

```

Then, we use it to compute the coordinates of the centroid shift:

```

t=np.linspace(-5000,5000,5000)

dxc1,dxc2=pl.deltaxc(t)
fig,ax=plt.subplots(1,1,figsize=(8,8))
ax.plot(dxc1*pl.EinsteinRadius()*1000,dxc2*pl.EinsteinRadius()*1000)
ax.set_xlim([-0.4,0.4])
ax.set_ylim([-0.4,0.4])

ax.set_xlabel(r'$\delta x_{\parallel}\theta_E$ [mas]',fontsize=20)
ax.set_ylabel(r'$\delta x_{\perp}\theta_E$ [mas]',fontsize=20)
ax.plot([0.0],[0.0],'*',markersize=20,color='red')
ax.xaxis.set_tick_params(labelsize=20)
ax.yaxis.set_tick_params(labelsize=20)

```

The result of this procedure is shown in Fig. 3.9.6. The red star indicates the unlensed position of the source. During the microlensing event, the light centroid follows an elliptical trajectory (blue solid line), as discussed in Sect. 3.6.

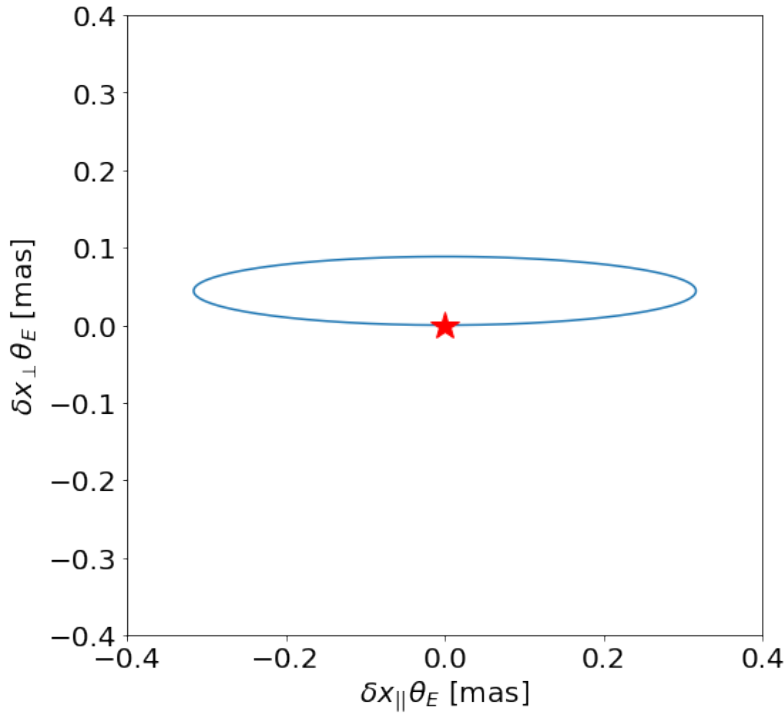


Figure 3.9.6: Trajectory of a source centroid of light during a microlensing event produced by a star of mass $M = 1M_\odot$ at distance $D_L = 5$ kpc, lensing a source at $D_S = 10$ kpc. The impact parameter is $y_0 = 0.2$.

3.9.5 Critical lines and caustics of a binary lens

In the following examples we will consider binary lenses composed of two point masses M_1 and M_2 . The two masses are related by $q = M_1/M_2$. They are placed at a distance d from each other (where d is in units of the lens Einstein radius). We choose the real axis to pass through the two point masses and assume that $z_2 = -z_1$.

The source is supposed to move behind the lens with a relative velocity v_{rel} along a linear trajectory forming an angle θ_s with the real axis. The impact parameter y_0 is measured with respect to $z = 0$. The source reaches the minimal distance from $z = 0$ at $t = t_0$. Consequently, the real and the imaginary parts of z_s are given by

$$\Re(z_s) = \cos(\theta_s)p + \sin(\theta_s)y_0$$

and

$$\Im(z_s) = \sin(\theta_s)p - \cos(\theta_s)y_0$$

where $p = (t - t_0)/t_E$. The effective Einstein radius, θ_E , and Einstein crossing time, t_E , are those of a point-mass lens with mass $M_{tot} = M_1 + M_2$.

As for the point lens D_L and D_S are the angular diameter distances to the lens and to the source.

The critical lines and caustics of the binary lens are determined by solving numerically the equation

$$\frac{\partial z_s}{\partial z^*} = e^{i\phi}$$

for any $\phi \in [0, 2\pi)$.

The equation can be turned into a fourth order complex polynomial, of which we shall find the roots:

$$p_4(z) = z^4 - z^2(2z_1^{*2} + e^{i\phi}) - zz_1^*2(m_1 - m_2)e^{i\phi} + z_1^{*2}(z_1^{*2} - e^{i\phi}) = 0$$

For each ϕ there are up to 4 roots (critical points). By using the lens equation, these can be mapped on the source plane to derive the caustics:

$$z_{cau} = z_{crit} - \frac{m_1}{z_{crit}^* - z_1^*} - \frac{m_2}{z_{crit}^* - z_2^*}.$$

The roots of the polynomial

$$p(x) = x^n + a_{n-1}x^{n-1} + \cdots + a_1x + a_0$$

can be found by building its companion matrix

$$C = \begin{bmatrix} 0 & 0 & \cdots & 0 & -a_0 \\ 1 & 0 & \cdots & 0 & -a_1 \\ 0 & 1 & \cdots & 0 & -a_2 \\ \vdots & \vdots & \ddots & \vdots & \vdots \\ 0 & 0 & \cdots & 1 & -a_{n-1} \end{bmatrix}$$

such as the characteristic polynomial

$$\det(xI - C) = p(x)$$

Consequently, the eigenvalues of C are the roots of $p(x)$. Therefore, to find the critical points of the binary lens, we may proceed as follows:

- we build of the companion matrix of $p_4(z)$;
- we diagonalize the matrix and find the eigenvalues;

This procedure is implemented in the `numpy.roots` method, which will be used below.

We begin by importing numpy:

```
import numpy as np
```

We build a class for binary lenses. The class uses some functions from the `point_lens` class discussed in the previous sections.

The object `binary_lens` will be built using the mass of the first lens, the mass ratio q and the distance between the lenses d in units of the equivalent Einstein radius. The other input parameters are not relevant for this example.

```
class binary_lens(object):
    def __init__(self,d1=5.0,ds=8,m1=1.0,q=1.0,d=2.0,t0=0.0,y0=0.1,
                 theta=np.pi/4,vrel=200.0):
        self.z1=complex(d/2.0,0.0)
        self.q=q
        self.d1=d1
        self.ds=ds
        m2=m1/q
        self.mtot=m1+m2
        self.m1=m1/self.mtot
        self.m2=m2/self.mtot
```

```

"""
we build a point_lens instance to compute the einstein radius
and the Einstein crossing time. This requires to define a
point source instance too.
"""

ps = point_source(ds=ds,vel=vrel)
pl = point_lens(ps=ps, mass=m1+m2, dl=d1)
self.thetaE=pl.EinsteinRadius()
self.tE=pl.EinsteinCrossTime()

self.t0=t0
self.y0=y0
self.theta=theta

```

As it can be seen, the complex notation is used to define the position of the first point mass.

Then we add a function to find the lens critical lines and caustics using the method outlined above.

```

def CritCau(self,ncpt=10000):
    # set the phase vector
    phi_=np.linspace(0,2.*np.pi,ncpt)

    x=[]
    y=[]
    xs=[]
    ys=[]

    # we need to find the roots of our fourth order polynomial
    # for each value of phi
    for i in range(phi_.size):
        phi=phi_[i]
        # the coefficients of the complex polynomial
        coeff = [1.0,0.0,-2*np.conj(self.z1)**2-np.exp(1j*phi),
                  -np.conj(self.z1)*2*(self.m1-self.m2)*np.exp(1j*phi),
                  np.conj(self.z1)**2*(np.conj(self.z1)**2-np.exp(1j*phi))]
        # use the numpy function roots to find the roots of the
        # polynomial
        z=np.roots(coeff) # these are the critical points!

        # use the lens equation (complex form) to map the critical
        # points on the source plane
        zs=z-self.m1/(np.conj(z)-np.conj(self.z1))\
                  -self.m2/((np.conj(z)-np.conj(-self.z1))) # these are the
        # caustics!

        # append critical and caustic points
        x.append(z.real)
        y.append(z.imag)
        xs.append(zs.real)

```

```

    ys.append(zs.imag)

    return(np.array(x),np.array(y),np.array(xs),np.array(ys))

```

The function returns four numpy arrays, containing the coordinates of the lens critical lines and caustics. The size of these arrays is defined by the input parameter ncpt. By default, we sample the critical lines and the caustics by generating 10,000 values of the phase ϕ .

3.9.6 Solving the lens equation of the binary lens

To find the positions of the images of a source at z_s , we can turn the lens equation into a 5-th order complex polynomial and find its roots using the same method used to find the critical points.

The polynomial can be written as:

$$p_5(z) = \sum_{i=0}^5 c_i z^i$$

and, after setting

$$\Delta m = \frac{m_1 - m_2}{2} \quad m = \frac{m_1 + m_2}{2} \quad z_2 = -z_1 \quad z_1 = z_1^*,$$

the coefficients turn out to be

$$\begin{aligned}
c_0 &= z_1^2 [4(\Delta m)^2 z_s + 4m\Delta m z_1 + 4\Delta m z_s z_s^* z_1 + 2mz_s^* z_1^2 + z_s z_s^{*2} z_1^2 - 2\Delta m z_1^3 - z_s z_1^4] \\
c_1 &= -8m\Delta m z_s z_1 - 4(\Delta m)^2 z_1^2 - 4m^2 z_1^2 - 4mz_s z_s^* z_1^2 - 4\Delta m z_s^* z_1^3 - z_s^{*2} z_1^4 + z_1^6 \\
c_2 &= 4m^2 z_s + 4m\Delta m z_1 - 4\Delta m z_s z_s^* z_1 - 2z_s z_s^{*2} z_1^2 + 4\Delta m z_1^3 + 2z_s z_1^4 \\
c_3 &= 4mz_s z_s^* + 4\Delta m z_s^* z_1 + 2z_s^{*2} z_1^2 - 2z_1^4 \\
c_4 &= -2mz_s^* + z_s z_s^{*2} - 2\Delta m z_1 - z_s z_1^2 \\
c_5 &= z_1^2 - z_s^{*2}
\end{aligned}$$

The function to be added to the `binary_lens` class is

```

def Images(self,ys1,ys2):
    zs=ys1+1j*ys2
    m=0.5*(self.m1+self.m2)
    Dm=(self.m2-self.m1)/2.0

    c5=self.z1**2-np.conj(zs)**2
    c4=-2*m*np.conj(zs)+zs*np.conj(zs)**2\
        -2*Dm*self.z1-zs*self.z1**2
    c3=4.0*m*zs*np.conj(zs)+4.0*Dm*np.conj(zs)*self.z1\
        +2.0*np.conj(zs)**2*self.z1**2-2.0*self.z1**4
    c2=4.0*m**2*zs+4.0*m*Dm*self.z1\
        -4.0*Dm*zs*np.conj(zs)*self.z1\
        -2.0*zs*np.conj(zs)**2\
        *self.z1**2+4.0*Dm*self.z1**3\
        +2.0*zs*self.z1**4
    c1=-8.0*m*Dm*zs*self.z1\
        -4.0*Dm**2*self.z1**2\

```

```

-4.0*m**2*self.z1**2\
-4.0*m*zs*np.conj(zs)*self.z1**2\
-4.0*Dm*np.conj(zs)*self.z1**3\
-np.conj(zs)**2*self.z1**4\
+self.z1**6
c0=self.z1**2*(4.0*Dm**2*zs\
+4.0*m*Dm*self.z1\
+4.0*Dm*zs*np.conj(zs)*self.z1+\
2.0*m*np.conj(zs)*self.z1**2\
+zs*np.conj(zs)**2*self.z1**2\
-2*Dm*self.z1**3-zs*self.z1**4)

coefficients=[c5,c4,c3,c2,c1,c0]

images=np.roots(coefficients)
# drop spurious solutions
z2=-self.z1
deltazs=zs-(images-self.m1/(np.conj(images)-np.conj(self.z1))-
-self.m2/(np.conj(images)-np.conj(z2)))
return (np.array([images.real[np.abs(deltazs)<1e-3]]),
np.array([images.imag[np.abs(deltazs)<1e-3]]))

```

The source position is specified in terms of the two coordinates y_{s1} and y_{s2} , which are used to compute the complex coordinate zs . The polynomial $p_5(z)$ has five roots. However, the source can have 3 or 5 images, depending on whether the source is inside or outside one caustic. Therefore, sometimes two roots have to be discarded because they are spurious solutions of the lens equation. For doing this, we check which solutions satisfy the lens equation. This is done at the end of the function above. Once determined the roots of the polynomial, we insert them in the lens equation to verify if we obtain the input source position. We compute the quantity $deltazs$, i.e. the difference between the input source position and the result of the lens equation, and we discard those solutions for which $deltazs$ is above some tolerance (10^{-3} in this example).

3.9.7 Light curve in a binary microlensing event

Finally, in this example we consider a source moving on a rectilinear trajectory with respect to the binary lens and derive its light curve. The parameters defining the trajectory of the source ($y0$, $t0$, $theta$, $vrel$) are used to initialize the `binary_lens` object.

The source position at a given time can be computed as follows:

```

def SourcePos(self,t):
    p=(t-self.t0)/self_tE.value
    zreal=np.cos(self.theta)*p+np.sin(self.theta)*self.y0
    zimag=np.sin(self.theta)*p-np.cos(self.theta)*self.y0
    return(zreal,zimag)

```

Then, the source position can be fed into the `Images` function to compute the corresponding images. For example, to produce Fig. 3.7.2, we used the following code:

```

times=np.linspace(-90,90,730)
bl=binary_lens(m1=1.0,q=1.0,d=1.,t0=0.0,y0=0.25,
               theta=np.pi/4.*3.0)

```

```

x1,x2,xs1,xs2=bl.CritCau()

color=iter(cm.rainbow(np.linspace(0,1,times.size)))

fig,ax=plt.subplots(1,2,figsize=(18,8))

for t in times:
    c=next(color)
    ys1,ys2=bl.SourcePos(t)
    xi1,xi2=bl.Images(ys1,ys2)
    ax[1].plot(ys1,ys2,'*',markersize=10,color=c)
    ax[0].plot(xi1,xi2,'o',markersize=10,color=c)

    ax[0].plot(x1,x2,',',color='blue')
    ax[1].plot(xs1,xs2,',',color='blue')

```

As in the case of microlensing by single lenses, multiple images remain undetected and the binary microlensing can be revealed only by means of how the magnification varies as a function of time.

The magnification of each image can be computed using the formula

$$\det A = 1 - \left| \sum_{i=1}^2 \frac{m_i}{(z^* - z_i^*)^2} \right|$$

considering that $\mu = \det A^{-1}$.

To perform these calculations, we use the following functions

```

def detA(self,z):
    z2=-self.z1
    deta=1-np.abs(self.m1/(np.conj(z)-
                           np.conj(self.z1))**2+
                  self.m2/(np.conj(z)-np.conj(z2))**2)
    return(deta)

def Magnification(self,t):
    ys1,ys2=self.SourcePos(t)
    xi1,xi2=self.Images(ys1,ys2)
    images=xi1+1j*xi2
    mu=1.0/self.detA(images)
    return(np.abs(mu).sum())

def LightCurve(self,times):
    p=(times-self.t0)/self_tE.value
    mu=[]
    for t in times:
        mu.append(self.Magnification(t))
    return(p, mu)

```

The function `detA(z)` returns the Jacobian determinant at the image positions z . The function `Magnification(t)` performs the following operations. First, the source position is computed at

time t . Second, the images are found by solving the lens equation. Third, the magnification of each image is calculated as the inverse of `detA`. Fourth, the sum of the unsigned image magnification is returned.

Finally, the function `LightCurve(t)` uses the function `Magnification` to compute the light curve, returning the scaled time $p = (t - t_0)/t_E$ and the corresponding magnification values.

The code below can be used to produce Fig. 3.7.3.

```
p, mu=bl.LightCurve(times)

fig,ax=plt.subplots(1,2,figsize=(18,8))

color=iter(cm.rainbow(np.linspace(0,1,times.size)))
ys1,ys2=bl.SourcePos(times)
for i in range(times.size):
    c=next(color)
    #ys1,ys2=bl.SourcePos(times[i])
    ax[0].plot(ys1[i],ys2[i],'*',markersize=10,c=c)
    ax[1].plot([p[i]],[mu[i]],'o',markersize=10,c=c)

ax[0].plot(ys1,ys2,'--',color='blue')
ax[1].plot(p,mu,'-')
ax[1].set_xlim([0.0,np.max(mu)*1.1])
ax[0].set_xlim([xmin_,xmax_])
ax[0].set_ylim([ymin_,ymax_])

ax[0].xaxis.set_tick_params(labelsize=20)
ax[0].yaxis.set_tick_params(labelsize=20)

ax[0].set_xlabel('$y_1$', fontsize=20)
ax[0].set_ylabel('$y_2$', fontsize=20)

ax[1].xaxis.set_tick_params(labelsize=20)
ax[1].yaxis.set_tick_params(labelsize=20)
ax[1].set_xlabel('$(t-t_0)/t_E$', fontsize=20)
ax[1].set_ylabel('$\mu(t)$', fontsize=20)
ax[0].plot(xs1, xs2, ',', color='blue')
```

4. Extended lenses

In this chapter, we review some properties of extended lenses, i.e. gravitational lenses which can be described by extended, bound, mass distributions. Cosmic structures like galaxies and galaxy cluster belong to this class of gravitational lenses.

First, we consider analytic lens models, i.e. models whose lensing properties are (almost) fully expressed by means of analytic formulas. We change a few properties of the lens mass distributions to understand how these impact the ability to produce gravitational lensing effects. In particular, we focus on:

- the density profile;
- the shape;
- the small scale perturbations;
- the effects of the environment.

4.1 Axially symmetric lenses

We begin with the simplest description of an extended lens, i.e. an axially symmetric, or circular, lens. For such lens, the lensing potential only depends on the distance from the lens center, independently on the direction. Given the symmetry properties of the lens, it is convenient to choose the origin of the reference frame at the center of the lens. Most of the equations therefore reduce to a one-dimensional form.

Deflection angle

Let the lensing potential be

$$\hat{\Psi}(\vec{\theta}) = \hat{\Psi}(\theta) \quad (4.1)$$

where $\vec{\theta}$ is the usual vector (in angular units) on the lens plane. To use physical units, we have to multiply by the angular diameter distance to the lens plane, $\xi = D_L \vec{\theta}$.

As seen, in Sect. 2.2, the (reduced) deflection angle, $\vec{\alpha}(\theta)$, is the gradient of the lensing potential (in angular units). It is convenient to use polar coordinates. Then, the gradient can be

written as

$$\vec{\nabla}_\theta \equiv D_L \left(\frac{\partial}{\partial \xi} \vec{e}_\xi + \frac{1}{\xi} \frac{\partial}{\partial \phi} \vec{e}_\phi \right) = \left(\frac{\partial}{\partial \theta} \vec{e}_\theta + \frac{1}{\theta} \frac{\partial}{\partial \phi} \vec{e}_\phi \right), \quad (4.2)$$

where ϕ is the polar angle, $\vec{e}_\xi = \vec{e}_\theta$ and \vec{e}_ϕ are unit vectors, the first pointing in the radial direction and the second perpendicular to it.

Since the lensing potential does not depend on ϕ , for axially symmetric lenses the gradient of $\hat{\Psi}(\theta)$ is

$$\nabla_\theta \hat{\Psi}(\vec{\theta}) = \hat{\Psi}'(\theta) \vec{e}_\theta = \vec{\alpha}(\vec{\theta}) = \alpha(\theta) \vec{e}_\theta. \quad (4.3)$$

Thus, the deflection angle is *central*, i.e. parallel to $\vec{\theta}$. In the equation above, we used the Lagrange notation for the derivatives, i.e. $\hat{\Psi}'(\theta) = \partial \hat{\Psi}(\theta) / \partial \theta$.

In addition, the laplacian of the lensing potential is twice the convergence, as shown in Eq. 2.24. Writing the laplacian operator in polar coordinates, we obtain

$$\frac{1}{\theta} \frac{\partial}{\partial \theta} \left(\theta \frac{\partial}{\partial \theta} \right) \hat{\Psi}(\theta) = 2\kappa(\theta). \quad (4.4)$$

From this equation, we derive that

$$\begin{aligned} \alpha(\theta) &= \frac{2 \int_0^\theta \kappa(\theta') \theta' d\theta'}{\theta} \\ &= \frac{2 \int_0^\theta \Sigma(\theta') \theta' d\theta'}{\theta \Sigma_{\text{cr}}} \\ &= \frac{D_{\text{LS}}}{D_{\text{S}}} \frac{4GM(\theta)}{c^2 D_{\text{L}} \theta} \\ &= \frac{D_{\text{LS}}}{D_{\text{S}}} \hat{\alpha}(\theta). \end{aligned} \quad (4.5)$$

This formula is identical to that of the deflection angle of the point-mass lens (e.g., Eq. 3.5), with the only difference that the mass M is substituted by the mass enclosed by the radius θ , $M(\theta)$.

As usual, we can use the dimensionless notation. This implies the choice of an arbitrary linear scale, ξ_0 , which corresponds to the angular scale $\theta_0 = \xi_0 / D_{\text{L}}$. From Eqs. 2.6 and 2.17, the reduced deflection angle in the dimensionless form is:

$$\begin{aligned} \alpha(x) &= \frac{D_{\text{L}} D_{\text{LS}}}{\xi_0 D_{\text{S}}} \hat{\alpha}(\xi_0 x) \\ &= \frac{D_{\text{L}} D_{\text{LS}}}{\xi_0 D_{\text{S}}} \frac{4GM(\xi_0 x) \pi \xi_0}{c^2 \xi} \frac{\pi \xi_0}{\pi \xi_0} \\ &= \frac{M(\xi_0 x)}{\pi \xi_0^2 \Sigma_{\text{cr}}} \frac{1}{x} \equiv \frac{m(x)}{x}, \end{aligned} \quad (4.7)$$

where we have introduced the *dimensionless mass* $m(x)$. Note that

$$\alpha(x) = \frac{2}{x} \int_0^x x' \kappa(x') dx' \Rightarrow m(x) = 2 \int_0^x x' \kappa(x') dx'. \quad (4.8)$$

Lens equation

Since $\vec{\alpha}(\vec{\theta})$ is parallel to $\vec{\theta}$, the lens equation (2.2) can be written omitting the vector notation. Using Eq. 4.6, we obtain

$$\beta = \theta - \frac{D_{\text{LS}}}{D_{\text{S}} D_{\text{L}}} \frac{4GM(\theta)}{c^2 \theta}. \quad (4.9)$$

Using the dimensionless notation and Eq. 4.8, the lens equation is written as

$$y = x - \frac{m(x)}{x}. \quad (4.10)$$

Convergence and shear

From Eq. 4.4, we can easily find that the convergence is

$$\kappa(\theta) = \frac{1}{2} \left[\hat{\Psi}''(\theta) + \frac{\hat{\Psi}'(\theta)}{\theta} \right], \quad (4.11)$$

Since

$$\hat{\Psi}'(\theta) = \alpha(\theta), \quad (4.12)$$

we obtain that

$$\kappa(\theta) = \frac{1}{2} \left[\alpha'(\theta) + \frac{\alpha(\theta)}{\theta} \right]. \quad (4.13)$$

The equation assumes the identical form using dimensionless units. Using Eq. 4.7, we can easily see that

$$\alpha'(x) = \frac{m'(x)}{x} - \frac{m(x)}{x^2}. \quad (4.14)$$

Thus,

$$\kappa(x) = \frac{1}{2} \frac{m'(x)}{x}. \quad (4.15)$$

The components of the shear are also readily derived by writing the partial derivative operators in polar coordinates,

$$\begin{aligned} \frac{\partial}{\partial \theta_1} &= \cos \phi \frac{\partial}{\partial \theta} - \frac{\sin \phi}{\theta} \frac{\partial}{\partial \phi}, \\ \frac{\partial}{\partial \theta_2} &= \sin \phi \frac{\partial}{\partial \theta} + \frac{\cos \phi}{\theta} \frac{\partial}{\partial \phi}. \end{aligned} \quad (4.16)$$

Since,

$$\begin{aligned} \alpha_1(\theta) &= \alpha(\theta) \cos \phi, \\ \alpha_2(\theta) &= \alpha(\theta) \sin \phi. \end{aligned} \quad (4.17)$$

from Eqs. 2.37 and 2.38, we obtain that

$$\begin{aligned} \gamma_1(\theta) &= \frac{1}{2} \left[\frac{\partial}{\partial \theta_1} \alpha_1(\theta) - \frac{\partial}{\partial \theta_2} \alpha_2(\theta) \right] \\ &= \frac{1}{2} \left[(\cos^2 \phi - \sin^2 \phi) \alpha'(\theta) - (\cos^2 \phi - \sin^2 \phi) \frac{\alpha(\theta)}{\theta} \right] \\ &= \frac{\cos 2\phi}{2} \left[\alpha'(\theta) - \frac{\alpha(\theta)}{\theta} \right], \end{aligned} \quad (4.18)$$

and

$$\begin{aligned} \gamma_2(\theta) &= \frac{\partial}{\partial \theta_2} \alpha_1(\theta) \\ &= \left[\sin \phi \cos \phi \alpha'(\theta) - \sin \phi \cos \phi \frac{\alpha(\theta)}{\theta} \right] \\ &= \frac{\sin 2\phi}{2} \left[\alpha'(\theta) - \frac{\alpha(\theta)}{\theta} \right]. \end{aligned} \quad (4.19)$$

Thus, using the dimensionless notation, we find that

$$\begin{aligned}\gamma(x) &= \frac{1}{2} \left| \frac{m'(x)}{x} - \frac{2m(x)}{x^2} \right| \\ &= |\kappa(x) - \bar{\kappa}(x)|,\end{aligned}\quad (4.20)$$

where $\bar{\kappa}(x)$ is the mean convergence within a circle of radius x :

$$\bar{\kappa}(x) = \frac{m(x)}{x^2} = 2\pi \frac{\int_0^x x' \kappa(x') dx'}{\pi x^2}. \quad (4.21)$$

Lensing Jacobian

We will continue to use the dimensionless notation in the following. Using the results above, the Jacobian matrix can be written as

$$A = \left[1 - \frac{m'(x)}{2x} \right] I - \frac{1}{2} \left[\frac{m'(x)}{x} - \frac{2m(x)}{x^2} \right] \begin{pmatrix} \cos 2\phi & \sin 2\phi \\ \sin 2\phi & -\cos 2\phi \end{pmatrix}. \quad (4.22)$$

This equation can be re-arranged in the form

$$A = I + \frac{m(x)}{x^2} C(\phi) - \frac{m'(x)}{2x} [I + C(\phi)], \quad (4.23)$$

where the matrix $C(\phi)$ is

$$\begin{aligned}C(\phi) &= \begin{pmatrix} \cos 2\phi & \sin 2\phi \\ \sin 2\phi & -\cos 2\phi \end{pmatrix} \\ &= \begin{pmatrix} \cos^2 \phi - \sin^2 \phi & 2 \sin \phi \cos \phi \\ 2 \sin \phi \cos \phi & \sin^2 \phi - \cos^2 \phi \end{pmatrix}.\end{aligned}\quad (4.24)$$

Given that

$$\begin{aligned}I + C(\phi) &= \begin{pmatrix} 1 + \cos 2\phi & \sin 2\phi \\ \sin 2\phi & 1 - \cos 2\phi \end{pmatrix} \\ &= 2 \begin{pmatrix} \cos^2 \phi & \sin \phi \cos \phi \\ \sin \phi \cos \phi & \sin^2 \phi \end{pmatrix},\end{aligned}\quad (4.25)$$

we find that

$$\begin{aligned}A &= I + \frac{m(x)}{x^2} \begin{pmatrix} \cos^2 \phi - \sin^2 \phi & 2 \sin \phi \cos \phi \\ 2 \sin \phi \cos \phi & \sin^2 \phi - \cos^2 \phi \end{pmatrix} - \\ &\quad \frac{m'(x)}{x} \begin{pmatrix} \cos^2 \phi & \sin \phi \cos \phi \\ \sin \phi \cos \phi & \sin^2 \phi \end{pmatrix}.\end{aligned}\quad (4.26)$$

The Jacobian matrix in terms of the cartesian coordinates, $(x_1, x_2) = (x \cos \phi, x \sin \phi)$, is

$$\begin{aligned}A &= I + \frac{m(x)}{x^4} \begin{pmatrix} x_1^2 - x_2^2 & 2x_1 x_2 \\ 2x_1 x_2 & x_2^2 - x_1^2 \end{pmatrix} \\ &\quad - \frac{m'(x)}{x^3} \begin{pmatrix} x_1^2 & x_1 x_2 \\ x_1 x_2 & x_2^2 \end{pmatrix}.\end{aligned}\quad (4.27)$$

The determinant of the Jacobian matrix is derived from the lens equation:

$$\begin{aligned}\det A &= \frac{y dy}{x dx} = \left[1 - \frac{\alpha(x)}{x} \right] [1 - \alpha'(x)] \\ &= \left[1 - \frac{m(x)}{x^2} \right] \left[1 + \frac{m(x)}{x^2} - \frac{m'(x)}{x} \right] \\ &= [1 - \bar{\kappa}(x)] [1 + \bar{\kappa}(x) - 2\kappa(x)].\end{aligned}\quad (4.28)$$

Critical lines and caustics

Since the critical lines form where $\det A = 0$, Eq. 4.28 implies that axially symmetric lenses with monotonically increasing $m(x)$ have at most two critical lines, where $\alpha(x)/x = m(x)/x^2 = \bar{\kappa}(x) = 1$ and $\alpha'(x) = m'(x)/x - m/x^2 = 2\kappa(x) - \bar{\kappa}(x) = 1$. Both these conditions define circles on the lens plane. The first condition defines the tangential critical line. On the contrary, the second condition defines the radial critical line. This can be seen as follows. Consider a point $(x, 0)$ on the first critical line. The Jacobian matrix at $(x, 0)$ is readily derived from Eq. 4.27:

$$A(x, 0) = I + \frac{m(x)}{x^2} \begin{pmatrix} 1 & 0 \\ 0 & -1 \end{pmatrix} - \frac{m'(x)}{x} \begin{pmatrix} 1 & 0 \\ 0 & 0 \end{pmatrix}. \quad (4.29)$$

Let consider a vector whose components are $(0, a)$ at $(x, 0)$. This vector is clearly tangential to the critical line at $(x, 0)$. Through the lens mapping, it is mapped onto

$$\begin{pmatrix} y_1 \\ y_2 \end{pmatrix} = A(x, 0) \begin{pmatrix} 0 \\ a \end{pmatrix} \quad (4.30)$$

If $(x, 0)$ lays on the tangential critical line, then $[1 - m(x)/x^2] = 0$ and

$$\begin{pmatrix} y_1 \\ y_2 \end{pmatrix} = \left[1 - \frac{m(x)}{x^2} \right] \begin{pmatrix} 0 \\ a \end{pmatrix} = \begin{pmatrix} 0 \\ 0 \end{pmatrix}. \quad (4.31)$$

Thus any vector tangent to the critical line is an eigenvector of A with 0 eigenvalue.

Consider now a vector $(b, 0)$, normal to the critical line at $(x, 0)$. Mapping it to the source plane we obtain:

$$\begin{pmatrix} y_1 \\ y_2 \end{pmatrix} = A(x, 0) \begin{pmatrix} b \\ 0 \end{pmatrix} = \left[1 + \frac{m(x)}{x^2} - \frac{m'(x)}{x} \right] \begin{pmatrix} b \\ 0 \end{pmatrix}. \quad (4.32)$$

If $(x, 0)$ lays on the radial critical line, then $[1 + m(x)/x^2 - m'(x)/x] = 0$, thus $(b, 0)$ is an eigenvector of A is 0 eigenvalue.

From the lens equation it can be easily seen that all the points along the tangential critical line are mapped on the point $y = 0$ on the source plane. Indeed:

$$y = x \left[1 - \frac{m(x)}{x^2} \right] = 0. \quad (4.33)$$

if x indicates a tangential critical point. Therefore, axially symmetric models have point tangential caustics. On the other hand, the points along the radial critical line are mapped onto a circular caustic on the source plane.

Image distortions near the critical lines

Let us consider now how the images are distorted near the critical lines. Consider a point $(x_c, 0)$ very close to the tangential critical line. At this point,

$$\frac{m(x)}{x^2} = 1 - \delta, \quad (4.34)$$

where $\delta \ll 1$.

Using Eq. 4.29, we see that near the tangential critical line the Jacobian is approximated by

$$A(x_c, 0) \simeq \begin{pmatrix} 2 - m'/x_c & 0 \\ 0 & \delta \end{pmatrix}. \quad (4.35)$$

In the first element of the matrix we have neglected δ and $m' = m'(x_c)$. Consider an ellipse around $\vec{x}_c = (x_c, 0)$,

$$\vec{c}(\phi) = \vec{x}_c + \begin{pmatrix} \rho_1 \cos \phi \\ \rho_2 \sin \phi \end{pmatrix}. \quad (4.36)$$

Through the lens mapping, the source of this ellipse is

$$\vec{d}(\phi) = \vec{y}_c + \begin{pmatrix} \rho_1(2 - m'/x_c) \cos \phi \\ \rho_2 \delta \sin \phi \end{pmatrix}. \quad (4.37)$$

Suppose that $\vec{d}(\phi)$ is a circle, i.e. $\rho_1(2 - m'/x_c) = \rho_2 \delta$. Then,

$$\frac{\rho_2}{\rho_1} = \frac{2 - m'/x_c}{\delta} \gg 1. \quad (4.38)$$

Thus, the ellipse is strongly elongated along the x_2 direction.

On the contrary, suppose that $(x_c, 0)$ is very close to the radial critical line. In this case,

$$\frac{m'}{x_c} - \frac{m}{x_c^2} = 1 - \delta, \quad (4.39)$$

with $\delta \ll 1$. The Jacobian matrix at $(x_c, 0)$ is then

$$A(x_c, 0) \simeq \begin{pmatrix} \delta & 0 \\ 0 & 1 - m/x_c^2 \end{pmatrix}. \quad (4.40)$$

The source corresponding to the ellipse in Eq. 4.36 is

$$\vec{d}(\phi) = \vec{y}_c + \begin{pmatrix} \rho_1 \delta \cos \phi \\ \rho_2(1 - m/x_c^2) \sin \phi \end{pmatrix}. \quad (4.41)$$

Thus, if $\vec{d}(\phi)$ is a circle,

$$\frac{\rho_1}{\rho_2} = \frac{1 - m/x_c^2}{\delta} \gg 1, \quad (4.42)$$

and the ellipse is now strongly elongated along the x_1 direction.

Summarizing, any image near the tangential critical curve is strongly distorted tangentially to the curve itself. On the contrary, any image near the radial critical curve is radially distorted.

Tangential and radial magnification of the images

The eigenvalues of the Jacobian matrix are the inverse magnifications of the image along the tangential and radial directions. Fig. (4.1.1) illustrates an infinitesimal source of diameter δ at position y and its image, which is an ellipse, whose minor and major axes are ρ_1 and ρ_2 respectively, at position x . With respect to the origin of the reference frame on the source plane, the circular source subtends an angle $\phi = \delta/y$. Due to the axial symmetry of the lens, $\phi = \rho_2/x$. Using the lens equation, we thus obtain

$$\frac{\delta}{\rho_2} = 1 - \frac{m(x)}{x^2}. \quad (4.43)$$

The lens mapping gives $\delta = \rho_1(dy/dx)$, from which

$$\frac{\delta}{\rho_1} = 1 + \frac{m(x)}{x^2} - 2\kappa(x) \quad (4.44)$$

This means that the image is stretched in the tangential direction by a factor $[1 - m(x)/x^2]^{-1}$ and in the radial direction by $[1 + m(x)/x^2 - 2\kappa(x)]^{-1}$.

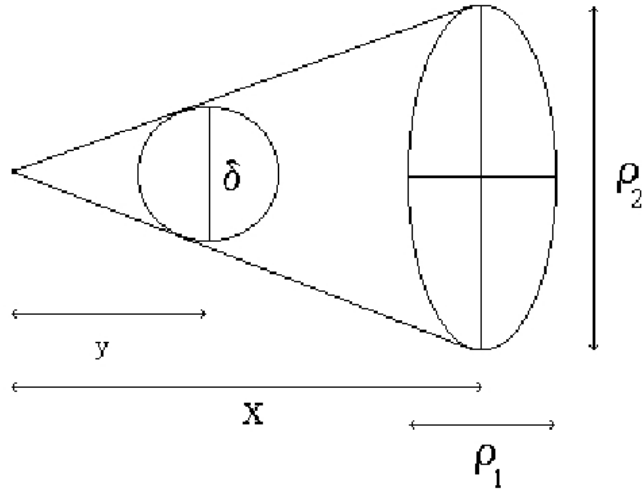


Figure 4.1.1: Sketch of the mapping of an infinitesimal circular source onto an elliptical image (Figure from Schneider et al., 1992).

4.2 Power-law lens

The formulas above are valid for any axially symmetric lens. Now, we consider a particular class of lenses, whose mass profile has a power-law form of the kind

$$m(x) = x^{3-n}. \quad (4.45)$$

Note that, using this definition, $m(1) = 1$. This implies that the Einstein radius in dimensionless units is $x = 1$.

The convergence profile is readily derived from Eq. 4.15 and is given by

$$\kappa(x) = \frac{m'(x)}{2x} = \frac{3-n}{2} x^{1-n}. \quad (4.46)$$

Depending on n being larger or smaller than one, $\kappa(x)$ is a decreasing or an increasing function of x . Values of $n < 1$ are of little interest in the context of lensing by extended and gravitationally bound lenses. Therefore, they are not considered here.

4.2.1 Lenses with $1 < n < 2$

We consider lenses with $1 < n < 2$ for the moment. The case $n = 1$ corresponds to a lens with constant convergence, $\kappa = 1$. The deflection angle is

$$\alpha(x) = \frac{m(x)}{x} = x^{2-n}. \quad (4.47)$$

Thus, this class of lenses have deflection angle profiles which monotonically increase with x and that are zero at the origin, $\alpha(0) = 0$. The case $n = 1$, gives $\alpha(x) = x$, which, when inserted into the lens equation, implies that $y(x) = 0$ for any x . Thus, this lens is perfectly convergent.

Critical lines and caustics

Because of the chosen normalization of the mass profile, the tangential critical line of the power-law lens is a circle with radius $x_t = 1$. This is the Einstein ring, whose radius can be derived in angular units as follows.

At the tangential critical line, we have that $m(x) = x^2$. Thus,

$$M(\theta_E) = \pi \Sigma_{\text{cr}} \theta_E^2 D_L^2. \quad (4.48)$$

Substituting Eq. 2.17 into Eq. 4.48 and solving for θ_E , we obtain

$$\theta_E = \sqrt{\frac{4GM(\theta_E)}{c^2} \frac{D_{\text{LS}}}{D_L D_S}}. \quad (4.49)$$

This equation is identical to Eq. 3.7, but the total lens mass M is now substituted by the mass within the Einstein radius, $M(\theta_E)$.

As seen earlier, inserting x_t into the lens equation leads to find that the tangential caustic is a point at $y = 0$.

Instead, the size of the radial critical line in units of the Einstein radius depends on the power-law index n . By using Eqs. 4.47 and ??, we find that

$$(2-n)x_r^{1-n} = 1, \quad (4.50)$$

which can be solved for x_r , obtaining

$$x_r = (2-n)^{1/(n-1)}. \quad (4.51)$$

In Fig. 4.2.1, we show how the size of the radial critical line (in units of the Einstein radius) varies as a function of n . By making the substitution $n' = 1/(n-1)$, we find that

$$x_r = \left(1 - \frac{1}{n'}\right)^{n'}. \quad (4.52)$$

Thus, for $n \rightarrow 1$, or $n' \rightarrow \infty$,

$$x_r = \lim_{n' \rightarrow \infty} \left(1 - \frac{1}{n'}\right)^{n'} = \frac{1}{e}. \quad (4.53)$$

The figure shows that the radial critical line becomes smaller as n increases, being zero for $n \rightarrow 2$. Thus, lenses with steep profiles have small radial critical lines.

In the same figure, we show also the size of the radial caustic. Contrary to the size of the radial critical line, the size of the radial caustic grows as a function of n . In particular, for $n \rightarrow 2$, $y_r \rightarrow 1$.

Multiple images

The number of multiple images that the power-law lens can produce can be readily discovered by inspecting the so called *image diagram*, shown in Fig. 4.2.2. The solid lines in the three panels show the curves $\alpha(x)$ corresponding to three values of the power under n , namely $n = 1.1, 1.5$ and 1.9 . The lens equation states that the images of a source at position y can be found by equalling $\alpha(x)$ and $f(x) = x - y$. The latter is a linear function with unit slope and intercept $-y$. Some examples, corresponding to values of y increasing from 0 to 1.2 , are given by the colored dashed lines. The interceptions between $f(x)$ and $\alpha(x)$ are marked with colored dots, which thus identify, when projected on the x axis, the locations of the multiple images of the source.

As we can see, the power-law lens with $1 < n < 2$ can produce either three or one image of the background source, depending on whether y is smaller or larger than a particular value y_r . In fact,

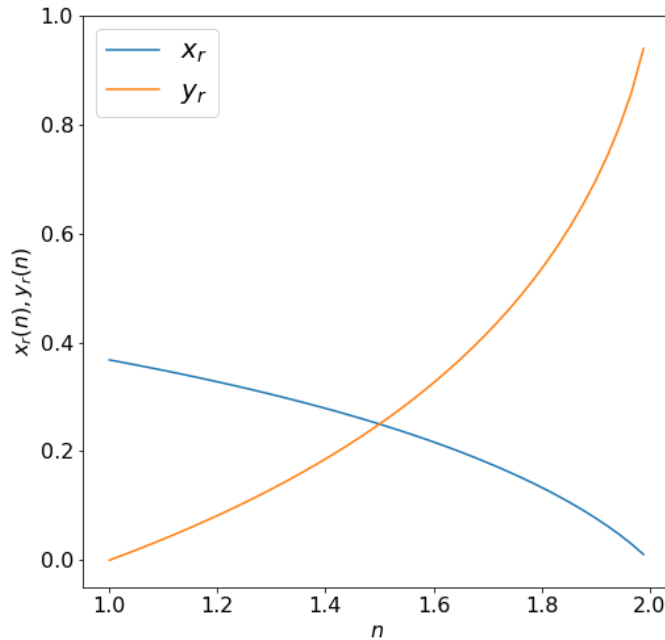


Figure 4.2.1: Size of the radial critical line and caustic (in units of the Einstein radius) as a function of the power-law index n .

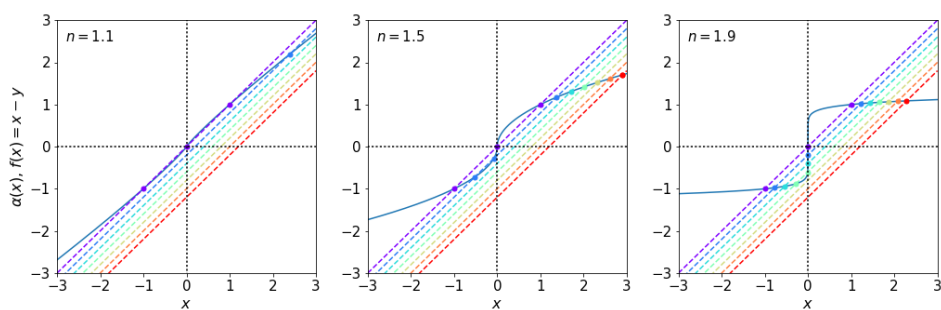


Figure 4.2.2: Image diagram for power-law lenses with $n = 1.1$ (left panel), $n = 1.5$ (central panel), and $n = 1.9$ (right panel). The solid curves show the function $\alpha(x)$. The colored dashed lines show the function $f(x) = x - y$ for a range of values of $y \in [0, 1.2]$.

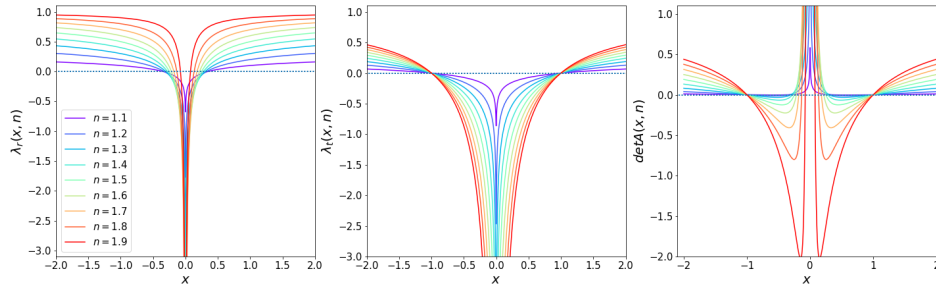


Figure 4.2.3: Left and central panels: Radial and tangential eigenvalues of the Jacobian matrix as a function of x for different values of n . Right panel: determinant of the lensing Jacobian, resulting from the product of the curves in the first two panels.

there exist a value of $y = y_r$ such that the line $f(x) = x - y_r$ is tangent to $\alpha(x)$. At the tangency point two images of the source merge, and for $y > y_r$, they no longer exist. Obviously, y_r is the radius of a caustic and the solution of the equation

$$\alpha(x_r) = x_r - y_r \quad (4.54)$$

gives the radius of a critical line. Indeed, the tangency condition is $\alpha'(x_r) = 1$ which defines the *radial* critical line.

Thus, multiple images exist only if the source is inside the radial caustic, $0 < y \leq y_r$. One image form on the positive x axis, with $x > y$. Moreover, such image is outside the Einstein ring, $x > 1$. Two additional images form inside the Einstein ring, on the negative x axis. Of these two images, the inner one is inside the radial critical line, $|x| < x_r$. The other is between the radial and the tangential critical line.



For $y = 0$, the innermost image form at $x = 0$. Thus, a source right behind a power-law lens with $1 < n < 2$ is mapped onto an Einstein ring and a central image.

Image magnification

The eigenvalues of the Jacobian matrix are readily derived

$$\lambda_t(x) = 1 - x^{1-n} \quad (4.55)$$

$$\lambda_r(x) = 1 - (2-n)x^{1-n}. \quad (4.56)$$

In the left and central panels of Fig. 4.2.3, these eigenvalues are shown as a function of x . The sign of each eigenvalue changes from outside to inside the critical lines. Thus, the overall parity of the images changes accordingly. In particular, the outermost image always have positive parity. Both eigenvalues are positive, meaning that this image correspond to a minimum of the time delay surface. The image forming in between the radial and the tangential critical lines has negative parity ($\mu < 0$). Indeed, the eigenvalues have opposite signs, thus the image is a saddle point of the time delay surface. The innermost image has again positive parity and the two eigenvalues are both negative. This image is a maximum of the time delay surface.

The right panel of Fig. 4.2.3 shows how the determinant of the lensing Jacobian matrix A varies as a function of x . For $|\det A| < 1$, the total magnification is larger than one. This is the case for the image outside the Einstein radius and for the inner images when they are close to the critical lines. On the contrary, the innermost image can be strongly de-magnified since $|\det A|$ can significantly exceed 1 near the center of the lens.

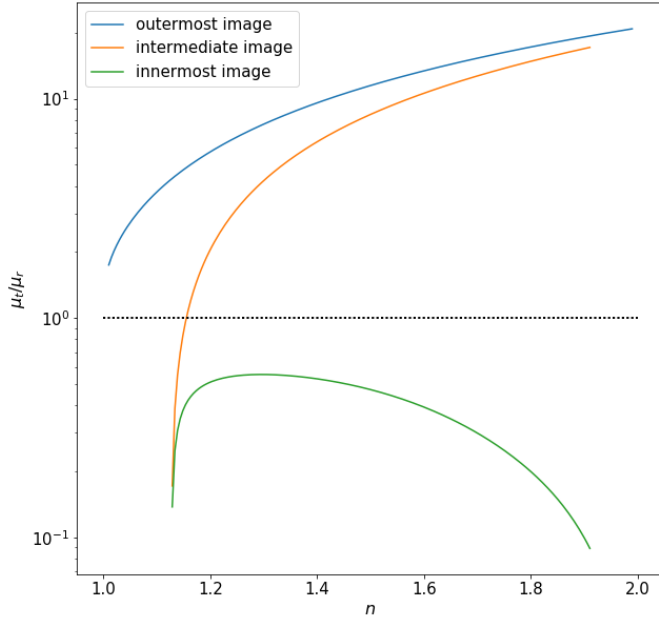


Figure 4.2.4: Magnification ratio at the position of the multiple images of a source at $y = 0.2$.

In Fig. 4.2.4, we show the ratio of the tangential to radial magnification for each of the three images for a given value of $y = 0.05$. The outermost image is characterized by a tangential to radial magnification which always exceeds one. Thus the overall distortion of this image is always tangential. The innermost image is predominantly radially distorted. In the case shown in the figure, the image is on the radial critical line for $n \sim 1.15$. For n smaller than this value, the source only has one image. Increasing n , the innermost image moves near the center (see Fig. 4.2.2), but so does the radial critical line. Consequently, the tangential-to-radial magnification ratio decreases also for large n . The intermediate image shows a transition from being predominantly radially to tangentially distorted as n increases. The reason is again that the radial critical line shrinks as n increases.

In Fig. ??, the results discussed above are visualized with four examples, corresponding to lenses with $n = 1.05, 1.2, 1.4$, and 1.9 (from the upper left to the bottom right panels). In each panel, we consider a circular source with radius $r = 0.02\theta_E$ (navy circle). The source is very close to the center of the lens projected onto the source plane ($y = 0.05$). The outermost, intermediate, and innermost images of the source are shown in orange, green, and the dark-red colors, respectively. The red and blue solid circles show the radial and the tangential critical lines of the lens. The dashed circle is the radial caustic. Note that the size of the caustic grows as the value of n increases. Therefore, the position of the source relative to the caustic changes as well. In the upper left panel, the source is outside the caustic, meaning that it has only one image. Not only is the tangential magnification of this image large, but so is also the radial magnification, due to the small value of $n = 1.05$. For $n = 1.2$ (upper right panel) the source extends across the radial caustic. The innermost and the intermediate images merge across the corresponding critical line. For larger n (bottom panels), the tangential magnification of the outermost and of the intermediate images largely exceeds the radial magnification. Thus, they appear as long arcs with length-to-width

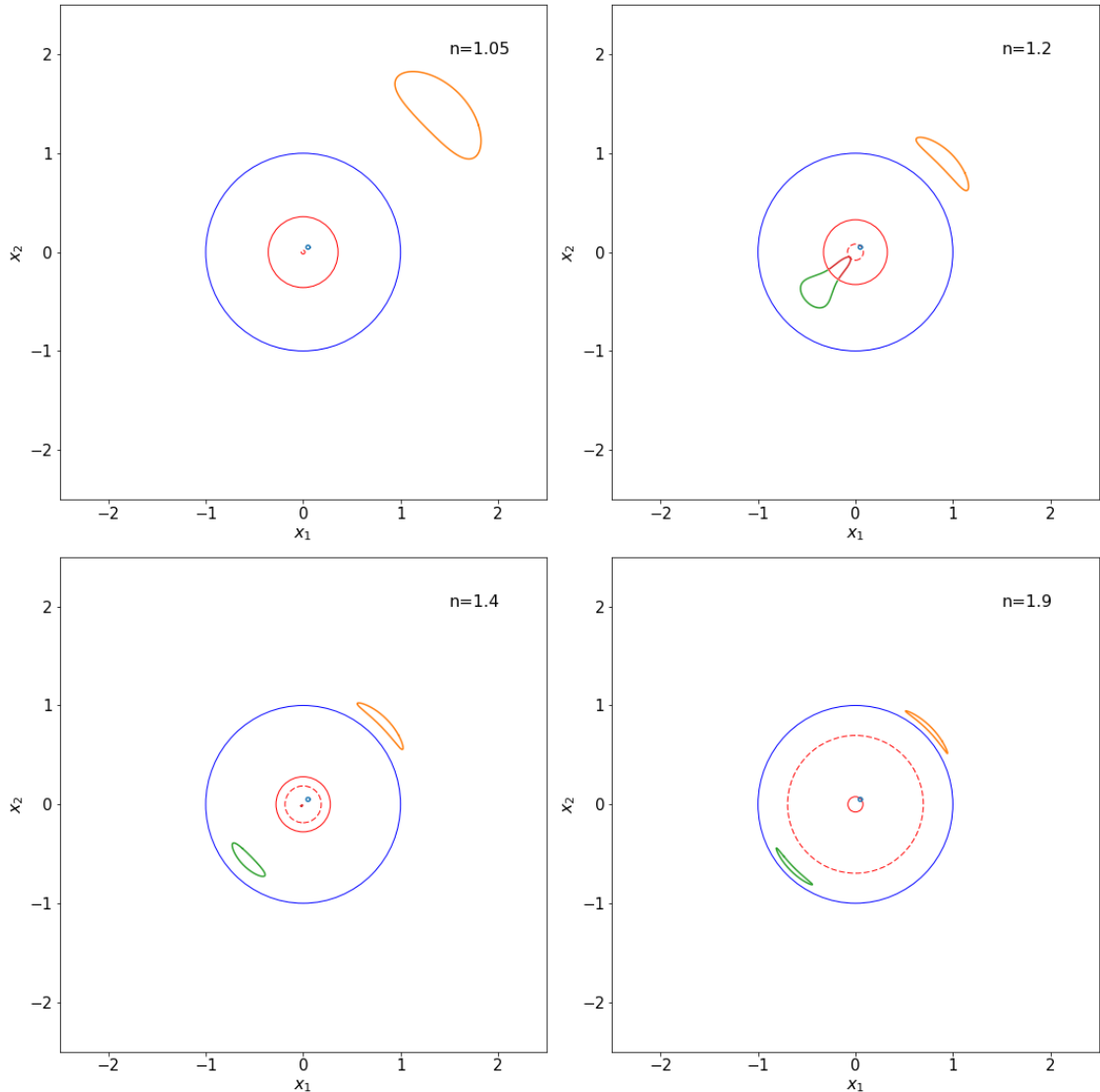


Figure 4.2.5: Images of a circular source (navy circle) placed at a distance $y = 0.05$ from the center of the power-law lenses with index $n = 1.05, 1.2, 1.4$, and 1.9 . In each panel we show the tangential and the radial critical lines (blue and red solid lines) and the radial caustic (dashed red line). The outermost, intermediate, and innermost images are shown in orange, green and dark-red. The source has a radius $r = 0.02\theta_E$.

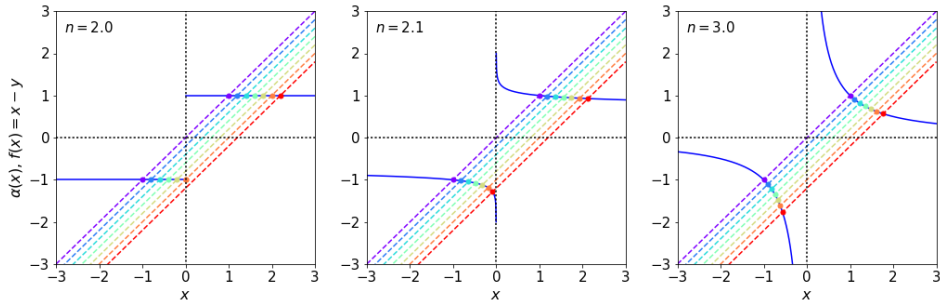


Figure 4.2.6: Image diagram for power-law lenses with $n = 2.0$ (left panel), $n = 2.1$ (central panel), and $n = 3.0$ (right panel). The solid curves show the function $\alpha(x)$. The colored dashed lines show the function $f(x) = x - y$ for a range of values of $y \in [0, 1.2]$.

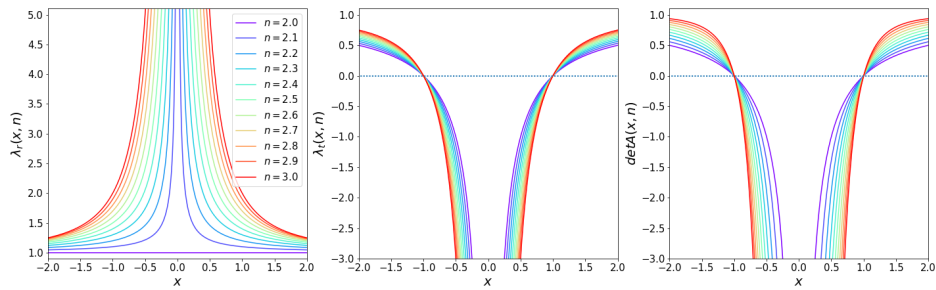


Figure 4.2.7: As in Fig. 4.2.3, but for $n \geq 2$.

ratio significantly larger than one. In particular, as $n \rightarrow 2$, the radial magnification $\mu_r = \lambda_r^{-1} \rightarrow 1$, meaning that the radial sizes of the arcs approach the diameter of the source. The innermost image is severely de-magnified and barely visible only in the bottom left panel.

4.2.2 Lenses with $n > 2$

The power-law lenses with $n \geq 2$ have the peculiarity that the deflection angle profile $\alpha(x)$ is either flat ($n = 2$) or singular $n > 2$. The case $n = 2$ will be discussed in the next section. Here, we briefly discuss the case $n > 2$. In particular, we focus on the image multiplicity. As shown in Fig. 4.2.6, such lenses always produce two images, one outside and one inside the Einstein radius. The image inside the Einstein radius approaches the lens center as y increases. For $y = 0$, the lens produces an Einstein ring. It can be easily seen that both images are radially de-magnified, being $\lambda_r(x) > 1$ for any x , as shown in the left panel of Fig. 4.2.7. The absolute tangential magnification, $|\mu_t|(x) = |\lambda_t^{-1}|(x)$, is larger than unity except near the lens center (central and right panels of Fig. 4.2.7). Thus, the observation of radially de-magnified tangential arcs may suggest that the lens has a steep surface density profile.

R Note that, for power-law lenses with $n > 2$ do not have radial critical lines. The case $n = 3$ corresponds to the point-mass lens. Indeed, $m(x) = m = \text{const.}$ and $\alpha(x) = m/x$ for such lens.

4.2.3 Singular Isothermal Sphere

One of the most widely used axially symmetric model is the Singular Isothermal Sphere (SIS hereafter). The density profile of this model can be derived assuming that the matter content of the

lens behaves as an ideal gas confined by a spherically symmetric gravitational potential. This gas is taken to be in thermal and hydrostatic equilibrium. One of the two (three-dimensional) density profiles satisfying these equations is given by

$$\rho(r) = \frac{\sigma_v^2}{2\pi G r^2} , \quad (4.57)$$

where σ_v is the velocity dispersion of the “gas” particles and r is the distance from the sphere center. By projecting the three-dimensional density along the line of sight, we obtain the corresponding surface density

$$\begin{aligned} \Sigma(\xi) &= 2 \frac{\sigma_v^2}{2\pi G} \int_0^\infty \frac{dz}{\xi^2 + z^2} \\ &= \frac{\sigma_v^2}{\pi G} \frac{1}{\xi} \left[\arctan \frac{z}{\xi} \right]_0^\infty \\ &= \frac{\sigma_v^2}{2G\xi} . \end{aligned} \quad (4.58)$$

This density profile has a singularity at $\xi = 0$, where the density is infinite. By choosing

$$\xi_0 = 4\pi \left(\frac{\sigma_v}{c} \right)^2 \frac{D_L D_{LS}}{D_S} \quad (4.59)$$

as the length scale on the lens plane, we obtain:

$$\Sigma(x) = \frac{\sigma_v^2}{2G\xi} \frac{\xi_0}{\xi} = \frac{1}{2x} \frac{c^2}{4\pi G} \frac{D_S}{D_L D_{LS}} = \frac{1}{2x} \Sigma_{cr} . \quad (4.60)$$

Thus, the convergence for the singular isothermal profile is

$$\kappa(x) = \frac{1}{2x} , \quad (4.61)$$

which shows that the SIS profile corresponds to the power-law lens with $n = 2$. Thus, the mass profile is

$$m(x) = |x| , \quad (4.62)$$

and the deflection angle is

$$\alpha(x) = \frac{x}{|x|} . \quad (4.63)$$

Obviously, ξ_0 defined in Eq. 4.59 is the Einstein radius of the SIS.

The lens equation reads

$$y = x - \frac{x}{|x|} . \quad (4.64)$$

As it can also be seen in the left panel of Fig. 4.2.6, if $y < 1$, two solutions of the lens equation exist. Their positions are $x_- = y - 1$ and $x_+ = y + 1$, on opposite sides with respect to the lens center. The corresponding angular positions of the images are

$$\theta_\pm = \beta \pm \theta_E . \quad (4.65)$$

The angular separation between the two images is always $\Delta(\theta) = 2\theta_E$.

On the other hand, if $y > 1$, Eq. (4.64) has a unique solution, $x_+ = y + 1$. Thus, the circle of radius $y = 1$ plays the same role of the radial caustic in the case of power-law lenses with $1 < n < 2$, separating the regions on the source plane corresponding to different image multiplicities. However, this circle is not a caustic, since $\alpha'(x) = 0$ for any x , implying that $\lambda_r = 1$. The circle of radius $y_c = 1$ is called the *cut*. We can see from the lens equation that

$$y_c = \lim_{x \rightarrow 0} y(x) = -\alpha(x). \quad (4.66)$$

The shear follows from Eqs. 4.18 and 4.19. The absolute value of γ is

$$\gamma(x) = \frac{1}{2x}, \quad (4.67)$$

i.e. the shear and the convergence profiles coincide. The shear components are

$$\gamma_1 = \frac{1}{2} \frac{\cos 2\phi}{x}, \quad (4.68)$$

$$\gamma_2 = \frac{1}{2} \frac{\sin 2\phi}{x}. \quad (4.69)$$

From Eq. (4.64), and given that $dy/dx = 1$, the magnification as a function of the image position is given by

$$\mu(x) = \frac{|x|}{|x| - 1}. \quad (4.70)$$

Images are only magnified in the tangential direction, since the radial eigenvalue of the Jacobian matrix is one everywhere.

If $y < 1$, the magnifications of the two images are

$$\mu_+(y) = \frac{y+1}{y} = 1 + \frac{1}{y} \quad ; \quad \mu_-(y) = \frac{|y-1|}{|y-1|-1} = \frac{-y+1}{-y} = 1 - \frac{1}{y}, \quad (4.71)$$

from which we see that for $y \rightarrow 1$, the second image becomes weaker and weaker until it disappears at $y = 1$. On the other hand, for $y \rightarrow \infty$, the source magnification obviously tends to unity: sources which are at large distance from the lens can only be weakly magnified by gravitational lensing.

Note that \vec{x}_+ is a minimum of the time-delay surface, being both eigenvalues of the Jacobian matrix positive at this location (positive parity). Instead, \vec{x}_- , is a saddle-point (negative parity), being the tangential eigenvalue negative.

In the left panel of Fig. 4.2.8, we show the cut (red circle) and the tangential caustic (blue point) of a SIS lens. In the same panel, several extended circular sources are displayed in different colors. In the right panel, the images of the same sources are shown, illustrating the results anticipated above. The blue circle is the tangential critical line, a.k.a. the Einstein ring. Note that a source placed on the caustic is imaged onto and extended Einstein ring.

4.3 Softened (Isothermal) Lenses

The class of lenses studied in the previous section is characterized by a central singularity in the convergence. Now, we discuss the properties of cored lenses. More precisely, we introduce a core in the SIS, obtaining a lens model which is often referenced as the Non-singular Isothermal Sphere (NIS).

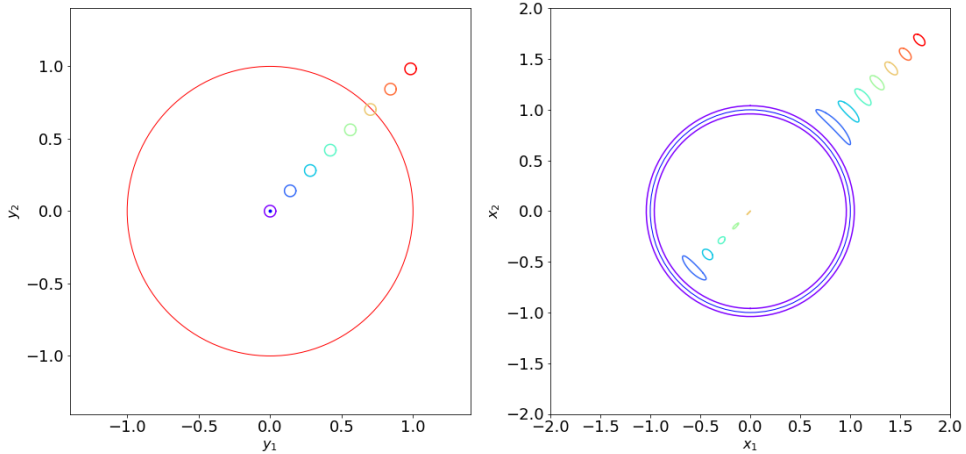


Figure 4.2.8: Imaging of extended sources by a SIS lens.

The core is introduced in the surface density profile of the SIS as follows (see e.g. Kormann, Schneider, and Bartelmann, 1994):

$$\Sigma(\xi) = \frac{\sigma_v^2}{2G} \frac{1}{\sqrt{\xi^2 + \xi_c^2}} = \frac{\Sigma_0}{\sqrt{1 + \xi^2/\xi_c^2}}. \quad (4.72)$$

With this modification, the profile reaches a constant density

$$\Sigma_0 = \frac{\sigma_v^2}{2G\xi_c} \quad (4.73)$$

for $\xi \ll \xi_c$.

If we choose $\xi_0 = 4\pi\sigma_v^2/c^2 D_L D_{LS}/D_S$ (the Einstein radius of the SIS) as scale length on the lens plane, then, using the dimensionless notation,

$$\kappa(x) = \frac{1}{2\sqrt{x^2 + x_c^2}} \quad (4.74)$$

It follows that the mass profile is

$$m(x) = 2 \int_0^x \kappa(x') x' dx' = \sqrt{x^2 + x_c^2} - x_c \quad (4.75)$$

and that the deflection angle profile is

$$\alpha(x) = \frac{m(x)}{x} = \sqrt{1 + \frac{x_c^2}{x^2}} - \frac{x_c}{x} \quad (4.76)$$

The convergence and the deflection angle profiles of the NIS lens model for different choices of x_c are shown in Fig 4.3.1. Note that in order to reach a central convergence $\kappa(0) > 1$, which implies that $\Sigma(0) > \Sigma_{cr}$, the core radius must be $x_c < 1/2$.

The shear can be derived from Eq. 4.20:

$$\gamma(x) = \frac{\sqrt{x^2 + x_c^2} - x_c}{x^2} - \frac{1}{2\sqrt{x^2 + x_c^2}} \quad (4.77)$$

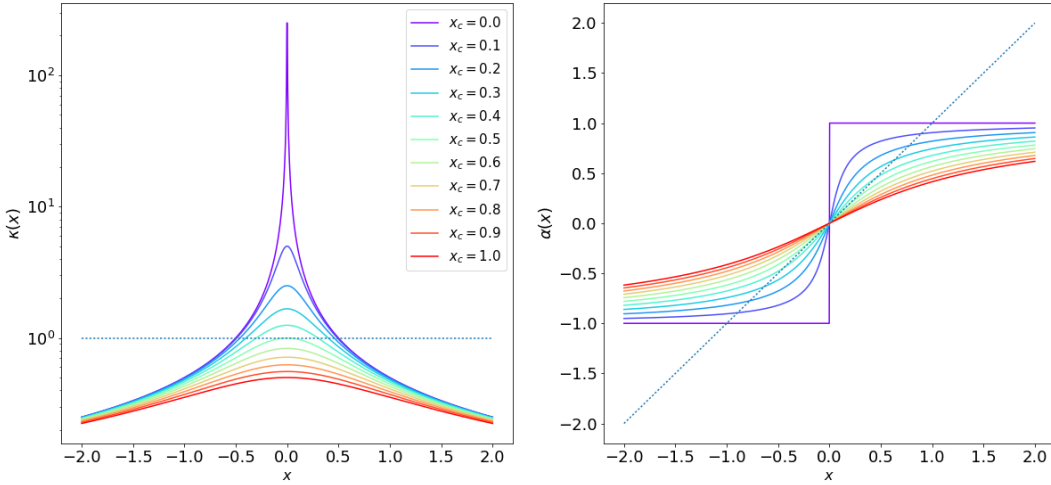


Figure 4.3.1: Convergence and deflection angle profiles of the NIS lens model. Different colors correspond to different values of the core radius x_c .

Note that ξ_0 is not the Einstein radius of the NIS. In units of ξ_0 , this can be calculated by solving the equation $y/x = 1 - m(x)/x^2 = 0$. which gives:

$$\sqrt{x^2 + x_c^2} - x_c = x^2 , \quad (4.78)$$

Getting rid of the square root, the equation can be written as

$$x^2(x^2 + 2x_c - 1) = 0 . \quad (4.79)$$

Discarding the solution $x = 0$, we find that

$$x_t = \sqrt{1 - 2x_c} . \quad (4.80)$$

Thus, the tangential critical line exists only for $x_c < 1/2$.

The radius of the radial critical line is found by solving the equation $dy/dx = 0$:

$$1 + \frac{\sqrt{x^2 + x_c^2} - x_c}{x^2} - \frac{1}{\sqrt{x^2 + x_c^2}} = 0 \quad (4.81)$$

which leads to

$$x_r^2 = \frac{1}{2} \left(2x_c - x_c^2 - x_c \sqrt{x_c^2 + 4x_c} \right) . \quad (4.82)$$

Note that $x_r^2 \geq 0$ for $x_c \leq 1/2$. Thus, the existence condition for the radial critical line is the same as for the tangential critical line.

While the tangential caustic is a point at $y_t = 0$, the radius of the radial caustic, y_r , can be obtained by inserting Eq. 4.82 into the lens equation.

The lens equation is

$$y = x - \frac{m(x)}{x} = x - \sqrt{1 + \frac{x_c^2}{x^2}} - \frac{x_c}{x} , \quad (4.83)$$

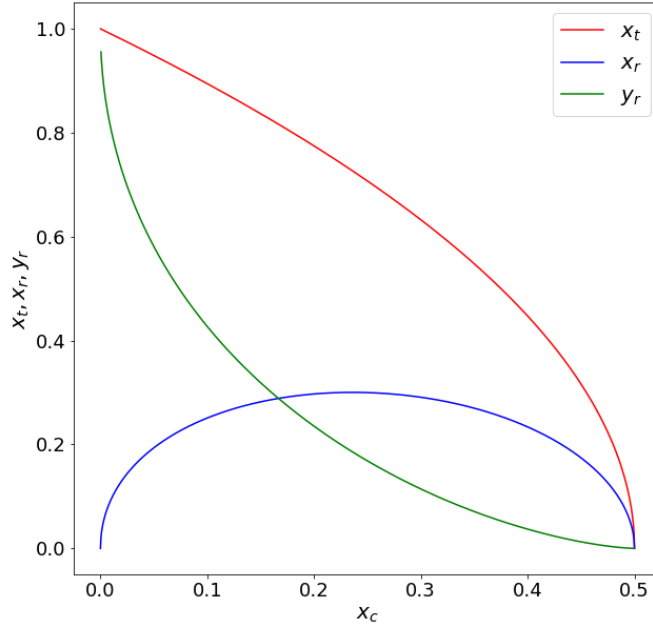


Figure 4.3.2: Radius of the radial and of the tangential critical lines as a function of the size of the core radius x_c . The green line shows the size of the radial caustic.

which can be reduced to the third order polynomial

$$x^3 - 2yx^2 + (y^2 + 2x_c - 1)x - 2yx_c = 0 . \quad (4.84)$$

Thus, the NIS can produce up to three images of a source at distance y from the lens. Whether the images are three or less depends on y and on x_c . In particular, the right panel of Fig. 4.3.1 shows that if $x_c > 1/2$, which implies $\alpha' < 1$ for any x , there is no line $f(x) = x - y$ which can intercept the function $\alpha(x)$ more than once. Thus, the lens cannot produce multiple images independently on the position of the source with respect to the lens. The left panel of Fig. 4.3.1 shows that for $x_c > 1/2$ the convergence never exceeds unity. This implies that the surface density $\Sigma(x)$ never exceeds the critical surface density Σ_{cr} .

On the contrary, if $x_c < 1/2$ multiple images exist whenever $y < y_r$. In the left panel of Fig. 4.3.3, some extended circular sources are placed at different distances y from the center of a NIS lens with $x_c = 0.1$. The blue point and the red circle show the tangential and the radial caustics. The right panel shows the corresponding critical lines (blue and red circles, respectively). The images of the sources displayed in the left panel are also shown. As seen for the power-law lens with $1 < n < 2$, one image form on the same side of the lens with respect to the source. This image, which corresponds to the minimum of the time-delay surface, is external to the Einstein ring. When the source is inside the radial caustic, two additional images form, one inside and one outside the radial critical line, which are located on the opposite side of the lens with respect to the source. As discussed earlier, the innermost image corresponds to the maximum of the time-delay surface, while the other image is at the saddle point. Thus the parity of this image is negative. If the source is overlapped to the radial caustic, these two image merge across the radial critical line, forming a radial arc. Bringing the source close to the tangential caustic causes the tangential distortion of the two outermost images to increase, until, when the source is exactly on the tangential caustic, the

two image merge into the Einstein ring. The central image, instead is increasingly de-magnified and shifted to the center of the lens.

R

We have shown that, if $x_c > 1/2$, the lens

- is sub-critical, $\kappa(x) < 1$ for any x ;
- does not develop critical lines, i.e. is not capable of producing large distortions;
- does not produce multiple images.

Under these circumstances, the lens is considered *weak*. On the contrary, a *strong* lens is capable of producing large distortions and multiple images. As seen earlier, the number of these images depends on the position of the source with respect to the caustics. Sources which lie within the radial caustic produce three images. Sources outside the radial caustic have only one image. This is shown in Fig. ???. Since the tangential critical curve does not lead to a caustic curve, but the corresponding caustic degenerates to a single point $\vec{y} = 0$, the tangential critical curves have no influence on the image multiplicity. Thus, pairs of images can only be created or destroyed if the radial critical curve exists.

For non-singular axially symmetric lenses, whose surface density is piecewise continuous and falls off at large radii, such that it is bound, i.e.

$$0 \leq \kappa(x) \leq \kappa_{\max} \quad (4.85)$$

and

$$\lim_{x \rightarrow \infty} x\kappa(x) = 0. \quad (4.86)$$

it can be shown that the following properties hold (Schneider, Ehlers, and Falco, 1992), which generalize what shown earlier for NIS:

1. if the source is at $y > 0$, any image with $x > 0$ is at $x \geq y$. This is easily seen from the lens equation:

$$x = y + \frac{m(x)}{x}. \quad (4.87)$$

Being $m(x) \geq 0$ and $x \geq 0$, it follows that $x \geq y$;

2. for sufficiently large y , there exists a single image. From Eq. 4.86, we see that there must be a constant c and a value a such that, for $|x| > a$, $\kappa(x) < c/|x|$. This bounds the mass:

$$\begin{aligned} m(x) &= 2 \int_0^x x' \kappa(x') dx' \\ &= m(a) + 2 \int_a^{|x|} x' \kappa(x') dx' < m(a) + 2c(|x| - a). \end{aligned} \quad (4.88)$$

Thus,

$$\left| \frac{m(x)}{x} \right| < b. \quad (4.89)$$

If y is sufficiently large, $y \geq b$, the lens equation tells us that

$$x = y + \frac{m(x)}{x} > 0, \quad (4.90)$$

thus $x \geq y$. Moreover, if $x > a$ then

$$\bar{\kappa} = \frac{m(x)}{x^2} = \frac{m(x)}{x} \frac{1}{x} < \frac{b}{x}. \quad (4.91)$$

Thus,

$$\lim_{x \rightarrow \infty} y = \lim_{x \rightarrow \infty} (1 - \bar{\kappa})x = x. \quad (4.92)$$

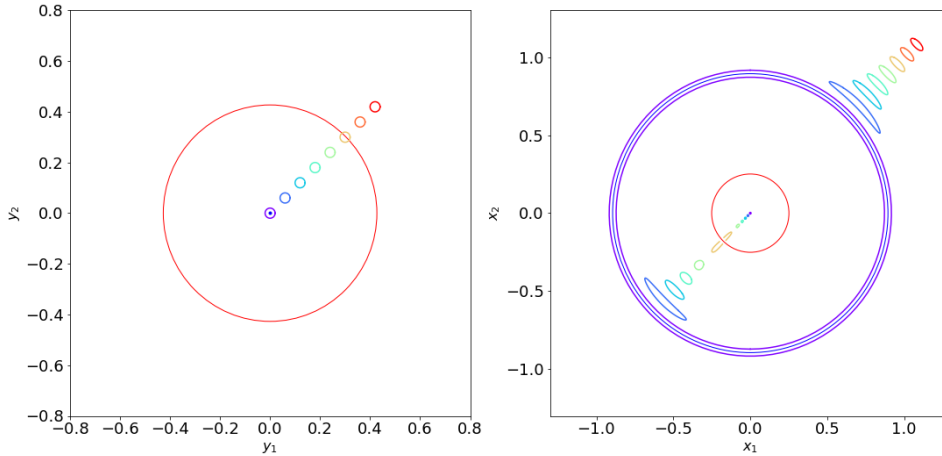


Figure 4.3.3: Imaging of extended sources by a NIS lens.

3. a lens can produce multiple images if and only if at least at one point $1 - 2\kappa(x) + \bar{\kappa}(x) < 0$: if $1 - 2\kappa(x) + \bar{\kappa}(x) > 0$ throughout, a lens produces no multiple images, since $y(x)$ increases monotonically. If on the other hand, there is a point where $dy/dx < 0$, there is at least one local maximum x_1 and one local minimum $x_2 > x_1$ of the curve $y(x)$ since $dy/dx \rightarrow 1$ for $|x| \rightarrow \infty$. For values of y such that $y(x_2) < y < y(x_1)$, there are at least three images;
4. a necessary condition for multiple images is that $\kappa > 1/2$ at one point in the lens: if $dy/dx < 0$ at one point, then $\kappa > (1 + \bar{\kappa})/2 \geq 1/2$; a sufficient condition for multiple imaging is that $\kappa > 1$ at one point. Indeed: if κ has a maximum at one point x_m where $\kappa(x_m) > 1$, then $\bar{\kappa}(x_m) \leq \kappa(x_m)$ and $dy/dx < 0$ at x_m . The statement then follows from (3);
5. if the surface density does not increase with x , $\kappa'(x) \leq 0$, $\kappa(0) > 1$: from (4) we know that it is sufficient that $\kappa > 1$ at one point for having multiple images. On the other hand if $\kappa(0) \leq 1$, then, since $y = x(1 - \bar{\kappa})$, we have for $x \geq 0$: $dy/dx = (1 - \bar{\kappa}) - x\bar{\kappa}'$. Since

$$\bar{\kappa}(x) = 2 \int_0^1 du u \kappa(ux), \quad (4.93)$$

then

$$\frac{d\bar{\kappa}}{dx} = 2 \int_0^1 du u^2 \kappa'(ux) \leq 0 \quad (4.94)$$

and $\bar{\kappa}(x) \leq \kappa(0) \leq 1$, we see that $dy/dx \geq 0$, so that no multiple images can occur.

4.4 Time delays

As seen in Sect. 2.6.1, lensing introduces a delay in the time needed to photons to reach the observer after being emitted by the source. The delay, which has both a geometrical and a gravitational component is different for multiple images of the same source. While the absolute delay of each image cannot be measured, it is possible, in some particular cases, to measure the relative delay of the images. For example, time delays can be measured when the source is intrinsically variable, like e.g. AGNs or supernovae.

In this section, we compute the time delays between images for the lens models introduced above. The formula for the light travel time is

$$t(x) = \frac{(1+z_L)}{c} \frac{D_L D_S}{D_{LS}} \frac{\xi_0^2}{D_L^2} \left[\frac{1}{2}(x-y)^2 - \Psi(x) \right] = \frac{(1+z_L)}{c} \frac{D_L D_S}{D_{LS}} \tau(x) \quad (4.95)$$

Obviously, in order to compute the light travel time, we need to provide the equations of the lensing potential.

For a power-law lens, the lensing potential is

$$\Psi(x) = \frac{1}{3-n} x^{3-n} \quad (4.96)$$

so that

$$\tau(x) = \frac{\xi_0^2}{D_L^2} \left[\frac{1}{2}(x-y)^2 - \frac{1}{3-n} x^{3-n} \right] \quad (4.97)$$

At the image positions

$$x-y = \alpha(x) = x^{2-n} \quad (4.98)$$

thus

$$\tau(x_i) = \frac{\xi_0^2}{D_L^2} \left[\frac{1}{2} x_i^{2(2-n)} - \frac{1}{3-n} x_i^{3-n} \right] \quad (4.99)$$

We can then compute the time delay between the images:

$$\Delta t_{ij} \propto \Delta \tau_{ij} = \frac{\xi_0^2}{D_L^2} \left[\frac{1}{2} (x_j^{2(2-n)} - x_i^{2(2-n)}) - \frac{1}{3-n} (x_j^{3-n} - x_i^{3-n}) \right] \quad (4.100)$$

For $n=2$, this formula gives:

$$\Delta \tau_{ij} = \frac{\xi_0^2}{D_L^2} (x_i - x_j) = \theta_E^2 \left(\frac{\theta_i}{\theta_E} - \frac{\theta_j}{\theta_E} \right) = \frac{1}{2} (\theta_i^2 - \theta_j^2) = \Delta \tau_{SIS} \quad (4.101)$$

Note that the lensing potential of the SIS lens is $\Psi(x) = x$.

A similar procedure can be followed to compute the time delays between the images in the case of a NIS lens. In this case, the lensing potential is given by

$$\Psi(x, x_c) = \sqrt{x^2 + x_c^2} - x_c \ln \left(x_c + \sqrt{x^2 + x_c^2} \right). \quad (4.102)$$

Fig. 4.4.1 shows the time delay function for a source at $y = 0.1$ for two classes of models, namely the power-law lens (left panel) and the NIS lens (right panel). In both panels, the delay is calculated with respect to outermost image (minimum of the time delay surface). As we can see, decreasing n and increasing x_c flattens-off the curves, thus reducing the time delays between the images.

4.5 Elliptical lenses

Having explored the effects of changing the slope of the density profile and of including a central core, we consider now how ellipticity affects the lens properties. This of course removes the axial symmetry of the lens. Consequently, the tangential caustic is no longer a point at the center of the lens. Instead, it becomes an astroid-like kind of caustic which can have two or four cusps.

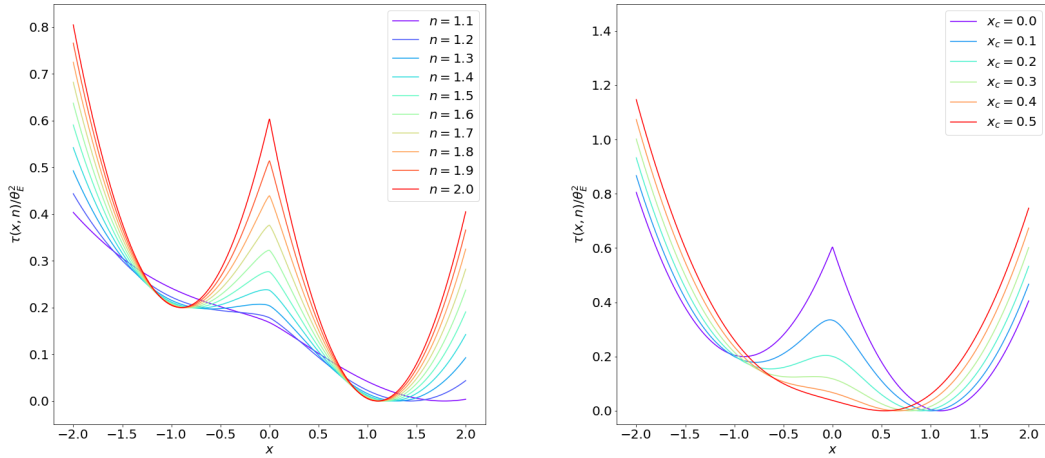


Figure 4.4.1: Time delay function for a number of power-law (left panel) and NIS lenses. In both cases the source is in $y = 0.1$.

4.5.1 Singular Isothermal Ellipsoid

As we have seen in the previous section, the singular isothermal profile is particularly tractable to derive its lensing properties. Similarly, it is quite straightforward to generalize to the elliptical case.

Convergence

As shown by Kormann, Schneider, and Bartelmann (1994), the Singular Isothermal Ellipsoid model (SIE) can be derived from the SIS by making the substitution

$$\xi \Rightarrow \sqrt{\xi_1^2 + f^2 \xi_2^2}, \quad (4.103)$$

Then, $\Sigma(\xi)$ becomes

$$\Sigma(\vec{\xi}) = \frac{\sigma_v^2}{2G} \frac{\sqrt{f}}{\sqrt{\xi_1^2 + f^2 \xi_2^2}}, \quad (4.104)$$

which is constant on ellipses with minor axis ξ and major axis ξ/f , oriented such that the major axis is along the ξ_2 axis. In the above formulas, f is the axis ratio of the ellipses, $0 < f \leq 1$. The normalization of the profile ensures that the mass within an elliptical iso-density contour for fixed Σ is independent on f .

By choosing $\xi_0 = \xi_{0,SIS}$ as reference scale and by repeating the same procedure outlined in Eq. 4.60 we obtain

$$\kappa(\vec{x}) = \frac{\sqrt{f}}{2\sqrt{x_1^2 + f^2 x_2^2}}. \quad (4.105)$$

By further using polar coordinates, we obtain

$$\kappa(x, \varphi) = \frac{\sqrt{f}}{2x\Delta(\varphi)}, \quad (4.106)$$

where

$$\Delta(\varphi) = \sqrt{\cos \varphi^2 + f^2 \sin \varphi^2}. \quad (4.107)$$

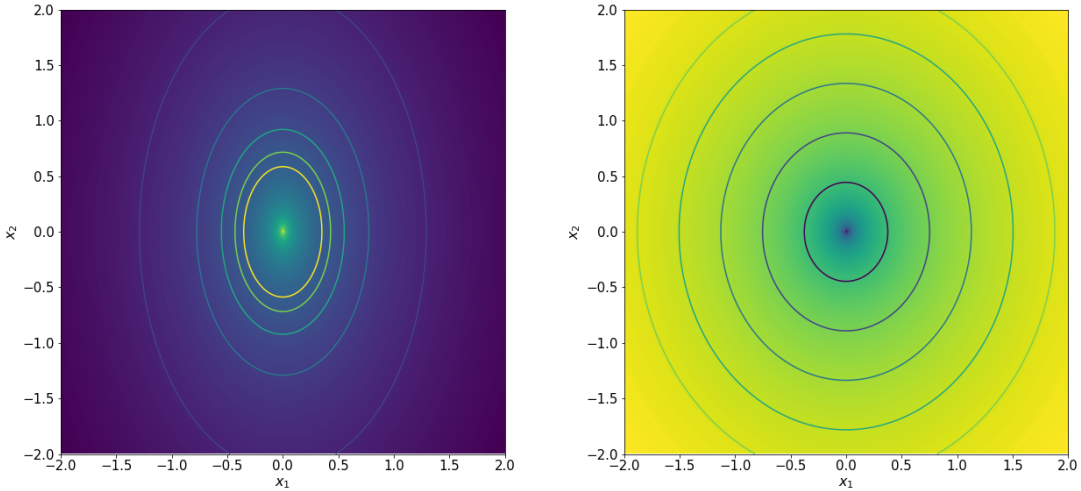


Figure 4.5.1: Maps of the convergence and of the lensing potential for a SIE lens with $f = 0.6$.

Lensing potential

The lensing potential can be found by solving the Poisson equation:

$$\frac{\partial^2 \Psi}{\partial x^2} + \frac{1}{x} \frac{\partial \Psi}{\partial x} + \frac{1}{x^2} \frac{\partial^2 \Psi}{\partial \varphi^2} = 2\kappa = \frac{\sqrt{f}}{x \Delta(\varphi)}. \quad (4.108)$$

Making the ansatz $\Psi(x, \varphi) := x \tilde{\Psi}(\varphi)$ we find:

$$\tilde{\Psi}(\varphi) + \frac{d^2}{d\varphi^2} \tilde{\Psi}(\varphi) = \frac{\sqrt{f}}{\Delta(\varphi)}. \quad (4.109)$$

This equation can be solved using Green's method, to obtain

$$\Psi(x, \varphi) = x \frac{\sqrt{f}}{f'} [\sin \varphi \arcsin(f' \sin \varphi) + \cos \varphi \operatorname{arcsinh}(f'/f \cos \varphi)]. \quad (4.110)$$

In the formula above we introduced $f' = \sqrt{1 - f^2}$.

In Fig. 4.5.1, we compare the map of the convergence and of the potential for a SIE lens. The contours of constant convergence are indeed ellipses with axis ratio $f = 0.6$. The iso-potential contours are much rounder and have axis ratios are $\sim 0.84 = 1.4f$.

Deflection angle

The deflection angle can be derived as usual by taking the gradient of the lensing potential. It is convenient to operate in polar coordinates, so that

$$\frac{\partial}{\partial x_1} = \cos \varphi \frac{\partial}{\partial x} - \frac{\sin \varphi}{x} \frac{\partial}{\partial \varphi} \quad (4.111)$$

and

$$\frac{\partial}{\partial x_2} = \sin \varphi \frac{\partial}{\partial x} + \frac{\cos \varphi}{x} \frac{\partial}{\partial \varphi}. \quad (4.112)$$

Thus, the components of the deflection angle are

$$\begin{aligned} \alpha_1(\vec{x}) &= \frac{\sqrt{f}}{f'} \operatorname{arcsinh} \left(\frac{f'}{f} \cos \varphi \right) \\ \alpha_2(\vec{x}) &= \frac{\sqrt{f}}{f'} \arcsin(f' \sin \varphi) \end{aligned} \quad (4.113)$$

As found for the SIS, the deflection angle of the SIE does not depend on x .

Shear

The further step is the derivation of the shear components. These can be derived by means of the derivatives of the deflection angle:

$$\begin{aligned}\gamma_1(\vec{x}) &= \frac{1}{2} \left(\frac{\partial \alpha_1}{\partial x_1} - \frac{\partial \alpha_2}{\partial x_2} \right), \\ \gamma_2(\vec{x}) &= \frac{\partial \alpha_1}{\partial x_2}.\end{aligned}\quad (4.114)$$

Using the differential operators in polar coordinates and the results above, we find that

$$\begin{aligned}\gamma_1(\vec{x}) &= -\frac{\sqrt{f}}{2x\Delta(\varphi)} \cos 2\varphi = -\kappa(\vec{x}) \cos 2\varphi \\ \gamma_2(\vec{x}) &= -\frac{\sqrt{f}}{2x\Delta(\varphi)} \sin 2\varphi = -\kappa(\vec{x}) \sin 2\varphi,\end{aligned}\quad (4.115)$$

which shows that $\gamma = \kappa$ as for the SIS.

Critical lines

We can now compute the lensing Jacobian. This is

$$A = \begin{bmatrix} 1 - \kappa - \gamma_1 & -\gamma_2 \\ \gamma_2 & 1 - \kappa + \gamma_1 \end{bmatrix} = \begin{bmatrix} 1 - 2\kappa \sin^2 \varphi & \kappa \sin 2\varphi \\ \kappa \sin 2\varphi & 1 - 2\kappa \cos^2 \varphi \end{bmatrix} \quad (4.116)$$

and that the tangential and radial eigenvalues are

$$\begin{aligned}\lambda_t(\vec{x}) &= 1 - \kappa(\vec{x}) - \gamma(\vec{x}) = 1 - 2\kappa(\vec{x}) \\ \lambda_r(\vec{x}) &= 1 - \kappa(\vec{x}) + \gamma(\vec{x}) = 1.\end{aligned}\quad (4.117)$$

It turns out that, as the SIS, even the SIE does not have a radial critical line, being the radial magnification always unity. Instead, the tangential critical line is the ellipse given by

$$\kappa(\vec{x}) = \frac{1}{2}, \quad (4.118)$$

which can be parametrized as follows:

$$\vec{x}_t(\varphi) = \frac{\sqrt{f}}{\Delta(\varphi)} [\cos \varphi, \sin \varphi]. \quad (4.119)$$

The critical lines of two SIE lenses with $f = 0.6$ and $f = 0.2$ are shown with dashed red lines in the left and in the right panels of Fig. 4.5.2. These lines can be mapped onto the source plane using the lens equation, to obtain the corresponding tangential caustics:

$$\begin{aligned}y_{t,1}(\varphi) &= \frac{\sqrt{f}}{\Delta(\varphi)} \cos \varphi - \frac{\sqrt{f}}{f'} \operatorname{arcsinh} \left(\frac{f'}{f} \cos \varphi \right) \\ y_{t,2}(\varphi) &= \frac{\sqrt{f}}{\Delta(\varphi)} \sin \varphi - \frac{\sqrt{f}}{f'} \operatorname{arcsin} (f' \sin \varphi).\end{aligned}\quad (4.120)$$

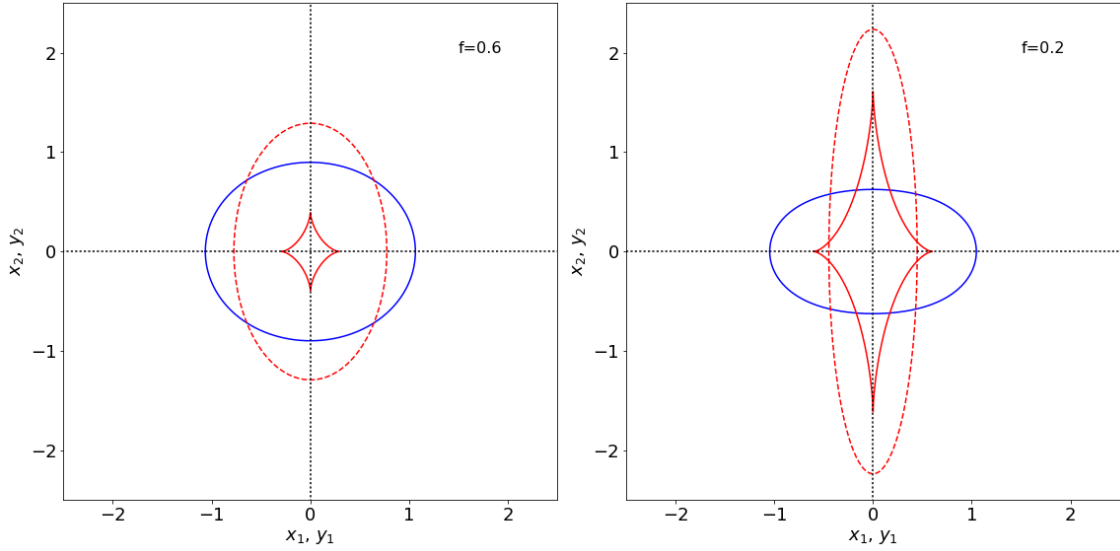


Figure 4.5.2: Critical line (dashed red), caustic (solid red), cut (solid blue) for two SIE lenses with $f = 0.6$ (left panel) and $f = 0.2$ (right panel).

Cut and caustic

As for the SIS (see Eq. 4.66), we can now search for the *cut*, which is given by

$$\vec{y}_c(\varphi) = \lim_{x \rightarrow 0} \vec{y}(x, \varphi) = -\vec{\alpha}(\varphi). \quad (4.121)$$

Thus, we obtain

$$\begin{aligned} y_{c,1}(\varphi) &= -\frac{\sqrt{f}}{f'} \operatorname{arcsinh} \left(\frac{f'}{f} \cos \varphi \right) \\ y_{c,2}(\varphi) &= -\frac{\sqrt{f}}{f'} \operatorname{arcsin} (f' \sin \varphi). \end{aligned} \quad (4.122)$$

Both the caustic and the cut are shown in each panel of Fig. 4.5.2 (red and blue curves, respectively).

The cut and the caustic intercept the y_1 and the y_2 axes in points that are symmetric with respect to the center of the lens. These points have coordinates

$$\begin{aligned} s_{1,\pm,c} &= [y_{c,1}(\varphi = 0, \pi), 0], \\ s_{2,\pm,c} &= [0, y_{c,2}(\varphi = \pi/2, -\pi/2)] \end{aligned} \quad (4.123)$$

for the cut, and

$$\begin{aligned} s_{1,\pm,t} &= [y_{t,1}(\varphi = 0, \pi), 0], \\ s_{1,\pm,t} &= [0, y_{t,2}(\varphi = \pi/2, -\pi/2)] \end{aligned} \quad (4.124)$$

for the caustic.

Fig. 4.5.3 shows how the axis intercepts s_1 and s_2 on the positive y_1 and y_2 axes of both the cut and the caustic vary as a function of f . Clearly, $s_{1,c} > s_{1,t}$ for any f . On the contrary, there exists a value, $f = f_0 = 0.3942$, such that

$$\begin{aligned} s_{2,c} &\leq s_{2,t} \text{ for } f \leq f_0, \\ s_{2,c} &> s_{2,t} \text{ for } f > f_0. \end{aligned} \quad (4.125)$$

Therefore, the tangential caustic is not always contained by the cut. For large ellipticity, corresponding to lower values of f , the tangential caustic extends outside the cut along the y_2 axis. The cusps which are not contained within the cut are called *naked*.

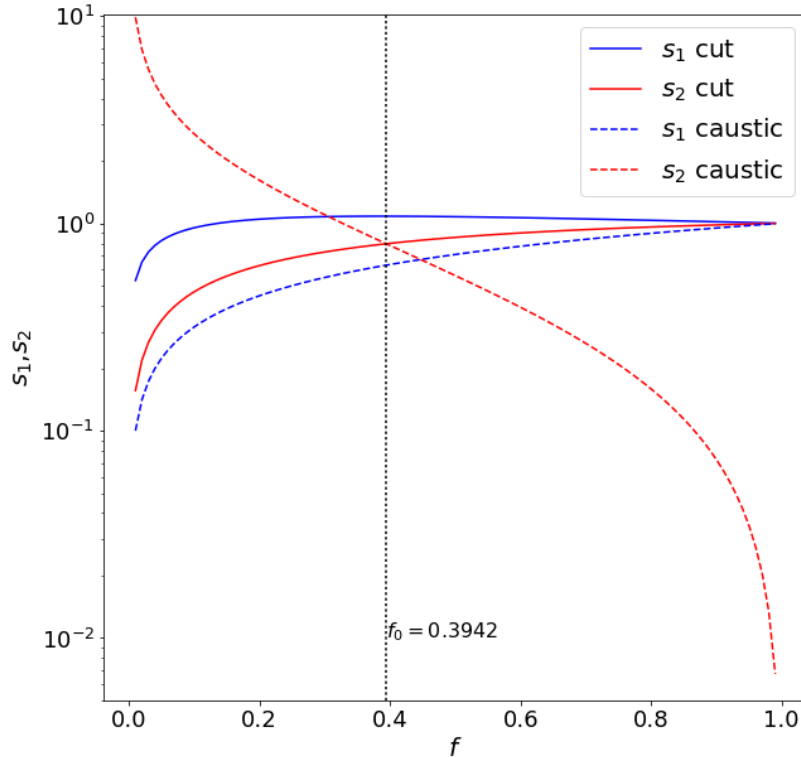


Figure 4.5.3: Intercepts between the cut (solid lines) and the caustics (dashed lines) with the positive y_1 and y_2 semi-axes (blue and red lines, respectively) as a function of f .

Multiple images

Finding the multiple images of a source lensed by the SIE model requires using numerical methods. The implementation of one of such algorithms in python is discussed in Sect. 4.10.1.

In order to understand how the mapping between the lens and the source plane works, it is useful to inspect how pieces of the tangential critical line are mapped onto the caustic. In the left panel of Fig. 4.5.4, we divide the critical line in four parts, corresponding to the quadrants in the lens plane. Different colors are used to indicate the critical points with polar angles in the ranges $[0, \pi/2]$, $[\pi/2, \pi]$, $[\pi, 3/2\pi]$, and $[3/2\pi, 2\pi)$ (see Eq. 4.119). In the right panel, the corresponding points on the caustic, obtained using Eq. 4.120, are shown using the same colors. We use the same color-code to visualize the points on the cut, depending on the polar angle φ .

We can see that the mapping of the critical points follows a left-right rule: the first and the fourth quadrants in the lens plane ($\varphi \in [0, \pi/2]$ and $\varphi \in [3/2\pi, 2\pi)$) are mapped onto the second and the third quadrants in the source plane, and vice versa.

The points on the cut, instead, follow a diagonal rule. For example, the portion of the cut in the first quadrant in the source plane, correspond to $\varphi \in [\pi, 3/2\pi]$.

- ④ As seen earlier, in lenses which have a radial critical line, the cut becomes the radial caustic. Thus the same diagonal rule works for the mapping of the radial critical points onto the radial caustic.

With these results in mind, we can easily guess where, on the source plane, a source originating

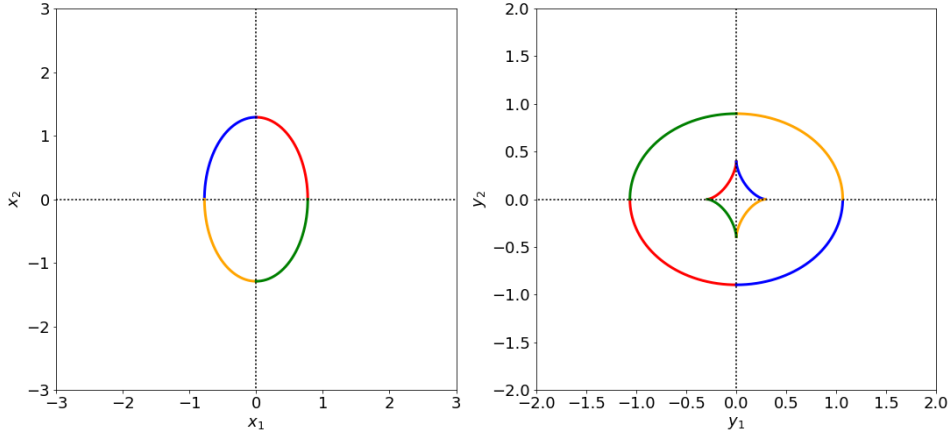


Figure 4.5.4: Mapping of points on the critical line onto the caustic. Different colors correspond to different quadrants on the lens plane. The mapping is shown also for the cut, which would become the radial caustic in presence of a core.

images near some portion of the critical line is located.

The multiplicity of the images that a SIE lens can produce depends on the structure of the caustics and cut, and on the relative position of the source. The following rules apply.

- a source far away from the lens, i.e. outside of both the cut and the caustic, has only one image;
- the number of images increases by one, if the source is inside the cut;
- the number of images increases by two, if the source is inside the caustic.

The last two rules do not exclude each other, i.e. if the source is inside the cut AND the caustic, the number of images is increased by three. Thus, a SIE lens can produce up to four images of a single source. More precisely:

- if $f > f_0$, the lens can produce either 1, 2, or 4 images, depending on the source being outside the cut, between the cut and the caustic, or inside the caustic;
- if $f \leq f_0$, the lens can produce 1, 2, 3, or 4 images. Indeed, for such lenses, a source can be located within the caustic but be outside the cut. Thus, an image multiplicity of three is allowed in this case.

In Fig. 4.5.5, the images of circular sources at different locations with respect to the caustic and the cut are shown. The SIE lens used in these examples has $f = 0.6$. The solid and the dashed lines in left panels indicate the caustics and the cut, respectively. The colored circles mark the positions of several circular sources with radius $r = 0.05\xi_0$. The corresponding images are shown in the right panels. The tangential critical lines are given by the black solid line.

The upper panels show how the image geometry changes when the source is brought closer to the lens center by crossing the cut and the fold of the caustic. Sources outside the cut have only one image, which is located in the same quadrant of the image plane onto which the source position is projected. When the source crosses the cut, one additional image appears near the center of the lens. This is not surprising, given that the cut is given by Eq. 4.121. As the source is brought closer towards the caustic, the central image moves away from the lens center in the quadrant of the lens plane opposite to that where source is projected. In this case, the above mentioned diagonal rule applies. At the caustic crossing two images appear on opposite sides of the critical line. Note that, if the source is near the fold in the first quadrant of the source plane, these two images appear in the second quadrant of the lens plane, following the left-right mapping rule which applies to the

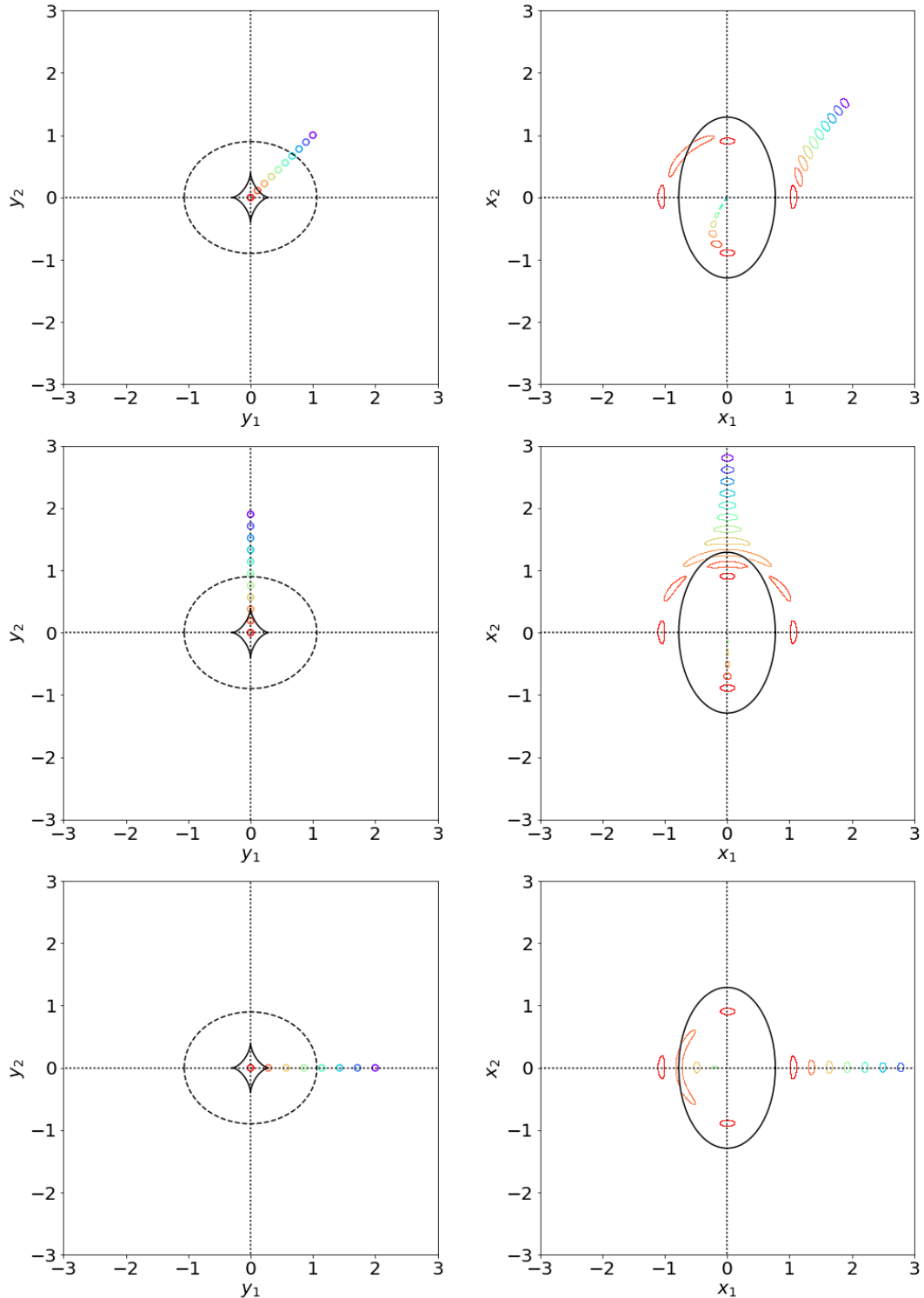


Figure 4.5.5: Lensing of circular sources by a SIE lens with $f = 0.6$. In the left panels, we show the sources with different colors depending on their distance from the center of the lens projected onto the source plane. Shown are also the caustic (solid black line) and the cut (dashed black line). The images (colored contours) and the critical line (solid black line) are shown in the right panels.

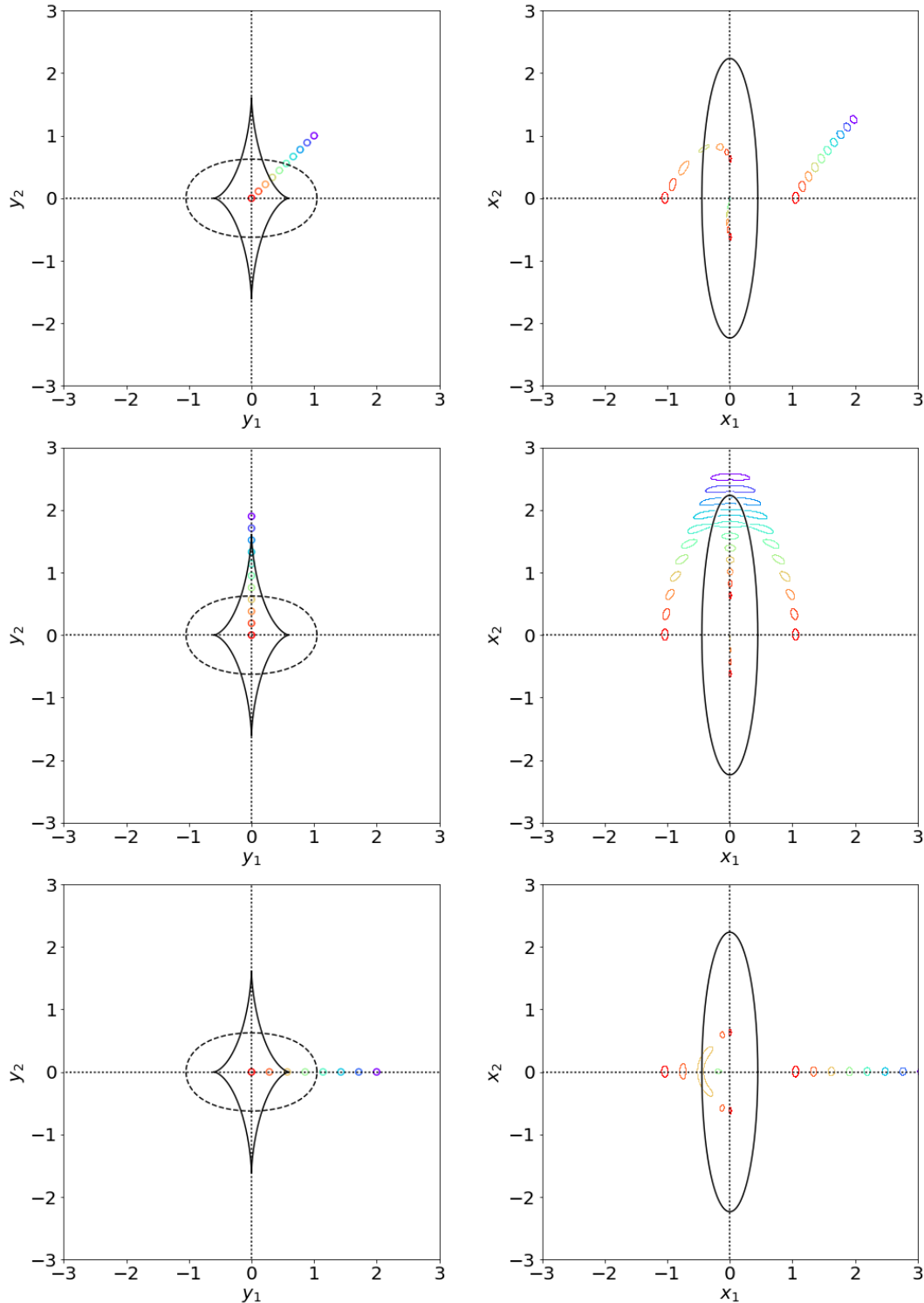


Figure 4.5.6: As in Fig. 4.5.5, but for a SIE lens with $f = 0.2$.

tangential critical points. As the source is brought even closer to the center of the lens, the images reach a symmetric configuration which is called *Einstein cross*.

The middle and the bottom panels refer to the same lens, but the source is moved from outside the cut towards the center of the lens passing through the cusps of the tangential caustic. At the

caustic crossing, three images meet at the critical line. Again, the left-right rule applies.

Fig. 4.5.6 is analogous to Fig. 4.5.5, but refers to a SIE lens with $f = 0.2$. Note that the middle panels show the image configurations for a source moved across the naked cusp. When the source is on the cusp, we find again that three images merge into a single image. When the source is inside the caustic but still outside the cut, the image multiplicity is three, as anticipated earlier.

Distortion and parity of the images

We can now comment on the magnification and parity. From Eqs. 4.106 and 4.115, we obtain that

$$\mu = \frac{1}{1 - 2\kappa}, \quad (4.126)$$

meaning that $\mu > 0$ for $\kappa < 0.5$. Therefore, the parity of the images is positive outside the critical line, negative otherwise.

Given the singularity of the lensing potential near the center, the images are either minima or saddle points of the time-delay surface. The images inside the critical line are saddle points. Those outside the critical line are minima.

The magnification of the images forming near the center of the lens is very small $|\mu| \sim 0$, being κ divergent. Because the radial magnification is always unity, this means that the images are tangentially squeezed if they are located near the center of the lens. Of course, the magnification of the images near the critical line diverges.

As discussed earlier, Figs. 4.5.5 and 4.5.6 show that the images forming near the critical line are distorted tangentially leading to the formation of gravitational arcs. The individual images are elongated and merge across the critical line. The largest gravitational arcs are the result of the merger of three images of sources near the cusp of the caustic.

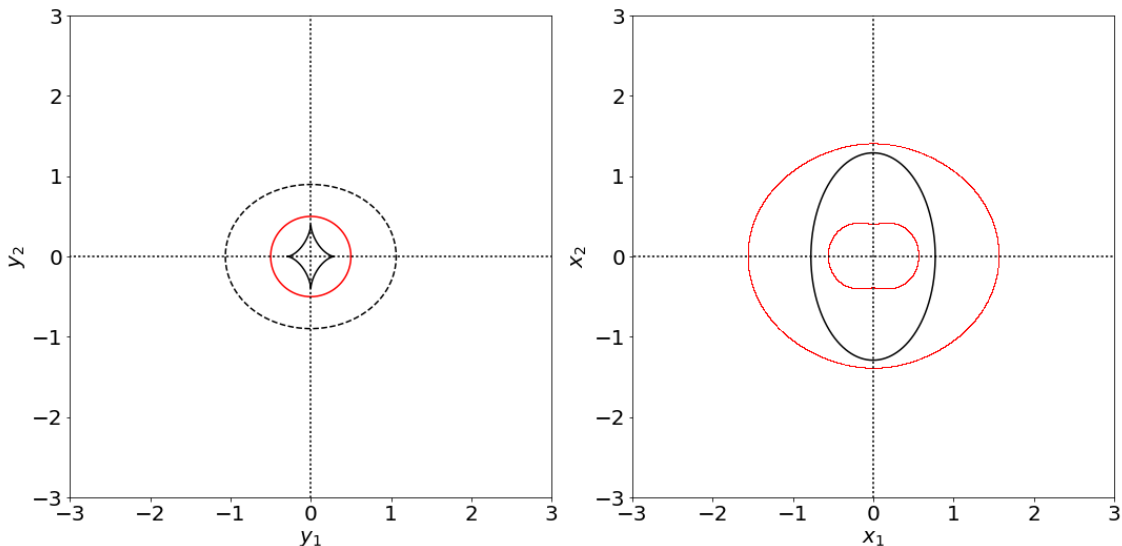


Figure 4.5.7: Lensing of an extended source of radius $r = 0.5$ (shown in red) by a SIE lens with $f = 0.6$. The black solid and dashed lines in the left panel show the caustic and the cut of the lens. The black solid line in the right panel is the critical line.

In the examples shown in Figs. 4.5.5 and 4.5.6 the source size is $r = 0.05$ in units of ξ_0 . In Fig. 4.5.7, we show how a source of radius $r = 0.5$ placed on the caustic is distorted to form a complete Einstein ring. Thus, the observed distortions depend on the size of the source relative to the size of the caustic. If the source size is comparable to the size of caustic, the effect of ellipticity is merely detectable as a distortion of the images compared to the case of an axially symmetric lens.

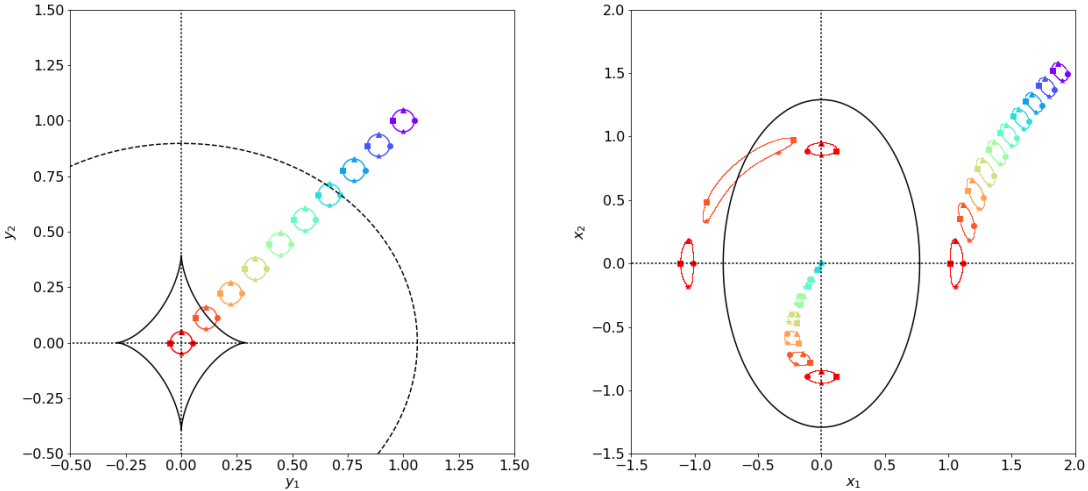


Figure 4.5.8: Lensing of an extended source of radius $r = 0.05$ by a SIE lens with $f = 0.6$ moved across the cut and the fold of the caustic. Four points on the source contours are marked with symbols. The same symbols are mapped onto the image plane on the image contours.

Fig. 4.5.8 illustrates how the parity of the images changes from inside to outside the critical line. Within each source in the left panel we mark four characteristic points. Starting from right-most and counting counter-clockwise, they are indicated by the symbols circle, triangle, square, and star. In the right panel, we can see that the same symbol sequence is preserved in images outside the critical line. On the other hand, in the images inside the critical line the circles and the squares are exchanged, following the left-right rule introduced above.

Note that half of the source overlapping with the fold of the caustic is outside the caustic itself. Therefore, only half of this source is mapped onto four images. For example, the points marked with the circle and the triangle in this source do not appear in the fold arc in the second quadrant of the lens plane.

4.5.2 Non-singular elliptical models

A core can be introduced also in the SIE model. In this case, however, the model becomes not easily tractable analytically. A discussion on the properties of the Non-singular Isothermal Ellipsoid (NIE) is given in Kormann, Schneider, and Bartelmann (1994). Similar complications arise from changing the slope of the density profile. A detailed description of the elliptical power-law lens can be found in Tessore and Metcalf (2015).

Here, we only summarize some properties of the NIE model, whose surface density is written as

$$\Sigma(\vec{\xi}) = \frac{\sigma^2}{2G} \frac{\sqrt{f}}{\sqrt{\xi_1^2 + f^2 \xi_2^2 + \xi_c^2}}, \quad (4.127)$$

where ξ_c is the core radius. With the usual choice of $\xi_0 = \xi_{0,SIS}$, the convergence profile becomes

$$\kappa(\vec{x}) = \frac{\sqrt{f}}{2\sqrt{x_1^2 + f^2 x_2^2 + x_c^2}}. \quad (4.128)$$

Kormann, Schneider, and Bartelmann (1994) showed that the critical lines and caustics of the NIE can be derived analytically. Some examples are shown in Fig. ???. Depending on the values of f and of x_c , the lens can have two separate critical lines and caustics (one radial and one tangential), only one tangential critical line and caustic, or no critical lines and caustics at all. In particular:

- if $x_c < f^{3/2}/2$ there are two distinguished critical lines and caustics. One caustic is the tangential caustic and has four cusps. The other is the radial one and it has not cusps. The tangential caustic is completely contained within the radial caustic if the ellipticity is small (f is large). Even in the case of mildly elliptical lenses, the radial caustic contains the tangential caustic if the core is small enough;
- if $f^{3/2}/2 < x_c < f^{3/2}/(1+f)$, the radial caustic is contained within the tangential caustic. In addition both the radial and the tangential caustics have only two cusps;
- if $f^{3/2}/(1+f) < x_c < f^{1/2}/(1+f)$, the lens has only a tangential critical line and caustic. The radial critical lines and caustics disappear for $x_c = f^{3/2}/(1+f)$;
- even the tangential caustic disappears if $x_c = f^{1/2}/(1+f)$. Thus, for $x_c > f^{1/2}/(1+f)$ the lens does not have critical lines and caustics.

Depending on the structure of the caustics, the NIE can produce 1, 3, or 5 images of a source. These cases are illustrated in Fig. 4.5.10.

4.5.3 Pseudo-elliptical models

Pseudo-elliptical lenses are generally referred as lenses whose iso-potential contours are elliptical and have constant axis ratio f , independent on Ψ . As a result, their surface density is not elliptical. In particular, the iso-density contours have a characteristic dumbbell shape, as shown in Fig. ?? (see e.g. Kassiola and Kovner, 1993). The figure displays the convergence map of a pseudo-NIE (pNIE) model with lensing potential

$$\Psi(\vec{x}) = \sqrt{x_1^2 + f^2 x_2^2 + x_c^2} \quad (4.129)$$

and axis ratio $f = 0.7$. The solid lines are contours of constant convergence while the dashed line show similar contours for a NIE lens with the same f . A certain value of the axis ratio of the iso-potential contours translates into a much smaller axis ratio of the iso-convergence contours.

The great advantage of including the ellipticity in the potential is that all lens properties can be derived more easily by means of its derivatives rather than integrations. This is generally less time consuming, even if done numerically. On the other hand, this approach produces unphysical mass distributions (e.g. with negative convergence) in the case of large ellipticity (2002A&A...390..821G; Kassiola and Kovner, 1993).

As shown by 2003MNRAS.340..105M and 2002A&A...390..821G from the elliptical potential, the components of the deflection angles can be derived as follows. We define

$$x_\epsilon = \sqrt{x_1^2 + f^2 x_2^2 + x_c^2}. \quad (4.130)$$

Then,

$$\begin{aligned} \alpha_1(\vec{x}) &= \frac{\partial \Psi}{\partial x_1} = \frac{\partial \Psi}{\partial x_\epsilon} \frac{\partial x_\epsilon}{\partial x_1} = \alpha(x_\epsilon) \cos \varphi, \\ \alpha_2(\vec{x}) &= \frac{\partial \Psi}{\partial x_2} = \frac{\partial \Psi}{\partial x_\epsilon} \frac{\partial x_\epsilon}{\partial x_2} = \alpha(x_\epsilon) f^2 \sin \varphi. \end{aligned} \quad (4.131)$$

4.6 Other profiles

4.6.1 The Navarro-Frenk-White model

nfw97 (NFW hereafter) found that the density profile of dark matter halos numerically simulated in the framework of CDM cosmogony can be very well described by the radial function

$$\rho(r) = \frac{\rho_s}{(r/r_s)(1+r/r_s)^2}, \quad (4.132)$$

within the wide mass range $3 \times 10^{11} \lesssim M_{vir}/(h^{-1}M_\odot) \lesssim 3 \times 10^{15}$. The logarithmic slope of this density profile changes from -1 at the center to -3 at large radii. Therefore, it is flatter than that of the SIS in the inner part of the halo, and steeper in the outer part. The two parameters r_s and ρ_s are the scale radius and the characteristic density of the halo.

NFW parameterized dark matter halos by their masses M_{200} , i.e. the masses enclosed in spheres with radius r_{200} in which the average density is 200 times the critical density. The relationship between M_{200} and r_{200} is given by

$$r_{200} = 1.63 \times 10^{-2} \left(\frac{M_{200}}{h^{-1}M_\odot} \right)^{1/3} \left[\frac{\Omega_0}{\Omega(z)} \right]^{-1/3} (1+z)^{-1} h^{-1} \text{ kpc}. \quad (4.133)$$

This definition depends on the redshift z at which the halo is identified as well as on the background cosmological model.

From the former definition of r_{200} , the *concentration*, $c \equiv r_{200}/r_s$, and the characteristic density are linked by the relation,

$$\rho_s = \frac{200}{3} \rho_{\text{cr}} \frac{c^3}{[\ln(1+c) - c/(1+c)]}. \quad (4.134)$$

Numerical simulations show that the scale radii of dark matter halos at any redshift z systematically change with mass in such a way that concentration is a characteristic function of M_{200} .

Several algorithms have been suggested for describing the concentration of dark matter halos. They are all based on the assumption that the central density of a halo reflects the mean cosmic density at the time when the halo formed. This is justified by numerical simulations of structure formation, which show that halos are the more concentrated the earlier they form. Originally, NFW devised the following approach. Each halo is assigned a collapse redshift, defined as the redshift at which half of the halo mass is contained in progenitors more massive than a fraction f_{NFW} of the final mass. Then, the characteristic density is taken to be some factor C times the mean cosmic density at the collapse redshift. For fitting the results of their numerical simulations, they use $f_{\text{NFW}} = 0.01$ and $C = 3 \times 10^3$.

bullock01 suggested a different definition, because they noticed that the concentrations of numerically simulated dark matter halos change more rapidly with redshift than predicted by the NFW approach. They define the collapse redshift such that the non-linear mass scale at that redshift is a fraction f_B of the final halo mass. The halo concentration is then assumed to be a factor K times the ratio of the scale factors at the redshift when the halo is identified and at the collapse redshift. The best fitting values they found when comparing to numerical simulations are $f_B = 0.01$ and $K = 4$.

Finally, **eke01** suggested another different approach. The collapse redshift of a halo of mass M is defined such that the suitably defined amplitude of the linearly evolving power spectrum at the mass scale M matches a constant C_E^{-1} . The halo concentration is then obtained by setting the characteristic density equal to the spherical collapse density at the collapse epoch. Numerical results are well represented assuming $C_E = 28$.

The mass-dependence of the concentration parameter c is shown in Fig. (??) for all the definitions of halo concentration discussed before and for different cosmological models. The main features of these plots can be summarized as follows:

- although halo concentrations produced by these different algorithms differ in detail, they have in common that the concentration increases toward lower masses in all the cosmological models considered. This is a direct result of the higher collapse redshift of less massive systems;
- the concentration depends on cosmology. The collapse redshift is determined by Ω_0 and $\Omega_{0\Lambda}$: halos form earlier in open low-density universes, then in flat low-density universes

and later in flat high-density universes. The concentration thus reflects the mean cosmic density at the time when they collapse. For example, halos in an OCDM model ($\Omega_0 = 0.3$, $\Omega_{0\Lambda} = 0$) are generally more concentrated than halos in Λ CDM ($\Omega_0 = 0.3$, $\Omega_{0\Lambda} = 0.7$) or SCDM ($\Omega_0 = 1$, $\Omega_{0\Lambda} = 0$) models, because they form earlier and the mean cosmic density is higher when they collapse. On the other hand, halos formed in a low-density Λ CDM model are less concentrated than those formed in the SCDM model: even if they have a higher collapse redshift, the mean cosmic density is lower when they form.

Several different aspects of lensing by halos with NFW or generalized NFW profiles can be found in Bartelmann **bartelmann96** Wright & Brainerd **wright00** Li & Ostriker **li02** Wyithe, Turner & Spergel **wyithe01** Perrotta et al. **perrotta02** Meneghetti et al. **meneghetti02** Bartelmann et al. **bartelmann02a**; **bartelmann02b** If we take $\xi_0 = r_s$, the density profile (4.132) implies the surface mass density

$$\Sigma(x) = \frac{2\rho_s r_s}{x^2 - 1} f(x), \quad (4.135)$$

with

$$f(x) = \begin{cases} 1 - \frac{2}{\sqrt{x^2-1}} \arctan \sqrt{\frac{x-1}{x+1}} & (x > 1) \\ 1 - \frac{2}{\sqrt{1-x^2}} \operatorname{arctanh} \sqrt{\frac{1-x}{1+x}} & (x < 1) \\ 0 & (x = 1) \end{cases}. \quad (4.136)$$

The lensing potential is given by

$$\Psi(x) = 4\kappa_s g(x), \quad (4.137)$$

where

$$g(x) = \frac{1}{2} \ln^2 \frac{x}{2} + \begin{cases} 2 \arctan^2 \sqrt{\frac{x-1}{x+1}} & (x > 1) \\ -2 \operatorname{arctanh}^2 \sqrt{\frac{1-x}{1+x}} & (x < 1) \\ 0 & (x = 1) \end{cases}, \quad (4.138)$$

and $\kappa_s \equiv \rho_s r_s \Sigma_{\text{cr}}^{-1}$. This implies the deflection angle

$$\alpha(x) = \frac{4\kappa_s}{x} h(x), \quad (4.139)$$

with

$$h(x) = \ln \frac{x}{2} + \begin{cases} \frac{2}{\sqrt{x^2-1}} \arctan \sqrt{\frac{x-1}{x+1}} & (x > 1) \\ \frac{2}{\sqrt{1-x^2}} \operatorname{arctanh} \sqrt{\frac{1-x}{1+x}} & (x < 1) \\ 1 & (x = 1) \end{cases}. \quad (4.140)$$

It is an important feature of the NFW lensing potential [Eq. (4.137)] that its radial profile is considerably less curved near the center than the SIS profile [Eq. (??)]. Since the local imaging properties are determined by the curvature of Ψ , this immediately implies substantial changes to the lensing properties [see Fig. (??)].

The convergence can be written as

$$\kappa(x) = \frac{\Sigma(\xi_0 x)}{\Sigma_{\text{cr}}} = 2\kappa_s \frac{f(x)}{x^2 - 1}, \quad (4.141)$$

from which we obtain the dimensionless mass,

$$m(x) = 2 \int_0^x \kappa(x') x' dx' = 4k_s h(x) . \quad (4.142)$$

The lens equation for this kind of lens model can be solved by using numerical methods. At fixed halo mass, the critical curves of an NFW lens are closer to its center than for SIS lens because of its flatter density profile. There, the potential is less curved, thus the image magnification is larger and decreases more slowly away from the critical curves. Therefore NFW lenses are less efficient in image splitting than SIS lenses, but comparably efficient in image magnification.

4.6.2 The Pseudo-Isothermal model

4.7 Environment

It is often necessary to embed a lens into an external shear field which is created by matter in the lens surroundings. A useful approach is to model this shear by means of a potential Ψ_γ , which must satisfy the following conditions:

$$\begin{aligned} \gamma_1 &= \frac{1}{2}(\Psi_{11} - \Psi_{22}) = \text{const.} \\ \gamma_2 &= \Psi_{12} = \text{const.} \\ \kappa &= \frac{1}{2}(\Psi_{11} + \Psi_{22}) = \text{const.} . \end{aligned} \quad (4.143)$$

If $\Psi_{11} \pm \Psi_{22}$ are required to be constant, Ψ_{11} and Ψ_{22} must separately be constants, thus

$$\Psi_\gamma = Cx_1^2 + C'x_2^2 + Dx_1x_2 + E . \quad (4.144)$$

This requires

$$\begin{aligned} \frac{1}{2}(\Psi_{11} - \Psi_{22}) &= C - C' = \gamma_1 \\ \Psi_{12} &= D = \gamma_2 \\ \frac{1}{2}(\Psi_{11} + \Psi_{22}) &= C + C' = \kappa \end{aligned} \quad (4.145)$$

Imposing $\kappa = 0$, we obtain

$$C = -C' \Rightarrow C = \frac{\gamma_1}{2} . \quad (4.146)$$

Therefore,

$$\Psi_\gamma = \frac{\gamma_1}{2}(x_1^2 - x_2^2) + \gamma_2 x_1 x_2 . \quad (4.147)$$

If ϕ_γ is the angle defining the direction of the external shear, i.e.

$$\begin{aligned} \gamma_1 &= \gamma \cos 2\phi_\gamma , \\ \gamma_2 &= \gamma \sin 2\phi_\gamma , \end{aligned} \quad (4.148)$$

then, in polar coordinates,

$$\Psi_\gamma = \frac{\gamma}{2} x^2 \cos 2(\phi - \phi_\gamma) . \quad (4.149)$$

Likewise, if we want to place our lens on a sheet of constant surface-mass density, the shear of that sheet must be zero (because no direction can be preferred), and from Eq. 4.145 we find

$$\Psi_\kappa = \frac{\kappa}{2}(x_1^2 + x_2^2) = \frac{\kappa}{2}x^2. \quad (4.150)$$

Irrelevant constants have been suppressed above.

We can now embed e.g. a softened isothermal sphere into a constant shear field,

$$\Psi = \sqrt{x^2 + x_c^2} + \frac{\gamma_1}{2}(x_1^2 - x_2^2) + \gamma_2 x_1 x_2 \quad (4.151)$$

yielding the deflection angle

$$\begin{aligned} \vec{\nabla}\Psi &= \frac{\vec{x}}{\sqrt{x^2 + x_c^2}} + \begin{pmatrix} \gamma_1 x_1 + \gamma_2 x_2 \\ -\gamma_1 x_2 + \gamma_2 x_1 \end{pmatrix} \\ &= \frac{\vec{x}}{\sqrt{x^2 + x_c^2}} + \begin{pmatrix} \gamma_1 & \gamma_2 \\ \gamma_2 & -\gamma_1 \end{pmatrix} \vec{x} \end{aligned} \quad (4.152)$$

and the convergence remains unchanged by construction.

The deflection angle of a sheet of constant surface-mass density is

$$\vec{\alpha} = \vec{\nabla}\Psi_\kappa = \kappa \vec{x}. \quad (4.153)$$

Thus, the lens equation reads, in this case,

$$\vec{y} = \vec{x} - \vec{\alpha} = \vec{x}(1 - \kappa). \quad (4.154)$$

If $\kappa = 1$, $y = 0$ for all images, i.e. this sheet focuses all light rays exactly on the origin. This gravitational lens thus has a well-defined focal point.

R When combining the potentials of the lens and of external perturbers the same scale ξ_0 must be chosen if using dimensionless units.

Note that this formalism to include external perturbations is equivalent to that used to describe first order lensing effects in Sect. 2.3. The mapping between the lens and the source plane is indeed linear and described by the Jacobian matrix

$$A = (1 - \kappa) \begin{pmatrix} 1 & 0 \\ 0 & 1 \end{pmatrix} - \gamma \begin{pmatrix} \cos 2\phi_\gamma & \sin 2\phi_\gamma \\ \sin 2\phi_\gamma & -\cos 2\phi_\gamma \end{pmatrix}.$$

4.8 Substructures

4.9 Mass-sheet degeneracy

4.10 Python applications

4.10.1 Multiple images by SIE lenses

4.10.2 Images of extended sources

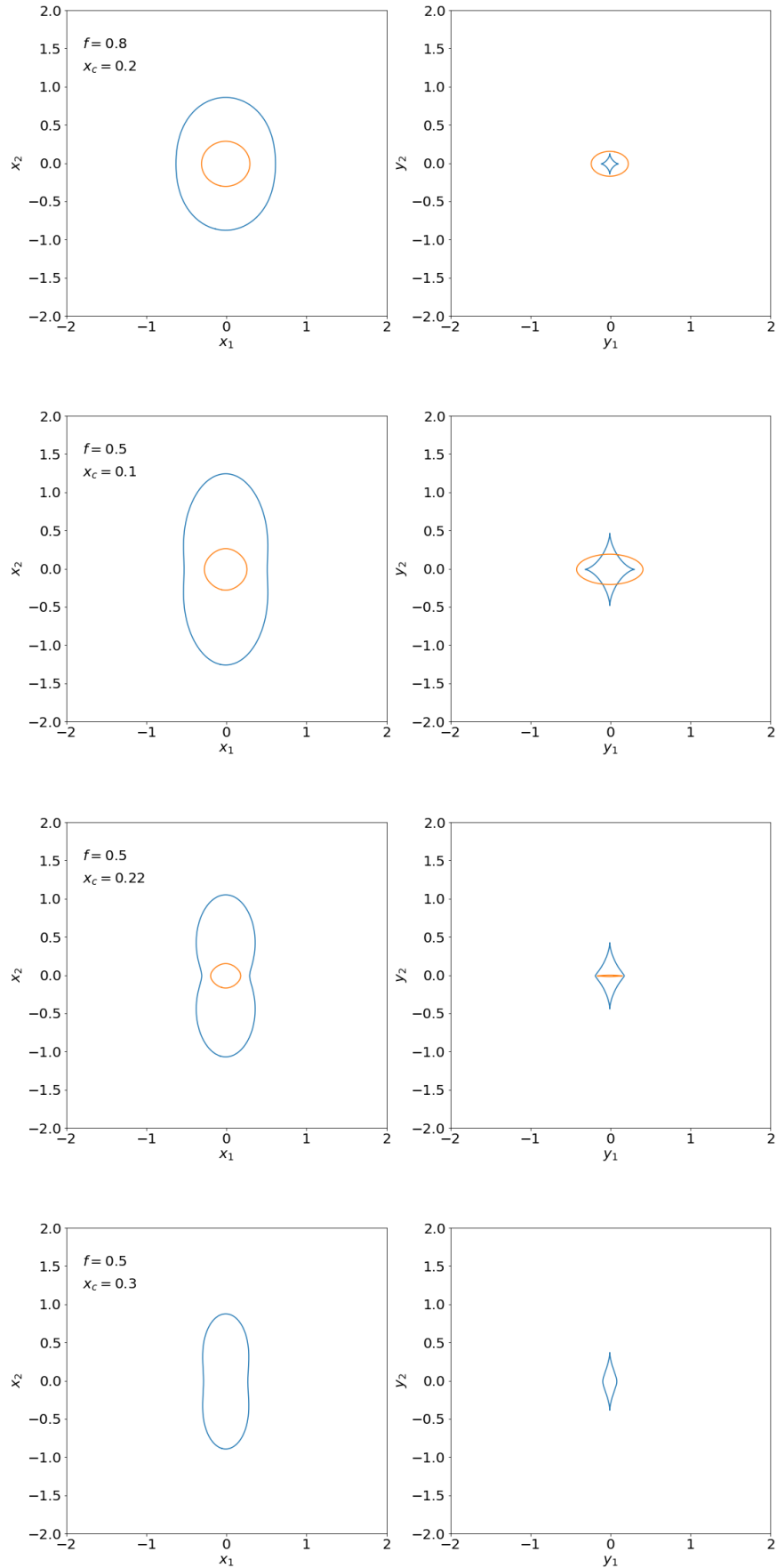


Figure 4.5.9: Critical lines and caustics for NIE lenses with different values of f and x_c . Examples of each topology are shown.

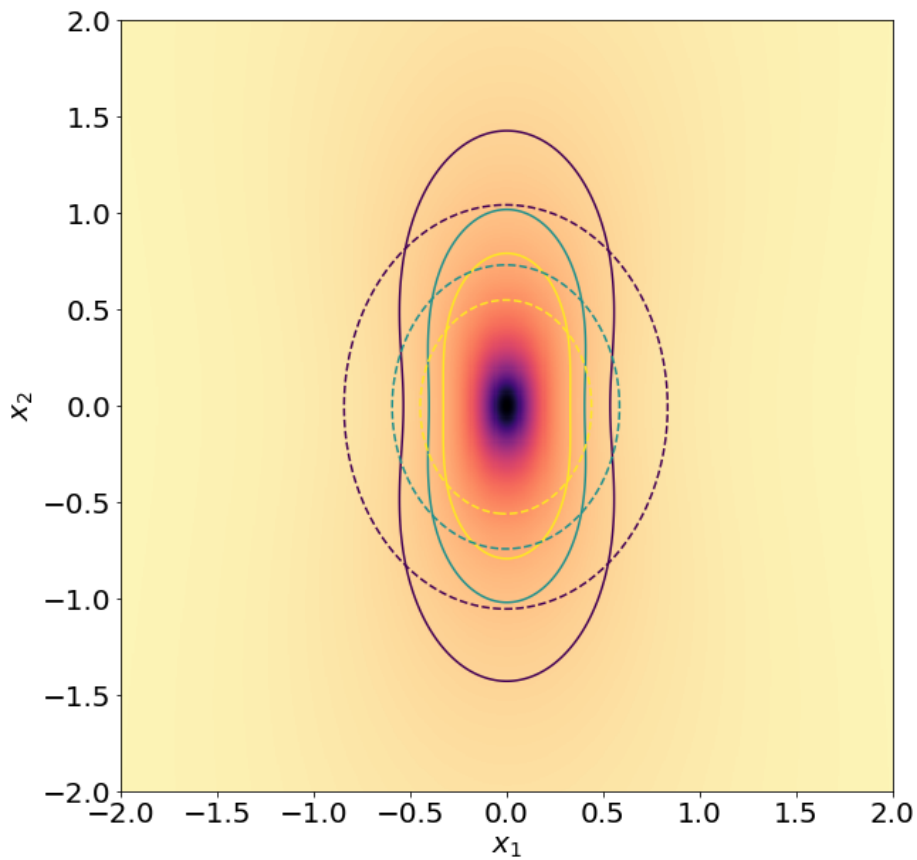


Figure 4.5.10: Convergence map of a pNIE lens with $f = 0.7$. The solid lines show some contours of constant convergence. For comparison, the dashed lines correspond to NIE lens with the same value of f .

Part Three: Appendixes

A	Python tutorial	179
A.1	Installation	
A.2	Documentation	
A.3	Running python	
A.4	Your first python code	
A.5	Variables	
A.6	Strings	
A.7	Lists	
A.8	Tuples	
A.9	Dictionaries	
A.10	Blocks and Indentation	
A.11	IF / ELIF / ELSE	
A.12	While loops	
A.13	For loops	
A.14	Functions	
A.15	Classes	
A.16	Modules	
A.17	Importing packages	
B	Cosmological background	189
B.1	The Robertson-Walker metric	
B.2	Redshift	
B.3	The Friedmann Equations	
B.4	Cosmological parameters	
B.5	Cosmological distances	
B.6	The Friedmann models	
B.7	Structure formation	
B.8	Mass function	
B.9	Quintessence models	
	Bibliography	207
	Index	211

A. Python tutorial

A.1 Installation

The codes discussed as part of these lectures have been developed and run using Anaconda python 2.7 by Continuum analytics. This is just one of the python distributions available for free and we expect that the codes proposed here should run without problems with any of them.

If the reader opts for the Anaconda distribution, she/he can download the installer, which is available for Windows, Mac OSX, and Linux platforms, from <https://www.continuum.io/downloads>.

Following the installation instructions, python should be ready for usage within few minutes.

A.2 Documentation

There are many resources online and books to learn how to program in python. The list below is just a starting point and does not want to be complete:

- the online official documentation can be found at this url: <http://www.python.org/doc>;
- several platforms for e-learning propose courses to learn python. For example, Codeacademy offers [an excellent course](#), which can be completed in only 13 hours;
- Google also offers a [python class](#) online;
- a more extensive (and practical) guide to python is given by [Learn python the hard way](#)

A.3 Running python

Python can be run in several ways:

- from the interactive interpreter: launch "python" in a shell. Quit with Ctrl+D or type "exit()" when finished.
- create your own script with an extension ".py" and run it in a shell by typing "python <script name>.py"
- use an Interactive Development Environment (IDE). These are software which include an editor for coding and capabilities for executing the code. There are several options available (e.g. spyder, Rodeo, etc.)

- We recommend to become familiar with [jupyter notebook](#), which is increasingly popular among python users for sharing code and ideas.

A.4 Your first python code

Try running the code:

```
# your first python code -- this is a comment
print ("Hello World!")
```

Congratulations! You have run your first python code!

A.5 Variables

Variables are names pointing to values or objects. Setting them in python is extremely easy, and you don't need to declare them before:

```
int_var = 4
float_var = 7.89778
boolean_var = True
string_var = "My name is Python"
obj_var=some_class_name(par1,par2)
```

A.6 Strings

String constants can be defined in three ways:

```
single_quotes = 'my name is Python'
double_quotes = "my name is Python"
triple_quotes = """my name is Python
and this is a multiline string.""" #This can contain line breaks!
```

Note that you can combine single and double quotes when you want to define strings which contain quotes themselves:

```
double_quotes1 = 'my name is "Python"'
double_quotes2 = "don't"
```

otherwise you have to use backslashes:

```
double_quotes3 = 'don\t'
\end{python}

Strings can be sliced:
\begin{minted}[bgcolor=bg]{python}
my_name='Massimo Meneghetti'
name = my_name[:7]
surname = my_name[8:]
a_piece_of_my_name=my_name[4:7]
```

You can make many operations with strings. These are objects and have many methods. Check out this url to learn more: <https://docs.python.org/2/library/stdtypes.html>

Some examples:

- String concatenation:

```
back_to_my_full_name=name+" "+surname
```

- Convert to upper case

```
my_name_uppercase=back_to_my_full_name.upper()
```

The built-in function `str` converts numbers to strings:

```
my_int=2
my_float=2.0
str_int=str(my_int)
str_float=str(my_float)
```

Another way to include numbers in strings:

```
my_string1 = 'My integer is %d.' % my_int
my_string2 = 'My float is %f.' % my_float
my_string3 = 'My float is %3.1f (with only one decimal)' % my_float
```

With several variables, we need to use parentheses:

```
a = 2
b = 67
my_string4 = '%d + %d = %d' % (a, b, a+b)

a = 2
b = 67.3
my_string5 = '%d + %5.2f = %5.1f' % (a, b, a+b)
```

Not only you can convert numbers to string, but you can do the reverse operation:

```
s = '23'
i = int(s)
s = '23'
i = float(s)
```

Strip spaces at beginning and end of a string:

```
stripped = a_string.strip()
```

Replace a substring inside a string:

```
newstring = a_string.replace('abc', 'def')
```

Important note: a Python string is "immutable". In other words, it is a constant which cannot be changed in place. All string operations create a new string. This is strange for a C developer, but it is necessary for some properties of the language. In most cases this is not a problem.

A.7 Lists

A list is a dynamic array of any objects. It is declared with square brackets:

```
a_list = [1, 2, 3, 'abc', 'def']
```

Lists may contain lists:

```
another_list = [a_list, 'abc', a_list, [1, 2, 3]]
```

Note that `a_list` in this case is a pointer.

Access a specific element by index (index starts at zero):

```
elem = a_list[2]
elem2 = another_list[3][1]
```

It's easy to test if an item is in the list:

```
if 'abc' in a_list:
    print 'bingo!'
```

Extracting a part of a list is called slicing:

```
list2 = a_list[2:4] # returns a list with items 2 and 3 (not 4)
```

Other list operations like appending:

```
a_list.append('ghi')
a_list.remove('abc')
```

Other list operations: <http://docs.python.org/lib/typesseq.html>

A.8 Tuples

A tuple is similar to a list but it is a fixed-size, immutable array. This means that once a tuple has been created, its elements may not be changed, removed, appended or inserted.

It is declared using parentheses and comma-separated values:

```
a_tuple = (1, 2, 3, 'abc', 'def')
```

but parentheses are optional:

```
another_tuple = 1, 2, 3, 'abc', 'def'
```

Tip: a tuple containing only one item must be declared using a comma, else it is not considered as a tuple:

```
a_single_item_tuple = ('one value',)
```



Tuples are not constant lists – this is a common misconception. Lists are intended to be homogeneous sequences, while tuples are heterogeneous data structures.

In some sense, tuples may be regarded as simplified structures, in which position has semantic value [e.g. (name,surname,age,height,weight)]. For this reason they are immutable, contrary to lists.

A.9 Dictionaries

A Dictionary (or "dict") is a way to store data just like a list, but instead of using only numbers to get the data, you can use almost anything. This lets you treat a dict like it's a database for storing and organizing data.

Dictionaries are initialized using curl brackets:

```
person = {'name': 'Massimo', 'surname': 'Meneghetti'}
```

You can access the elements of the dictionary by using the entry keys:

```
person['name']
```

The keys can also be numbers:

```
person = {'name': 'Massimo', 'surname': 'Meneghetti', 1: 'new data'}
person[1]
```

A.10 Blocks and Indentation

Blocks of code are delimited using indentation, either spaces or tabs at the beginning of lines. This will become clearer in the next sections, when loops will be introduced.

Tip: NEVER mix tabs and spaces in a script, as this could generate bugs that are very difficult to be found.

A.11 IF / ELIF / ELSE

Here is an example of how to implement an IF/ELIF/ELSE loop:

```
if a == 3:
    print 'The value of a is:'
    print 'a=3'

if a == 'test':
    print 'The value of a is:'
    print 'a="test"'
    test_mode = True
else:
    print 'a!="test"'
    test_mode = False
    do_something_else()

if a == 1 or a == 2:
    pass # do nothing
elif a == 3 and b > 1:
    pass
elif a==3 and not b>1:
    pass
else:
    pass
```

A.12 While loops

```
a=1
while a<10:
    print a
    a += 1
```

A.13 For loops

```
for a in range(10):
    print a

my_list = [2, 4, 8, 16, 32]
for a in my_list:
    print a
```

A.14 Functions

Functions can be defined in python as follows:

```
def compute_sum(arg1,arg2):
    # implement function to calculate the sum of two numbers
    res=arg1+arg2
    return(res)
```

The function can be called by typing the function name. If the function returns a value or object, this is assigned to a variable as follows:

```
summa=compute_sum(3.0,7.0)
```

Otherwise, the function can just be called without setting it equal to any variable.

```
c=3

def change_global_c(val):
    # this function change the value of a global variable
    global c
    c=val

change_global_c(10)
```

A.15 Classes

Classes are a way to group a set of functions inside a container. These can be accessed using the . operator. The main purpose of classes is to define objects of a certain type and the corresponding methods. For example, we may want to define a class called 'square', containing the methods to compute the square properties, such as the perimeter and the area. The object is initialized by means of a "constructor":

```

class square:

    #the constructor:
    def __init__(self,side):
        self.side=side

        #area of the square:
    def area(self):
        return(self.side*self.side)

        #perimeter of the square:
    def perimeter(self):
        return(4.0*self.side)

```

We can then use the class to define a square object:

```

s=square(3.0) # a square with side length 3
print s.area()
print s.perimeter()

```

As in other languages (e.g. C++), python supports inheritance. A class can be used as an argument for another class. In this case the new class will inherit the methods of the parent class. For example:

```

class geometricalFigure(object):

    def __init__(self,name):
        self.name=name

    def getName(self):
        print 'this is a %s' % self.name

class square(geometrical_figure):

    #the constructor:
    def __init__(self,side):
        geometricalFigure.__init__(self,'square')
        self.side=side

        #area of the square:
    def area(self):
        return(self.side*self.side)

        #perimeter of the square:
    def perimeter(self):
        return(4.0*self.side)

class circle(geometrical_figure):

    #the constructor:

```

```

def __init__(self, radius):
    geometricalFigure.__init__(self, 'circle')
    self.radius=radius

    #area of the square:
def area(self):
    return(3.141592653*self.radius**2)

    #perimeter of the square:
def perimeter(self):
    return(2.0*self.radius*3.141592653)

s=square(3.0)
c=circle(3.0)
s.getName()
c.getName()

```

In the example above, `square` and `circle` are two examples of `geometricalFigure`. They have some specialized methods to compute the area and the perimeter, but both can access the method `getName`, which belongs to `geometricalFigure`, because they have inherited it from the parent class.

A.16 Modules

A module is a file containing Python definitions and statements (constants, functions, classes, etc). The file name is the module name with the suffix `.py` appended.

Modules can be imported in another script by using the `import` statement:

```
import modulename
```

The functions and statements contained in the module can be accessed using the `.` operator.

Modules can import other modules. It is customary but not required to place all import statements at the beginning of a module (or script, for that matter).

There is a variant of the import statement that imports names from a module directly into the importing module's symbol table. For example:

```
from modulename import something
```

A.17 Importing packages

Packages can be added to your python distribution by using either the `pip` or `easy_install` utilities. Anaconda has its own utility for installing a (limited) set of supported packages, called `conda`. To learn more, check out <https://packaging.python.org/installing/>

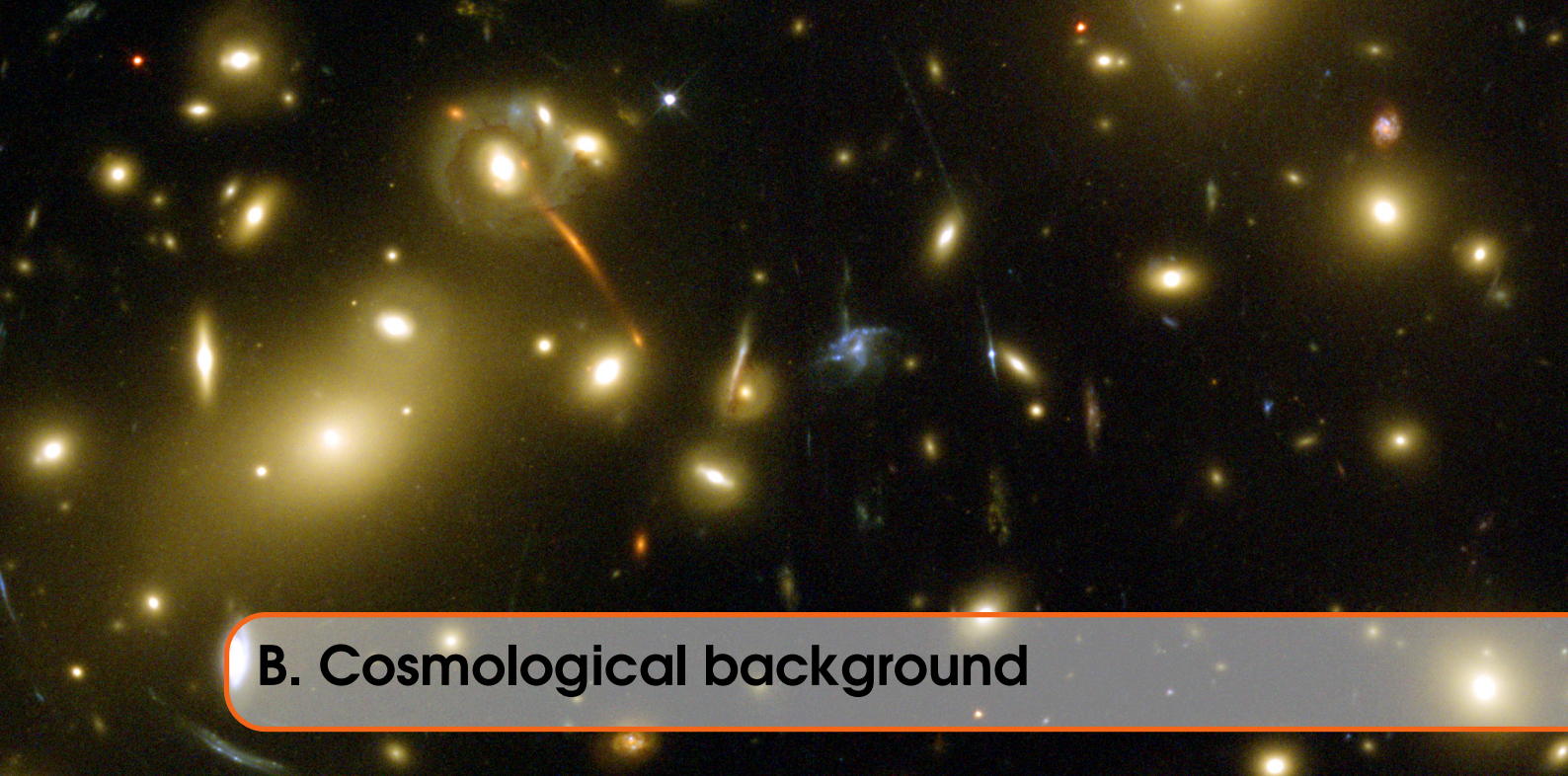
Packages can be used by importing modules and classes in the code as discussed above.

Some packages that we will use a lot:

- `numpy`: fundamental package for scientific computing with Python (powerful N-dimensional array object, sophisticated functions, tools for integrating C/C++ and Fortran code, useful linear algebra, Fourier transform, and random number capabilities);

- [scipy](#): provides many user-friendly and efficient numerical routines such as routines for numerical integration and optimization;
- [matplotlib](#): a Python 2D plotting library which produces publication quality figures in a variety of hardcopy formats and interactive environments across platforms;
- [astropy](#): a community effort to develop a single core package for Astronomy in Python and foster interoperability between Python astronomy packages.

Other packages will be introduced in the examples.



B. Cosmological background

We review in this appendix those aspects of the standard cosmological model which are relevant for understanding gravitational lensing and its applications.

The standard model is based on the assumption of the so called “*Cosmological Principle*”, which states that the Universe is homogeneous and isotropic on large scales. The metric properties of the space-time are described by the Robertson-Walker metric, in which hypersurfaces of constant time are homogeneous and isotropic three-spaces, either flat or curved. The time dependence of these hypersurfaces is given by a scale factor, which is a function of time only.

Structures grow from initial density fluctuations via gravitational collapse. The origin of these initial seed perturbations is still unclear. The most common hypothesis is that their statistics is Gaussian. Given that their amplitude remains small for most of their evolution, the growth of the initial density perturbations can be appropriately described by the linear perturbation theory until late stages. After that, the growth of perturbations starts to depart from linearity and enters into the non-linear regime. Then, structure evolution becomes very complicated and numerical methods are required for a realistic description.

B.1 The Robertson-Walker metric

The standard cosmological models is based on the assumption of the “*Cosmological Principle*”. This is the assertion that, on sufficiently large scales (beyond those traced by the large-scale structure of the galaxy distribution), the Universe is homogeneous and isotropic. Originally introduced by Einstein and subsequent relativistic cosmologists without strict empirical justification, the Cosmological Principle is today accepted because it agrees with observations: data concerning radio galaxies, clusters of galaxies, quasars and the microwave background all demonstrate that the level of anisotropy of the universe on very large scales is about one part in 10^5 .

The geometrical properties of the space-time are described by a metric. All events in the space-time have one time coordinate $x^0 = ct$, where c is the velocity of light and t is the proper time, and three space coordinates x^1, x^2, x^3 . The interval between two events in the space-time can

be written as

$$ds^2 = g_{ij}dx^i dx^j , \quad (\text{B.1})$$

where repeated suffixes imply summation and i, j both run from 0 to 3. The tensor g_{ij} is the metric tensor, which describes the space-time geometry.

The most general space-time metric describing a universe in which the Cosmological Principle is obeyed is the *Robertson-Walker* metric. Adopting this metric, Eq. (B.1) can be written as

$$ds^2 = (cdt)^2 + a(t)^2 \left[\frac{dr^2}{1 - Kr^2} + r^2(d\theta^2 + \sin\theta^2 d\phi^2) \right] , \quad (\text{B.2})$$

where r, θ and ϕ are spherical polar coordinates. As can be easily seen in Eq. (B.2), the distance between two points in space depends on time only through the scale factor $a(t)$, whose form will be shown later. Given that r, θ and ϕ are time independent variables, these coordinates are called *comoving*. The parameter K determines the curvature of spatial hypersurfaces. It is a constant which can be scaled to assume only the values 1, 0 or -1 . The case $K = 0$ corresponds to the flat, Euclidean space, whose properties are familiar. The other two cases, $K = 1$ and $K = -1$, correspond, respectively, to hyperspheres and spaces of constant negative curvature: the first is a closed space, with finite volume and no boundary; the second is an open (hyperbolic) space, i.e. infinite.

B.2 Redshift

If the scale factor $a(t)$ changes with time, i.e. if the universe expands or shrinks, photons which are emitted by a source are redshifted or blueshifted while propagating to the observer.

Consider a luminous source at comoving distance r , emitting photons whose wavelength is λ_e at time t_e , and an observer placed at the origin of the coordinate system ($r = 0$). We define the *redshift* z of the source as

$$z = \frac{\lambda_o - \lambda_e}{\lambda_e} , \quad (\text{B.3})$$

where λ_o is the wavelength of radiation from the source measured by the observer at time t_o .

Given that radiation travels along null geodesics in the space-time (i.e. $ds^2 = 0$), we obtain from Eq. (B.2):

$$\int_{t_e}^{t_o} \frac{cdt}{a(t)} = \int_0^r \frac{dr'}{(1 - Kr'^2)} = f(r) . \quad (\text{B.4})$$

The same result of Eq. (B.4) can be obtained also for light which is emitted by the source at time $t'_e = t_e + \delta t_e$ and received by the observer at time $t'_o = t_o + \delta t_o$:

$$\int_{t'_e}^{t'_o} \frac{cdt}{a(t)} = f(r) . \quad (\text{B.5})$$

Eq. (B.4) and (B.5) imply that, if δt_e and δt_o are small,

$$\frac{\delta t_o}{a_o} = \frac{\delta t_e}{a_e} , \quad (\text{B.6})$$

where $a_o = a(t_o)$ and $a_e = a(t_e)$. Identifying the inverse of the time intervals t_o and t_e with the inverse frequencies of the observed and emitted radiation, v_o and v_e , Eq. (B.6) can be written as

$$v_e a_e = v_o a_o , \quad (\text{B.7})$$

or equivalently,

$$\frac{a_e}{\lambda_e} = \frac{a_o}{\lambda_o}, \quad (\text{B.8})$$

from which

$$1 + z = a_o/a_e. \quad (\text{B.9})$$

This Eq. shows the relationship between the redshift z and the scale factor $a(t)$: if the universe expands and $a_o > a_e$, then the light observed from distant sources is redshifted ($z > 0$).

B.3 The Friedmann Equations

The geometry of space-time, expressed by the metric tensor g_{ij} , is related to the matter content of the universe, expressed by the energy-momentum tensor T_{ij} , through *Einstein's field equations*,

$$R_{ij} - \frac{1}{2}Rg_{ij} - \Lambda g_{ij} = \frac{8\pi G}{c^4}T_{ij}, \quad (\text{B.10})$$

where R_{ij} and R are the Ricci tensor and Ricci scalar, respectively.

The term Λ is called the *cosmological constant*. It was introduced by Einstein to enable for static cosmological solutions of the field equations. However, even after the expansion of the universe was observationally established, the cosmological constant refused to die. Its physical meaning can be easily understood by considering Eq. (B.10) in vacuum. In that case, the energy-momentum tensor is

$$T_{ij}^{vac} = -\frac{c^4\Lambda}{8\pi G}g_{ij}. \quad (\text{B.11})$$

In other words, if the cosmological constant differs from zero, the vacuum has non-zero energy density and pressure.

The energy-momentum tensor of the universe is that of an homogeneous perfect fluid, which is characterized by its density $\rho(t)$ and pressure $p(t)$. For the Robertson-Walker metric the Einstein's equations simplify to the *Friedmann equations*,

$$\left(\frac{\dot{a}}{a}\right)^2 = \frac{8\pi G}{3}\rho - \frac{Kc^2}{a^2} + \frac{\Lambda c^2}{3} \quad (\text{B.12})$$

$$\frac{\ddot{a}}{a} = -\frac{4}{3}\pi G\left(\rho + \frac{3p}{c^2}\right) + \frac{\Lambda c^2}{3}. \quad (\text{B.13})$$

These two equations are not independent: the second can be recovered from the first if one takes the adiabatic expansion of the universe into account, i.e. if we assume that the change of internal energy equals minus the pressure times the change in proper volume,

$$\frac{d}{dt}[a^3(t)\rho(t)c^2] = -p\frac{da^3(t)}{dt}. \quad (\text{B.14})$$

The time dependence of the scale factor $a(t)$ can then be determined by integrating these differential equations and by fixing its value at one instant of time. We choose $a = 1$ at the present epoch t_0 .

B.4 Cosmological parameters

Before going further, it is convenient to define some parameters which will be largely used in the following sections. First of all, we introduce the parameter used to quantify the relative expansion rate of the universe,

$$H(t) \equiv \frac{\dot{a}(t)}{a(t)}, \quad (\text{B.15})$$

which is called the *Hubble parameter*. Its value at the present epoch, $H_0 = H(t_0)$, is known as the *Hubble constant*. Current measurements of this quantity roughly fall in the range $H_0 = (50 \div 80)$ km s⁻¹ Mpc⁻¹: the *HST Key Project* team find $H_0 = 72 \pm 8$ km s⁻¹ Mpc⁻¹ **freedman01** while Saha et al. **saha01** using their Cepheid calibration for a sample of galaxies with Type Ia supernovae, find a smaller value, $H_0 = 59 \pm 6$ km s⁻¹ Mpc⁻¹. The uncertainty in H_0 is commonly expressed as $H_0 = 100h$ km s⁻¹ Mpc⁻¹, with $h = (0.5 \div 0.8)$.

We then define the present *critical density* of the universe as

$$\rho_{0,\text{cr}} \equiv \frac{3H_0^2}{8\pi G} \approx 1.9 \times 10^{-29} h^2 \text{g cm}^{-3}, \quad (\text{B.16})$$

where G is the gravitational constant.

The density of the universe in units of $\rho_{0,\text{cr}}$ is the *density parameter*,

$$\Omega_0 \equiv \frac{\rho_0}{\rho_{0,\text{cr}}}. \quad (\text{B.17})$$

As will be discussed later, the value of Ω_0 is crucial for cosmology.

All the components of the universe contribute to its density: baryonic and non-baryonic matter, radiation and vacuum. As was pointed out in the previous section, a non-null cosmological constant means that the vacuum has a finite density. This density can be written in units of the critical density as

$$\Omega_{0\Lambda} \equiv \frac{\Lambda c^2}{3H_0^2}. \quad (\text{B.18})$$

The acquisition of the latest results from high-redshift Type Ia supernovae searches and from microwave background experiments indicate that the total density parameter of the universe is very close to unity and that the largest contribution to it comes from the cosmological constant.

The values of Ω_0 and $\Omega_{0\Lambda}$ are related to the curvature of the spatial hypersurfaces. Using the previous definitions, Eq. (B.12) can be written for $a = a_0 = 1$ as

$$H_0^2(1 - \Omega_0 - \Omega_{0\Lambda}) = -Kc^2, \quad (\text{B.19})$$

from which we see that if $K = 0$, then $\Omega_0 + \Omega_{0\Lambda} = 1$. Moreover, the sign of K is positive if $\Omega_0 + \Omega_{0\Lambda} > 1$, negative otherwise.

Finally, we define the *deceleration parameter*

$$q_0 = -\frac{\ddot{a}a}{\dot{a}^2} \quad (\text{B.20})$$

at $t = t_0$. The sign of this parameter tells us if the universe is in decelerated expansion or not.

B.5 Cosmological distances

Several types of distance between two points can be defined in a curved space-time. Indeed, distance definitions in terms of different measurement prescriptions generally lead to different distances.

The *proper distance* of P from P_0 , which we can take as the origin of the polar coordinate system r, ϕ, θ , is the distance measured at time t by a chain of observers connecting P to P_0 . From Eq. (B.2), this distance is

$$d_{\text{pr}} = \int_0^r \frac{adr'}{(1-Kr'^2)^{1/2}} = af(r) , \quad (\text{B.21})$$

where a is the scale factor at time t , $a = a(t)$, and the radial function $f(r)$ is

$$f(r) = \begin{cases} \arcsin r & K = 1 \\ r & K = 0 \\ \operatorname{arcsinh} r & K = -1 \end{cases} . \quad (\text{B.22})$$

Given the time dependence of the scale factor, also the proper distance changes with time. Therefore, the point P has a radial velocity with respect to P_0 given by

$$v_r = \dot{a}f(r) = \frac{\dot{a}}{a}f(r) = H(t)d_{\text{pr}} . \quad (\text{B.23})$$

This Eq. is called the *Hubble Law*.

The proper distance at the actual time t_0 defines the *comoving distance*

$$d_c = f(r) = a^{-1}d_{\text{pr}} . \quad (\text{B.24})$$

This is the distance on the spatial hyper-surface $t = t_0$ between the world-lines of points P and P_0 comoving with the cosmic flow.

The *angular diameter distance* is defined in analogy to the relation in the Euclidean space between the physical diameter D_{pr} of a source and the angle $\Delta\theta$ that it subtends. From Eq. (B.2), it results in $D_{\text{pr}} = ar\Delta\theta$ and the angular diameter distance is then

$$d_A = \frac{D_{\text{pr}}}{\Delta\theta} = ar . \quad (\text{B.25})$$

The distance defined in such a way to preserve the Euclidean inverse-square law for the decrease of luminosity with distance from a source is called *luminosity distance*. If L is the amount of energy emitted by a source in P per unit time and l is the amount of energy received per unit time and per unit area by an observer in P_0 , the luminosity distance between these two points is defined as

$$d_L = \left(\frac{L}{4\pi l} \right)^{1/2} . \quad (\text{B.26})$$

The area of a spherical surface centered on P and passing through P_0 at time t_0 is just $4\pi r^2$. The photons emitted by the source arrive at this surface having been redshifted by the expansion of the universe by a factor a . Also, photon arrival times are delayed by another factor a . Therefore, the flux l is given by

$$l = \frac{L}{4\pi r^2} a^2 , \quad (\text{B.27})$$

from which

$$d_L = a^{-1}r = a^{-2}d_A . \quad (\text{B.28})$$

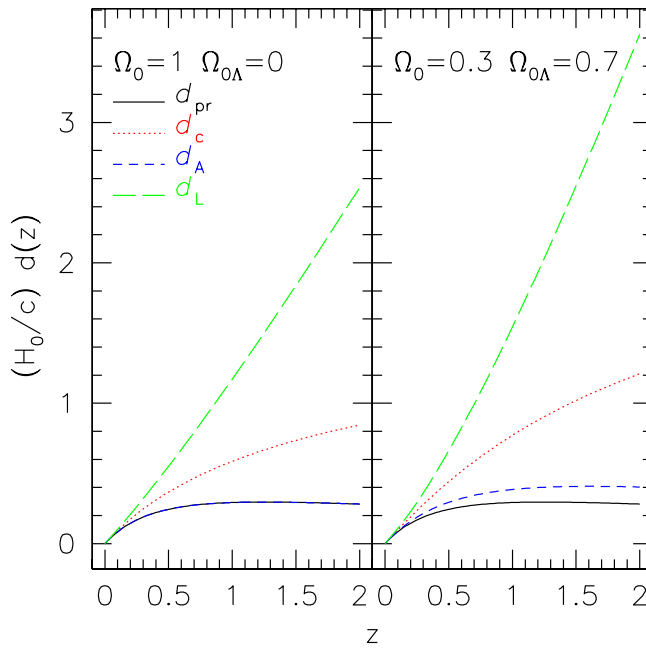


Figure B.5.1: Four distance measures are plotted as a function of redshift in two cosmological models: a model with $\Omega_0 = 1$ and $\Omega_{0\Lambda} = 0$ (left panel) and a model with $\Omega_0 = 0.3$ and $\Omega_{0\Lambda} = 0.7$ (right panel). These are the proper distance d_{pr} (solid line), the comoving distance d_c (dotted line), the angular-diameter distance (short-dashed line) and the luminosity distance (log-dashed line).

We plot the four distances d_{pr} , d_c , d_A and d_L as a function of redshift in Fig.(B.5.1). Given that they depend on the curvature of the space time, distances change for different values of Ω_0 and $\Omega_{0\Lambda}$: they are larger for lower cosmic density and higher cosmological constant. The largest differences are at high redshift, while at low redshift all distances follow the Hubble law,

$$\text{distance} = \frac{cz}{H_0} + O(z^2). \quad (\text{B.29})$$

B.6 The Friedmann models

We now introduce the standard cosmological models described by the equations (B.12) and (B.13). They receive their name from A. Friedmann, who derived them in 1922. The main assumptions on which these cosmological models are based are:

- the universe can be approximated by a perfect fluid with some density ρ and pressure p ;
- the appropriate equation of state, relating pressure to density, can be cast, either exactly or approximately, in the form

$$p = w\rho c^2 \quad (\text{B.30})$$

The perfect fluid is, in fact, quite a realistic approximation in many situations. For example, if the scale of particle interaction is much smaller than the scale of physical interest, as is the case for the global properties of the universe, the fluid can be treated as perfect. Even the second assumption on the fluid equation of state is quite appropriate in many cases of physical interest.

Ordinary matter, which can be considered as pressureless, is frequently called *dust*, and corresponds to the case $w = 0$. This approximation is valid in general for any non-relativistic gas, which can then be treated as a fluid of dust.

On the other hand, relativistic matter and radiation correspond to the case $w = 1/3$.

Inserting these expressions into Eq. (B.14), we obtain:

$$\rho = \begin{cases} \rho_0 a^{-3} = \rho_0(1+z)^4 & \text{for dust, } p=0 \\ \rho_0 a^{-4} = \rho_0(1+z)^3 & \text{for relativistic matter, } p=\frac{1}{3}\rho c^2 \end{cases} . \quad (\text{B.31})$$

The energy density of relativistic matter therefore drops more rapidly than that of ordinary matter. This can be understood by considering a comoving box containing N particles. Let us assume that the box expands, with an expansion factor $a(t)$, and particles within it are neither created nor destroyed. In the case of non-relativistic matter, the density of particles simply changes as the inverse of the box volume, i.e. as a^{-3} . If the particles are relativistic, they behave like photons: not only their number density decreases as a^{-3} , but their wavelength λ is also increased by a factor a . Since the energy per particle is proportional to λ^{-1} , the total energy density decreases as a^{-4} .

The relativistic matter component candidates today are photons and neutrinos. Their cosmic density contribution, $\Omega_{R,0} = \Omega_{\gamma,0} + \Omega_{\nu,0}$, is estimated to be $\sim 3.2 \times 10^{-5} h^{-2}$. This is four orders of magnitude smaller than the today-estimated value of the matter density parameter of the universe, and can thus be considered negligible. At the epoch when the density of the relativistic matter component equaled that of the non-relativistic one, the expansion scale factor was

$$a_{\text{eq}} = \frac{\Omega_{R,0}}{\Omega_0} = 3.2 \times 10^{-5} \Omega_0^{-1} h^{-2} . \quad (\text{B.32})$$

Much before that epoch, i.e. for $a \ll a_{\text{eq}}$, the expansion of the universe therefore was radiation-dominated.

An important property of the Friedmann models with no cosmological constant is that, if $w > -1/3$, they possess a point in time where $a = 0$, which is called the *Big-Bang singularity*. Indeed, inserting Eq. (B.30) into Eq. (B.12), we obtain

$$H^2(t) = \left(\frac{\dot{a}}{a}\right)^2 = H_0^2 a^{-2} \left[\Omega_{0w} a^{-(1+3w)} + (1 - \Omega_{0w}) \right] , \quad (\text{B.33})$$

where $\Omega_{0w} = \rho_{0w}/\rho_{\text{cr}}$ is the actual density parameter of the fluid. Suppose that at some generic time t the universe is expanding, so that $\dot{a}(t) > 0$. If $w > -1/3$, from Eq. (B.12) we see that $\ddot{a} < 0$ for all t . The graph describing $a(t)$ therefore is necessarily concave and there must be a time, which we can set as $t = 0$, when $a(0) = 0$ and when the density diverges.

B.6.1 Single component models

We discuss in this Section the solutions of Eq. (B.12) for flat, open and closed models in the simple case of single-component universes.

The solution appropriate to a flat universe, i.e. with $\Omega_{0w} = 1$, without cosmological constant is known as the *Einstein-de Sitter universe*. In this case, integrating Eq. (B.12), we obtain

$$a(t) = \begin{cases} \left(\frac{t}{t_0}\right)^{2/3} & \text{for the matter-dominated universe, } w=0 \\ \left(\frac{t}{t_0}\right)^{1/2} & \text{for the radiation-dominated universe, } w=\frac{1}{3} \end{cases} . \quad (\text{B.34})$$

A general property of these models therefore is that the expansion parameter a grows indefinitely with time. Moreover, the deceleration parameter is constant and positive in both the cases of matter- and radiation-dominated universes. This means that the expansion in these models is decelerated.

The solutions for curved models are rather more complicated. At early times, they behave in a manner very similar to flat models, and the solutions seen for the Einstein-de Sitter model can be

applied. Then, when $a(t) \gg a(t^*) = a^*$, where a^* is given by

$$a^* = \left| \frac{\Omega_{0w}}{1 - \Omega_{0w}} \right|^{1/(1+3w)}, \quad (\text{B.35})$$

solutions differ. In models with $\Omega_{0w} < 1$ (open universes), for $t \gg t^*$ the scale factor grows with time as

$$a(t) \simeq a^* \frac{t}{t^*}, \quad (\text{B.36})$$

and the deceleration parameter is approximately zero.

In models with $\Omega_w > 1$, at $t = t^*$ the scale factor reaches a maximum $a_m = a_*$. After that time $a(t)$ starts to decrease symmetrically around a_m . At time $t = 2t^*$ there is another singularity in a symmetrical position with respect to the *Big-Bang*, called the *Big-Crunch*.

Analytical solutions exist for both matter- and radiation-dominated universes. For a more detailed discussion, see [coles02](#)

B.6.2 Multiple component models

Considering a model universe made of matter, radiation and cosmological constant, Eq. (B.12) becomes

$$H^2(t) = H_0^2 \left[\frac{\Omega_{R,0}}{a^4} + \frac{\Omega_0}{a^3} + \frac{1 - \Omega_0 - \Omega_{0\Lambda}}{a^2} + \Omega_{0\Lambda} \right]. \quad (\text{B.37})$$

There is generally no simple solution to this Equation. Qualitatively, we can say that at very early times the universe is flat and radiation-dominated. Even the term depending on the cosmological constant is negligible at that time. Therefore, solutions for the Einstein-de Sitter model are appropriate for describing the evolution of the scale factor during this period. Then, after equivalence, matter starts to dominate over radiation and the cosmological constant term becomes increasingly more significant.

Using Eq. (B.37), we can determine the dependence of Ω and Ω_Λ on the scale factor a . For a matter dominated universe, we find

$$\Omega(a) = \frac{8\pi G}{3H^2(a)} \rho_0 a^{-3} = \frac{\Omega_0}{a + \Omega_0(1-a) + \Omega_{0\Lambda}(a^3-a)}, \quad (\text{B.38})$$

$$\Omega_\Lambda(a) = \frac{\Lambda c^2}{3H^2(a)} = \frac{\Omega_{0\Lambda} a^3}{a + \Omega_0(1-a) + \Omega_{0\Lambda}(a^3-a)}. \quad (\text{B.39})$$

Whatever the values of Ω_0 and $\Omega_{0\Lambda}$ are at the present epoch, Eqs. (B.38) and (B.39) show that $\Omega \rightarrow 1$ and $\Omega_\Lambda \rightarrow 0$ for $a \rightarrow 0$. On the other hand, if $\Omega_0 + \Omega_{0\Lambda} \leq 1$, $\Omega \rightarrow 0$ and $\Omega_\Lambda \rightarrow 1$ monotonically for $a \rightarrow \infty$. Therefore, for this kind of models we can define a time t_Λ such that for $a \gg a_\Lambda = a(t_\Lambda)$, the dominant term in Eq. (B.37) is the cosmological constant one. Neglecting all the other terms, the solution of the Friedmann equations at that time is that of the so-called *de Sitter universe*, which is written in the form

$$a(t) \propto \exp \left[\left(\frac{1}{3} \Lambda \right)^{1/2} ct \right]. \quad (\text{B.40})$$

This means that at a given time t_{acc} , the cosmological constant term starts to accelerate the expansion of the universe. This can be explained, if one remembers that the cosmological constant is proportional to the energy density and pressure of vacuum. In particular, from Eq. (B.11) we see that the vacuum has a negative-pressure equation of state:

$$p_{\text{vac}} = -\rho_{\text{vac}} c^2. \quad (\text{B.41})$$

This means that the pressure of vacuum can be interpreted as a source of gravitational repulsion. Therefore, we can assume that, when the matter density is sufficiently low, gravity loses its efficiency to decelerate the expansion of the universe and the vacuum pressure starts to accelerate it.

B.7 Structure formation

B.7.1 Linear growth of density perturbations

The standard model assumes that structure in the universe formed via gravitational collapse from initial density fluctuations. The origin of these fluctuations is still unclear, but the general idea is that they were generated during an inflationary epoch from quantum fluctuations. They are assumed to be uncorrelated and the distribution of their amplitudes is assumed to be Gaussian.

Density perturbations are characterized by the density contrast

$$\delta(\vec{r}, a) = \frac{\rho(\vec{r}, a) - \bar{\rho}(a)}{\bar{\rho}(a)}, \quad (\text{B.42})$$

where $\bar{\rho}$ is the average cosmic density and ρ is the density at the position given by \vec{r} .

Until $\delta \ll 1$, it is possible to study the evolution of the density perturbations using the linear approach. First, we consider a universe dominated by baryonic matter, i.e. gas having pressure p . The time evolution of a small density perturbation δ is determined by two opposite forces: the first is the pressure force, which acts such as to cancel the density fluctuation; the second is the gravitational force, which tends to amplify it. If the fluctuation is contained in a region of radius R , the pressure force per unit mass can be written as

$$F_p \approx \frac{pR^2}{M} = \frac{v_s^2}{R}, \quad (\text{B.43})$$

where $M = \rho R^3$ is the mass of the fluctuation and $v_s \sim \sqrt{p/\rho}$ is the sound velocity in the fluid. On the other hand, the gravitational force per unit mass is

$$F_g \approx \frac{GM}{R^2} = G\rho R. \quad (\text{B.44})$$

The density perturbation can grow only if $F_g \geq F_p$. Equaling Eqs. (B.43) and (B.44), we obtain that this condition is satisfied only if the size of the region where the fluctuation happens is larger than the *Jeans radius*,

$$R_J = \left(\frac{v_s^2}{G\rho} \right)^{1/2}. \quad (\text{B.45})$$

Density perturbations on scales $\lambda \geq R_J$ therefore are amplified. Perturbations on scales $\lambda < R_J$ do not grow and propagate as acoustic waves.

Linear theory shows that perturbations on scales larger than the Jeans radius grow like

$$\delta(a) \propto \begin{cases} a^2 & \text{before } a_{\text{eq}} \\ a & \text{after } a_{\text{eq}} \end{cases}, \quad (\text{B.46})$$

as long as the Einstein-de Sitter limit holds. If $\Omega_0 \neq 1$ and $\Omega_{0\Lambda} \neq 0$, this approximation, however, does not apply anymore for $a \gg a_{\text{eq}}$. Then, the linear growth of density perturbations is changed according to

$$\delta(a) = \delta_0 a \frac{g'(a)}{g'(1)} \equiv \delta_0 a g(a), \quad (\text{B.47})$$

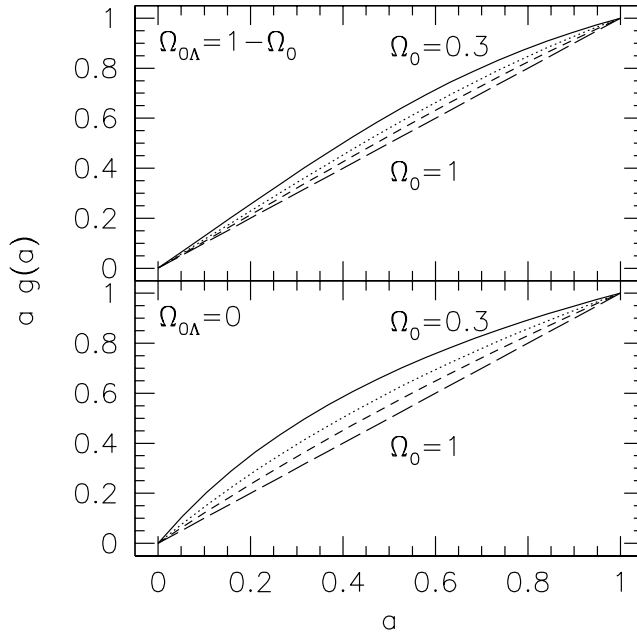


Figure B.7.1: The growth function $ag(a)$ given in Eqs. (B.47) and (B.48) for different values of Ω_0 between $\Omega_0 = 0.3$ and $\Omega_0 = 1.0$: the solid, dotted, short-dashed and long-dashed lines refer to $\Omega_0 = 0.3, 0.5, 0.7$ and 1 , respectively. Curves are displayed for flat models with $\Omega_{0\Lambda} = 1 - \Omega_0$ (top panel) and for open models with $\Omega_{0\Lambda} = 0$ (bottom panel).

where δ_0 is the density contrast linearly extrapolated to the present epoch and $g'(a)$ is the linear growth function, which depends on $\Omega(a)$ and $\Omega_\Lambda(a)$ as given by the fitting function

$$g'(a; \Omega_0, \Omega_{0\Lambda}) = \frac{5}{2} \Omega(a) \left[\Omega^{4/7}(a) - \Omega_\Lambda(a) + \left(1 + \frac{\Omega(a)}{2} \right) \left(1 + \frac{\Omega_\Lambda(a)}{70} \right) \right]^{-1}. \quad (\text{B.48})$$

The growth function $ag(a)$ is shown in Fig. (B.7.1) for a variety of parameters Ω_0 and $\Omega_{0\Lambda}$: the growth rate is constant for the Einstein-de Sitter model ($\Omega_0 = 1$; $\Omega_{0\Lambda} = 0$), while for low Ω_0 models it is higher for $a \ll 1$ and lower for $a \approx 1$. This feature means that structures form earlier in low-density than in high-density models, which will turn out to be of great importance for the further discussion on arc statistics.

Instead of using the size of fluctuations, we can deal with their mass. For a perturbation of density ρ and size R , the mass is defined as

$$M = \frac{4}{3} \pi R^3 \rho. \quad (\text{B.49})$$

This permits us to define the *Jeans mass*, $M_J \equiv M(R_J) = (4/3)\pi R_J^3 \rho$. Only perturbations of mass $M \geq M_J$ can be amplified by gravity.

Before equivalence, the Jeans mass M_J grows like $M_J \propto a^3$. Then, while the matter is coupled with radiation, it is constant, $M_J(a_{\text{eq}}) \sim 10^{16} M_\odot/h$. When radiation and matter decouple, the Jeans mass drops down to $M_J \sim 10^5 M_\odot/h$. This is very important, because the perturbations which initially had mass $M < M_J$ and oscillated without being amplified, can now start to grow.

Density fluctuations can be on scales even larger than the size of the causally connected regions in the universe. This size is called the *cosmological horizon*. It is given by the distance by which a photon can travel in the time t since the Big Bang. Since the appropriate time scale is given by the

inverse Hubble parameter $H^{-1}(a)$, the horizon size is $R_H = cH^{-1}(a)$. The mass inside a sphere with radius R_H is called the *horizon mass*,

$$M_H = \frac{4}{3}\pi R_H^3 \rho . \quad (\text{B.50})$$

Considering only the matter contribution to the density ρ , the horizon mass grows like $M_H \propto a^3$ before equivalence, being $M_H(a_{\text{eq}}) \sim 10^{15} M_\odot/h$, and like $M_H \propto a^{3/2}$ after equivalence. When a perturbation has $M \leq M_H$ it can experience all the physical processes, like dissipation, which happen in the expanding universe.

Before the epoch a_{rec} of the hydrogen recombination, when matter and radiation are still coupled, the baryonic matter in the universe can be considered as a plasma of photons, electrons and protons. Dissipative effects arise in this plasma mainly due to the diffusion of photons. The size of the region which is affected by the dissipation effects grows with time like $R_S \propto (c^2 \tau_{\gamma e} t)^{1/2}$, where $\tau_{\gamma e}$ is the time scale for the collisions between photons and electron-proton pairs. The *dissipation mass* (or *Silk mass*) is then

$$M_S = \frac{4}{3}\pi R_S^3 \rho . \quad (\text{B.51})$$

This mass grows like $M_S \propto a^{9/2}$ before equivalence, when $M_S(a_{\text{eq}}) \sim 10^{11} M_\odot/h$, and like $M_S \propto a^{15/4}$ after equivalence. After recombination, the dissipation mass drops to zero. It is important to note that dissipation obliterates the fluctuations on all scales smaller than the Silk mass almost immediately. In a collisional fluid, no structure will therefore be formed on all mass scale less than the Silk mass at recombination, $M_S(a_{\text{rec}}) \sim 10^{14} M_\odot/h$. Smaller structures can only form by fragmentation of the larger ones.

The main problem of this model for structure formation is that the cosmic microwave background reveals relative temperature fluctuations of order 10^{-5} on large scales. By the Sachs-Wolfe effect **sachs67** these temperature fluctuations reflect baryonic density fluctuations of the same order of magnitude at recombination. Given that recombination occurs at $a \sim 10^3$, Eq. (B.46) implies that density fluctuations today should only reach a level of 10^{-2} . Instead structure (e.g. galaxies) with $\delta \gg 1$ are observed.

This is one of the strongest arguments for the existence of an additional matter component which does not couple electromagnetically (probably only weakly), i.e. the *dark matter*. If this matter component exists, then fluctuations in that component can grow as soon as it decouples from the cosmic plasma, well before photons decouple from baryons to set the cosmic microwave background free.

We can consider the dark matter as a collisionless fluid. Previous definitions of Jeans mass, horizon mass and dissipation mass can be extended even to this fluid by substituting the sound velocity with the average velocity v_\star of the collisionless particles. In this case fluctuations on mass scales less than the Jeans mass do not propagate as acoustic waves but are damped by the velocity dispersion of particles. This dissipation process is called *free streaming*. Perturbations are completely canceled when their mass is equal to the *free streaming mass*,

$$M_{FS} = \frac{4}{3}\pi R_{FS}^3 \rho_{DM} , \quad (\text{B.52})$$

where R_{FS} is the free streaming length,

$$R_{FS} = a \int_0^t \frac{v(t')}{a(t')} dt' . \quad (\text{B.53})$$

If we assume that dark matter decoupled from the cosmic plasma when it was already non-relativistic (*Cold Dark Matter*), the Jeans mass and the free streaming mass are almost identical

and much lower than the masses of cosmological interest, being $M_J(a_{\text{rec}}) \simeq M_{FS}(a_{\text{rec}}) \sim 10^5 M_\odot/h$. Structures can thus form starting at the smallest scales. Baryons can then fall into the potential wells of the dark matter structures once they decouple from radiation.

Among the fluctuations of mass $M \leq M_J(a_{\text{rec}})$, those which enter the horizon at $a \leq a_{\text{eq}}$ cannot grow until radiation ceases dominating the expansion of the universe: before a_{eq} , the expansion timescale $t_{\text{exp}} \sim (G\rho_R)^{-1/2}$ is smaller than the collapse time scale $t_{DM} \sim (G\rho_{DM})^{-1/2}$ of dark-matter fluctuations. In other words, the radiation-driven expansion of the universe prevents dark-matter perturbations from collapsing. Since the time evolution of density perturbations before equivalence is $\delta \propto a^2$, fluctuations of mass $M < M_H(a_{\text{eq}})$ which enter the horizon at a_{enter} are suppressed at equivalence by a factor

$$f_{\text{sup}} = \left(\frac{a_{\text{enter}}}{a_{\text{eq}}} \right)^2. \quad (\text{B.54})$$

B.7.2 Density power spectrum

It is very convenient to think of the linear perturbations as of superpositions of plane waves which evolve independently while the fluctuations are still linear. In other words, we can decompose the density contrast into Fourier modes. This description should be valid only in flat space, but we can use it also for curved models because 1) at early times space can be considered flat in all cosmological models and 2) at late times the interesting scales of the density perturbations are much smaller than the curvature radius of the universe.

We therefore write the density contrast as

$$\delta(\vec{r}) = \int \frac{d^3k}{(2\pi)^3} \hat{\delta}(\vec{k}) e^{-i\vec{k}\vec{r}}, \quad (\text{B.55})$$

where \vec{k} is the wavevector and $\hat{\delta}$ denotes the Fourier transform of δ ,

$$\hat{\delta}(\vec{k}) = \int d^3r \delta(\vec{r}) e^{i\vec{k}\vec{r}}. \quad (\text{B.56})$$

The *Power spectrum* of the density fluctuations is then defined as

$$P(k) \equiv \langle |\hat{\delta}^2(\vec{k})| \rangle. \quad (\text{B.57})$$

It is commonly assumed that the primordial power spectrum has a power-law form,

$$P_i(k) = A_i k^{n_i}. \quad (\text{B.58})$$

Moreover, if we require that the primordial power spectrum is *scale invariant*, i.e. the fluctuations in the gravitational potential are independent of the length scale, the power index must be $n_i = 1$. This power spectrum is then called the *Harrison-Zel'dovich spectrum*, which is compatible with predictions from inflationary models, although they tend to require $n_i \lesssim 1$.

The primordial power spectrum is later modified by all the physical processes which affect the growth of density perturbations. In particular, we must take into account the suppression of the fluctuations which enter the horizon before equivalence. Given that the time a_{eq} when a perturbation of comoving length λ or wavenumber $k = \lambda^{-1}$ enters the horizon is $a_{\text{enter}} \propto k^{-1}$ for $a_{\text{enter}} \ll a_{\text{eq}}$, the suppression factor (B.54) can be written as

$$f_{\text{sup}} = \left(\frac{k_0}{k} \right)^2, \quad (\text{B.59})$$

where k_0 is the wavenumber corresponding to a perturbation which enters the horizon at a_{eq} . Combining the primordial spectrum with this suppression of small scale modes, we obtain

$$P(k) \propto \begin{cases} k & \text{for } k \ll k_0 \\ k^{-3} & \text{for } k \gg k_0 \end{cases}. \quad (\text{B.60})$$

Several methods are available for normalizing the power spectrum. The first is based on the measurements of the temperature of the cosmic microwave background. The COBE satellite has measured temperature fluctuations at the *rms* level of $\Delta T/T \sim 1.3 \times 10^{-5}$ at angular scales of $\sim 7^\circ$. If a shape for the power spectrum is assumed, these fluctuations can be translated into an amplitude of $P(k)$. However, due to the large scale of the measurements, this method sets the amplitude on large scale (small k) only.

The second possibility is that based on the local variance of galaxy counts. One then must assume that galaxies are biased tracers of underlying dark matter fluctuations. Conventionally, the variance of galaxy counts $\sigma_{8,\text{gal}}$ is measured within spheres of radius $8 h^{-1}\text{Mpc}$. Recent measurements find $\sigma_{8,\text{gal}} \approx 1$. However, in order to set the amplitude of $P(k)$ properly, the correct expression for bias must be known.

Finally, the normalization can be made by using the local abundance of galaxy clusters [white93a](#); [eke96](#); [viana96](#). Indeed, galaxy clusters form by gravitational instability from dark matter density perturbations. Their spatial number density can then be used for setting the amplitude of the power spectrum on the scales of the density fluctuations collapsing to form galaxy clusters. This scale is of order $6 \div 10 \text{ Mpc}/h$.

B.7.3 Non-linear evolution

Once the non linear regime is reached by the density perturbations, their evolution is separated from the universal expansion and they start to collapse to form virialized objects. It is very difficult to properly describe the collapse process unless one makes strong assumptions, for example on the symmetry of the perturbations.

The simplest assumption we can make is that the collapse is spherical. In absence of the cosmological constant, the radius R of a mass shell in a spherically symmetric density perturbation evolves according to

$$\frac{d^2R}{dt^2} = -\frac{GM}{R^2}, \quad (\text{B.61})$$

where M is the mass within the mass shell. Integrating this equation, we obtain

$$\frac{1}{2} \left(\frac{dR}{dt} \right)^2 - \frac{GM}{R} = E. \quad (\text{B.62})$$

If the energy $E < 0$, the shell collapses. Using this spherical approximation, the solution of Eq. (B.62) is characterized by

- a maximum expansion, $R = R_{\max}$, at $t = t_{\max}$, when the perturbation density is $\rho_p(t_{\max}) = (3\pi/4)^2 \bar{\rho}(t_{\max}) \approx 5.5 \bar{\rho}(t_{\max})$, where $\bar{\rho}$ is the average density of the unperturbed background;
- a singularity, $R = 0$, at the collapse time $t_c = 2t_{\max}$, when density ideally goes to infinity at the center.

In fact, when the density is high, small departures from spherical symmetry will result in the formation of shocks and considerable pressure gradients. Heating of the material will occur due to the dissipation of shocks which converts the kinetic energy of collapse into heat. The final result will therefore be an equilibrium state which is not a singular point but some extended configuration with radius R_{vir} and mass M . This happens when the system reaches the virial equilibrium. From

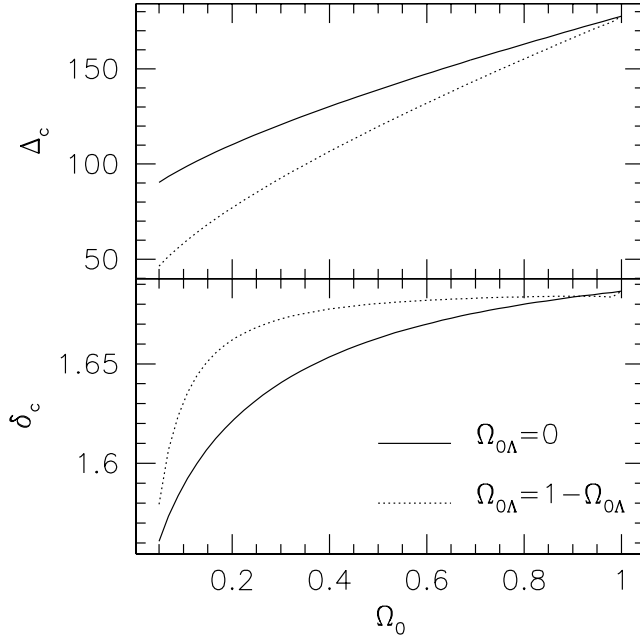


Figure B.7.2: Lower panel: virial over density of collapsed objects in units of the critical density as a function of Ω_0 . Results are plotted for open models with $\Omega_{0\Lambda} = 0$ (solid line) and flat models with $\Omega_0 + \Omega_{0\Lambda} = 1$ (dotted line). Upper panel: linear extrapolation of the density contrast at the collapse time t_c . The solid and the dotted lines are as in the upper panel.

the virial theorem, $R_{\text{vir}} = R_{\max}/2$. In an Einstein-de Sitter universe, the perturbation density in units of the critical density at t_c is

$$\Delta_c \equiv \frac{\rho_p(t_c)}{\rho_{\text{cr}}(t_c)} = 18\pi^2 \approx 178 . \quad (\text{B.63})$$

An extrapolation of linear theory would give a density contrast $\delta_c = \delta(t_c) = 3(12\pi)^{2/3}/20 \approx 1.687$ with a weak dependence on the cosmological parameters.

We show in Fig. (B.7.2) how Δ_c and δ_c for halos collapsing at $z_c = 0$ change for a variety of parameters Ω_0 and $\Omega_{0\Lambda}$. The critical overdensity δ_c has only a weak dependence on Ω_0 for both open models with $\Omega_{0\Lambda} = 0$ and flat models with $\Omega_0 + \Omega_{0\Lambda} = 1$. The dependence of Δ_c on the cosmological models is much stronger.

Of course, non-linearity affects the shape of the power spectrum $P(k)$ in a very complicated way. Numerical methods are required for properly evaluating the non-linear power spectrum. Analytic formulae can be obtained only under some strong assumptions. For example, starting from the *ansatz* that the two point correlation functions in the linear and non-linear regimes are related by a general scaling relation **hamilton91** analytic formulae describing the non-linear behavior of $P(k)$ have been derived **jain95; peacock96; smith02** We show in Fig. (B.7.3) the CDM power spectrum corresponding to an Einstein-de Sitter model with $h = 0.5$ and normalized to the local cluster abundance. The solid line shows the results obtained by assuming a primordial Harrison-Zel'dovich spectrum and linear evolution of the density perturbations on all scales. The dashed curve shows the non-linear evolution of the previous spectrum to $z = 0$. Non-linearity affects the small-scale (large k) part of the spectrum, because small scale perturbations are the first which enter the non-linear regime.

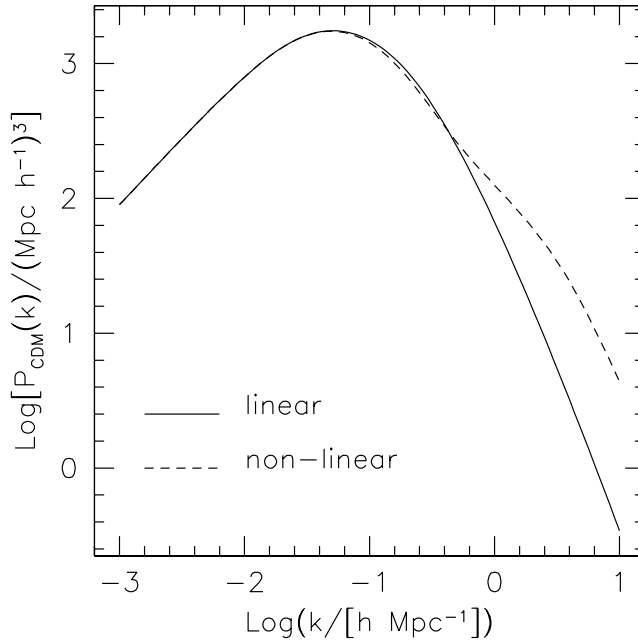


Figure B.7.3: CDM power spectrum, normalized to the local cluster abundance, for an Einstein-de Sitter universe with $h = 0.5$. The solid curve shows the linear power spectrum, extrapolated to the present time; the dashed line shows its non-linear evolution.

B.8 Mass function

The mass distribution of dark matter halos undergoing spherical collapse in the framework of CDM models is described by the Press & Schechter function [press74](#). The number density of collapsed lumps at redshift z with mass in the range $[M, M + dM]$ is

$$n(M, z)dM = \frac{\bar{\rho}}{M} f(v) \frac{dv}{dM} dM, \quad (\text{B.64})$$

where $\bar{\rho}$ is the universe mean density at redshift z . The function f depends only the variable $v = \delta_c(z)\sigma_M$ and is normalized such that $\int f(v)dv = 1$. $\delta_c(z)$ is the linearly extrapolated density contrast of halos collapsed at redshift z (see previous section). The r.m.s. density fluctuation at the mass scale M , σ_M , is given by

$$\sigma_M = \frac{1}{2\pi^2} \int_0^\infty dk k^2 P(k) W^2(kR), \quad (\text{B.65})$$

where $W(kR)$ is the Fourier transform of the window function, which describes the shape of the volume from which the collapsing object is accreting material. Finally, R is the comoving size of the fluctuation of mass M .

In their original derivation of the cosmological mass function, Press & Schechter obtained

$$f(v) = \frac{1}{\sqrt{2\pi}} \exp\left(-\frac{v^2}{2}\right). \quad (\text{B.66})$$

The mass function has been used in this form for more than a decade. However, the last generation of N -body simulations revealed significant deviations of the original Press & Schechter function from the numerical description of the mass distribution of dark matter halos. Correcting the

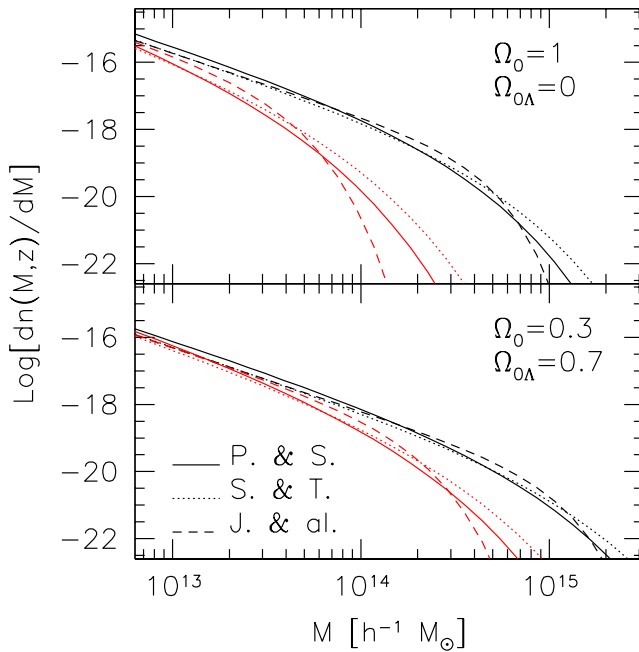


Figure B.8.1: Differential mass function of dark matter halos. Three different mass functions are showed: the original Press & Schechter function (solid lines), its modification obtained by including non-spherical collapse by Sheth & Tormen (dotted lines) and the mass function derived from numerical simulations by Jenkins et al. (dashed lines). Results are plotted for a flat model with $\Omega_0 = 0.3$ and $\Omega_{0\Lambda} = 0.7$ and for an open model with $\Omega_0 = 0.3$ and $\Omega_{0\Lambda} = 0$. Black and red lines show the mass functions of halos at redshift $z = 0$ and $z = 1$, respectively.

Press-Schechter approach by incorporating the effects of non-spherical collapse, Sheth & Tormen [sheth99](#) found

$$f(v) = \sqrt{\frac{2A}{\pi}} C \left(1 + \frac{1}{(Av^2)^q} \right) \exp \left(-\frac{Av^2}{2} \right), \quad (\text{B.67})$$

where $A = 0.707$, $C = 0.3222$ and $q = 0.3$. This equation reduces to the Press & Schechter expression for $A = 1$, $C = 0.5$ and $q = 0$. Fitting the results of N -body simulations, Jenkins et al. [jenkins01](#) found a formula which is statistically not distinguishable from the Sheth & Tormen one with $A = 0.75$.

We plot in Fig. (B.8.1) the three different mass functions by Press & Schechter, Sheth & Tormen and Jenkins et al. The original Press & Schechter function underpredicts the abundance of large mass halos with respect to the Sheth & Tormen and the Jenkins et al. functions. The last two are very close to each other; there is only a small difference in the very high mass tail.

B.9 Quintessence models

As seen in the previous sections, the cosmological constant is strongly connected to the energy density of vacuum. Actually most favored cosmological models predict that today this vacuum energy density is of the same order of magnitude as the amount of dark and baryonic matter energy density in the universe, $\varepsilon \approx (10^{-3} \text{ eV})^4$. This number is tiny in terms of the natural scale of primordial energy density given by the Planck mass $M_p = 1.22 \times 10^{19} \text{ GeV}$. A dominant radiation or matter energy density decreases as $\rho \sim M_p^2 t^{-2}$ and the present age of the universe is $t_0 \approx 1.5 \times 10^{10}$

yr. It is therefore very easy to explain the smallness of the actual matter energy density in terms of the long duration of the cosmological expansion. On the other hand, assuming that the vacuum energy density is constant, it is very difficult to understand why the cosmological constant is so small today.

In order to solve this problem, it has been proposed that even Λ might be very small now because it has been rolling toward zero for a very long time. This idea that the universe contains nearly to homogeneous dark energy, called *Quintessence*, that approximates a time-variable cosmological “constant” arose also in particle physics, through the discussion of phase transition in the early universe and through the search for a dynamical cancellation of the vacuum energy density. We shall not present a rigorous treatment of quintessence models here, but only summarize some basic concepts. For a more quantitative discussion, we refer to the excellent reviews by Peebles & Ratra **peebles02** and by Wetterich **wetterich02**

Dark energy is usually modeled as that of a homogeneous scalar field, Φ . In this case, if spatial curvature can be neglected, the field equation is

$$\ddot{\Phi} + 3\frac{\dot{a}}{a}\dot{\Phi} + \frac{dV}{d\Phi} = 0, \quad (\text{B.68})$$

where V is the potential energy density, which is a function of the field Φ .

The energy-momentum tensor of this homogeneous field is diagonal in the rest frame of an observer moving such that the universe appears isotropic, and its time and space parts along the diagonal define the energy density and pressure,

$$\rho_\Phi = \frac{1}{2}\dot{\Phi}^2 + V(\Phi), \quad (\text{B.69})$$

$$p_\Phi = \frac{1}{2}\dot{\Phi}^2 - V(\Phi). \quad (\text{B.70})$$

The general form of the equation of state relating ρ_Φ to p_Φ is again

$$p_\Phi = w\rho_\Phi c^2, \quad (\text{B.71})$$

with $w < -1/3$. If the scalar field varies slowly in time ($\dot{\Phi}^2 \ll V(\Phi)$), the field energy approximates the effect of the Einstein’s cosmological constant with $p_\Phi \simeq -\rho_\Phi c^2$.

This condition is verified during the inflationary epoch but not at its the end, when $V \sim 0$. When this happens, Φ oscillates. The scalar field is supposed to vary rapidly enough to produce the entropy of our universe and the field or the entropy may produce the baryons, leaving ρ_Φ small or zero. If, after inflation, the time evolution of ρ_Φ starts to slow down and becomes slower than that of the matter density, there comes a time when ρ_Φ starts to dominate and the universe appears to have a cosmological constant.

There are many and well justified forms for the potential of this slowly evolving field (e.g. Lucchin & Matarrese **lucchin85**). A very simple model assumes a potential of the form

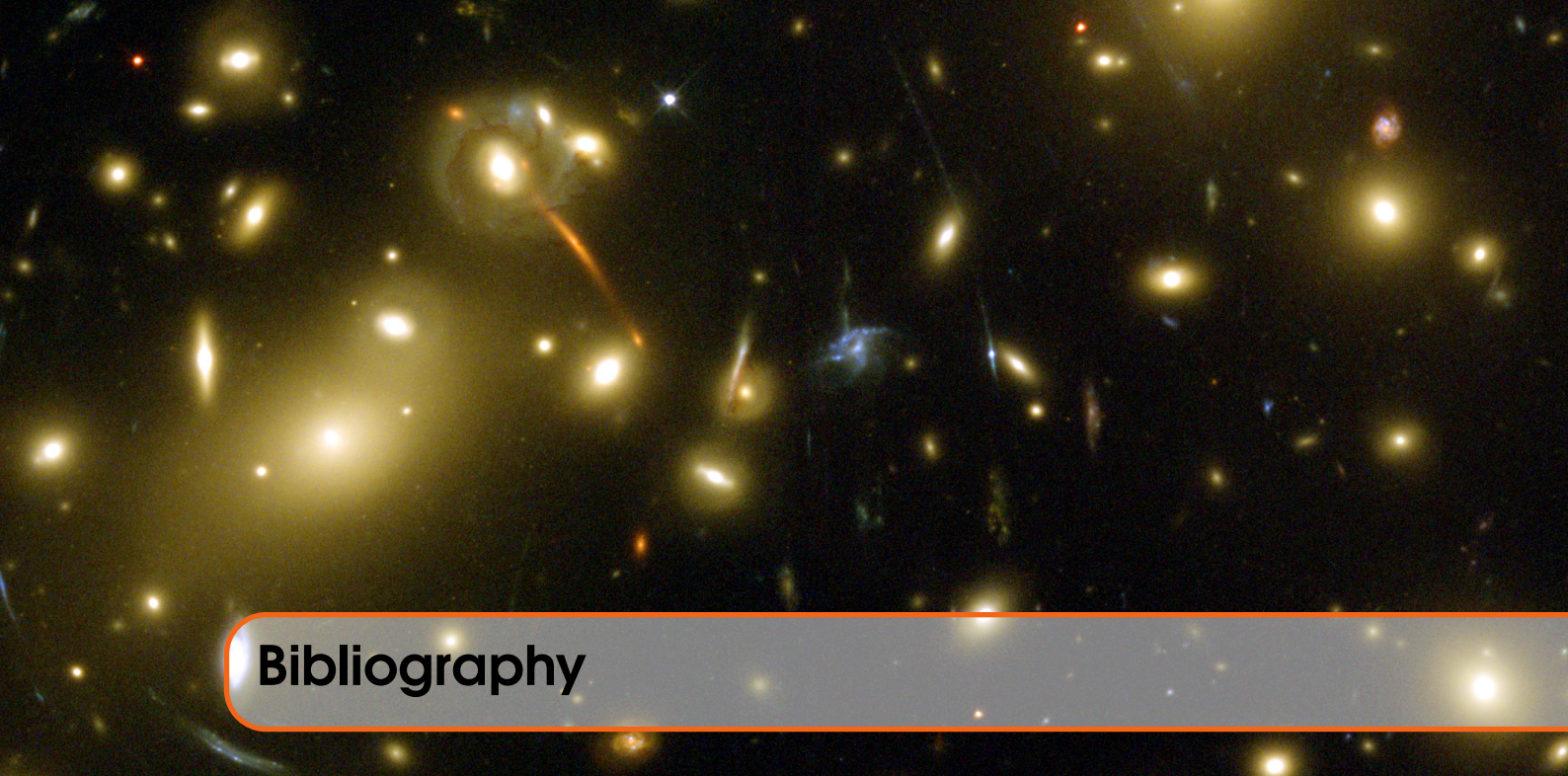
$$V = \frac{Q}{\Phi^\alpha}, \quad (\text{B.72})$$

where the constant Q has dimensions of mass raised to the power $\alpha + 4$. Using this potential, the ratio of the mass densities in the scalar field and in the matter or radiation turns out to be

$$\frac{\rho_\Phi}{\rho} \propto t^{4/(2+\alpha)}. \quad (\text{B.73})$$

In the limit where the parameter $\alpha = 0$, ρ_Φ is constant and this model is equivalent to the Einstein cosmological constant. Solutions as those obtained by using this potential for $\alpha > 0$ have two properties that seem desirable. First, they are said to be attractors **ratra88** or trackers **steinhardt99**

meaning that they are asymptotic solutions for a broad range of initial conditions at high redshift. For example, energy distribution becomes nearly homogeneous even when gravity has collected the other matter into non-relativistic clumps. Second, the energy density in the attractor solution decreases less rapidly than that of matter and radiation.



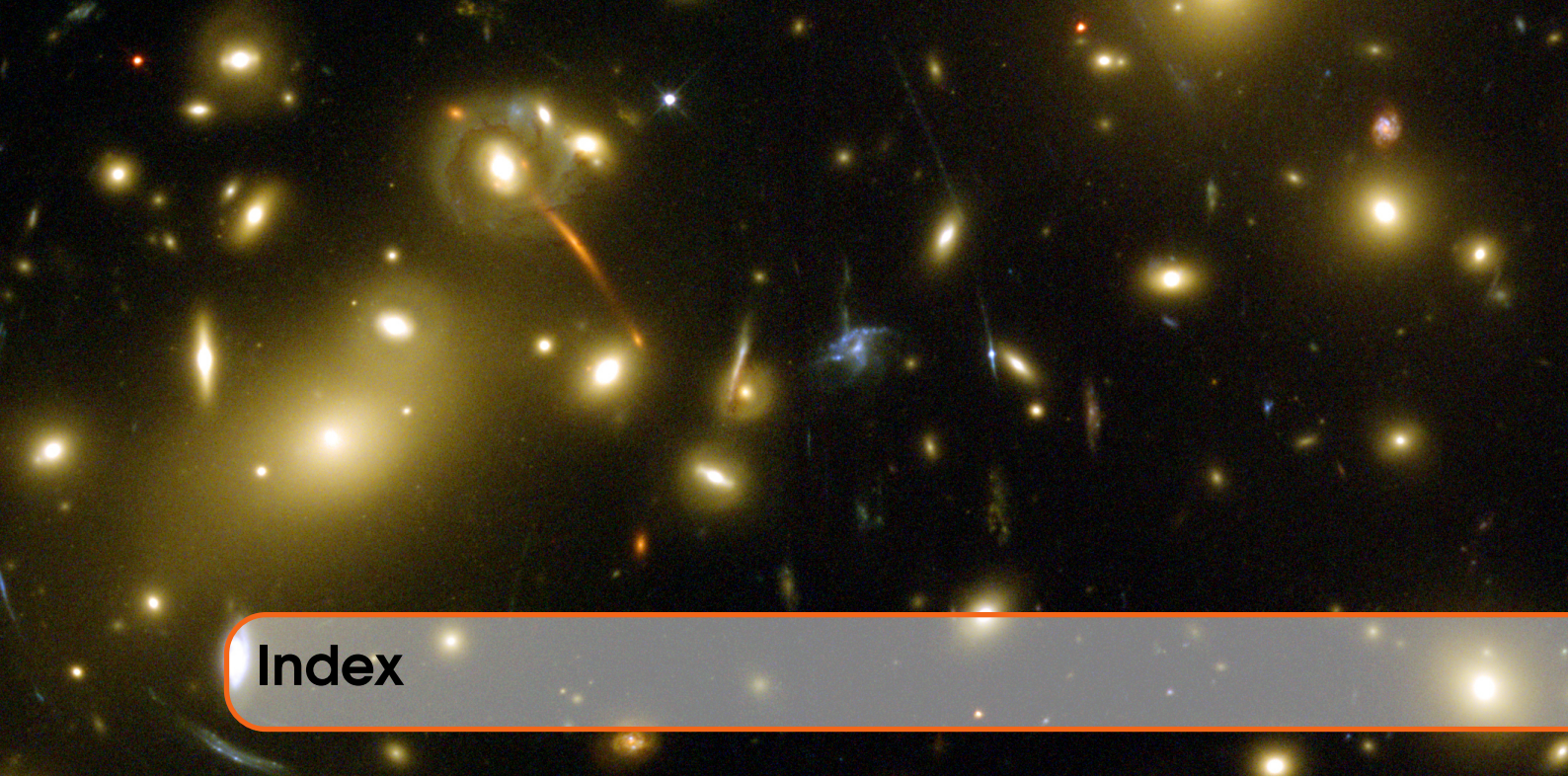
Bibliography

- Alard, C. et al. (1995). “The DUO programme: first results of a microlensing investigation of the Galactic disk and bulge conducted with the ESO Schmidt telescope.” In: *The Messenger* 80, pages 31–34 (cited on page 94).
- Alcock, C. et al. (1995). “First Observation of Parallax in a Gravitational Microlensing Event”. In: *ApJL* 454, page L125. DOI: [10.1086/309783](https://doi.org/10.1086/309783). eprint: [astro-ph/9506114](https://arxiv.org/abs/astro-ph/9506114) (cited on pages 87, 88).
- Aubert, D., A. Amara, and R. B. Metcalf (2007). “Smooth Particle Lensing”. In: *MNRAS* 376, pages 113–124. DOI: [10.1111/j.1365-2966.2006.11296.x](https://doi.org/10.1111/j.1365-2966.2006.11296.x). eprint: [astro-ph/0604360](https://arxiv.org/abs/astro-ph/0604360) (cited on page 18).
- Barnes, J. and P. Hut (1986). “A hierarchical O($N \log N$) force-calculation algorithm”. In: *Nature* 324, pages 446–449. DOI: [10.1038/324446a0](https://doi.org/10.1038/324446a0) (cited on page 18).
- Bartelmann, M. and P. Schneider (2001). “Weak gravitational lensing”. In: *Phys.Rep.* 340, pages 291–472. DOI: [10.1016/S0370-1573\(00\)00082-X](https://doi.org/10.1016/S0370-1573(00)00082-X). eprint: [astro-ph/9912508](https://arxiv.org/abs/astro-ph/9912508) (cited on page 30).
- Batista, V., J.-P. Beaulieu, et al. (2015). “Confirmation of the OGLE-2005-BLG-169 Planet Signature and Its Characteristics with Lens-Source Proper Motion Detection”. In: *ApJ* 808, 170, page 170. DOI: [10.1088/0004-637X/808/2/170](https://doi.org/10.1088/0004-637X/808/2/170). arXiv: [1507.08914 \[astro-ph.EP\]](https://arxiv.org/abs/1507.08914) (cited on page 114).
- Batista, V., A. Gould, et al. (2011). “MOA-2009-BLG-387Lb: a massive planet orbiting an M dwarf”. In: *A & A* 529, A102, A102. DOI: [10.1051/0004-6361/201016111](https://doi.org/10.1051/0004-6361/201016111). arXiv: [1102.0558 \[astro-ph.EP\]](https://arxiv.org/abs/1102.0558) (cited on page 115).
- Beaulieu, J.-P. et al. (2006). “Discovery of a cool planet of 5.5 Earth masses through gravitational microlensing”. In: *Nature* 439, pages 437–440. DOI: [10.1038/nature04441](https://doi.org/10.1038/nature04441). eprint: [astro-ph/0601563](https://arxiv.org/abs/astro-ph/0601563) (cited on page 115).
- Bennett, D. P., J. Anderson, et al. (2006). “Identification of the OGLE-2003-BLG-235/MOA-2003-BLG-53 Planetary Host Star”. In: *ApJL* 647, pages L171–L174. DOI: [10.1086/507585](https://doi.org/10.1086/507585). eprint: [astro-ph/0606038](https://arxiv.org/abs/astro-ph/0606038) (cited on page 114).

- Bennett, D. P., A. Bhattacharya, et al. (2015). “Confirmation of the Planetary Microlensing Signal and Star and Planet Mass Determinations for Event OGLE-2005-BLG-169”. In: *ApJ* 808, 169, page 169. DOI: [10.1088/0004-637X/808/2/169](https://doi.org/10.1088/0004-637X/808/2/169). arXiv: [1507.08661 \[astro-ph.EP\]](https://arxiv.org/abs/1507.08661) (cited on page 114).
- Bond, I. A. et al. (2004). “OGLE 2003-BLG-235/MOA 2003-BLG-53: A Planetary Microlensing Event”. In: *ApJL* 606, pages L155–L158. DOI: [10.1086/420928](https://doi.org/10.1086/420928). eprint: [astro-ph/0404309](https://arxiv.org/abs/astro-ph/0404309) (cited on page 114).
- Bozza, V. (2010). “Gravitational lensing by black holes”. In: *General Relativity and Gravitation* 42, pages 2269–2300. DOI: [10.1007/s10714-010-0988-2](https://doi.org/10.1007/s10714-010-0988-2). arXiv: [0911.2187 \[gr-qc\]](https://arxiv.org/abs/0911.2187) (cited on page 17).
- Calchi Novati, S. et al. (2018). “Spitzer Microlensing Parallax for OGLE-2016-BLG-1067: a sub-Jupiter Orbiting an M-dwarf in the Disk”. In: *ArXiv e-prints*. arXiv: [1801.05806 \[astro-ph.EP\]](https://arxiv.org/abs/1801.05806) (cited on page 115).
- Capaccioli, M. et al. (1989). “Properties of the nova population in M31”. In: *AJ* 97, pages 1622–1633. DOI: [10.1086/115104](https://doi.org/10.1086/115104) (cited on page 60).
- Cooley, James W and John W Tukey (1965). “An algorithm for the machine calculation of complex Fourier series”. In: *Mathematics of computation* 19(90), pages 297–301 (cited on page 19).
- Darwin, C. (1959). “The Gravity Field of a Particle”. In: *Proceedings of the Royal Society of London Series A* 249, pages 180–194. DOI: [10.1098/rspa.1959.0015](https://doi.org/10.1098/rspa.1959.0015) (cited on page 17).
- Dominik, M. and K. C. Sahu (1998). “Astrometric Microlensing of Stars”. In: *ArXiv Astrophysics e-prints*. eprint: [astro-ph/9805360](https://arxiv.org/abs/astro-ph/9805360) (cited on page 94).
- Dong, S. et al. (2009). “Microlensing Event MOA-2007-BLG-400: Exhuming the Buried Signature of a Cool, Jovian-Mass Planet”. In: *ApJ* 698, pages 1826–1837. DOI: [10.1088/0004-637X/698/2/1826](https://doi.org/10.1088/0004-637X/698/2/1826). arXiv: [0809.2997](https://arxiv.org/abs/0809.2997) (cited on page 115).
- Erdl, H. and P. Schneider (1993). “Classification of the multiple deflection two point-mass gravitational lens models and application of catastrophe theory in lensing”. In: *A & A* 268, pages 453–471 (cited on page 103).
- Gaudi, B. S. (2012). “Microlensing Surveys for Exoplanets”. In: *Annu.Rev.Astron.Astrophys.* 50, pages 411–453. DOI: [10.1146/annurev-astro-081811-125518](https://doi.org/10.1146/annurev-astro-081811-125518) (cited on pages 108, 115, 126).
- Gaudi, B. S. et al. (2008). “Discovery of a Jupiter/Saturn Analog with Gravitational Microlensing”. In: *Science* 319, page 927. DOI: [10.1126/science.1151947](https://doi.org/10.1126/science.1151947). arXiv: [0802.1920](https://arxiv.org/abs/0802.1920) (cited on page 111).
- Gould, A. (1994). “Proper motions of MACHOs”. In: *ApJL* 421, pages L71–L74. DOI: [10.1086/187190](https://doi.org/10.1086/187190) (cited on pages 84, 126).
- Gould, A. and A. Loeb (1992). “Discovering planetary systems through gravitational microlenses”. In: *ApJ* 396, pages 104–114. DOI: [10.1086/171700](https://doi.org/10.1086/171700) (cited on page 115).
- Gould, A., A. Udalski, et al. (2009). “The Extreme Microlensing Event OGLE-2007-BLG-224: Terrestrial Parallax Observation of a Thick-Disk Brown Dwarf”. In: *ApJL* 698, pages L147–L151. DOI: [10.1088/0004-637X/698/2/L147](https://doi.org/10.1088/0004-637X/698/2/L147). arXiv: [0904.0249 \[astro-ph.GA\]](https://arxiv.org/abs/0904.0249) (cited on pages 88, 90).
- Han, C. (2006). “Properties of Planetary Caustics in Gravitational Microlensing”. In: *ApJ* 638, pages 1080–1085. DOI: [10.1086/498937](https://doi.org/10.1086/498937). eprint: [astro-ph/0510206](https://arxiv.org/abs/astro-ph/0510206) (cited on page 109).
- Han, C. and B. S. Gaudi (2008). “A Characteristic Planetary Feature in Double-Peaked, High-Magnification Microlensing Events”. In: *ApJ* 689, 53-58, pages 53–58. DOI: [10.1086/592723](https://doi.org/10.1086/592723). arXiv: [0805.1103](https://arxiv.org/abs/0805.1103) (cited on page 114).
- Han, C., Y. K. Jung, et al. (2013). “Microlensing Discovery of a Tight, Low-mass-ratio Planetary-mass Object around an Old Field Brown Dwarf”. In: *ApJ* 778, 38, page 38. DOI: [10.1088/0004-637X/778/1/38](https://doi.org/10.1088/0004-637X/778/1/38). arXiv: [1307.6335 \[astro-ph.EP\]](https://arxiv.org/abs/1307.6335) (cited on page 115).

- Hog, E., I. D. Novikov, and A. G. Polnarev (1995). “MACHO photometry and astrometry.” In: *A & A* 294, pages 287–294 (cited on page 94).
- Jung, Y. K., A. Udalski, I. A. Bond, et al. (2017). “OGLE-2016-BLG-1003: First Resolved Caustic-crossing Binary-source Event Discovered by Second-generation Microlensing Surveys”. In: *ApJ* 841, 75, page 75. DOI: [10.3847/1538-4357/aa7057](https://doi.org/10.3847/1538-4357/aa7057). arXiv: [1705.01531 \[astro-ph.SR\]](https://arxiv.org/abs/1705.01531) (cited on page 114).
- Jung, Y. K., A. Udalski, T. Sumi, et al. (2015). “OGLE-2013-BLG-0102LA,B: Microlensing Binary with Components at Star/Brown Dwarf and Brown Dwarf/Planet Boundaries”. In: *ApJ* 798, 123, page 123. DOI: [10.1088/0004-637X/798/2/123](https://doi.org/10.1088/0004-637X/798/2/123). arXiv: [1407.7926 \[astro-ph.SR\]](https://arxiv.org/abs/1407.7926) (cited on page 115).
- Jung, Y. K., A. Udalski, J. C. Yee, et al. (2017). “Binary Source Microlensing Event OGLE-2016-BLG-0733: Interpretation of a Long-term Asymmetric Perturbation”. In: *AJ* 153, 129, page 129. DOI: [10.3847/1538-3881/aa5d07](https://doi.org/10.3847/1538-3881/aa5d07). arXiv: [1611.00775 \[astro-ph.SR\]](https://arxiv.org/abs/1611.00775) (cited on page 114).
- Kassiola, A. and I. Kovner (1993). “Elliptic Mass Distributions versus Elliptic Potentials in Gravitational Lenses”. In: *ApJ* 417, page 450. DOI: [10.1086/173325](https://doi.org/10.1086/173325) (cited on page 170).
- Kervella, P. et al. (2004). “Cepheid distances from infrared long-baseline interferometry. III. Calibration of the surface brightness-color relations”. In: *A & A* 428, pages 587–593. DOI: [10.1051/0004-6361:20041416](https://doi.org/10.1051/0004-6361:20041416) (cited on page 85).
- Kormann, R., P. Schneider, and M. Bartelmann (1994). “Isothermal elliptical gravitational lens models”. In: *A & A* 284, pages 285–299 (cited on pages 154, 160, 169).
- Koshimoto, N., Y. Shvartzvald, et al. (2017). “MOA-2016-BLG-227Lb: A Massive Planet Characterized by Combining Light-curve Analysis and Keck AO Imaging”. In: *AJ* 154, 3, page 3. DOI: [10.3847/1538-3881/aa72e0](https://doi.org/10.3847/1538-3881/aa72e0). arXiv: [1704.01724 \[astro-ph.EP\]](https://arxiv.org/abs/1704.01724) (cited on page 115).
- Koshimoto, N., A. Udalski, et al. (2014). “OGLE-2008-BLG-355Lb: A Massive Planet around a Late-type Star”. In: *ApJ* 788, 128, page 128. DOI: [10.1088/0004-637X/788/2/128](https://doi.org/10.1088/0004-637X/788/2/128). arXiv: [1403.7005 \[astro-ph.EP\]](https://arxiv.org/abs/1403.7005) (cited on page 115).
- Lee, C. -H. et al. (2009). “Finite source effects in microlensing: A precise, easy to implement, fast and numerical stable formalism”. In: *Astrophys. J.* 695, pages 200–207. DOI: [10.1088/0004-637X/695/1/200](https://doi.org/10.1088/0004-637X/695/1/200). arXiv: [0901.1316 \[astro-ph.GA\]](https://arxiv.org/abs/0901.1316) (cited on pages 84, 85).
- Lissauer, J. J. (1987). “Timescales for planetary accretion and the structure of the protoplanetary disk”. In: *Icarus* 69, pages 249–265. DOI: [10.1016/0019-1035\(87\)90104-7](https://doi.org/10.1016/0019-1035(87)90104-7) (cited on page 115).
- Mao, S. (2008). “Introduction to Gravitational Microlensing”. In: *ArXiv e-prints*. arXiv: [0811.0441](https://arxiv.org/abs/0811.0441) (cited on page 91).
- Meneghetti, M. et al. (2010). “Weighing simulated galaxy clusters using lensing and X-ray”. In: *A & A* 514, A93, A93. DOI: [10.1051/0004-6361/200913222](https://doi.org/10.1051/0004-6361/200913222). arXiv: [0912.1343](https://arxiv.org/abs/0912.1343) (cited on page 18).
- Miyamoto, M. and Y. Yoshii (1995). “Astrometry for Determining the MACHO Mass and Trajectory”. In: *AJ* 110, page 1427. DOI: [10.1086/117616](https://doi.org/10.1086/117616) (cited on page 94).
- Paczynski, B. (1986). “Gravitational microlensing by the galactic halo”. In: *ApJ* 304, pages 1–5. DOI: [10.1086/164140](https://doi.org/10.1086/164140) (cited on page 93).
- Paulin-Henriksson, S. et al. (2003). “The POINT-AGAPE survey: 4 high signal-to-noise microlensing candidates detected towards M 31”. In: *A & A* 405, pages 15–21. DOI: [10.1051/0004-6361:20030519](https://doi.org/10.1051/0004-6361:20030519). eprint: [astro-ph/0207025](https://arxiv.org/abs/astro-ph/0207025) (cited on page 94).
- Poleski, R. et al. (2014). “Super-massive Planets around Late-type Stars: the Case of OGLE-2012-BLG-0406Lb”. In: *ApJ* 782, 47, page 47. DOI: [10.1088/0004-637X/782/1/47](https://doi.org/10.1088/0004-637X/782/1/47). arXiv: [1307.4084 \[astro-ph.EP\]](https://arxiv.org/abs/1307.4084) (cited on page 115).

- Proft, S., M. Demleitner, and J. Wambsganss (2011). “Prediction of astrometric microlensing events during the Gaia mission”. In: *A & A* 536, A50, A50. DOI: [10.1051/0004-6361/201117663](https://doi.org/10.1051/0004-6361/201117663). arXiv: [1201.4000 \[astro-ph.GA\]](https://arxiv.org/abs/1201.4000) (cited on page 94).
- Rhie, S. H. (2001). “Can A Gravitational Quadruple Lens Produce 17 images?” In: *ArXiv Astrophysics e-prints*. eprint: [astro-ph/0103463](https://arxiv.org/abs/astro-ph/0103463) (cited on page 99).
- Rhie, S. H. (2003). “n-point Gravitational Lenses with 5(n-1) Images”. In: *ArXiv Astrophysics e-prints*. eprint: [astro-ph/0305166](https://arxiv.org/abs/astro-ph/0305166) (cited on page 99).
- Sérsic, J. L. (1963). “Influence of the atmospheric and instrumental dispersion on the brightness distribution in a galaxy”. In: *Boletin de la Asociacion Argentina de Astronomia La Plata Argentina* 6, page 41 (cited on page 60).
- Shin, I.-G. et al. (2016). “A Super-Jupiter Microlens Planet Characterized by High-Cadence KMTNeT Microlensing Survey Observations of OGLE-2015-BLG-0954”. In: *Journal of Korean Astronomical Society* 49, pages 73–81. DOI: [10.5303/JKAS.2016.49.3.073](https://doi.org/10.5303/JKAS.2016.49.3.073). arXiv: [1603.00020 \[astro-ph.EP\]](https://arxiv.org/abs/1603.00020) (cited on page 115).
- Shvartzvald, Y. et al. (2014). “MOA-2011-BLG-322Lb: a ‘second generation survey’ microlensing planet”. In: *MNRAS* 439, pages 604–610. DOI: [10.1093/mnras/stt2477](https://doi.org/10.1093/mnras/stt2477). arXiv: [1310.0008 \[astro-ph.EP\]](https://arxiv.org/abs/1310.0008) (cited on page 115).
- Smith, James (2015). “Bending space–time: a commentary on Dyson, Eddington and Davidson (1920) - A determination of the deflection of light by the Sun’s gravitational field”. In: 373, page 2039 (cited on page 16).
- Street, R. A. et al. (2013). “MOA-2010-BLG-073L: An M-dwarf with a Substellar Companion at the Planet/Brown Dwarf Boundary”. In: *ApJ* 763, 67, page 67. DOI: [10.1088/0004-637X/763/1/67](https://doi.org/10.1088/0004-637X/763/1/67). arXiv: [1211.3782 \[astro-ph.EP\]](https://arxiv.org/abs/1211.3782) (cited on page 115).
- Sumi, T., D. P. Bennett, et al. (2010). “A Cold Neptune-Mass Planet OGLE-2007-BLG-368Lb: Cold Neptunes Are Common”. In: *ApJ* 710, pages 1641–1653. DOI: [10.1088/0004-637X/710/2/1641](https://doi.org/10.1088/0004-637X/710/2/1641). arXiv: [0912.1171 \[astro-ph.EP\]](https://arxiv.org/abs/0912.1171) (cited on page 115).
- Sumi, T., K. Kamiya, et al. (2011). “Unbound or distant planetary mass population detected by gravitational microlensing”. In: *Nature* 473, pages 349–352. DOI: [10.1038/nature10092](https://doi.org/10.1038/nature10092). arXiv: [1105.3544 \[astro-ph.EP\]](https://arxiv.org/abs/1105.3544) (cited on pages 93, 126).
- Tessore, N. and R. B. Metcalf (2015). “The elliptical power law profile lens”. In: *A & A* 580, A79, A79. DOI: [10.1051/0004-6361/201526773](https://doi.org/10.1051/0004-6361/201526773). arXiv: [1507.01819](https://arxiv.org/abs/1507.01819) (cited on page 169).
- Udalski, A. et al. (2005). “A Jovian-Mass Planet in Microlensing Event OGLE-2005-BLG-071”. In: *ApJL* 628, pages L109–L112. DOI: [10.1086/432795](https://doi.org/10.1086/432795). eprint: [astro-ph/0505451](https://arxiv.org/abs/astro-ph/0505451) (cited on pages 114, 115).
- Witt, H. J. (1990). “Investigation of high amplification events in light curves of gravitationally lensed quasars”. In: *A & A* 236, pages 311–322 (cited on pages 99, 101).
- Witt, H. J. and S. Mao (1994). “Can lensed stars be regarded as pointlike for microlensing by MACHOs?” In: *ApJ* 430, pages 505–510. DOI: [10.1086/174426](https://doi.org/10.1086/174426) (cited on page 84).
- Witt, H. J. and S. Mao (1995). “On the Minimum Magnification Between Caustic Crossings for Microlensing by Binary and Multiple Stars”. In: *ApJL* 447, page L105. DOI: [10.1086/309566](https://doi.org/10.1086/309566) (cited on pages 101, 105).
- Yee, J. C. et al. (2015). “First Space-based Microlens Parallax Measurement of an Isolated Star: Spitzer Observations of OGLE-2014-BLG-0939”. In: *ApJ* 802, 76, page 76. DOI: [10.1088/0004-637X/802/2/76](https://doi.org/10.1088/0004-637X/802/2/76). arXiv: [1410.5429 \[astro-ph.SR\]](https://arxiv.org/abs/1410.5429) (cited on pages 87, 89).



Index

Deflection of a light corpuscle, [9](#)

Deflection of light according to General Relativity, [11](#)

Figure, [10](#), [18](#), [30](#), [51–56](#), [58](#), [59](#), [71](#), [74](#), [79](#),
[82–86](#), [88–90](#), [95–98](#), [102](#), [104](#), [106–113](#), [119](#), [122](#), [123](#), [126](#), [127](#), [132](#),
[147–151](#), [155](#), [156](#), [160](#), [161](#), [163–169](#), [175](#), [176](#)